DEPARTMENT OF ELECTRIC DRIVES AND TRACTION

CZECH TECHNICAL UNIVERSITY IN PRAGUE

FACULTY OF ELECTRICAL ENGINEERING

CONTROLLED INDUCTION MOTOR DRIVE IN RAILWAY TRACTION

HABILITATION THESIS

NOVEMBER 2020

JAN BAUER

ACKNOWLEDGEMENT

I would like to thank my wife Irena and son Matyáš for their patience and support.

I convey a special thanks to doctoral students and my friends Ondřej Lipčák a Pavel Karlovský, that have helped me most during my work presented in this thesis. I thank many other former and current colleagues from FEE too.

I would also like to thank the company CRRC, which funded part of this research.

ABSTRACT

This habilitation thesis presents improvements in selected areas of induction motor drive application in railway traction vehicles. One of the most common induction motor control strategies in railway traction drives, is the Rotor Flux-Oriented Control. To reach high performance and high efficiency of the drive, precise knowledge of the induction motor equivalent circuit parameters is needed. Inaccurate knowledge of the induction motor equivalent circuit parameters leads to FOC detuning, which causes misalignment of the estimated flux position and, thus, inaccuracy of the whole control part. The problematics of induction motor drive parameter identification and accuracy of the induction motor model is one of the key points of the thesis.

The other part of the thesis describes a slip controller's development for freight locomotive with the induction motor drive, that is based on adhesion-slip characteristic slope detection. The proposed slip controller is designed to cope with a nonlinearity of the adhesion-slip characteristic and noise that occurs in the system. Moreover, the proposed slip controller does not need to know the train velocity, the wheelset velocity is only required parameter. The slip controller is designed as modular, and it consists of the adhesion-slip characteristic slope detection part and a controller part with acceleration protection.

Keywords: Induction Motor, Field Oriented Control, Adhesion Characteritsc, Slip

ABSTRAKT

Tato habilitační práce prezentuje možnosti vylepšení ve vybraných oblastech použití asynchronního pohonu v trakčních vozidlech. Jednou z nejběžněji používaných řídicích strategií je řízení orientované na rotorový tok. Pro dosažení vysoké dynamiky a účinnosti pohonu je nutné přesně znát parametry náhradního schématu motoru. Jejich nepřesné určení vede k nepřesnému určení polohy prostorového vektoru toku, a tím nepřesnosti celého řízení. Problematika identifikace parametrů pohonu asynchronního motoru a přesnosti modelu je jedním z klíčových bodů práce.

Druhá část práce popisuje vývoj regulátoru skluzu pro nákladní lokomotivu, založeného na detekci sklonu adhezní charakteristiky. Regulátor je navržen tak, aby respektoval nelinearitu adhezní charakteristiky a nepřesností měření. Regulátor navíc pracuje bez znalosti posuvné rychlost vlaku, využívá znalost rychlosti dvojkolí. Návrh regulátoru je proveden modulárně a skládá se z části pro detekci sklonu adhezní charakteristiky a části PI regulátoru s rozšířením o akcelerační ochranu.

Klíčová slova: Asynchronní motor, vektorové řízení, adhezní charakteristika, skluz

TABLE OF CONTENT

LIST OF FIGURES

LIST OF TABLES

INTRODUCTION

Nicola Tesla patented the first three-phase Alternating Current (AC) Induction Motor (IM) in 1888. Tesla knew his invention was more efficient and reliable than Thomas Edison's direct current (DC) motor. However, IM's speed control isn't a simple process, and even after decades since their massive spread into industrial applications, it remained a difficult task. That is why DC motors were still used in applications that required precise motion control and significant power output. Before the 1980s, induction motors as Variable Speed Drives (VSD) were used only in heavy industry for large motors.

Rapid development in AC motor control technology during the 1980s and 1990s meant VSD based on IM started to spread from heavy industry to other fields. Advancements in semiconductor technology, control hardware, and software made VSDs more reliable and affordable enough to compete with the more traditional controlled DC motors.

Due to its robustness, low maintenance, and simple construction, the IM drive became one of the most spread electromechanical converters globally. It covers wide applications from drives in Heating, Ventilation, and Air-Conditioning (HVAC) units with speed control requirements to drives requiring high dynamics and control accuracy in metalworks or traction applications. IMs are manufactured with powers starting at a few watts up to 1 MW.

Today's IM standard control strategy for demanding tasks is the so-called Field-Oriented Control (FOC). This strategy, originating in the 1970s in Germany, was developed for high-performance applications where smooth operation over the full speed range, the possibility of production of full motor torque at zero speed, and high dynamic performance, including fast acceleration and deceleration, are required. However, FOC is becoming an attractive option even for lower-performance applications, mainly due to the possibility of motor size, cost, and power consumption reduction. Within FOC, the stator currents of a three-phase IM or AC motor, respectively, are transformed into two orthogonal synchronously rotating components that can be visualized as a vector. One component defines the magnetic flux of the motor, the other the torque. FOC algorithm calculates the corresponding current component references from the flux and speed references required by the superior control system.

Compared to the relatively straightforward DC drive control, FOC is based on IM's mathematical model and its real-time calculation in the drive controller. However, the real-time model calculation was not possible until the early 1980s, when the first microprocessors came to the market. Since that, controlled AC drives have started to replace the older DC motors in literally all applications.

An IM model requires the knowledge of parameters such as the machine's stator and rotor resistances and inductances. The accuracy of the parameters directly influences the accuracy and dynamics of the control strategy. Furthermore, since electric motors consume a considerable part of the world's electric energy, electric motor drives' energy savings are an important topic, too.

Due to its robustness and low maintenance requirements, IM drives found their place in traction vehicles, where the advantage of maximal torque at zero speed plays an important role. The majority of railway traction vehicles are driven thanks to the transfer of traction, braking, or guiding force by a small contact area between wheels and rail (steal to steal contact) [1]. The ability to transfer the force by a contact area or the sum of the contact area's physical properties, respectively, is called the adhesion. The railway traction vehicle dependence on the adhesion represents a fundamental difference compared to many other drive methods.

The adhesion has substantial importance for efficient utilization of IM drive equipped railway traction vehicles, which is why it is under research and development for more than one hundred years. The power of these vehicles is continuously increasing. Thus, the requirements for efficient processing of the adhesion phenomenon in a vehicle control system (i.e., providing vehicles with a higher value of tractive and braking effort) are also increasing. The significant impulse for

speeding up the adhesion phenomenon research and development has been done at the end of the 1980s when controlled electrical drives were introduced and started to be used in everyday praxis. Tractive or braking effort depends on the force generated by the traction drive and the transfer of generated force through the wheel-rail contact area using adhesion phenomena. Many methods for better use of the adhesion were developed in the last decades [2] - [6].

This habilitation thesis presents improvements of the current state of the art in selected areas of IM drive application in railway traction vehicles. Part of the thesis is focused on increasing the accuracy and efficiency of FOC algorithms. The problematics of IM drive parameter identification and accuracy of the IM model is one of the key points that was the subject of the author's research. As a result of the research, in collaboration with doctoral student O. Lipčák, of whom I am a supervisor specialist, two novel methods for determining the magnetization inductance were proposed and practically verified. Practical evaluation of the methods also includes the analysis of magnetizing inductance detuning effect on the accuracy of RFOC. The other part of the thesis describes a slip controller's development for freight locomotive with the IM drive controlled by FOC. A new method of detecting the actual position on the adhesion characteristics that does not require information about locomotive longitudinal velocity was developed. In addition to the academic impact, the presented results also have a practical use, as they were used in collaborative projects with CRRC.

CHAPTER 1: ADHESION CHARACTERISTICS AND SLIP CONTROLLERS

Since railway vehicles transfer traction power by friction between the rail and the wheels, driving power over adhesive effort causes a slip. Generally, the adhesive effort is dependent on the vehicle weight and the variable adhesion coefficients between the rail and the wheel. The adhesion coefficient is strongly affected by the conditions between the rail and the wheels, such as humidity, dust, and oil. A sudden drop in the adhesion coefficients causes a slip by driving power beyond adhesive effort [1]. Therefore, to prevent the slip, it is necessary to find traction control utilizing maximum adhesive effort and reaching the limit of the friction's tractive effort. Generally, this means that the wheel's force has to be decreased to slow down the wheel velocity to an acceptable value [7].

Generally, all traction vehicles operate mostly in the stable area of the traction characteristics, although they may operate in its different sections. Commuter trains are usually driven by all wheelsets and have a relatively small ratio between the maximal traction power and normal force between the wheel and the rail that correspond to the maximum adhesion coefficient equal to approx. 0.25. That is why the commuter trains usually operate near the origin of the characteristic and seldom around the maximum. Passenger train locomotives are used for driving the passenger train with a weight of approx. 600 tons. Therefore, the ratio between the maximal pulling force and normal force between the wheel and rail is greater than 0.3 and can reach values close to 0.4. However, for lower loading, they usually operate with values up to 0.3; therefore, they operate on the higher part of the adhesion characteristics, or under bad adhesion conditions, in an unstable region. Freight train locomotives are used for pulling heavy trains whose weight is more than 1500 tons. The ratio between the maximal pulling force and normal force between the wheel and rail is greater than 0.35. These trains work close to the peak of the adhesion characteristics or behind the peak in the unstable area. That is why the demands on estimating the actual operating point and its proper control are highest from all the trains [8].

The adhesion phenomenon is also important for the automotive industry, where controllers that regulate the force transfer between the wheels and the surface are deployed, too [9]. However, in this case, additional types of forces have to be considered due to the rubber tires, like side forces or a tire cornering stiffness coefficient [10]-[12]. But the principles of the controllers are similar.

As a difference between the wheel's longitudinal and circumference speed, the adhesion coefficient changes its value during the train operation. Therefore, it is usually considered as a random variable. During the train run, the value of the adhesion coefficient changes every few meters (maximally, it can be constant up to 11 meters distance), influencing the maximal value of the transferable force. Understanding the adhesion phenomenon principle is essential for a slip controller design since its nonlinearity can influence the slip control methods' function. Therefore, the adhesion phenomenon will be described in this chapter in greater detail.

Because the slip controllers and re-adhesion controllers are being developed for many decades, various types exist now, with the development continuing [2], [3], [5], [7], [15], [30]. It is also caused by the fact, that the correct function of the methods designed for electric multiple units cannot be guaranteed for freight locomotives or some methods also depends on the actual adhesion function. Generally, a proper method selection may also depend on the target application. Therefore, the aim of this chapter is also to summarizes the most widely utilized slip control approaches.

1.1 Adhesion

The adhesive effort (or tangential force) is defined as a function of the normal force N of an electric locomotive and the adhesion coefficient μ between the rail and the driving wheel as

$$F_t = \mu N. \tag{1-1}$$

The diagram of forces that affect the vehicle motion is depicted in Fig. 1-1. If a wheel is driven by torque T, the tangential force F_t is transmitted from wheel to rail by generated friction. The vehicle is moved by force F_d in the opposite direction. The tangential force F_t depends on the vehicle mass m acting on the wheel, the gravitation acceleration g, and the adhesion coefficient μ. An adhesive effort is strongly affected by the conditions between the rail and the driving wheel. When the adhesive effort decreases suddenly, the electric locomotive encounters a slip phenomenon. The transformation of torque through the driving force to the tangential force depends on the instantaneous value of the adhesion coefficient and the difference between the longitudinal vehicle velocity and the wheel circumferential velocity.

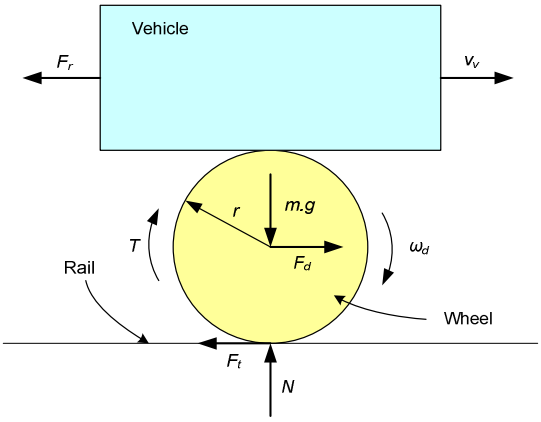

Fig. 1-1 Forces acting on vehicle and in forces in contact between the wheel and rail

1.1.1 Adhesion Coefficient

The adhesion coefficient is a function of the skid/slip speed v_s, which is defined as the difference between the circumference wheel velocity v_c and the longitudinal vehicle velocity v_v, i.e.,

$$v_s = v_c - v_v. \tag{1-2}$$

The slip is then defined as the ratio of skid/slip velocity and the vehicle velocity as

$$s = \frac{v_s}{v_v}. \tag{1-3}$$

The general shape of the adhesion coefficient is depicted in Fig. 1-2. The slip range of the adhesion characteristic is divided into two parts – stable region and unstable region. In the stable region, where the locomotive is usually operated, the adhesion coefficient increases to a maximum value μ_{max}. In the unstable region, the adhesion coefficient slowly decreases. The slip controller's task is to keep the operating point in the stable region [8]. The transition to the unstable region is a fault state where the wheel and rail wear increases.

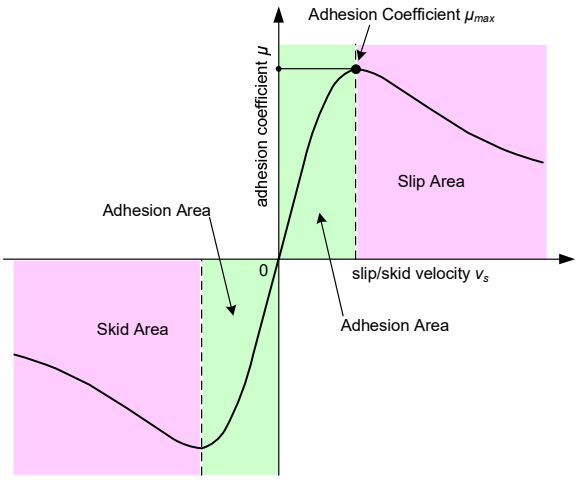

Fig. 1-2 General shape of the adhesion coefficient μ depending on the slip/skid velocity v_s

The characteristics' actual shape depends on the conditions in the contact between the wheel and the rail. Humidity, snow, or fallen leaves influence the maximum of the adhesion coefficient $\mu_{\max}$ in the range from 0,05 to 0,4. The adhesion characteristic variations for some wheel-rail conditions as a parameter are shown on the left-hand side of Fig. 1-3. The adhesion coefficient has a well-expressed local maximum for a dry or dry & sanded rail. In wet or muddy conditions, the maximum might be very flat or practically nonexistent [4], [5]. The adhesion coefficient also depends on the longitudinal velocity of the traction vehicle. The approximate dependence is shown on the right-hand side of Fig. 1-3.

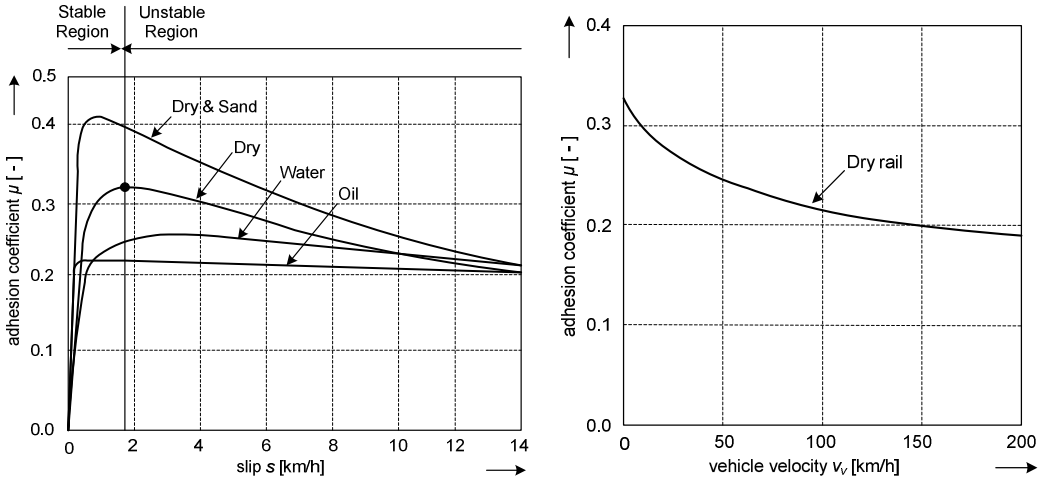

Fig. 1-3 Adhesion coefficient μ vs. slip s for different rail conditions (left) and speed (right)[15], [16]

1.1.2 Adhesion Slip Characteristics Modelling

The knowledge of the actual shape of the adhesion characteristics or actual value of the adhesion coefficient is essential for some slip controllers' operation and tuning their parameters. Therefore, different approaches to modeling the characteristics were developed [14]. The first set of methods use wheel-rail contact parameters and contact theories [17], i.e., they require an understanding of how the force is transferred between the wheel and the rail. The second group of methods uses measured characteristics or their approximation by a proper mathematical function.

In traction vehicles, the wheels and rail are made of steel, and their contact area has a surface of only a few square centimeters. Moreover, the wheel and railhead have cylindrical shapes.

Therefore, according to the Hertz theory, the contact area has an elliptical shape. The creep force can be modeled with Polach's formula [19] as

$$F = \frac{2Q\mu}{\pi}\left(\frac{\varepsilon}{1+\varepsilon^2} + \tan^{-1}\varepsilon\right), \tag{1-4}$$

where

$$\varepsilon = \frac{1}{4}\frac{C\pi a^2 b}{Q\mu} v_\mathrm{s}, \tag{1-5}$$

and where C is the proportionality coefficient characterizing contact shear stiffness that can be obtained from Kalker's linear theory [17]. In order to respect different rail surface conditions, it is necessary to introduce reduction coefficients k_a and k_s into (1-4), i.e.,

$$F = \frac{2Q\mu}{\pi}\left[\frac{k_\mathrm{a}\varepsilon}{1+(k_\mathrm{a}\varepsilon)^2} + \tan^{-1}(k_\mathrm{s}\varepsilon)\right]. \tag{1-6}$$

Finally, the adhesion coefficient can be expressed as

$$\mu = \mu_0[(1-A)\mathrm{e}^{-Bv_\mathrm{s}} + A], \tag{1-7}$$

where A is a constant.

There are several ways how to model adhesion characteristics as a beam or bristle model [20]. The complexity of the model depends on the amount of computational power available for the calculation. Some authors tend to make very precise models. Others use only rough approximation. For precise modeling of the wheel-to-rail contact, Finite Element Methods (FEM) can be utilized [17], [21], [22]. By employing FEM, the precise distribution of the forces and pressure can be obtained; however, the model's simulation is quite time-consuming.

The models that strive to fit the adhesion characteristics by fitting measured values are more straightforward than those previously described [23], [24]. On the other hand, the approximation is not too accurate, and equations have to contain parameters respecting the rail surface's actual conditions. To most simple formula for the adhesion characteristics approximation can be written as [24]

$$\mu = 0.161 + \frac{7.5}{v_\mathrm{v} + 44}. \tag{1-8}$$

For speeds above 40 km·h^{-1}, the formula changes to

$$\mu = 0.116 + \frac{9}{v_\mathrm{v} + 42}. \tag{1-9}$$

In the above two approximations, the speed is considered in km·h^{-1}. An example of 3D characteristics obtained from (1-8) and (1-9) is given in Fig. 1-4.

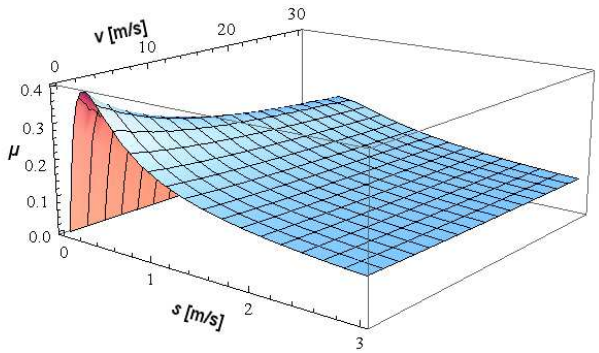

Fig. 1-4 3D model of adhesion characteristics obtained from (1-8) and (1-9)

Another way to approximate adhesion characteristics is given by the formula [25]

$$\mu = c\mathrm{e}^{-as} - d\mathrm{e}^{-bs}, \tag{1-10}$$

where a, b, c, d are parameters designed to correspond to the different rail surface conditions whose example is given in Tab. 1-1.

Tab. 1-1 Adhesion-slip characteristics coefficients for (1-10)

Adhesion conditions	a	b	c	d
high	0,54	1,2	1	1
medium	0,54	1,2	0,2	0,2
low	0,54	1,2	0,1	0,1
very low	0,05	0,05	0,08	0,08

Determining the coefficients describing the rail surface conditions can be difficult. Therefore, another description that eliminates this disadvantage can be used. The formula is given as

$$\mu = \frac{2K_{\mathrm{s}}\mu_{\max}^2 v_{\mathrm{s}}}{\mu_{\max}^2 v_{\mathrm{s}} + K_{\mathrm{s}}^2}, \tag{1-11}$$

where K_{s} is a multiplication of $\mu_{\max}$ and v_{s} that occur at $\mu_{\max}$. An example of the coefficients' numerical values in (1-11) for different adhesion conditions is given in Tab. 1-2 [25]. An example of the modeled characteristics based on (1-10) is shown in Fig. 1-5.

Tab. 1-2 Adhesion-slip characteristics coefficients for (1-11)

Adhesion conditions	$\mu_{\max}$	v_{s}	K_{s}
high	0.289	1.3	0.375
medium	0.029	1.2	0.034
very low	0.056	5.1	0.284

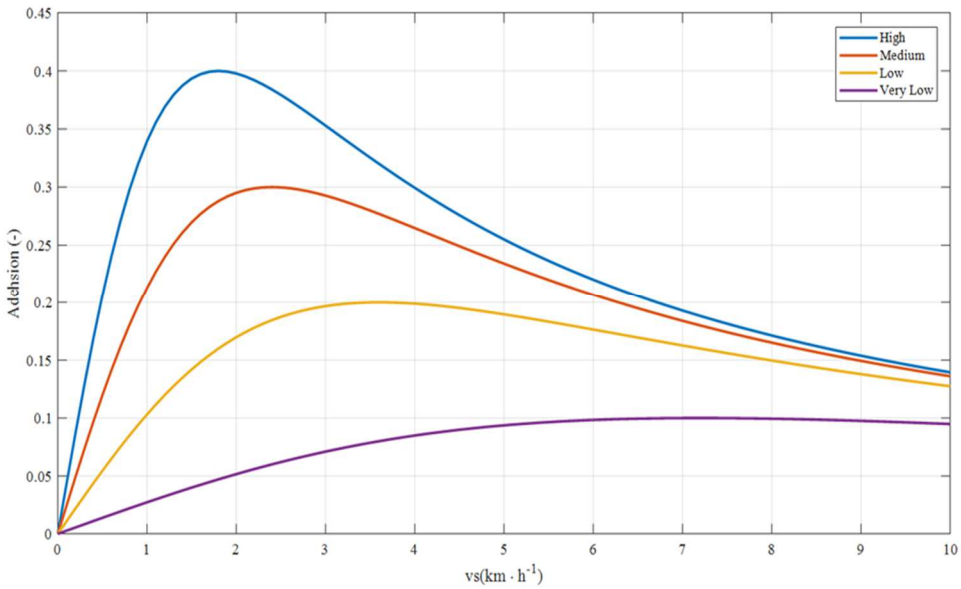

Fig. 1-5 Adhesion characteristics fitting based on (1-10)

1.2 Slip Identification and its Control

The slip controller's operation principle is to keep the operating point in the stable region of the adhesion characteristics before or near the maximum (even slightly in the unstable region) [8]. The closer the operating point to the characteristics' maximum, the better the vehicle adhesion properties. However, this leads to increased slip and re-adhesion control performance. Furthermore, if the operating point is closer to the curve maximum, the damping of the oscillations generated by wheelsets and bogies is weaker. Consequently, the mechanical stress on all parts of the vehicle's transmission system (gearbox, wheel tire, and rail) increases, and these parts experience increased wearing. Various quantities can be used to detect the slip phenomena like wheel-vehicle velocity difference, wheel acceleration, drive current or voltage, torque, slope, and the peak of the adhesion characteristics, wheelset torsional vibration, and more [2], [9], [13], [15], [16], [18], [25] - [27].

1.2.1 Re-adhesion Control

A re-adhesion control system's primary task is to reduce the tractive effort if the slip/skid arises to reestablish axle adhesion rolling. The re-adhesion system itself does not prevent vehicles from the arising slip/skid phenomenon and does not guarantee maximum utilization of the vehicle's adhesion. Another re-adhesion control system's task is to protect the drive-torque transmission chain against excessive wearing or damage. Re-adhesion control systems are historically older and are supplemented or entirely replaced by slip control systems in recent years.

1.2.2 Slip Controller

A slip control system's primary task is to reduce the tractive effort so the slip/skid phenomenon will be suppressed or entirely excluded. The is achieved by keeping the wheel-rail contact in the stable region of the adhesion characteristics. The slip control system basic requirements are [29], [30]:

- To quickly find the correct operating point inside the stable region of the adhesion characteristics or near the characteristics' maximum (alternatively to set the operating point's distance from the adhesion characteristics' peak to utilize vehicle adhesion capabilities, i.e., to utilized vehicle weight efficiently).
- To make sure the slip control system operates correctly if the adhesion conditions or the normal force change fast and unpredictably.
- To modify required drive torque quickly and continuously.
- To exclude or to efficiently damp the torque transmission chain mechanical oscillations.
- To use only sensors that are available for the drive torque control system.

The slip controller reaction principle can be explained based on the borderline situations depicted in Fig. 1-6. Let us assume that starting conditions correspond to waveform 1. Suddenly, the rail surface conditions change to waveform 2. In this case, the slip controller's operating point has to move from point A to point C if the adhesion is to be fully utilized. Suppose there is no reaction of the slip controller. In that case, the operating point moves to B, which means high slip velocity and, consequently, slippage because the acceleration force accelerates the wheels. The position of point B depends on the slip controller reaction.

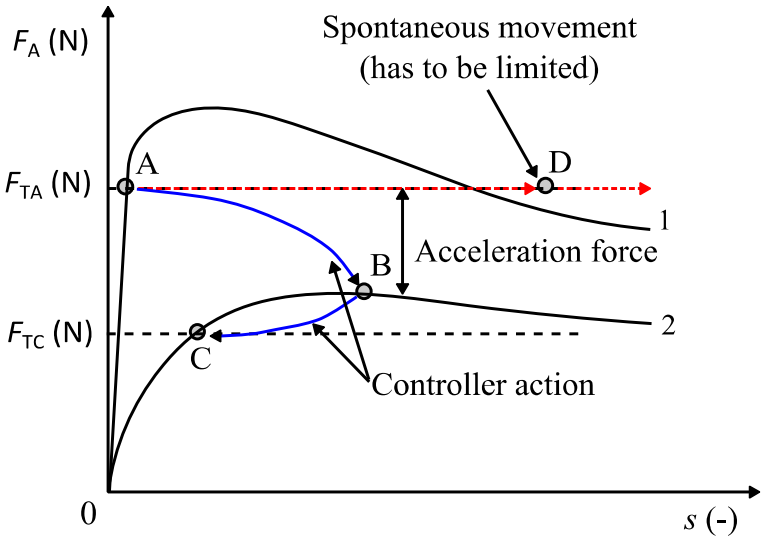

Fig. 1-6 Controller reaction under change of adhesion characteristics [30]

For the slip control, PID or PSD controllers, fuzzy controllers, or state-space controllers can be utilized [27], [28]. Every type of controller has some advantages and some disadvantages. Generally, the fuzzy controllers and state-space controllers provide better regulation than the PID controllers, but their realization is more difficult [28], [31].

1.2.2.1 Speed Difference Methods

The method based on applying the vehicle-wheel speed difference or wheel acceleration for slip/skid control is one of the oldest ones [33]-[36]. Within this method, the difference between the longitudinal vehicle velocity and the wheel circumferential velocity is calculated. An intervention of the re-adhesion control system or slip control system is generated if the calculated value is greater than a predefined threshold. The principle of the slip/skid and re-adhesion control method that utilizes the vehicle-wheel velocity difference is depicted in Fig. 1-7.

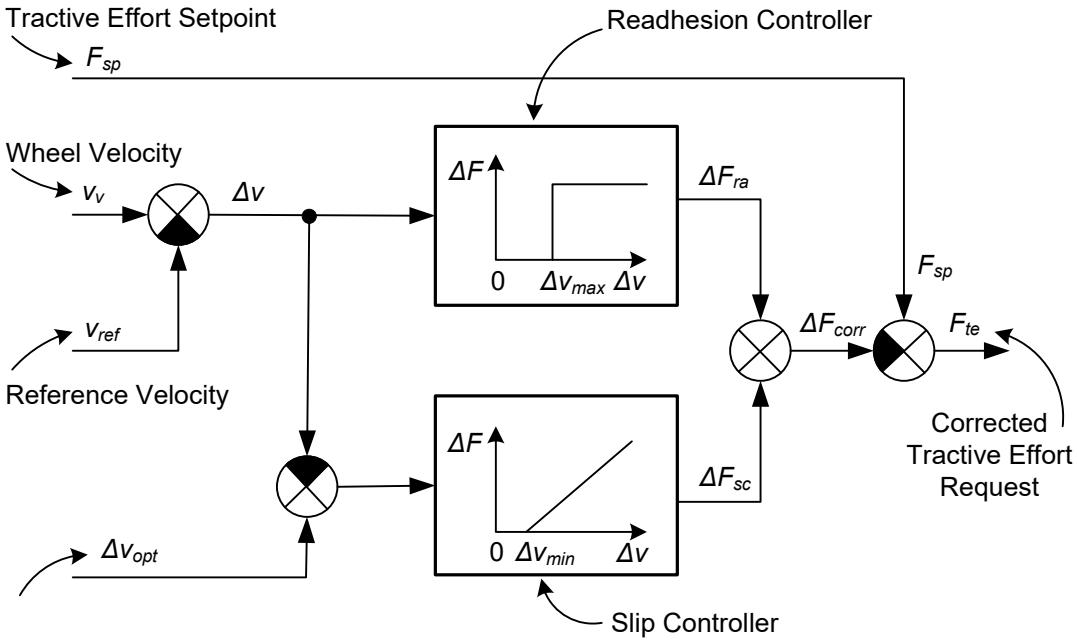

Fig. 1-7 Speed difference-based slip and re-adhesion control method [8]

The main disadvantage of this method is the necessary knowledge of the longitudinal velocity. This velocity is not usually accurately known (is not measured directly), or its estimation

is not accurate [35]-[39]. Secondly, the threshold value when the re-adhesion control system has to react, or the value which has to be held by the slip/skid control system is usually not determined accurately enough. Moreover, the method is sensitive to the accuracy of the wheel circumference velocity measurement and the wheel diameter's precise knowledge.

1.2.2.2 Adhesion Characteristics Maximum Detection Methods

The method utilizes the adhesion characteristics shape and is based on the tracing of its peak value (maximum) [40]-[42]. The motor torque and the tangential traction force are modulated with a depth of about 5 % to 10 % of their nominal values so that the operating point permanently moves around the peak. The torque value in the adhesion characteristics maximum point is stored in the memory of the slip controller. The stored value is then used for the determination of the next torque direction. The additional timeout block has to be part of the system to reset the torque modulation direction if the adhesion coefficient curve has no local maximum. The method principle is depicted in Fig. 1-8. The slip controller structure is depicted in Fig. 1-9. The dynamics of the drive torque control has to be high. The method requires measurement of motor torque value or torque estimation from motor parameters.

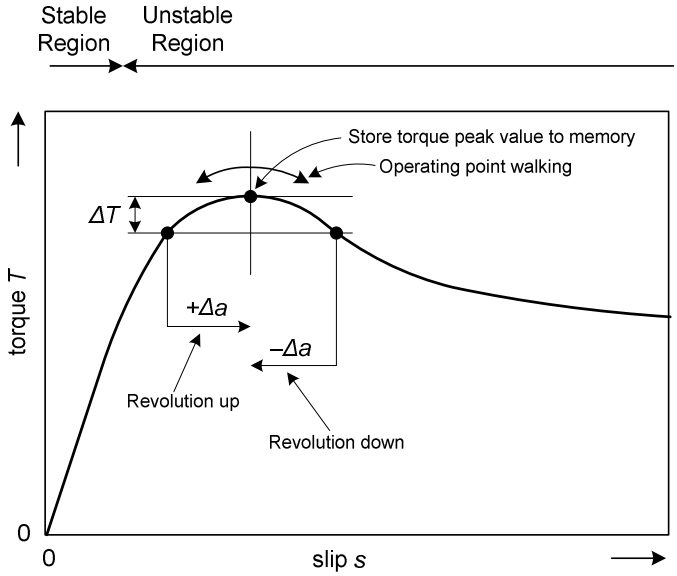

Fig. 1-8 Adhesion characteristic maximum detection methods

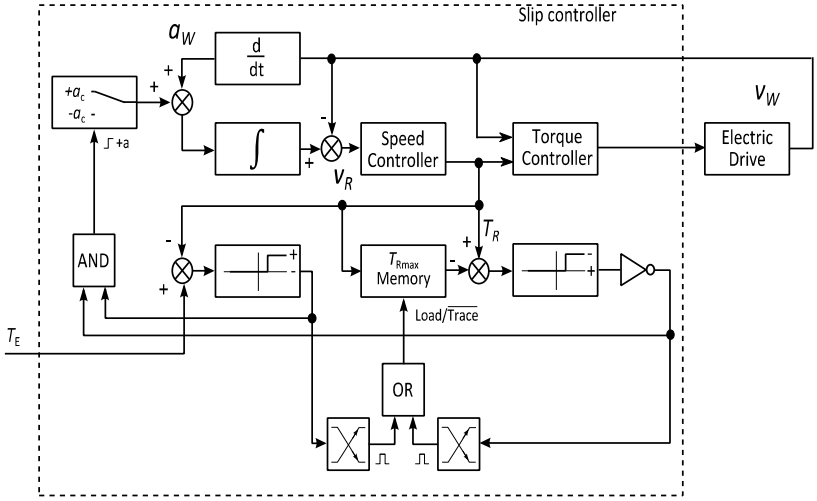

Fig. 1-9 Adhesion characteristic maximum detection method structure [41]

1.2.2.3 Adhesion Characteristics Slope Detection Methods

These types of methods make use of the adhesion characteristics waveform shape. They are based on the tracing of the adhesion coefficient curve slope followed by the regulation of the operating point at a predefined value in the stable region [14], [43], [44]. The operating point is held at a suitable distance from the adhesion characteristics' peak (maximum). The slope tracing method's advantage is that the system is less prone to torsional vibrations. The consequence is that the stress induced to the vehicle torque transmission system is smaller, and the wheels and the rail wearing is reduced.

The first possibility is to use an observer to estimate the force tra Ω nitted between the wheel-rail contacts (Fig. 1-10). The slope of the adhesion characteristics is calculated as differentiation of the tangential force F_t with respect to slip as

$$\frac{\mathrm{d}F_\mathrm{t}}{\mathrm{d}s} = \frac{\frac{\mathrm{d}F_\mathrm{t}}{\mathrm{d}t}}{\frac{\mathrm{d}s}{\mathrm{d}t}}. \tag{1-12}$$

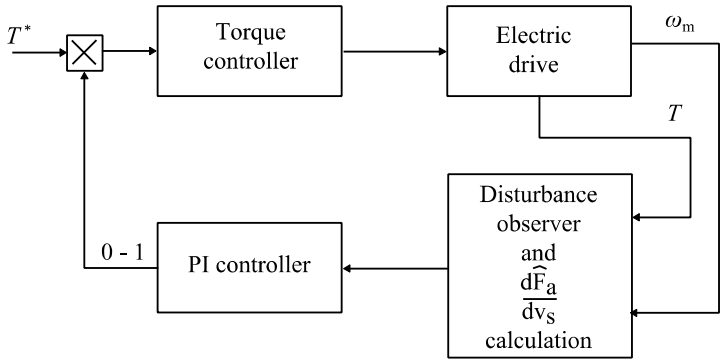

Fig. 1-10 Adhesion characteristic slope detection method based on observer

The second group of methods is based on injecting small periodic disturbance torque ΔT_D to the motor torque T [45] - [48]. The disturbance torque causes oscillations of the motor torque resulting in oscillations of angular speed. Between the modulated motor torque and its image in angular speed, a phase shift occurs. The phase shift φ_s is proportional to the actual adhesion-slip characteristics' slope. The method can be used when the self-oscillations' frequency is sufficiently high and the torque control is sufficiently fast. The principle is based on the following formula

$$T = T^* + \Delta T_\mathrm{D}\, \sin(\omega_\mathrm{f} t), \tag{1-13}$$

where ω_f is the angular modulation frequency. Measured motor angular velocity Ω have to be filtered to get back the modulated motor angular velocity ω_mf, i.e.,

$$\omega_\mathrm{mf} = \Delta\omega_\mathrm{m}\, \sin(\omega_\mathrm{f} t - \varphi_\mathrm{s}) \tag{1-14}$$

To extract the modulation signal's image, the measured angular velocity is multiplied by the following sine and cosine waves

$$a_\mathrm{f} = \frac{\omega_f}{2\pi} \int_0^{2\pi/\omega} \omega_\mathrm{mf}\, \sin(\omega_\mathrm{f} t)\, \mathrm{d}t, \tag{1-15}$$

$$b_\mathrm{f} = \frac{\omega_f}{2\pi} \int_0^{2\pi/\omega} \omega_\mathrm{mf}\, \cos(\omega_\mathrm{f} t)\, \mathrm{d}t. \tag{1-16}$$

The phase φ_s – a quantity that is proportional to the position of the operation point on the adhesion curve can be evaluated as

$$\varphi_s = \tan^{-1}\frac{b_f}{a_f}. \tag{1-17}$$

The method demands specific restrictions in the drive torque control structure. It might be necessary to complete the slip control with blocks for active suppression of the torsional vibration even if the operating point is held below the adhesion characteristics' peak because the modulation signal can excite oscillations of the system in the unstable part of adhesion characteristics. The modulation signal frequency has to be below the lowest frequency of the vehicle torque transmission chain's self-oscillation. The phase shift between the assigned torque and measured motor velocity required by the slip control algorithm is calculated according to the structure shown in Fig. 1-11. The adhesion characteristics' slope can be specified based on the calculated phase shift. The method has extreme requirements for the drive torque control dynamics and is sensitive to the drive-torque transmission chain parameters.

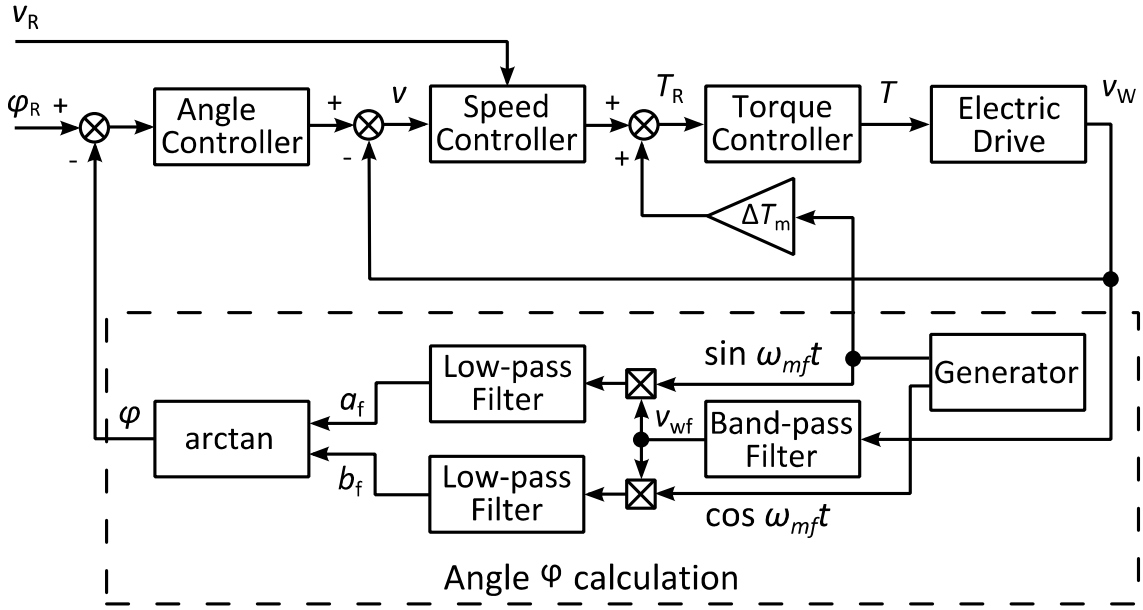

Fig. 1-11 Adhesion characteristic slope detection method [48]

The phase shift value depends on the used modulation frequency. Generally, the modulation frequency has to be lower than the lowest eigenfrequency of the drive mechanics. On the other hand, lower modulation frequency means a longer initialization and detection time delay. The disturbance torque can be a sinusoidal wave with a frequency from 5 to 12 Hz and amplitude from 2 to 4 % of the nominal torque. Currently, this method belongs to one of the most perspective ones.

1.2.2.4 Other Types of Slip Controllers

Various other methods can estimate the adhesion coefficient. However, most of them attract only academic attention due to their computational complexity requirements or expensive additional sensors [13], [18], [25], [49], [51]. Among these approaches, the methods based on the torsional vibrations between a motor and gearbox and between the wheels can be included. The torsional vibrations exist due to the non-rigid shafts between the rotating masses. The slip controller is based on the assumption that the adhesion coefficient damps the dynamic motions.

Other methods include the analysis of acoustics spectra produced by movement [49] - [51]. The slip controller then requires microphones mounted on bogies. The noise caused by the wheel-rail contact is analyzed and compared with a spectrum that depends on the track's current position. The position is determined by a GPS.

The newest proposed slip controller uses a Hilbert-Huang Transformation (HHT) for slip control [51]-[53]. The HHT is an empirical data analysis method for obtaining the frequency spectrum. If the operating point gets to an unstable part of the adhesion-slip characteristics, torsional vibrations are excited. The Hilbert energy spectrum, which is calculated from the signal amplitude of the wheel velocity signal, can then be used for the slippage determination – the actual energy spectrum is compared to the average spectrum.

The overview of the pros and cons of the methods presented so far is given in Tab. 1-3.

Tab. 1-3 Slip controller summary

	Speed difference method	**Adhesion Characteristic Maximum Detection**	**Adhesion Characteristic Slope Detection – Observer-Based**	**Adhesion Characteristic Slope Detection – Observer-Based**	**Adhesion Coefficient Estimation Based on Wheel-rail Contact Noise**
Principle	Compares calculated slip speed with the set threshold	Search maximal value on the adhesion coefficient curve	Detect the adhesion characteristics' slope	Detect the adhesion characteristics' slope	Detects slip from the frequency spectra of the noise produced by the movement of the traction vehicle
Requirements	Wheel speed, train speed, a threshold value	Wheel speed, motor torque	Wheel/rail forces, train speed, wheelset mechanical parameters	Motor set torque, motor speed	Train position, track profile Noise detector
Advantages	Simple decision-making algorithm Low CPU load	Better adhesion use. No knowledge of train speed necessary	Optimum operating point set-up possibility. Higher adhesion use	Optimum operating point set-up possibility. Higher adhesion use	-
Disadvantages	Lower adhesion use Difficult to determine correct train speed Synchronous slip problem	Complex decision-making algorithm and complex drive controller structure. Higher CPU calculation power requirements Problems if current adhesion characteristic shape is without clear maximum.	Quality depends on the knowledge of the mechanical parameters. Computation power requirements. Train speed knowledge necessary.	Motor torque modulation. Higher CPU computation power requirements The method is strongly protected by patent rights Requirements on the structure of the drive controller	Too much complex sensors required

1.2.3 Controller Incorporation into System

The above paragraphs describe ways to select a variable used later for slip identification; however, the controller itself and its connection into the system have not been described yet. The slip controller's detection part can be a maximal torque, required slip velocity, or ratio of the derivative of the adhesion force or angle. Generally, the controller aims to hold the actual operating point in the required position. It has to be able to react to quick and slow changes, and last but not least, on the generated motor torque change. A slow controller cannot fulfill these requirements, and a too fast controller can cause oscillations of the drive and mechanical parts [16], [18]. The slip controller output oscillations can appear when the detection method's reaction is slower than the controller's or when the operating point exceeds particular adhesion coefficient maxima (in case of the too fast controller) [27], [41].

A PID controller is a well-known and most used type of controller in many applications. Its advantages include simple structure, easy tuning, and the fact that it is not dependent on the controlled system structure. The main disadvantage is that in nonlinear systems, the controller constants are designed only for a specific operating point. In such a case, the advantage of fuzzy controllers can be used utilized [27]. On the other hand, the fuzzy controllers use a linguistic approach and are tuned based on expert knowledge, and require more parameters than the PID controllers [28], [31]. Other possibilities include state-space controllers or sliding mode controllers. However, their accuracy is influenced by knowledge of the controlled system model parameters (moments of inertia, stiffnesses, damping).

The slip controller has to be incorporated between the vehicle controller and the electric drive controller. The controller can be connected either parallelly or in series with the drive control structure, as shown in Fig. 1-12. In a parallel connection, the locomotive driver's required effort is multiplied by a correction value from the slip controller that decreases the required torque according to actual adhesion conditions. A predefined ramp limits the rate of change of torque. If the controller is connected is in series, a required traction effort is corrected continuously by the slip controller and outputted as a required torque to the drive controller.

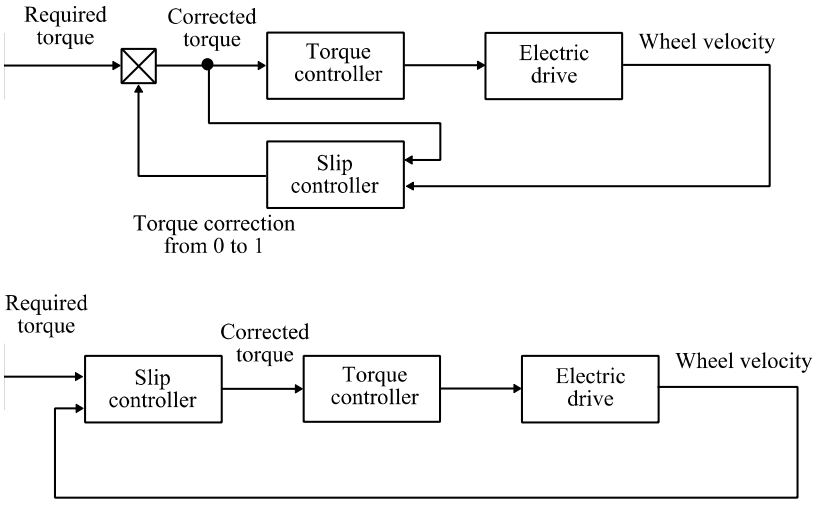

Fig. 1-12 Controller incorporation into the drive system

CHAPTER 2: SLIP CONTROLLER DESIGN

Based on the theory survey, two slip controllers were designed. Both of them are based on the adhesion characteristics' slope detection. The first one is based on the state estimator and Unscented Kalman filter and is described in the defended Ph.D. thesis [30]. The second controller, tested on an actual locomotive, is based on principle depicted in Fig. 1-11.

2.1 System Model

The model of the controlled system is not essentially necessary for the slip controller design. However, it speeds up the design procedure and enables the controller tuning without access to the locomotive. If an SW MATLAB model is available, it acts as a substitution of the real system for the controller design. The model can be used for selecting parameters of modulation frequency, too. This sets special requirements on model design because it has to comprise the knowledge of the locomotive's real system's behavior. Different model types of different complexity can be found in the literature. Complex models tend to simulate the whole locomotive while simulating inner parts in a simplified form. Other models focus on locomotive parts like drive, controller, and wheelset to simulate only features important for a particular problem. For the slip controller design purpose, models focused on a single wheelset will be used. The model comprises of:

- Model of the locomotive's induction motor drive with an included control strategy. In this case, the model was reduced to a transfer function and time delay because the slip controller design requires only drive response to a required torque command. The electrical behavior of the motor and inverter is not essential in this case. The Padé approximation of the transfer function with the time delay was used because for the simulation with a time variable input, it is better to replace the transfer function with a state-space representation and solve it as a differential equation [56]. The transfer function takes a form

$$T_{\mathrm{FP}} = \frac{\tau^2 s^2 - 6\tau s + 12}{\tau^2 s^2 + 6\tau s + 12} \frac{K}{\vartheta^2 s^2 + 2\xi\vartheta + 1}, \tag{2-1}$$

  where τ is the required time delay, K is steady-state gain, ϑ is the second-order system eigenfrequency, and ξ is damping ratio. Symbol s represents the Laplace operator in this equation.
- Model of gearbox formed by pinion and gear wheel, which is typically represented by its gear ratio and masses. However, complex models respecting the teeth shape influencing the gearbox properties (e.g., stiffness between the wheels during the rotation) exist.
- Locomotive wheelset model formed by two wheels connected by a shaft where also the gear wheel is mounted. The wheels on the locomotive can have a different diameter, load, and adhesion conditions. Every wheel can transfer different forces to rails, causing oscillations between the wheelset wheels and between the motor and the wheelset.

For modeling purposes, all components mentioned above are represented by their masses connected by shafts. The shafts are not considered as rigid; thus, they represent stiffness and elasticity in the system. Fig. 2-1 shows the five-mass model of the locomotive wheelset. Black rectangles represent masses of 1 Induction Motor Rotor; 2 Pinion; 3 Gear Wheel; 4 Direct driven wheel; 5 Indirect driven wheel and 6 Mass of the train. Symbols c_{ij} represent corresponding stiffness and d_{ij} elasticity, T_{IM} represents torque produced by the induction motor, T_6 represents the torque transferred by the wheels (torque accelerating the locomotive), and T_{46} and T_{56} represent feedback of the torque on the wheels with respect to adhesion.

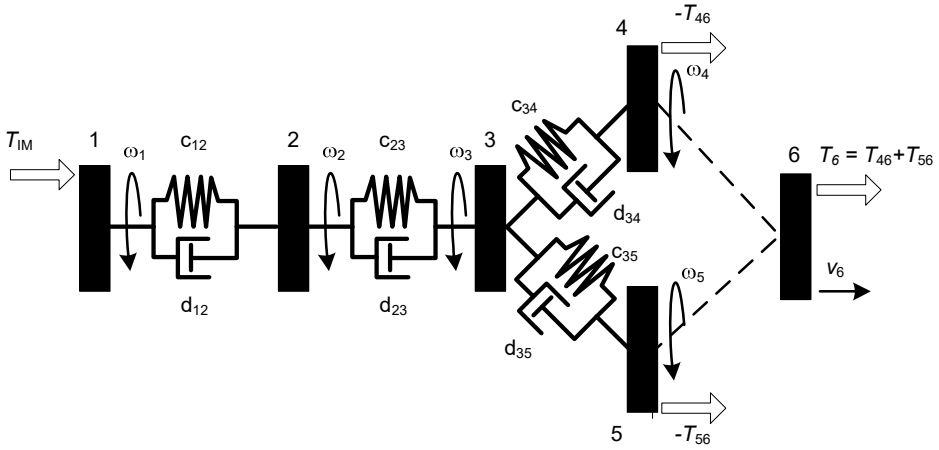

Fig. 2-1 Five mass model of the locomotive wheelset

Based on this representation, the set of differential equations that represents the system was established

$$\mathbf{T} = \mathbf{J}_\mathrm{M}\omega + \mathbf{D}_\mathrm{M}\varepsilon + \mathbf{C}_\mathrm{M}\varphi, \tag{2-2}$$

where, $\mathbf{T}$ is the torque vector, $\mathbf{J_M}$ represents moment of inertia matrix, $\mathbf{D}_\mathrm{M}$ is the matrix representing the damping of system parts, $\mathbf{C}_\mathrm{M}$ is the matrix representing the stiffness of the elements in the torque transmission chain. Variable ε, ω, and φ are responses of acceleration, velocity, and displacement, respectively, in the system. The matrices $\mathbf{J_M}$, $\mathbf{D}_\mathrm{M}$, $\mathbf{C}_\mathrm{M}$ are defined as

$$\mathbf{J}_\mathrm{M} = \mathrm{diag}\,[J_1 \quad J_2 \quad J_3 \quad J_4 \quad J_5 \quad J_6], \tag{2-3}$$

$$\mathbf{C}_\mathrm{M} = \begin{bmatrix} c_{12} & -c_{12} & 0 & 0 & 0 & 0 \\ -c_{12} & c_{12}+c_{23} & -c_{23} & 0 & 0 & 0 \\ 0 & -c_{23} & c_{23}+c_{34}+c_{35} & -c_{34} & -c_{35} & 0 \\ 0 & 0 & -c_{34} & c_{34} & 0 & 0 \\ 0 & 0 & -c_{35} & 0 & c_{35} & 0 \\ 0 & 0 & 0 & 0 & 0 & 0 \end{bmatrix}, \tag{2-4}$$

$$\mathbf{D}_\mathrm{M} = \begin{bmatrix} d_{12} & -d_{12} & 0 & 0 & 0 & 0 \\ -d_{12} & d_{12}+d_{23} & -d_{23} & 0 & 0 & 0 \\ 0 & -d_{23} & d_{23}+d_{34}+d_{35} & -d_{34} & -d_{35} & 0 \\ 0 & 0 & -d_{34} & d_{34}+d_{46} & 0 & 0 \\ 0 & 0 & -d_{35} & 0 & d_{35}+d_{56} & -d_{56} \\ 0 & 0 & 0 & -d_{46} & -d_{56} & d_{46}+d_{56} \end{bmatrix}. \tag{2-5}$$

For simulation purposes, the system is described in state-space form as

$$\frac{\mathrm{d}\mathbf{x}}{\mathrm{d}t} = \mathbf{A}\mathbf{x} + \mathbf{B}\mathbf{u}. \tag{2-6}$$

The state vector $\mathbf{x}$ is defined as

$$\mathbf{x} = [\varphi_1 \quad \varphi_2 \quad \varphi_3 \quad \varphi_4 \quad \varphi_5 \quad \varphi_6 \quad \omega_1 \quad \omega_2 \quad \omega_3 \quad \omega_4 \quad \omega_5 \quad \omega_6]^\mathrm{T}. \tag{2-7}$$

The system matrix $\mathbf{A}$ is given by

$$\mathbf{A} = \begin{bmatrix} \mathbf{O} & \mathbf{I} \\ -\mathbf{C}'_\mathrm{M} & -\mathbf{D}'_\mathrm{M} \end{bmatrix}, \tag{2-8}$$

where **O** and **I** are zero and unity square matrices, respectively, of the rank 6 and the matrices $\mathbf{C}'_{\mathrm{M}}$ and $\mathbf{D}'_{\mathrm{M}}$ corresponds to the matrices $\mathbf{C}_{\mathrm{M}}$ and $\mathbf{D}_{\mathrm{M}}$ whose *i*-th rows are divided by the *i*-th diagonal element of the matrix $\mathbf{J}_{\mathrm{M}}$.

The input vector **u** is formed as

$$\mathbf{u} = \begin{bmatrix} T_m \\ 0 \\ 0 \\ -T_{46} \\ -T_{56} \\ T_{46} + T_{56} \end{bmatrix}, \tag{2-9}$$

where the torques on the wheels are given by

$$T_{46} = rF_{46} = rN\mu_4(v_s), \tag{2-10}$$

$$T_{56} = rF_{56} = rN\mu_5(v_s). \tag{2-11}$$

The adhesion coefficient between the corresponding wheel and rail can be calculated as

$$\mu_4 = f(v_s) = f(r\Delta\omega) = f\big(r(\omega_4 - \omega_6)\big), \tag{2-12}$$

$$\mu_5 = f(r(\omega_5 - \omega_6)). \tag{2-13}$$

The variables connected with the components behind the gearbox, i.e., variables with subscripts 1, 2 have to be recalculated. For the recalculation, gearbox ratio is used, i.e.,

$$u = \frac{z_2}{z_1}. \tag{2-14}$$

where u represents the gear ratio, z_1 is the number of teeth on the pinion, and z_2 is the number of teeth on the gearwheel. The recalculation of all torques, moments of inertia, stiffnesses, and elasticities to the wheel coordinates are given by

$$T' = uT_{\mathrm{IM}},\ \ J_1 = J'_1\left(\frac{\omega_1}{\omega_3}\right)^2 = u^2 J'_1,\ \ c_{12} = u^2 c'_{12},\ \ d_{12} = u^2 d'_{12}. \tag{2-15}$$

The model SW MATLAB was used to analyze system eigenfrequencies and frequency response. These analyses were necessary because the system's oscillations significantly influenced the proposed stick-slip controller's behavior. For the controller's functionality, avoiding these frequencies was essential. A performed analysis shows that the modeled wheelset system used on the locomotive has four critical frequencies – 32.9 Hz, 67.1 Hz, 300.8 Hz, 742.9 Hz. These frequencies correspond to the eigenvalues of the system matrix **A**. The following figures Fig. 2-2, Fig. 2-3 show the influence/reaction of a particular frequency on the system's masses. The values on the *y*-axis correspond to the angular displacement of a particular mass. The values are normalized so that the oscillation's maximal amplitude in the system corresponds to 1. Masses on the *x*-axis correspond to the rotor, pinion, gearwheel, direct driven wheel, and indirect driven wheel. From Fig. 2-2, it is evident that the two frequencies below 100 Hz have a different sign for the rotor and the wheels, which means the wheels oscillate against the rotor. The two frequencies above 100 Hz, oscillating in the gearbox, probably represent torsional oscillations. Frequencies above 200 Hz can be neglected because they are far from the supposed modulation frequency f_{mf}. The full Bode diagram of the 5-mass model is shown in Fig. 2-3.

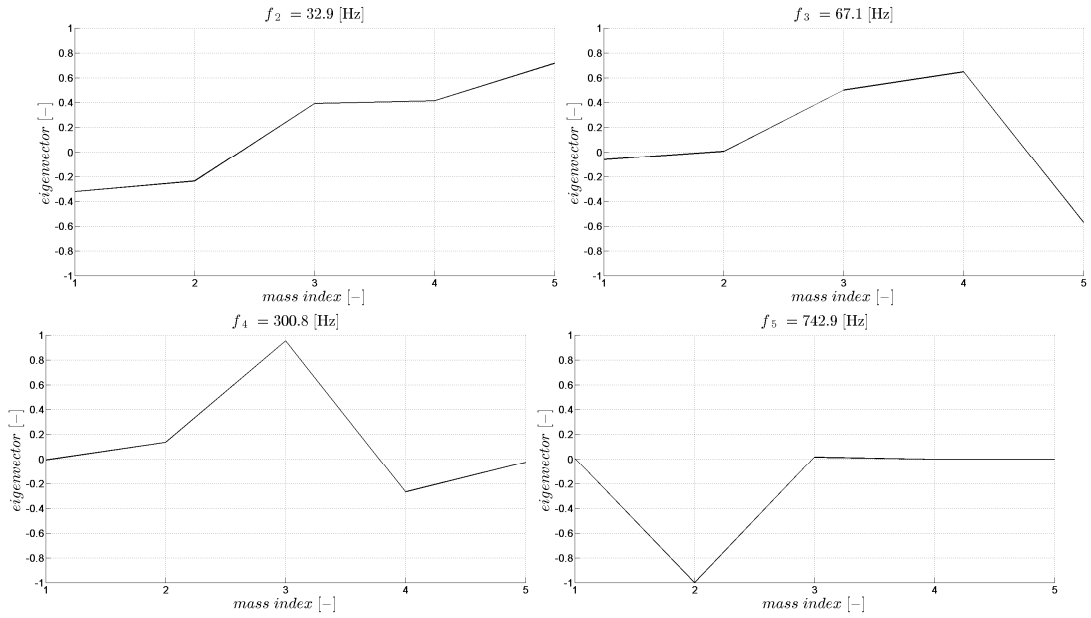

Fig. 2-2 Critical frequencies of the 5-mass model; mass indexes correspond to elements in Fig. 2-1

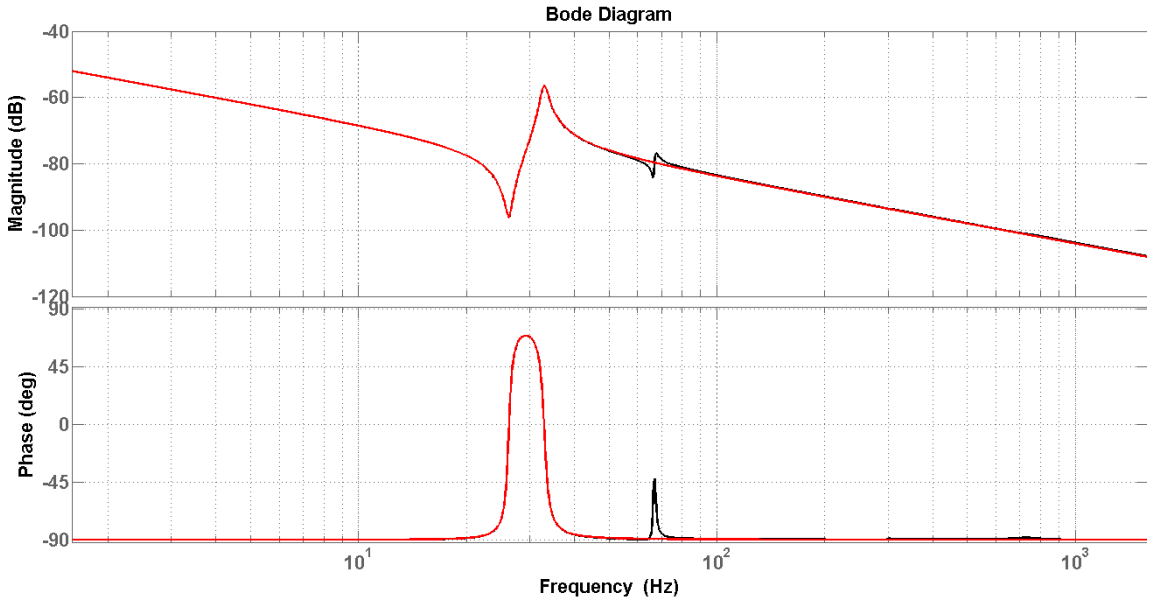

Fig. 2-3 Bode plot of the simulated 5-mass model

2.2 Slip Controller Selection

Based on the pros and cons of the different slip control methods presented in Tab. 1-3, a method of adhesion slope detection based on an injected signal was selected. This method's basic idea is to superimpose a small sinusoidal signal on the reference torque with the amplitude ranging from 2 % to 5 % of the rated motor torque. The modulation signal frequency f_{mf} has to lie below the lowest frequency of the vehicle torque transmission chain's self-oscillation. This signal is detectable at the measured angular velocity. Actual adhesion conditions act as variable damping, causing a variation of the phase shift between the modulation signal (present in the motor torque) and its image (present in the measured motor speed). The phase shift is calculated in the "Signal analyzer" block.

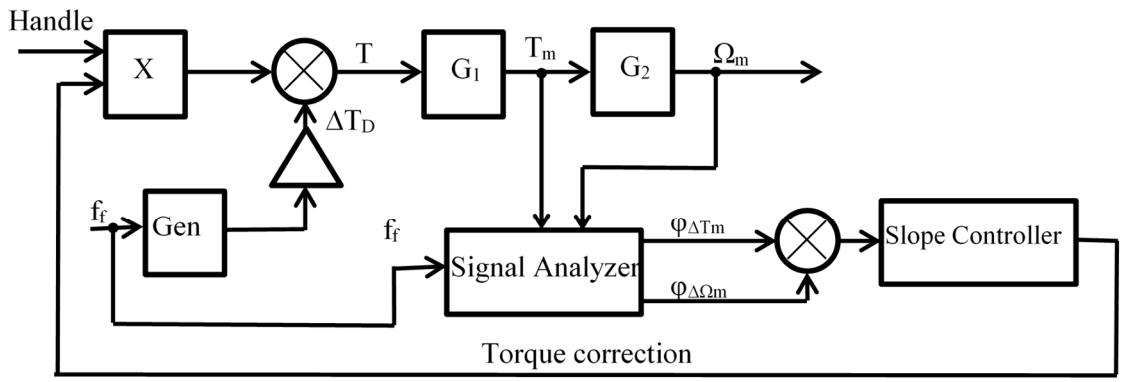

Fig. 2-4 Principal block diagram of the proposed controller

Transfer function G_1 in Fig. 2-4 represents the drive controller with the frequency converter and an induction motor's stator. Its output is the real torque T_m in the motor. Transfer function G_2 represents the mechanical chain composed of a rotor of an induction motor, gearbox, wheel axis, and two wheels. Its input is the real motor torque $T_{\delta,}$ and its output is the angular speed of the motor rotor Ω_m. A block "Gen" represents a function generator with the constant input f_f and with the output $\sin(2\pi f_\mathrm{f} t)$. This output is multiplied by a constant value $\Delta T_{\mathrm{m},}$ and a result of the multiplication is added reference torque set by drivers handle. The block "Signal Analyzer" represents the mathematical processing of two input signals – the real motor torque T_m (in our case torque producing current component i_q) and the angular speed of the rotor Ω_m. The phase shift between signals ΔT_m and $\Delta\Omega_\mathrm{m}$ with the same frequency f_f in both input signals can be mathematically determined as one of Fourier expansion terms. A difference between the phase shift $\varphi_{\Delta T_\mathrm{m}}$ of the signal ΔT_m and the phase shift $\varphi_{\Delta\Omega_\mathrm{m}}$ of the signal $\Delta\Omega_\mathrm{m}$is the input into the block "Slope Controller," whose output is the continuous correction of signal from driver's handle in order to operate close to the adhesion characteristics top.

An essential part of the controller design is selecting the amplitude and frequency of the modulation signal f_f. Therefore, the system's transfer functions modeled in Section 2.1 for various frequencies below the system's first eigenfrequency were calculated first – the transfer functions were calculated for different points on the adhesion characteristics for possible f_mf candidates from 5 Hz to 30 Hz. Plotted functions are shown in Fig. 2-5 to Fig. 2-8.

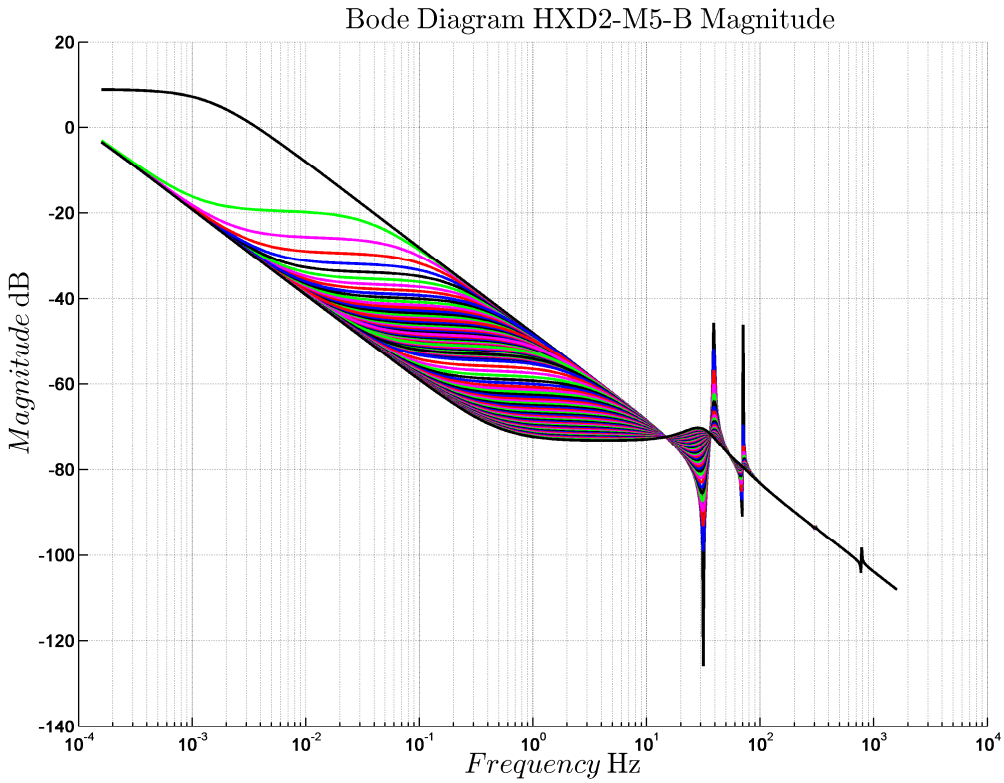

Fig. 2-5 Bode diagram – amplitude of the mechanical chain transfer function G_2 for dry rail

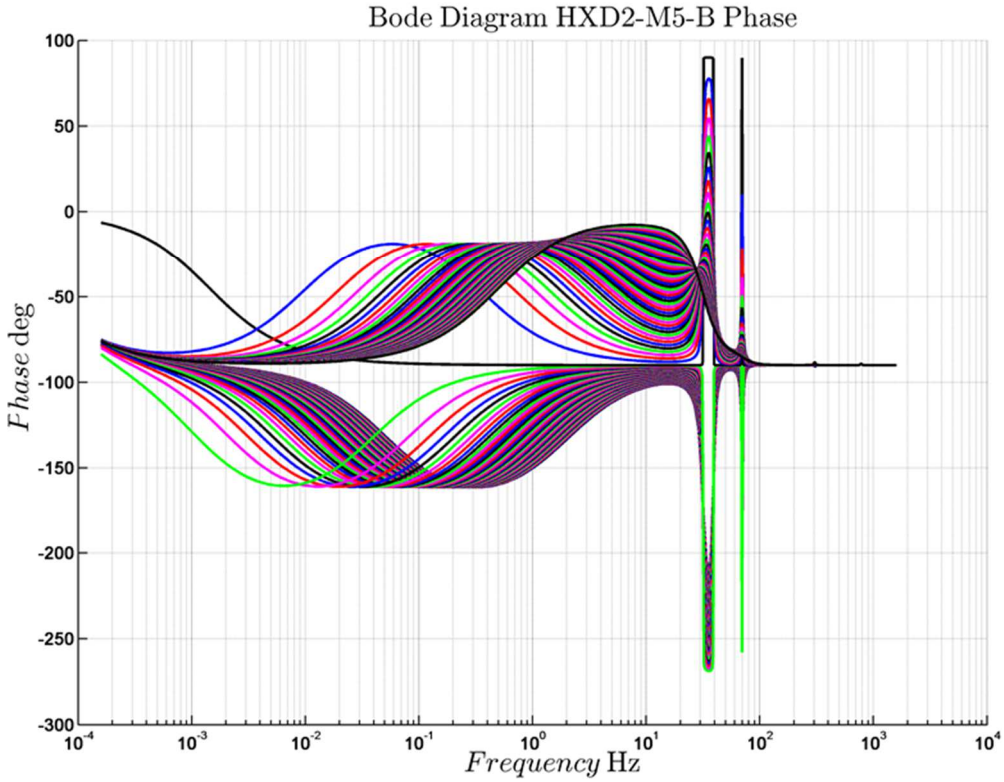

Fig. 2-6 Bode diagram – phase of the mechanical chain transfer function G_2 for dry rail

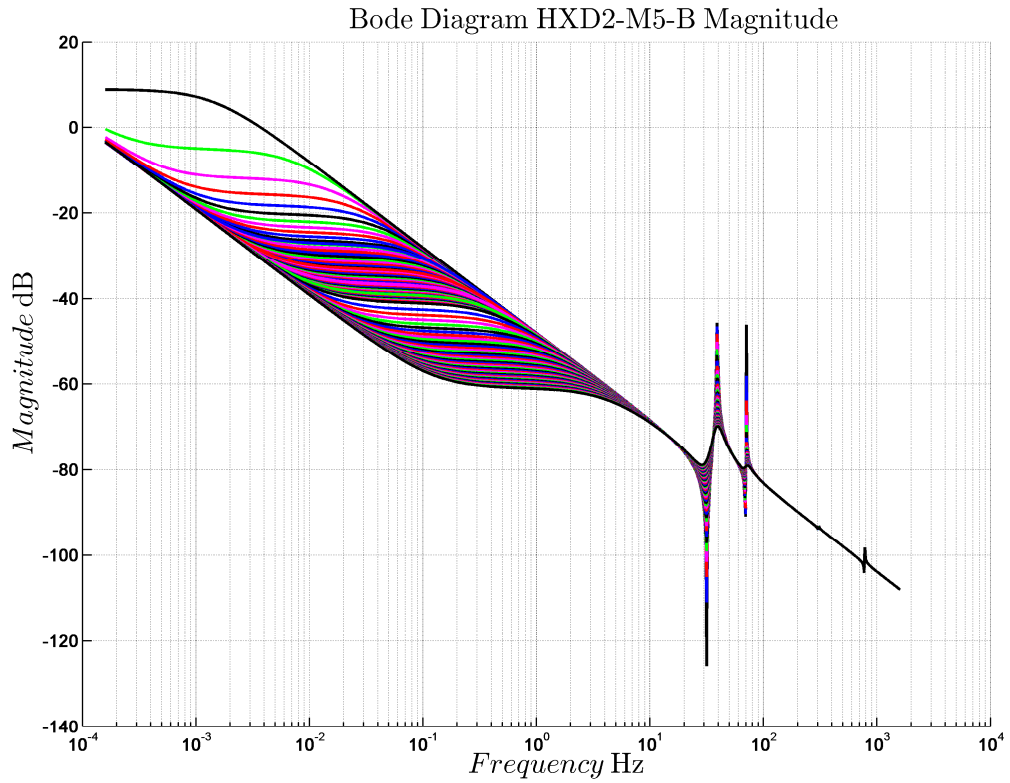

Fig. 2-7 Bode diagram – amplitude of the mechanical chain transfer function G_2 for wet rail

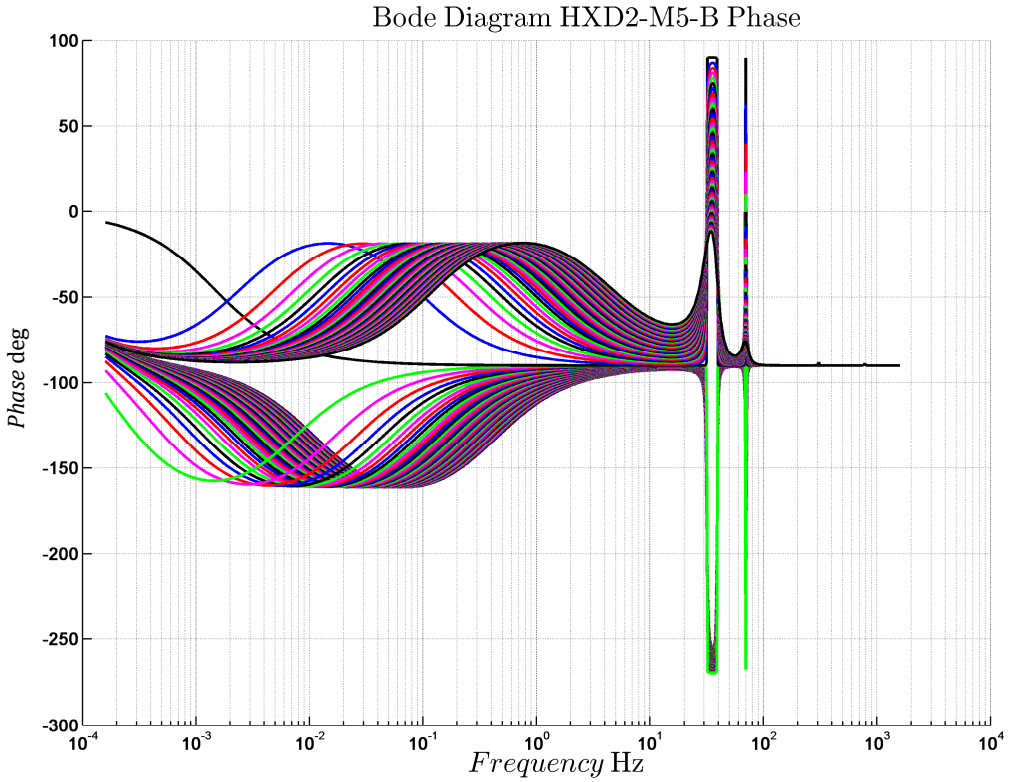

Fig. 2-8 Bode diagram – phase of the mechanical chain transfer function G_2 for wet rail

The linearity of the phase change can be seen better in Fig. 2-9, where, for better visibility, the damping in s·m^{-1} is used on the horizontal axis scale. When searching for the optimal modulation frequency, we can proceed from the theoretical assumption that the damping can be defined as a tangent slope at the adhesion characteristics' operating point. The damping has a zero value at the top of the adhesion characteristics. For further consideration about suitable modulation frequency, the frequencies that do not change phase linearly have to be discarded. This is the case of waveforms for 5 Hz and 30 Hz in Fig. 2-10. Therefore, these frequencies are not suitable for the adhesion controller. Waveforms in the range from 10 Hz to 20 Hz are linear, and therefore these frequencies present viable candidates for the phase (quantity φ_s) determination.

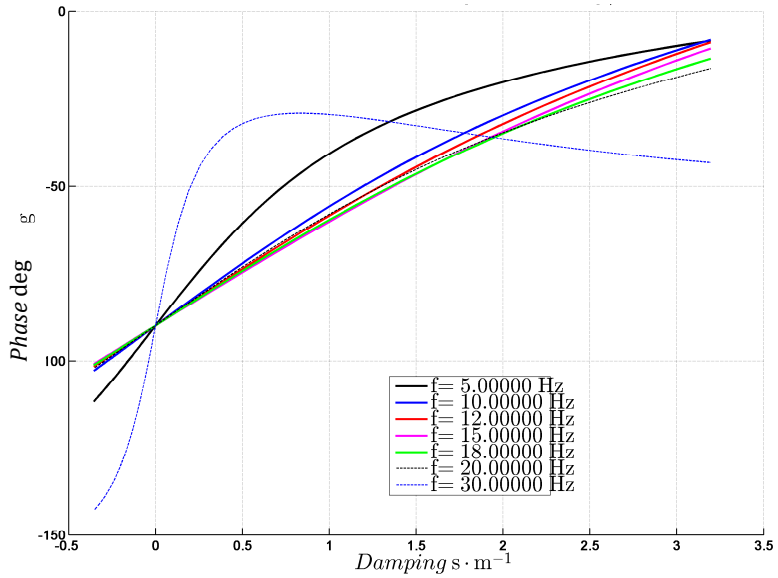

Fig. 2-9 Diagram of the phase of the mechanical chain transfer function G_2 as the function of damping for dry rail

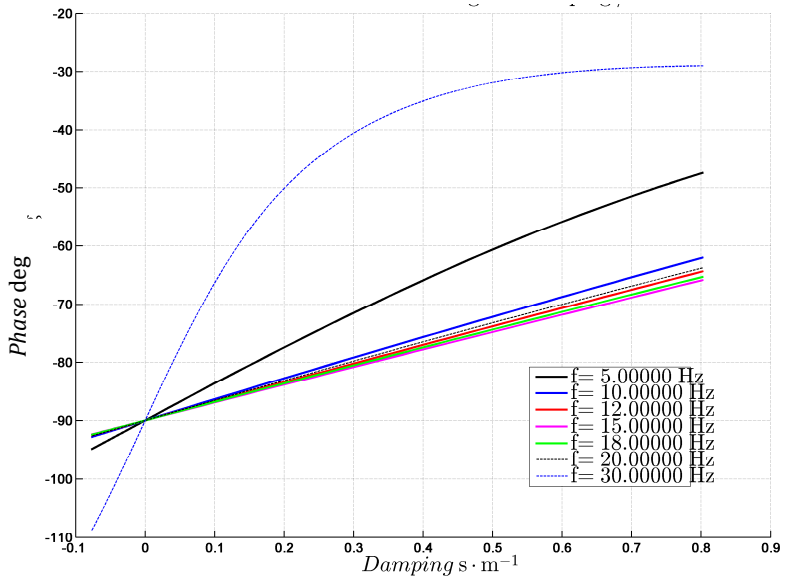

Fig. 2-10 Diagram of the phase of the mechanical chain transfer function G_2 as the function of damping for wet rail

Based on simulation analyses presented in Fig. 2-9 and Fig. 2-10, two candidates selected for the modulation frequency f_{mf} were selected. These candidates were tested on the locomotive

running on the test track. Finally, frequency 12 Hz was selected as a compromise between the phase's linear change during the starting slip and signal analyzer initialization and response.

2.3 Influence of Speed Measurement Method on Slip Controller

The motor's speed measurement accuracy directly influences the slip controller performance [38], [57]. Especially during the train start when the applied forces are high, and the measured velocities change slowly due to the measurement principle. Furthermore, the measured velocity can be zero because of signal filtering, even though the train is moving. These situations are caused by the used incremental encoder with a low number of pulses per revolution (90 pulses).

The incremental encoder signals used for the speed measurement can be processed according to the period between two edges – the period measurement, or according to the number of edges measured during a particular time frame – the frequency measurement. The period measurement method is suitable for the measurement in the low-speed area. Its limitation is the microcontroller's timer range. The used 150 MHz DSP TMS320F28335 from Texas Instruments is equipped with a 32-bit timer. In this case, the lowest measurement times are tens or hundreds of milliseconds (time between two edges is 75.3 ms for wheel speed 0.1 km·h^{-1}). The principle of the method is shown in Fig. 2-11. The main problems of the methods are caused by the timer edge and incremental encoder edge misalignment.

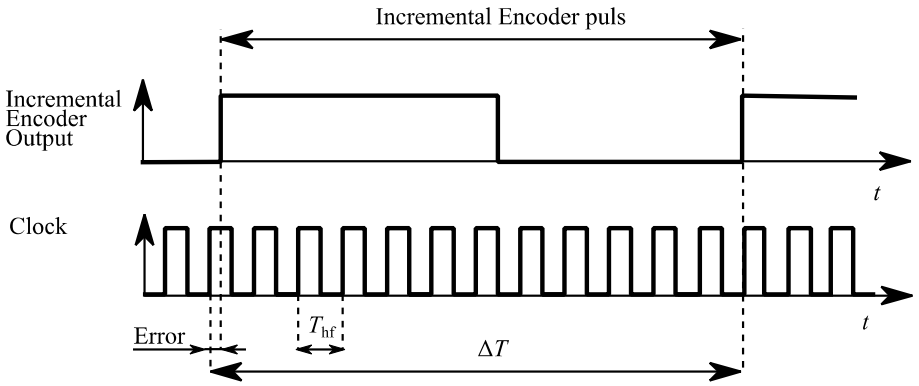

Fig. 2-11 Principle of period measurement

The rotor angular speed is calculated in the case of the period method as

$$\Omega(k) \approx \frac{2\pi}{\Delta T N_{\mathrm{PG}}}, \tag{2-16}$$

where $\Omega(k)$ is the rotor angular speed at time instant k, ΔT is the total time elapsed for single position movement, and N_{PG} is the incremental encoder's constant. If ΔT is measured between two rising edges, then N_{PG} is the same as the number of incremental encoder "teeth." But if ΔT is measured between two adjacent edges, then N_{PG} is two times greater than the number of incremental encoder pulses. The relative error of the method is defined as

$$\varepsilon_{\mathrm{p}} = \frac{N_{\mathrm{PG}} \omega T_{\mathrm{hf}}}{2\pi}. \tag{2-17}$$

The frequency measurement method is better for higher speed areas. The method's basic principle is shown in Fig. 2-12. The method measures either the number of incremental encoder pulses or the number of edges for a given constant period T_s. The method's error is caused by a misalignment between the constant frequency rising edge and incremental encoder rising edge, as shown in Fig. 2-12. The rotor angular speed can be calculated for the frequency measurement method as

$$\Omega(k) \approx \frac{2\pi}{N_{\mathrm{PG}}} \frac{N_S}{T_S}, \tag{2-18}$$

where T_s is constant or variable (depends on the method type) measurement period, and N_s is the number of pulses per T_s period. The relative error of the frequency method is given by

$$\varepsilon_f = \frac{2\pi}{N_{PG}\omega T_S}. \tag{2-19}$$

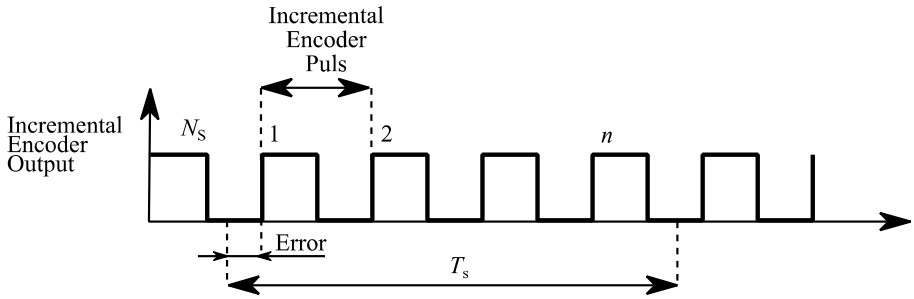

Fig. 2-12 Principle of frequency measurement

The frequency measurement method can be further improved by adjusting the sampling period T_s. The measuring period starts when the incremental encoder edge arrives and ends after the last incremental encoder edge that fits inside the measuring period. The methods' error comparison is depicted in Fig. 8. The figure shows that the improved frequency method does not work for low speed but has low relative error for higher speeds.

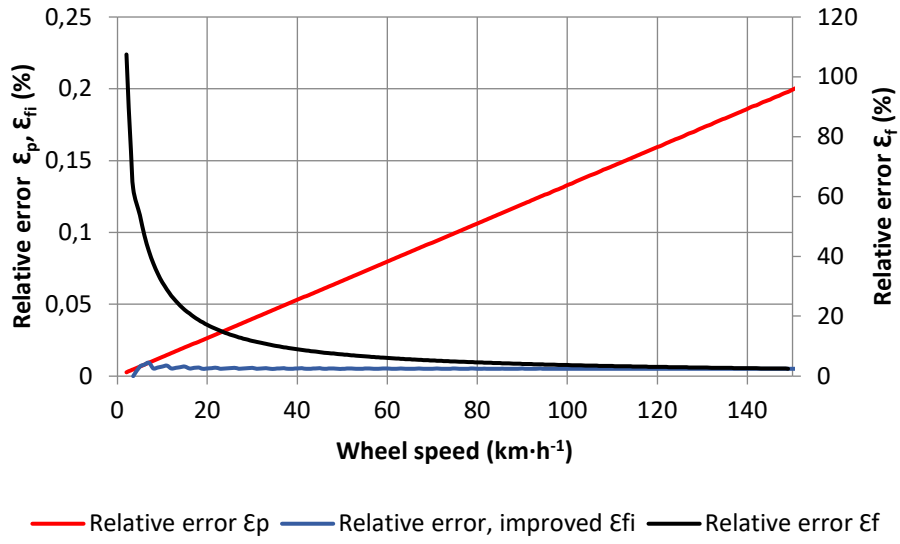

Fig. 2-13 Method error comparison

An example of a wrongly selected strategy for angular speed evaluation with high filtering capability but low accuracy is the following speed measurement utilized on the locomotive by CRRC. The used method measures time t between N pulses (averaging filter over N pulses). The time is measured by the eCAP module of TMS320F2833S, which considers only rising edges of the incremental encoder output signal. Every rising edge causes an interrupt where the eCAP timer is reset, and the timer value is saved. From the stored values, the period of one pulse is calculated as

$$T = \frac{t}{N'}, \tag{2-20}$$

where T is the incremental encoder signal period. The number of rising edges N' required for the speed averaging depends on actual angular speed of IM and is calculated as

$$N' = (\text{int})\,(\omega \cdot 0{,}1 + 1). \tag{2-21}$$

The measurement period t starts with the rising edge and stops after the N^{th} rising edge (Fig. 2-14). The measurement period t depends on the rotor speed (2-21). Fig. 2-15 shows the time between N edges and the number of edges for the wheel circumference velocity. The value of t can be a source of a measurement error caused by a long time delay that is not negligible, especially during the train start.

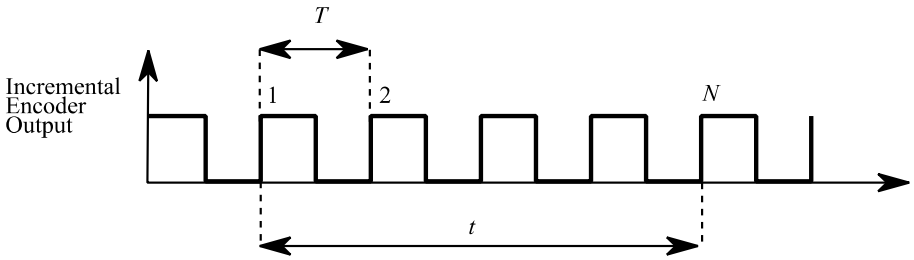

Fig. 2-14 Used speed measurement method

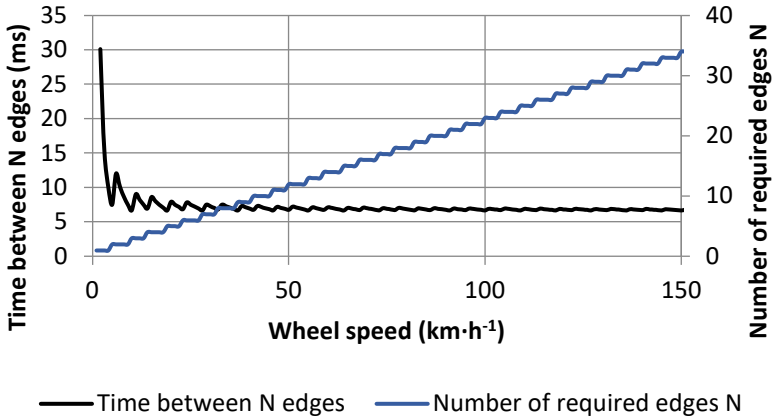

Fig. 2-15 Time between required edges and number of required edges

The impact of the method selected for speed measurement can be seen in Fig. 2-16, where waveforms of train speed (blue), speed estimated by the "wrong" method (red) and speed estimate by the frequency (cyan) and period (black) method (eQEP) measurement are compared. Out of the figures, it is evident that, especially during the locomotive start, the method based on the period measurement generate incorrect information about the speed caused by small numbers on IRC, thus long interval between measurements. In fact, the drive is for almost 300 ms running and speed information is still zero, this has negative influence the slip controller. In higher speeds is information refresh rate sufficient, but still averaging causes delay compared to real speed. The influence of low speed inaccuracy is described in [57] in more detail. The impact of the real implementation on the controlled drive can be seen in Fig. 2-17, which is based on data downloaded from the drive controller during the run of the locomotive. It can be seen that the speed signal is distorted by wrong speed estimation, caused by inaccurate speed measurement form rising edges of IRC and averaging over certain period. Moreover, inaccurate speed information leads to instability of FOC current controllers, that can be seen in detail of Fig. 2-17, where green signal represent actual measured value of torque producing component of current i_q.

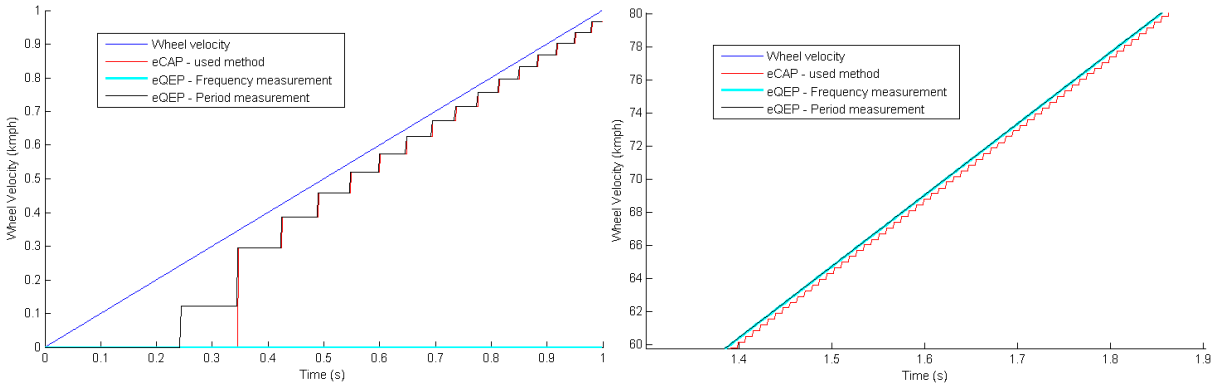

Fig. 2-16 Speed measurement comparison for low speed (left) and high speed (right)

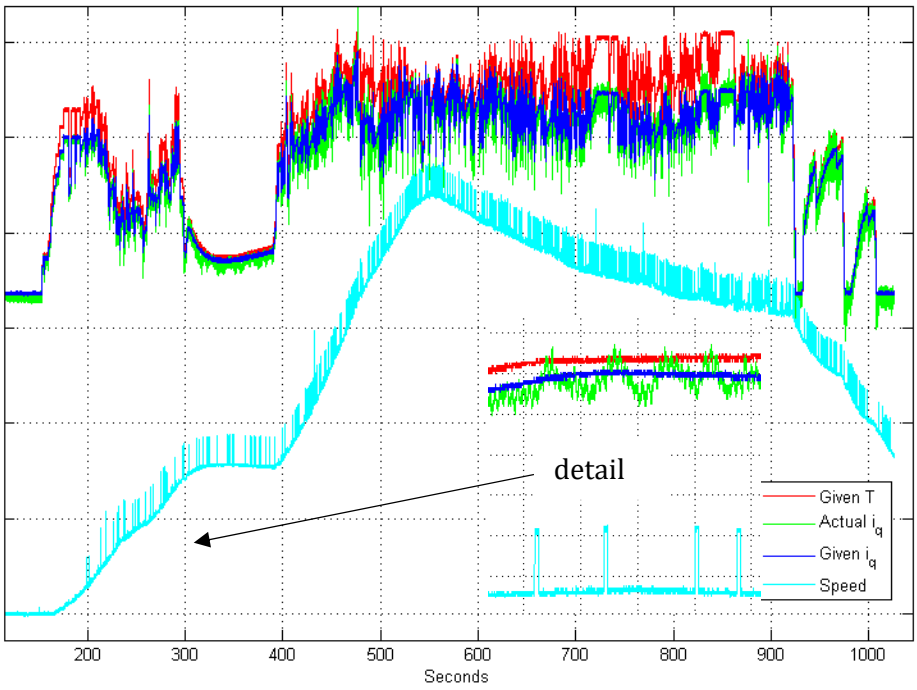

Fig. 2-17 Measured data form DSP drive controller – angular velocity (cyan); required torque producing current component (blue); actual torque producing current component (light green)

2.4 Controller Implementation

The company CRRC asked for a slip controller that would replace the already implemented one in 8 MW freight eight axle locomotive HXD2. The currently used slip controller was working on the principle of speed difference slip controller (Fig. 1-7) and was degrading the locomotive's performance. According to the problem analysis, the bad performance was caused by a wrongly selected speed measurement technique in the drive's controllers and because of the used method's principle (speed update period 2ms), which needed the actual information about speed for its function. However, due to the implementation of the drive controller and vehicle communication bus MVB, the information about the speed of other axles was obtained with a variable time delay from 4 ms to 32ms. Therefore, the tuning of the controller was difficult. Because the FOC and other functions were already implemented, the requirement from CRRC was that the new controller had to be developed as a kind of addendum to the functional system

without additional HW modifications. The controller had to meet maximum computational time $t_{\max} = 100$ µs (free time of DSP), operate with speed sensor with 90 pulses per revolution, and controller execution loop $t_{\text{exec}} = 400$ µs. Because of this fact, and because of the variable delays in MVB communication, the adhesion slope detection algorithm was selected. The block diagram of the final version of the controller is shown in Fig. 2-18.

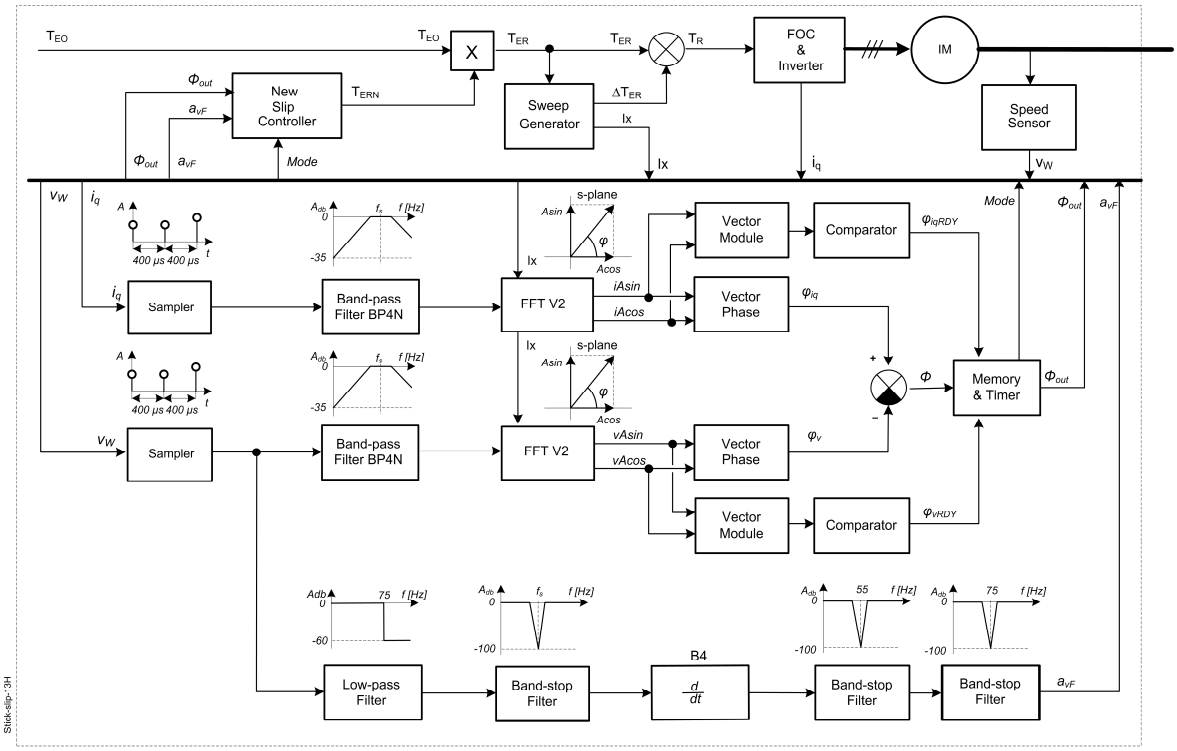

Fig. 2-18 The block diagram of the developed slip controller and slip protection

Because the value of IM's torque T_{m} in Fig. 1-11 can't be easily measured, the actual value of measured torque producing current component i_q was used instead. The image of the modulation signal is obtained from the wheel speed Ω measured by IRC mounted to IM shaft. Both quantities are sampled and further processed in a 400 µs period. The current component signal i_q is filtered in the "Band-pass filter" block. This filter is tuned to let pass the modulation frequency f_{mf} and second, it aims to eliminate the DC component in the signal.

The output signal of block "Band-pass filter" is connected to block "FFT V2," whose outputs are the instantaneous values of sine approximation *iAsin* and cosine approximation *iAcos* of the input signal. This FFT block is also syncing input *Ix*, which synchronizes inner variables used for FFT calculation. Syncing is done at the beginning of the modulation period.

Because of the DSP implementation, the following numerical approximation approximates the integrals:

$$a_k(n) = \frac{1}{\text{m}} \sum_{i=0}^{\text{m}} x_{i+n} \sin(k\Omega\tau_{i+n}), \tag{2-22}$$

$$b_k(n) = \frac{1}{\text{m}} \sum_{i=0}^{\text{m}} x_{i+n} \cos(k\Omega\tau_{i+n}), \tag{2-23}$$

where m is the number of samples in one period, n is the sample number. The implementation of the calculation algorithm in C language is shown right below.

```
void fftExtraFncFloat(float sampleValue, TfftExtraVarsFloat *pDe,
TfftVarsFloat *pD)      //calculate value of fft with supressed mean value
influence
{
```

```
	int m, i;
	float pS, pC;
	float x;

	fftExtraFifoReadFloat(pDe);
	x = pDe->fifoHeadValue;
	fftExtraFifoWriteFloat(pDe,-sampleValue);
	sampleValue = (sampleValue + x) /2.0l;

	m = (int)(pD->fifoLen/2);
	i = pD->kIndex;
	pS = pD->kSin[i] * sampleValue;
	pC = pD->kCos[i] * sampleValue;
	// Get analyzed sin*x and cos*x values at FIFO head
	fftFifoReadFloat(pD);
	// Integrate
	pD->sumSin = pD->sumSin + pS - pD->fifoHeadSinValue;
	pD->sumCos = pD->sumCos + pC - pD->fifoHeadCosValue;
	// Save new values at FIFO tail
	fftFifoWriteFloat(pD, pS, pC);

	i++;
	if(i >= pD->fifoLen)
		i = 0;
	pD->kIndex = i;
	// Save new sin/cos amplitudes
	pD->ampSin = pD->sumSin / m;
	pD->ampCos = pD->sumCos / m;
}

void fftExtraFifoReadFloat(TfftExtraVarsFloat *pD)    //read   value   form
extra fft fifo
{
	int i = 0;
	i = pD->fifoHeadIndex;
	pD->fifoHeadValue = pD->fifo[i];
	i++;
	if (i >= pD->fifoLen)
		i = 0;
	pD->fifoHeadIndex = i;
}

void fftExtraFifoWriteFloat(TfftExtraVarsFloat *pD, float value)  //write
value to extra fft fifo
{
	int i = 0;
	i = pD->fifoTailIndex;
	i++;
	if (i >= pD->fifoLen)
		i = 0;
	pD->fifoTailIndex = i;
	pD->fifo[i] = value;
}
```

The module and phase of signals *iAsin* and *iAcos* are calculated in blocks "Vector Module" and "Vector Phase." The signal Φ which is representing actual working point position on the adhesion characteristics, is calculated as subtraction of the actual phase φ_{iq} from the actual value of the phase φ_{v}. The signal Φ is then controlled by a conventional PS controlled

To increase the controller's robustness, acceleration protection (Fig. 2-18 bottom part) was implemented (because the adhesion loss can also be detected using acceleration). The concrete mathematical method for the determination of the acceleration was also proposed. Input signal

v_w is filtered in block "Low-pass Filer" with the cutoff frequency 75 Hz. Next block "d/dt" calculates the derivative of the input signal using the following Bernstein polynomial:

$$B(x) = \binom{n}{k} x^k (1-x)^{n-k} P_k, \tag{2-24}$$

where P_k are the signal samples, and n = 4 and x = 0,5. The resulting equation for calculation is given by

$$\frac{dy}{dt} \approx \frac{-y_{-2} - 2y_{-1} + 2y_1 + y_2}{8T_s}. \tag{2-25}$$

This numerical derivative was selected to obtain smooth continuous value without additional filtration. Therefore, the calculated derivative is filtered only with respect to the sweep frequency f_{mf} and eigenfrequencies of the mechanical system. The time consumption of implemented blocks in DSP TMS320F28335 are given in Tab. 2-1.

Tab. 2-1 Computational requirements of slip controller blocks

Slip controller	***t* (µs)**
Band Pass BP4N Filter	15.8
FFT	8.8
Modified atan2	1.2
Module calculation	1.8
PI controller	5.4
Whole slip controller	100.7

Acceleration protection	***t* (µs)**
Low pass IIR filter	36.4
Derivative	2.8
Band-stop filter	3.7
Band-stop filter	3.7

2.5 Obtained Results

Fig. 2-19 shows the detail of slip controller activation during the run of the locomotive on the dry rail with a constant speed of 18.16 km·h^{-1} (measured by GPS). Only the first axle of the locomotive was at the operation during the measurement; other axles were switched off. At time instant 89.53 s, the slip controller was triggered. This activation is visible on signal *AdhCtrl.CorK*. At the same instant, the motor speed was recalculated to wheel speed 18.7 km·h^{-1}. Slip – the difference between the motor's speed and the locomotive's speed has a value of 0.54 km·h^{-1}. Out of the reference torque (signal *MotorCtrl.TeRamp*), it is evident that it was decreased from 10 kN to 7 kN (about 30 % of the initial value).

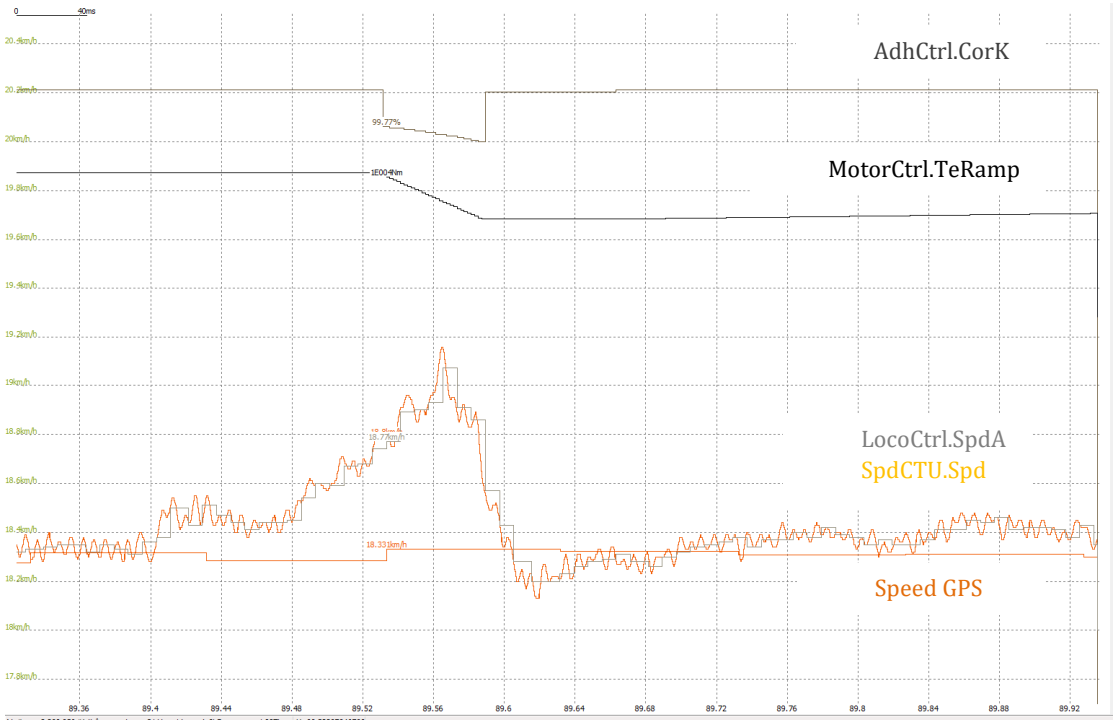

Fig. 2-19 Detail of slip controller reaction

Fig. 2-20hows the detail of the inadequate reaction of the slip controller. At time instant 41.85 s, the controller is first activated, and the reference torque (*MotorCtrl.TeRamp*) decreases. However, the motor speed is still rising. The second activation of the slip controller is at 41.86 s. The required torque is decreased from 8.42 kN to 7.55 kN. Here, the speed of the motor starts to decrease. At time instant 41.89 s, the slip controller is triggered for the third time. The activation lasts 7 ms, and the required torque is further decreased from 7.55 kN to 7.19 kN.

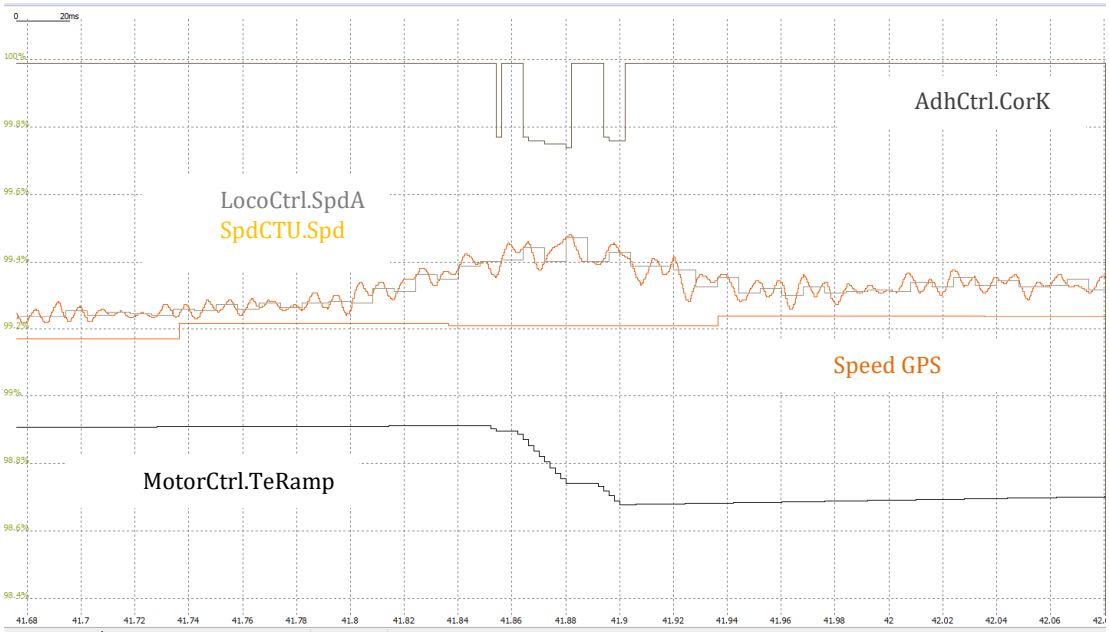

Fig. 2-20 Detail of slip controller wrong reaction

The developed slip controller's reaction is depicted in Fig. 2-21. The controller starts to react when the phase drops below -60°, i.e., approx. 100ms after the slip starts to develop.

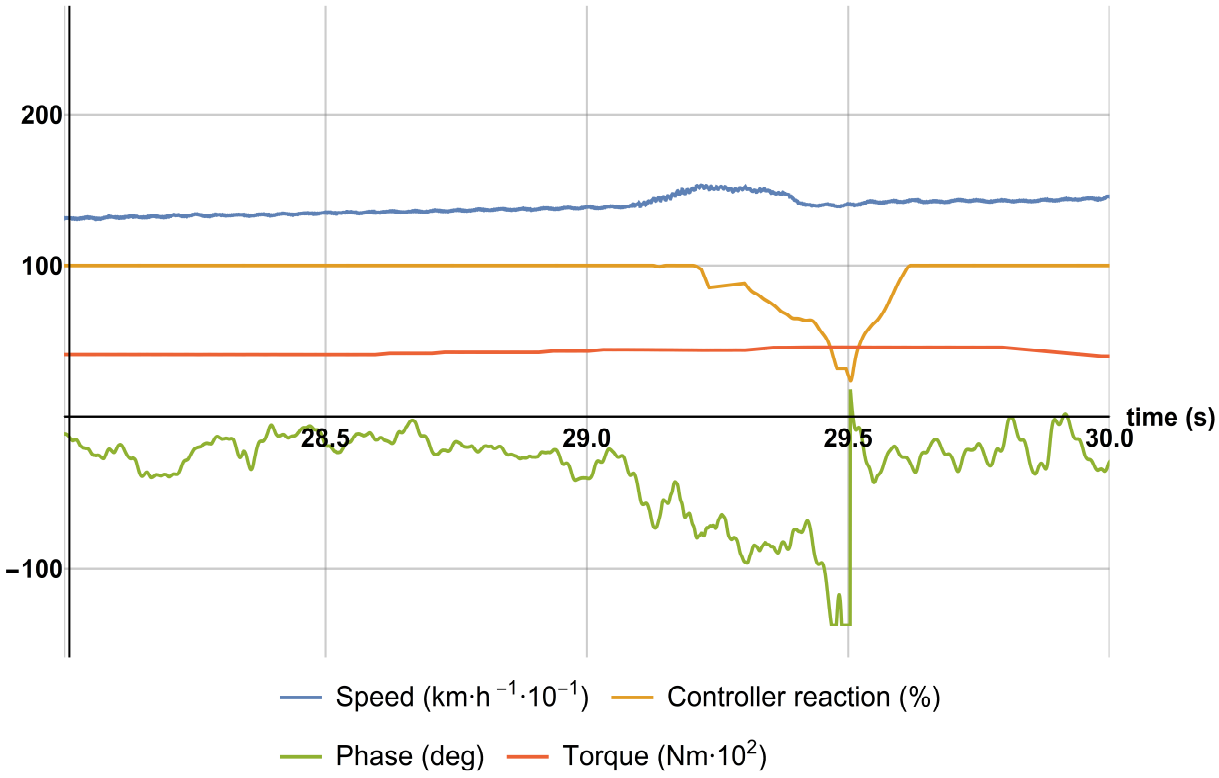

Fig. 2-21 Developed controller's reaction

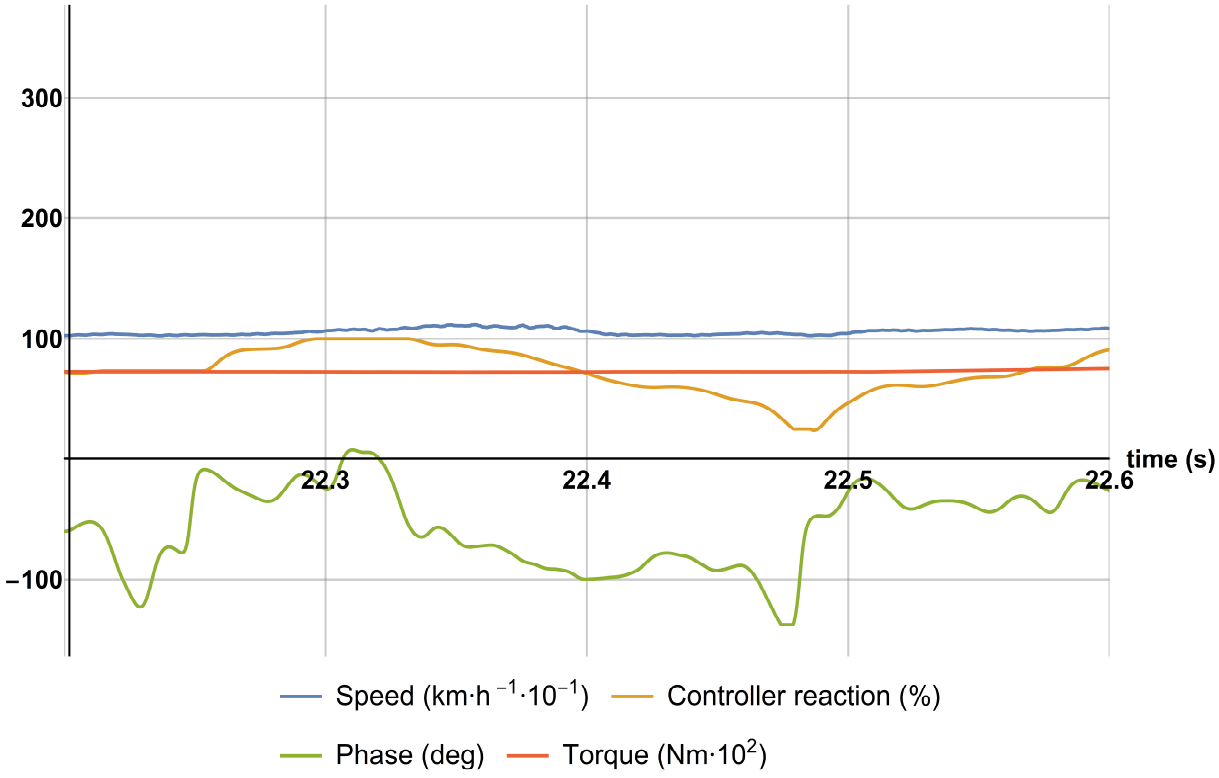

Fig. 2-22 Developed controller's reaction – slowly increasing slip

Fig. 2-23 presents a comparison of the controllers during acceleration with 100 % traction effort on a dry rail. It can be seen that in two cases, the proposed controller was better than the

currently used one. Fig. 2-24 presents a comparison of the controllers during the acceleration on wet rail. Here, the performance of the slip controllers is almost the same. Different conditions influenced the measurement because not all runs were done in the same sections of the track.

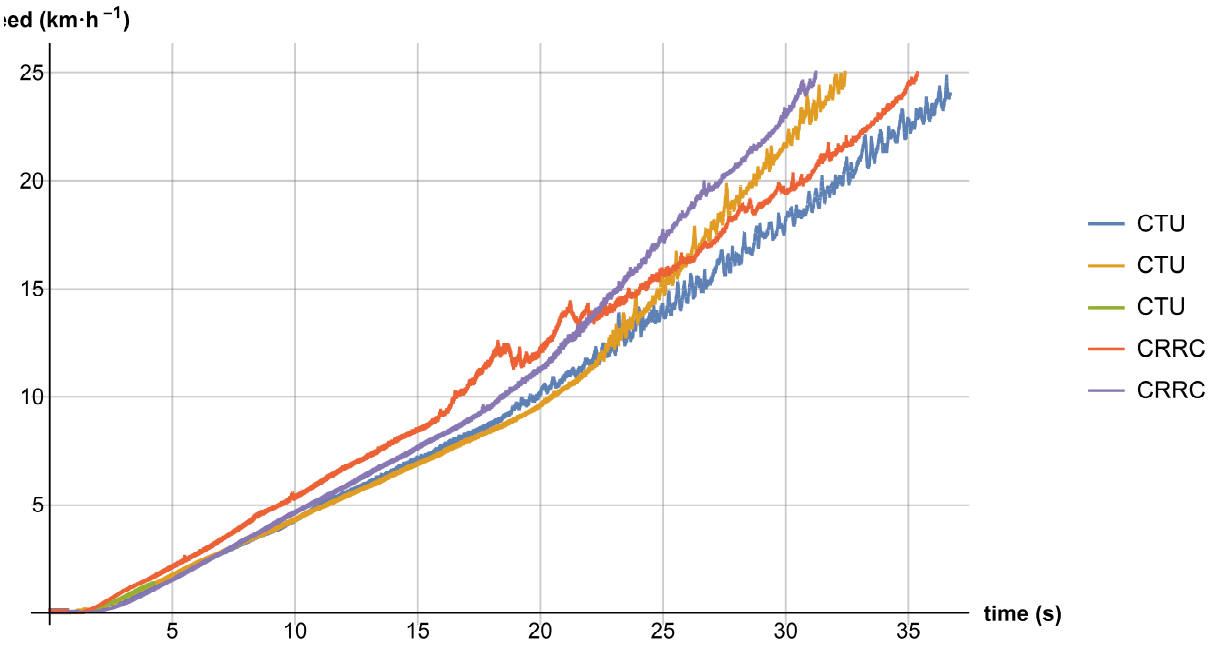

Fig. 2-23 Slip controllers' comparison on dry rail – new controller (CTU), CRRC controller (CRRC)

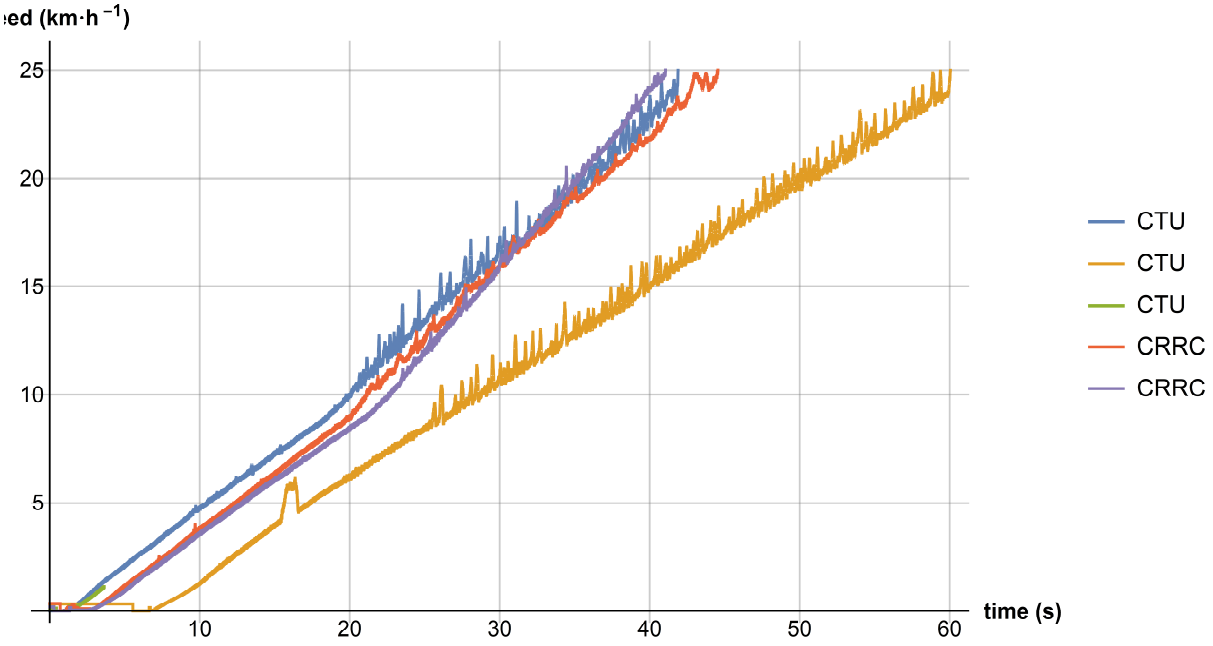

Fig. 2-24 Slip controllers' comparison on wet rail – new controller (CTU), CRRC controller (CRRC)

2.6 Author's Contribution

Dr. Bauer was a member of the team that was working on the project. He was responsible for the controller source code programming. He participated in developing the Matlab simulation model presented in this chapter. He has analyzed influences of implemented FOC strategy and inverter's modulation on the functionality of the controller and controller's reverse effects on the IM drive. He has visited 6 times the Peoples Republic of China. He was responsible for integrating the developed source codes into the existing locomotive control system, its testing, data acquisition, data analysis and code functionality validation. He has co-written manuscript [57], 20 project report delivered to the CRRC and 2 patents.

Publications and patents related to this section:

1) PICHLÍK P. and BAUER J., "Analysis of the Locomotive Wheel Slip Controller Operation During Low Velocity," in IEEE Transactions on Intelligent Transportation Systems.doi: 10.1109/TITS.2020.2971832 – Early acces (Appendix A)
2) České vysoké učení technické v Praze. Zařízení pro řízení skluzu kol kolejového vozidla a způsob řízení skluzu kol kolejového vozidla v tomto zařízení. Původci: J. BAUER et al. Česká republika. Patent CZ PV 2019-525. 2020-01-08.
3) České vysoké učení technické v Praze. Způsob pro odhad sklonu adhezní charakteristiky kolejového vozidla v pracovním bodě a zařízení pro provádění tohoto způsobu. Původci: J. BAUER et al. Česká republika. Patent CZ PV 2019-526. 2020-01-08.

CHAPTER 3: INFLUENCE OF INDUCTION MOTOR DRIVE PARAMETER INACCURACY ON CONTROL QUALITY

One of the most common IM control strategies in demanding applications, including railway traction drives, is the Rotor Flux-Oriented Control (RFOC) [62], [63]. To reach high performance and high efficiency of the drive, precise knowledge of the IM equivalent circuit parameters is needed. These parameters are used within the RFOC to get the correct setpoints for the controllers. Inaccurate knowledge of the IM equivalent circuit parameters leads to RFOC detuning, which causes misalignment of the estimated flux position and, thus, inaccuracy of the whole control [60], [62], [63], [82], [83]. Some phenomena (e.g., AC vs. DC resistance) can be quite safely omitted without affecting the IM control quality much. Considering RFOC based on the reduced-order model that was implemented in the CRRC locomotive, the most decisive influence on the control quality represents the magnetizing inductance and rotor resistance detuning that can:

- reduce the locomotive's torque capabilities,
- cause incorrect operation of field weakening (field weakening is always employed in traction vehicles),
- cause incorrect operation of current optimization strategies,
- lead to increased current drawn from the source.

The last two points in the list represent an important aspect since electric motors consume a considerable part of the world's electric energy [58], [61], [62]. In the case of a locomotive with a few megawatts' rated power, the savings achieved by correct IM parameter determination can be quite significant.

Also, today's requirements for reliability and cost reduction lead to the deployment of sensorless control strategies. In the case of a sensorless drive, the incorrect parameters' negative influence is even more pronounced. Furthermore, within VSD, the utilization of a frequency converter, most of the time, based on a two-level Voltage-Source Inverter (VSI), is necessary. However, due to the strong nonlinear and operating point-dependent behavior of the power electronics devices, the VSI cannot be simply considered a linear amplifier of the voltage command. Therefore, if the implemented IM mathematical model requires the knowledge of the stator voltage, a proper VSI nonlinearity compensation is needed, especially in the low-speed low-torque area.

3.1 Induction Machine Model

RFOC is based on a mathematical model of the machine. Before the model derivation, several simplifications have to be accepted – that the stator and rotor windings are symmetrical and sinusoidally distributed, that the magnetic circuit is linear and lossless, that all the parameters (i.e., resistances and inductances) are frequency-independent, and that the airgap is perfectly smooth. In such a way, the resulting model is put into a convenient form directly utilizable in the control algorithm. However, the omission of the aspects mentioned above, such as the iron nonlinearity, iron losses, and the stator and rotor resistances' thermal change, will cause deviations between the real motor and its twin modeled in the controller [63], [82], [83]. Such a discrepancy will cause a degradation of RFOC performance that is, especially for heavy freight locomotive, essential.

The T-equivalent circuit (Fig. 3-1) is a generally accepted equivalent model of IM [69], [70]. With the help of space vector theory, it can be mathematically described as:

$$\underline{u}_1^k = R_1 \underline{i}_1^k + \frac{\mathrm{d}\,\underline{\psi}_1^k}{\mathrm{d}t} + \mathrm{j}\omega_k\,\underline{\psi}_1^k, \tag{3-1}$$

$$\underline{u}_2^k = 0 = R_2 \underline{i}_2^k + \frac{\mathrm{d}\,\underline{\psi}_2^k}{\mathrm{d}t} + \mathrm{j}(\omega_k - \omega)\,\underline{\psi}_2^k, \tag{3-2}$$

$$\underline{\psi}_1^k = L_{1\sigma}\underline{i}_1^k + L_\mathrm{m}\underline{i}_\mathrm{m}^k, \tag{3-3}$$

$$\underline{\psi}_2^k = L_{2\sigma}\underline{i}_2^k + L_\mathrm{m}\underline{i}_\mathrm{m}^k, \tag{3-4}$$

$$\underline{u}_\mathrm{m}^k = \frac{\mathrm{d}\,\underline{\psi}_\mathrm{m}^k}{\mathrm{d}t} = R_\mathrm{Fe}\underline{i}_\mathrm{Fe}^k + \mathrm{j}\omega_k\,\underline{\psi}_\mathrm{m}^k, \tag{3-5}$$

$$\underline{i}_1^k + \underline{i}_2^k = \underline{i}_\mathrm{m}^k + \underline{i}_\mathrm{Fe}^k, \tag{3-6}$$

$$\underline{\psi}_\mathrm{m}^k = L_\mathrm{m}\underline{i}_\mathrm{m}^k, \tag{3-7}$$

$$T_\mathrm{e} = \frac{3}{2}p_\mathrm{p}\frac{L_\mathrm{m}}{L_{2\sigma}}\left(\underline{\psi}_2^k \times \underline{i}_\mathrm{m}^k\right), \tag{3-8}$$

where $\underline{\psi}_1^k$, $\underline{\psi}_2^k$ and $\underline{\psi}_\mathrm{m}^k$ are the stator, rotor, and magnetizing flux linkage space vectors, respectively, $\underline{u}_1^k$, $\underline{u}_2^k$ and $\underline{u}_\mathrm{m}^k$ are the stator, rotor, and magnetizing voltage space vectors, respectively, $\underline{i}_1^k$, $\underline{i}_2^k$ and $\underline{i}_\mathrm{m}^k$ are the stator, rotor, and magnetizing current space vectors, respectively, $\underline{i}_\mathrm{Fe}^k$ is the current space vector of the equivalent iron loss resistance path, R_1 and R_2 denote the stator and rotor resistance, respectively, R_Fe is the equivalent iron loss resistance, ω_k is the electrical angular speed of the general reference frame, ω is the rotor electrical angular speed, L_m is the magnetizing inductance, p_p denotes the number of pole-pairs, T_e is the electromechanical torque, and the symbol j represents an imaginary unit ($\mathrm{j}^2 = -1$). A squirrel-cage rotor is considered; therefore, the rotor voltage equals zero. The stator inductance L_1 is defined as $L_1 = L_\mathrm{m} + L_{1\sigma}$, where $L_{1\sigma}$ is the stator leakage inductance and the rotor inductance L_2 is defined as $L_2 = L_\mathrm{m} + L_{2\sigma}$, where $L_{2\sigma}$ is the rotor leakage inductance. The superscript k indicates that the quantities are expressed in a general reference frame. Furthermore, it is supposed that the magnetizing inductance is a function of the flux level and load and that the iron loss resistance is a function of the flux level and frequency.

In the following sections, α and β denote the real and imaginary axis, respectively, of the stator-fixed coordinate system, and d and q denote the real and imaginary axis, respectively, of the synchronously rotating coordinate system.

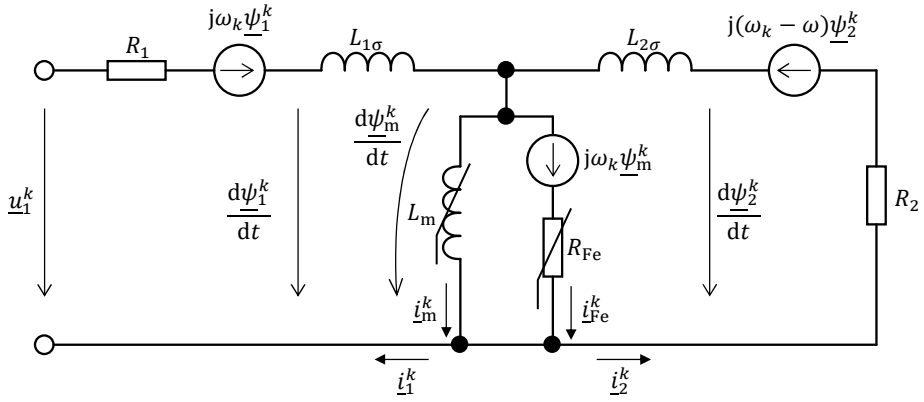

Fig. 3-1 T-equivalent circuit of a saturated induction machine with included fictitious iron loss resistance

3.2 Magnetic Saturation

Magnetic saturation is one of the sources of RFOC detuning [79], [82]. Due to the material savings, induction motors are usually designed so that their nominal operation point lies inside the magnetization curve's knee. With the utilization of advanced RFOC control strategies, the magnetizing inductance may change in a wide range during the drive operation. Saturation characteristics can be obtained from the conventional no-load test of induction motor [66]-[68]. However, with the self-tuning-tuning algorithms, advanced methods based on MRAS or observers were proposed in the literature [67], [68], [72], [80]. Also, some papers try to identify the inductance by high-frequency signal injection. Within most papers, the magnetizing inductance is expressed as

$$L_{\mathrm{m}} = f(i_{\mathrm{m}}) = f(\psi_{\mathrm{m}}). \tag{3-9}$$

However, if the motor is equipped with a rotor equipped with closed and/or skewed slots, the magnetizing inductance can be heavily dependent on the rotor current [75], [77], [78]. This phenomenon is not usually respected within the works of other authors.

3.2.1 Load-Dependent Saturation

The first reason for the dependence of the magnetizing inductance on the rotor current can be seen in Fig. 3-2. The figure shows the T-equivalent circuit magnetic flux vector diagram (a) with marked magnetic flux paths (b). The main flux passes through the stator and rotor yoke and teeth. If the rotor slots are closed, then the bridge provides a path for the leakage flux. However, because the slot bridges are relatively narrow, the rotor leakage flux saturates strongly as the rotor current's function. In Fig. 3-2, it can be seen that the saturation at the rotor surface and in the slot bridges caused by the rotor current appear in the main flux path, which causes the dependence of the main flux on the rotor current [75].

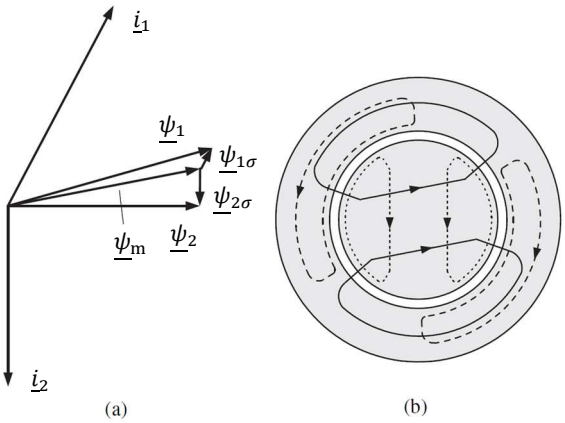

Fig. 3-2 (a) Space vector diagram and (b) magnetic paths: main flux (solid), stator leakage flux (dashed), and rotor leakage flux (dotted)

The second cause of the load-dependent saturation is the rotor skewing. The rotor slots of the majority of low and middle power IM are skewed due to the reduction of the cogging and asynchronous and synchronous parasitic torques. In linear magnetic conditions, the skewing increases the rotor resistance, and the rotor leakage inductance and decreases the magnetizing inductance [72], [73]. A skewed rotor can be modeled as an infinite number of elemental machines connected in series on the same axis. Each element is then shifted towards the previous one by the angle corresponding to the skewing. Fig. 3-3 shows the vector diagram for the case when the rotor is modeled as three phase-shifted slices. In all cases, the stator is geometrically identical. Each slice contains a different equivalent rotor current vector due to the mutual rotor winding phase shift. The equation for resulting magnetizing inductance can be written as

$$L_{\mathrm{m}} = \frac{\psi_{\mathrm{m}(1)} + \psi_{\mathrm{m}(2)} + \psi_{\mathrm{m}(3)}}{i_{\mathrm{m}(1)} + i_{\mathrm{m}(2)} + i_{\mathrm{m}(3)}}. \tag{3-10}$$

Under saturated magnetic conditions, the operating point in every rotor slice is located in a different part of the magnetization curve, which causes the overall decrease of the resulting magnetizing inductance, as seen in Fig. 3-3.

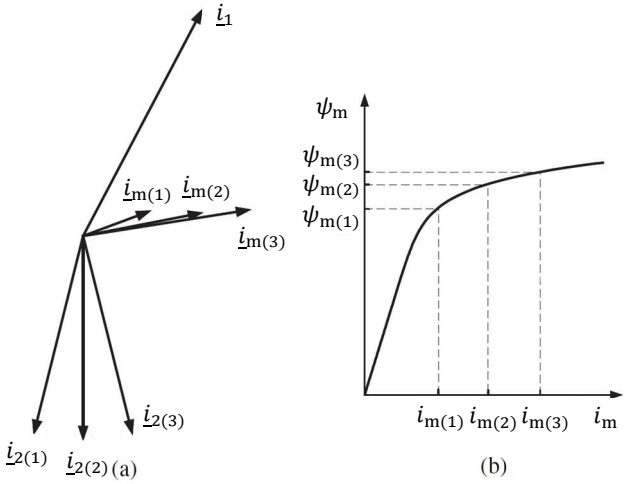

Fig. 3-3. Effect of the skewed rotor when the motor consists of three slices with different rotor positions: (a) current space vectors and (b) saturation characteristics. Currents at the end slices are marked by subscripts (1) and (3) and current in the middle slice by the subscript (2)

3.2.1.1 Experimental Methods for Load-dependent Saturation Identification [82], [83]

The thesis author participated in the development of two experimental methods for the determination of the load-dependent saturation of IM. Both methods are based on hardware that is used during the drive's regular operation or commissioning. The methods' functionality assumes that the model and nonlinearities of the drive feeding VSI must be accurately determined [62], [68]. Within the published methods, the magnetizing inductance is considered to be the function of the rotor flux linkage vector and the torque-producing current magnitudes, i.e.,

$$L_{\mathrm{m}} = f\left(\left|\underline{\psi}_2\right|, i_{1q}\right) = f\left(\psi_{2d}, i_{1q}\right) = f\left(\psi_2, i_{1q}\right). \tag{3-11}$$

In (3-11), the saturation due to the nonlinear properties of the magnetic circuit is respected by $L_{\mathrm{m}} = f(\psi_2)$ and the load-dependent saturation by $L_{\mathrm{m}} = f(i_{1q})$.

The first published paper is based on the comparison of the results from the so-called IM voltage and (3-12) and current models (3-13) [82].

$$\underline{\psi}_2 = \frac{L_2}{L_{\mathrm{m}}}\left[\int_0^t \left(\underline{u}_1 - R_1\underline{i}_1\right)\mathrm{d}\tau - \sigma L_1\underline{i}_1\right], \tag{3-12}$$

$$\frac{\mathrm{d}\underline{\psi}_2}{\mathrm{d}t} = \frac{L_{\mathrm{m}}R_2}{L_2}\underline{i}_1 - \frac{R_2}{L_2}\underline{\psi}_2 + \mathrm{j}\omega\underline{\psi}_2. \tag{3-13}$$

Both of these models estimate the same physical quantity, i.e., the rotor flux linkage vector. If the results obtained from these models differ, there has to be some parameter mismatch.

The principle of the method is very straightforward. It is based on the assumption that all parameters from Fig. 3-1 but the magnetizing inductance are known. The magnetizing inductance can be then obtained using an iterative algorithm as:

$$\varepsilon_\psi = \psi_{2\mathrm{VM}} - \psi_{2\mathrm{CM}}, \tag{3-14}$$

where $\psi_{2\mathrm{VM}}$ and $\psi_{2\mathrm{CM}}$ are the rotor flux linkage vector amplitudes obtained from the IM's voltage and current model, respectively. The following iterative algorithm can be then used to obtain the magnetizing inductance:

1. Set $k = 0$. Choose an initial value $L_\mathrm{m}(k) = L_{\mathrm{m}0}$. Choose an incremental inductance ΔL_m; $\Delta L_\mathrm{m} \in \mathbb{R}^+$. Specify the minimal tolerance δ; $\delta \in \mathbb{R}^+$.
2. Calculate $\varepsilon_\psi(k)$. If $|\varepsilon_\psi(k)| \leq \delta$ then $L_\mathrm{m} = L_\mathrm{m}(k)$ and the algorithm stops. Otherwise, go to step 3.
3. If $\varepsilon_\psi(k) > \delta/2$ then calculate $L_\mathrm{m}(k+1) = L_\mathrm{m}(k) + \Delta L_\mathrm{m}$, if $\varepsilon_\psi(k) < -\delta/2$ then calculate $L_\mathrm{m}(k+1) = L_\mathrm{m}(k) - \Delta L_\mathrm{m}$. Increase k by one and go to step 4.
4. If the convergence is too slow or if the output oscillates, adjust ΔL_m by multiplication with relaxation factor $\lambda \in \mathbb{R}^+$ and go back to step 2.

After calculating a new inductance, it is necessary to wait for RFOC to reach a new steady-state. The main disadvantage of the method is the need for accurate knowledge of the other IM parameters. The advantage of the method is that it permits the determination of the no-load magnetizing characteristics, too. Comparison of the saturation characteristics obtained from the standard no-load test and the proposed method is depicted in Fig. 3-4.

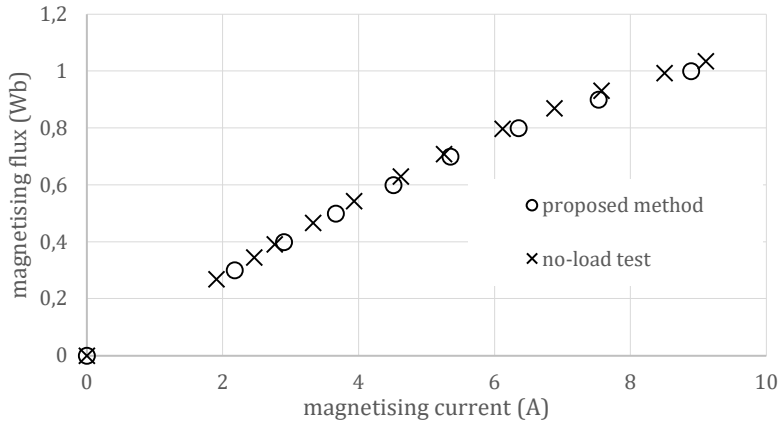

Fig. 3-4 Comparison of the magnetizing curve reconstructed from the proposed method in [82] and the standard no-load test

The second published paper [83] presents an improved version of the method presented in the previous paper. The previous method was based on the comparison of two non-measurable quantities. The improved method strives to compare one estimated and one directly measurable quantity – the magnetizing inductance identification is based on the comparison of the measured torque and torque estimated by the IM current model (3-13). Under the same assumptions as in the case of the previous method, we can obtain the magnetizing inductance by minimizing the following error

$$\varepsilon_T = T - T_\mathrm{e}, \tag{3-15}$$

where T is the measured and T_e is the estimated IM torque. The method utilizes the same iteration algorithm as in the case of the previous method. It is recommended to average the values of ε_T along with T and T_e over multiple sampling periods. The advantage of this method is that the current model of IM does not depend on the stator resistance. Therefore, one variable drifting with temperature is excluded. The dependence of the rotor resistance on the temperature can be compensated by implementing the inverse rotor time constant estimation by Q-MRAS (see section 3.3) parallelly to the numerical algorithm. These two algorithms compensate each other since the Q-MRAS quite significantly depends on the magnetizing inductance.

The resulting 3D map of identified magnetizing inductance respecting the rotor current-caused saturation obtained from the second method is in Fig. 3-5. Such identified characteristics can be implemented into the controller easily as a Look-Up Table (LUT).

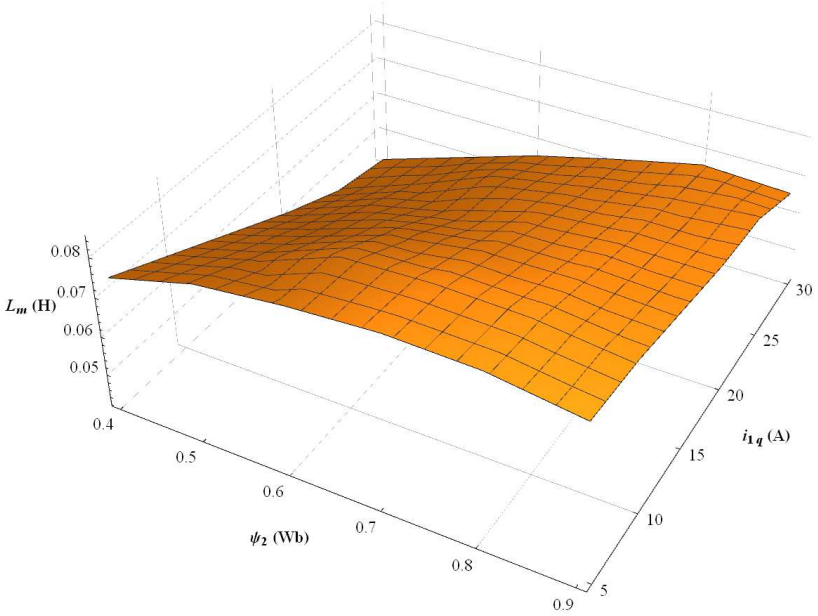

Fig. 3-5 Measured dependence of the magnetizing inductance on the magnitude of the rotor flux vector and torque producing current component [83]

3.3 Identification of Inverse Rotor Time Constant

The rotor resistance is present in the current model of IM that is usually used within RFOC controllers for flux amplitude and position estimation. Rotor resistance variation will affect the proper field orientation and, thus, the control algorithm's performance. The change of the rotor resistance must be respected online during the drive operation. Contrary to the stator resistance, whose temperature can be measured by a thermistor mounted into the stator winding, the rotor body is not accessible. Therefore, the rotor resistance and/or its change have to be estimated. Many times it is not estimated directly but is included in the so-called inverse rotor time constant defined as

$$\tau_{\mathrm{r}}^{-1} = \frac{R_2}{L_2}. \tag{3-16}$$

There are several techniques for the rotor time constant/resistance estimation. However, the real-time calculation requirement leads mostly to utilizing the so-called Model Reference Adaptive System (MRAS) algorithm. The advantage is that MRAS estimation is based on computationally not demanding equations. On the other hand, the MRAS techniques' main disadvantage is the presumption that the reference and adaptive model's difference is caused by the estimated quantity only.

The MRAS estimator evaluates parallelly two mathematical models – the so-called reference and adaptive model. The reference model's output does not depend on the estimated quantity; the adaptive model's output does. An adaptation mechanism (usually a simple PI controller) is used to drive the difference between the models to zero by controlling the adaptive model's estimated variable. For the MRAS design, the Lyapunov theory or Popov hyperstability theory can be utilized.

In the case of rotor time constant estimation, the adaptive model usually does not utilize it directly – the time constant and the adaptive model are interconnected through slip speed and flux estimation. The output quantity of models used for the rotor time constant estimation can be

flux, electromagnetic torque, the dot product of the stator current and rotor flux, active power, or reactive power. The reactive power MRAS (Q-MRAS) is used in most cases because it does not depend on the stator resistance and is stable in most operating points [85]. However, it depends on the accurate knowledge of the magnetizing inductance.

Based on the Lyapunov theory, the following general formula for the time inverse rotor time constant estimation can be derived:

$$\frac{\mathrm{d}}{\mathrm{d}t}\tau_r^{-1} = \lambda\left[(L_\mathrm{m} + f_2)i_{1q}\psi_{2q} - f_1(\psi_{2d}^* - \psi_{2d})\right], \tag{3-17}$$

where λ is a positive number. The individual MRAS schemes are obtained by a special selection of f_1 and f_2 (Tab. 3-1).

Tab. 3-1 Overview of individual MRAS schemes for rotor time constant estimation [85]

Configuration parameter	Functional candidate in MRAS	Reference model	Adjustable model	Information needed in tuning signal
$\boldsymbol{f_1 = f_2 = 0}$	q-axis rotor flux	0	ψ_{2q}	i_{1q}
	d-axis stator voltage	u_{1d}	$R_1 i_{1d} - \omega_\mathrm{s}\sigma L_1 i_{1q}$	$i_{1q}, \omega_\mathrm{s}$
$\boldsymbol{f_2 = -L_\mathrm{m}}$	d-axis rotor flux	$L_\mathrm{m} i_{1d}$	ψ_{2d}	–
	q-axis stator voltage	u_{1q}	$R_1 i_{1q} + \omega_\mathrm{s}\sigma L_1 i_{1d}$	ω_s
$\boldsymbol{f_1 = i_{1q}^2, f_2 = L_\mathrm{m} - i_{1d}}$	electromagnetic torque	$L_\mathrm{m} i_{1q} i_{1d}$	$i_{1q}\psi_{2d} - i_{1d}\psi_{2q}$	i_{1q}
	active power	$i_{1q}u_{1q} + i_{1d}u_{1d}$	$R_1(i_{1d}^2 + i_{1q}^2) + \omega_\mathrm{s} L_\mathrm{m}^2 i_{1d} i_{1q}/L_2$	$i_{1q}, \omega_\mathrm{s}$
$\boldsymbol{f_1 = L_\mathrm{m} i_{1d}, f_2 = 0}$	inner product of $\underline{i}_1$ and $\underline{\psi}_2$	$L_\mathrm{m} i_{1d}^2$	$i_{1d}\psi_{2d} + i_{1q}\psi_{2q}$	–
	inner product of $\underline{i}_1$ and $\underline{\psi}_1$	$L_1 i_{1d}^2 + \sigma L_1 + i_{1q}^2$	$i_{1d}\psi_{1d} + i_{1q}\psi_{1q}$	–
	reactive power	$i_{1d}u_{1q} - i_{1q}u_{1d}$	$\omega_\mathrm{s}(L_1 i_{1d}^2 + \sigma L_1 i_{1q}^2)$	ω_s

3.3.1 Q-MRAS

The Q-MRAS reference model is based on the calculation of the instantaneous value of reactive power

$$Q = \Im\left\{\underline{u}_1^k \bar{i}_1^{-k}\right\} = u_{1y}i_{1x} - u_{1x}i_{1y}, \tag{3-18}$$

where x and y denote the real and imaginary part, respectively, of the general reference frame. For online calculation, it is convenient to calculate the reference model in the stationary $\alpha\beta$ system. The adaptive model $\hat{Q}$ represents a steady-state reactive power and is obtained by substituting for the voltage components in (3-18) from IM model equations, i.e.,

$$\hat{Q} = \omega_s L_1(i_{1d}^2 + \sigma i_{1q}^2), \tag{3-19}$$

where $\sigma = 1 - L_\mathrm{m}^2/L_1 L_2$ is the leakage factor and ω_s is the synchronous speed be calculated as

$$\omega_s = \omega + \omega_\mathrm{slip}, \tag{3-20}$$

where ω is the measured electrical rotor speed and ω_slip is the slip speed is given by

$$\omega_\mathrm{slip} = \hat{\tau}_\mathrm{r}^{-1}\frac{i_{1q}}{i_{1d}}. \tag{3-21}$$

The input to the adaptation mechanism is the error ε_τ between the reference and adaptive system

$$\varepsilon_\tau = Q - \hat{Q}. \tag{3-22}$$

The output of the PI controller is the deviation $\Delta\tau_{\mathrm{r}}^{-1}$ from the initial inverse rotor time constant τ_{r0}^{-1}, i.e.,

$$\Delta\tau_{\mathrm{r}}^{-1}(t) = K_{\mathrm{p}}\varepsilon_{\tau}(t) + K_{\mathrm{i}}\int_{0}^{t}\varepsilon_{\tau}(\tau)\mathrm{d}\tau. \tag{3-23}$$

Finally, the inverse rotor time constant is obtained as

$$\hat{\tau}_{\mathrm{r}}^{-1} = \tau_{\mathrm{r0}}^{-1} + \Delta\tau_{\mathrm{r}}^{-1}. \tag{3-24}$$

The resulting block diagram of MRAS for the inverse rotor time constant estimation is shown in Fig. 3-6. However, there are some practical limitations when considering the utilization of Q-MRAS implementation. The Q-MRAS should be active if the motor speed and torque are at least higher than 10 % of their nominal values.

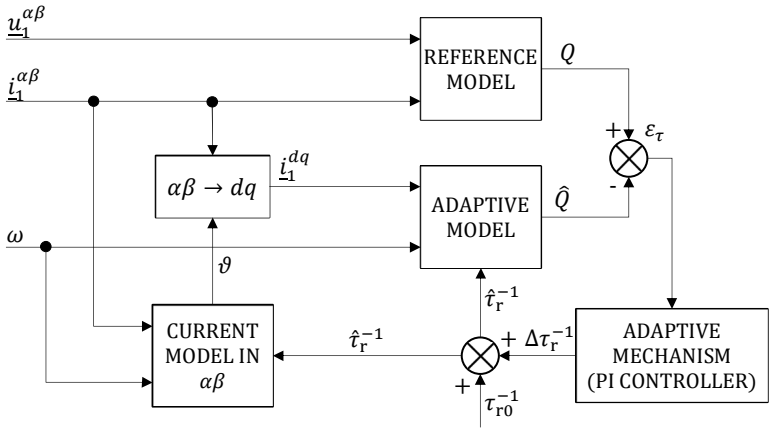

Fig. 3-6 Principle of inverse rotor time constant estimation by Q-MRAS

The quality of the rotor resistance estimation in conjunction with the 3D identified magnetizing inductance c is shown in Fig. 3-7. The figure shows the drive response to a step input of reference speed for two cases. On the right-hand side, Q-MRAS was active without the magnetizing inductance compensation (constant value inductance). On the right-hand side, the inductance compensation was based on the 3D magnetizing characteristics identified by [82]. Based on the observation of the measured and calculated torque after the mechanical transient, it can be concluded that the value of the estimated resistance on the left-hand side does not correspond to the real one because there is a difference of approx. 10 Nm between the measured and calculated torque. On the contrary, it can be stated that the estimated steady-state resistance value on the right-hand side is close to the real one because the measured and calculated torque after the mechanical transient are almost identical. Also, the drive reaches the reference speed faster, i.e., the drive dynamics is increased.

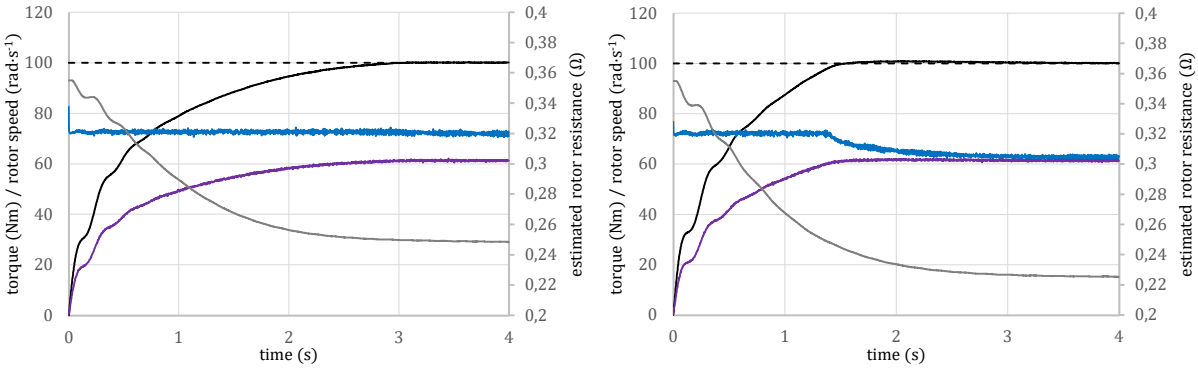

Fig. 3-7 The response of the drive to step reference speed – left: inactive magnetizing inductance compensation, right: active compensation based on [82]; reference speed (black dashed), measured speed (black solid), calculated IM torque (blue), measured torque (purple), estimated rotor resistance (grey)

3.4 Inverter Nonlinearity and Its influence on FOC Accuracy

Many IM control algorithms are based on the actual stator voltage vector's knowledge applied to IM terminals [58]-[61]. Because induction motors are fed mostly by VSI, it becomes complicated or hardware demanding to measure the stator voltage directly. Because of that, the voltage is mostly determined indirectly [62], which means the determination of the stator voltage vector without any additional hardware.

Some papers try to reconstruct the voltage vector from the gating signals of the IGBT‘s and measured DC-link voltage [62]. Another method widely described in the literature is based on using the reference voltage vector, i.e., the modulator's input [85]-[87]. This method is simple and can be quite efficient, but a key problem is the nonlinear behavior of the VSI caused by the semiconductor switches (the semiconductor’s finite turn-on and turn-off times, the voltage drop across the devices, and, also, necessary protective time, i.e., dead-time inserted by the microcontroller or the transistor driver) [88], [89].

The compensation techniques are usually hardware or software-based [86], [87], [89]. The software compensation strategies are preferred because they can be simply modified or tuned. The existing approaches can be divided into estimator-based methods or instantaneous average voltage methods. The average voltage methods require information about the motor currents [84], [85]. These include the square-wave models, trapezoidal models, and LUT or analytical functions that strive to model the zero current clamping effect accurately. The VSI models' parameters are obtained by the DC test or direct VSI measurement [87], [89].

The stator voltage vector applied to the motor terminals is usually formed by Space Vector Modulation (SVM), where the microcontroller’s PWM usually operates in a complementary manner (if one switch in the VSI leg is on, the second is off and vice versa). The turn-on signals contain the dead-time T_{dt} protecting transistors against shoot-through. The switching process (on and off) of an IGBTs, which is the most commonly used devices within VSI, is depicted in Fig. 3-8. The IGBT switching characteristics depend on the value of the collector current I_{C}, junction temperature T_{j}, collector-emitter voltage U_{CE}, gate-emitter voltage U_{GE}, the value of the used gate resistor R_{G} and the load type [88].

3.4.1 Dead Time

The dead time distorts the inverter line-to-neutral voltage u_{a0} (Fig. 3-9). This distortion is significant in the case of small voltage vectors (i.e., during low-speed) [62], [68]. During the dead time, both switches are off, and the polarity of the voltage u_{a0}, depends on the direction of the current i_{a}. If i_{a} is positive, then D_2 must conduct and u_{a0} is equal to $-U_{\mathrm{DC}}/2$. If i_{a} is negative, then D_1 conducts and u_{a0} is equal to $+U_{\mathrm{DC}}/2$ (see Fig. 3-9).

3.4.2 IGBT Switching

The next source of VSI nonlinearity is the own process of IGBT switching, which is heavily influenced by the IGBT parasitic capacitances (Fig. 3-10). During the switching of Q_2, the inductance of the load can be treated as a current source. In the beginning, Q_2 is off; therefore, the load current must flow through D_1. After applying the switching pulse to the driver of Q_2, the gate-emitter voltage U_{GE} starts to charge the gate-emitter capacitance C_{GE} and when it crosses the threshold voltage, the collector current I_C of Q_2 starts to rise. When the forward current of D_1 reaches zero, an opposite reverse recovery current starts to flow through D_1 adding itself to the collector current I_C. Around the peak of the recovery current, the U_{CE} of Q_2 starts to sharply fall to zero.

For the switching off process – when the U_{GE} crosses the threshold voltage, the collector-emitter voltage U_{CE} starts to rise to the full DC-link value with a drop in the collector current I_C. That means the parasitic collector-emitter capacitance C_{CE} is being charged by the load or collector current, respectively. That is why there exists a strong dependence of the turn-off times on the collector current. When the collector-emitter voltage reaches the DC-link voltage, D_1 starts conduct and takes over the current. In the IGBT datasheet, the manufacturers usually define the turn-on delay time $T_{d(on)}$, turn-on rise time T_r, turn-off delay time $T_{d(off)}$ and turn-off fall time T_f. However, these times are related to the current waveforms, not voltage waveforms, and are, therefore, not suitable for the voltage compensation algorithms.

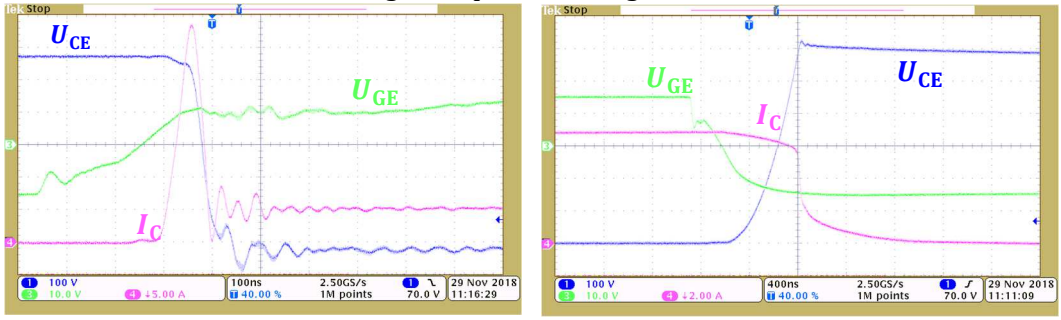

Fig. 3-8. Switching on (left) and off (right) IGBT module CM100DY-24NF; U_{CE} collector-emitter voltage, U_{GE} gate-emitter voltage, I_C collector current

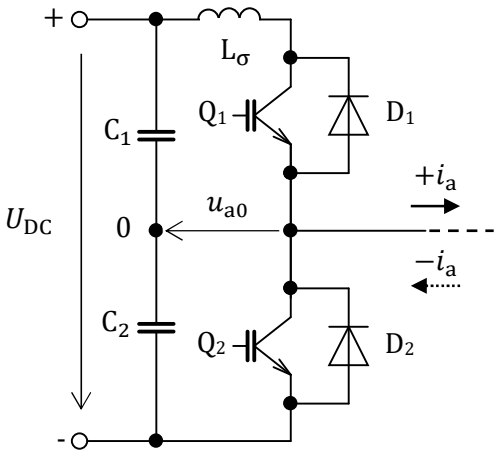

Fig. 3-9. One leg of the two-level voltage-source inverter

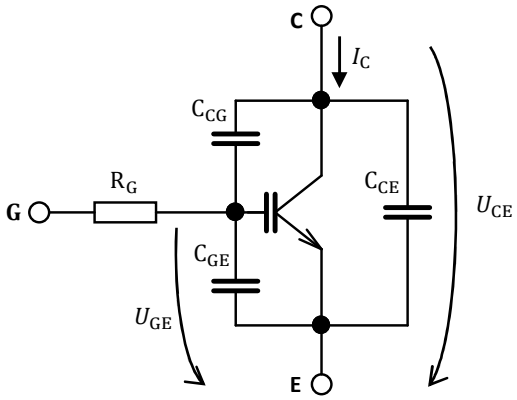

Fig. 3-10. IGBT parasitic capacitances

3.4.3 Distorting Voltage Vector

The effect of the dead time and IGBT nonlinearity on the distortion of the resulting line-to-neutral VSI voltage u_{a0} is shown in Fig. 3-12. In the figure, T_{on} and T_{off} represent the equivalent delay between the microcontroller's control signal for the respective IGBT and the actual transition of the collector-emitter voltage during the switching on and off, respectively. Following Fig. 3-12, we can define the so-called effective dead time $T_{eff(x)}$ as [89]

$$T_{eff(x)} = T_{dt} + T_{on}(i_x) - T_{off}(i_x) \quad x = a, b, c. \tag{3-25}$$

In (3-25), the symbols a, b, c represent the individual motor phases. The resulting distorting voltage vector can be then expressed as

$$\Delta \underline{u}_1 = K \begin{bmatrix} \operatorname{sgn} i_a \\ \operatorname{sgn} i_b \\ \operatorname{sgn} i_c \end{bmatrix}^T \begin{bmatrix} 1 & 0 & 0 \\ 0 & \mathbf{a} & 0 \\ 0 & 0 & \mathbf{a}^2 \end{bmatrix} \begin{bmatrix} \Delta u_{a0} \\ \Delta u_{b0} \\ \Delta u_{c0} \end{bmatrix}, \tag{3-26}$$

where $\mathbf{a} = \exp(j2/3\pi)$, K is Clarke's transformation constant and

$$\Delta u_{x0} = \frac{T_{eff(x)}}{T_{PWM}} U_{DC} \quad x = a, b, c. \tag{3-27}$$

Separating (3-26) into the real and imaginary part, respectively, yields

$$\Delta u_\alpha = K \left[\operatorname{sgn} i_a \, \Delta u_{a0} - \frac{1}{2} \operatorname{sgn} i_b \, \Delta u_{b0} - \frac{1}{2} \operatorname{sgn} i_c \, \Delta u_{c0} \right], \tag{3-28}$$

$$\Delta u_\beta = K \frac{\sqrt{3}}{2} [\operatorname{sgn} i_b \, \Delta u_{b0} - \operatorname{sgn} i_c \, \Delta u_{c0}]. \tag{3-29}$$

3.4.4 Voltage Compensation

Among the simplest algorithms for the voltage compensation, we can include methods that either adjust the reference voltage vector entering the modulator or adjust the respective VSI leg's duty cycle. In the first case, the distorting voltage components (3-28) and (3-29) are added to the reference voltage vector components $u^*_{1\alpha}$ and $u^*_{1\beta}$, i.e.,

$$u'_{1\alpha} = u^*_{1\alpha} + \Delta u_{1\alpha}, \tag{3-30}$$

$$u'_{1\beta} = u^*_{1\beta} + \Delta u_{1\beta}. \tag{3-31}$$

where $u'_{1\alpha}$ and $u'_{1\beta}$ are the corrected reference voltage vector components. However, less computationally demanding is duty-cycle compensation [89]. For SVM, it is convenient to define

the duty-cycle d_x for each VSI leg such that the average value of the corresponding inverter line-to-neutral voltage u_{x0} per modulation period equals to $-U_{\mathrm{DC}}/2$ if $d_x = 0$ and $+U_{\mathrm{DC}}/2$ if $d_x = 1$. Then the relation between the reference d_x^* and the compensated duty cycle d_x' takes the following form [89]

$$d_x' = d_{\mathrm{x}}^* + \frac{T_{\mathrm{eff}(x)}}{T_{\mathrm{PWM}}}\mathrm{sgn}(i_x) \quad x = \mathrm{a, b, c.} \tag{3-32}$$

Fig. 3-11 shows the measured compensation characteristic for the inverter equipped with IGBT modules CM100DY-24NF [88].

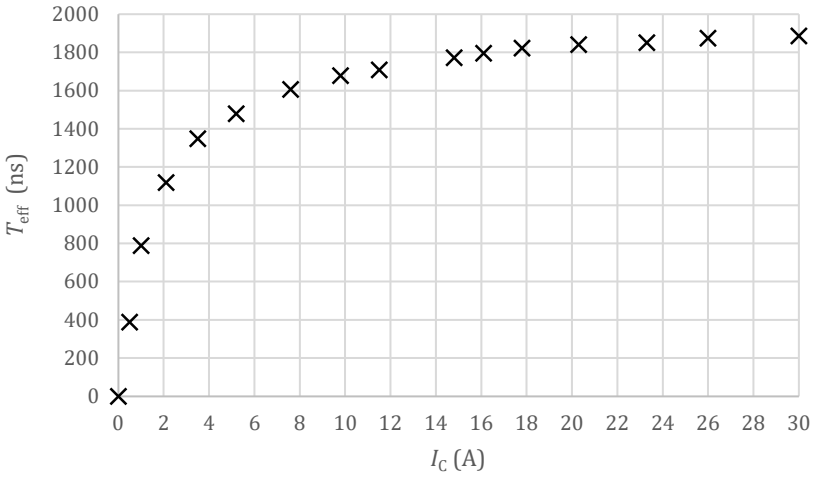

Fig. 3-11 Measured dependence of the effective dead-time on the collector current for IGBT modules CM100DY-24NF; actual dead-time selected as 2 μs

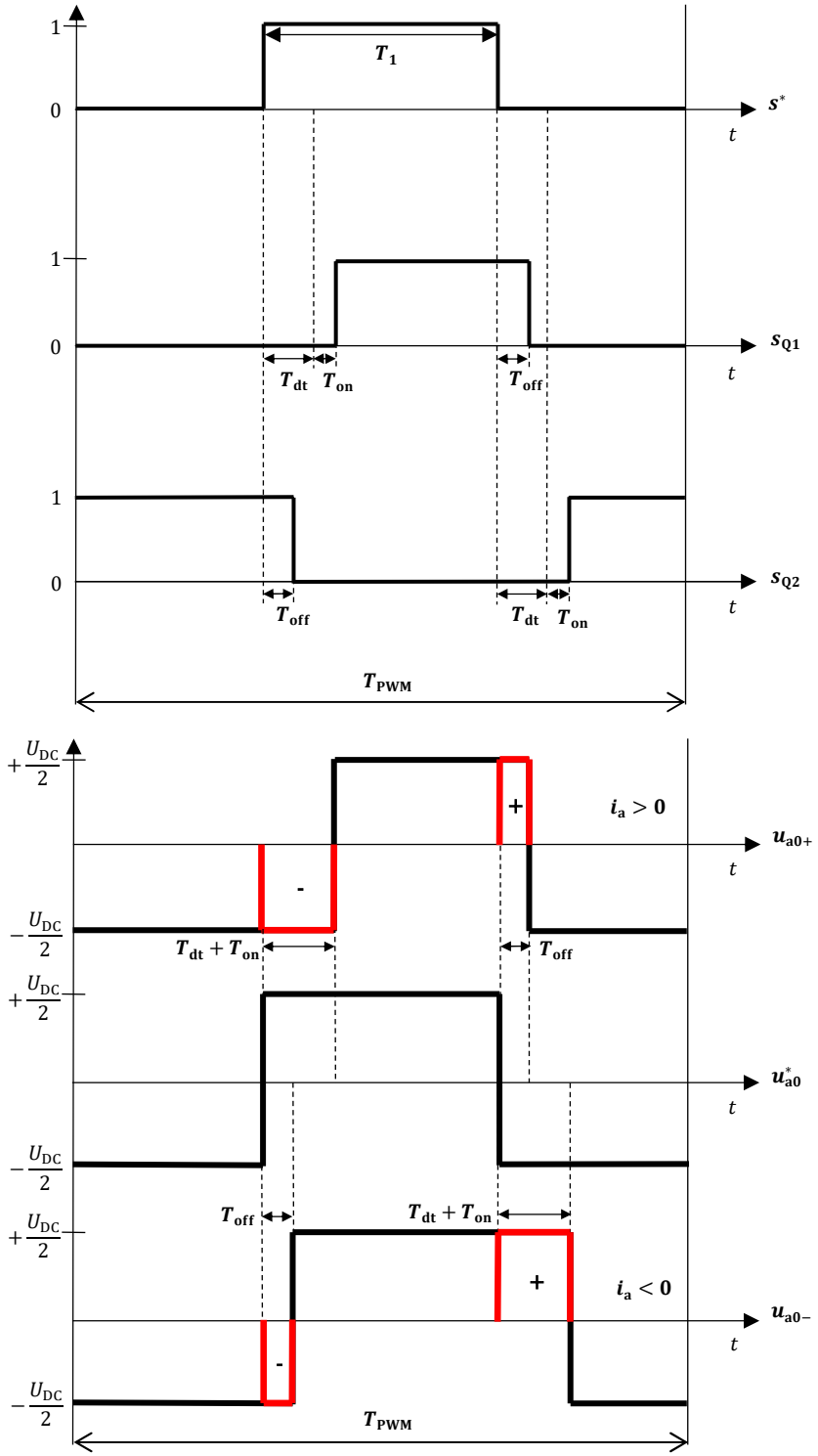

Fig. 3-12. Inverter line-to-neutral voltage distortion due to the dead time and IGBT switching; s^* ideal gating pulse for Q1 (for Q2 negated), s_{Q1} (s_{Q2}) logical state (1 on, 0 off) of Q1 (Q2) considering deadtime and switching effects, u^*_{a0} desired inverter phase voltage, u_{a0+}(u_{a0-}) actual inverter phase voltages for $i_a > 0$ ($i_a < 0$)

3.5 Author's Contribution

Dr. Bauer has supervised all work presented in this chapter as supervisor specialist of doctoral student O. Lipčák. He participated in proposing and developing the above-presented methods and analyses. He proposed methods for validation experiments and co-analyzed measured results. He also consulted DSP algorithms implementation and their validity. He co-wrote listed papers [82], [83], [89].

Publications and patents related to this section:

1) LIPČÁK O. and BAUER J., "Offline method for experimental identification of load-dependent saturation of induction motor taking into account variation of inverse rotor time constant," in *IET Power Electronics*. 2019, ISSN 1755-4543. (Appendix B)
2) LIPČÁK, O.; BAUER, J.; KOBRLE, P. „Offline Method for Determination of Nonlinear Dependence of Induction Machine Magnetising Inductance Utilising Parallel Operation of Current and Voltage Model" *IET Power Electronics*. 2019, ISSN 1755-4543. (Appendix C)
3) LIPČÁK, O., J. BAUER a M. CHOMÁT. „Reactive Power MRAS for Rotor Resistance Estimation Taking Into Account Load-Dependent Saturation of Induction Motor". In: *2019 International Conference on Electrical Drives & Power Electronics (EDPE)*. Nový Smokovec, The High Tatras, 2019-09-24/2019-09-26. Košice: Technical University of Košice, 2019. s. 255-260. ISSN 1339-3944. ISBN 978-1-7281-0389-1. DOI 10.1109/EDPE.2019.8883887. (Appendix D)
4) LIPČÁK, O. a J. BAUER. „Analysis of Voltage Distortion and Comparison of Two Simple Voltage Compensation Methods for Sensorless Control of Induction Motor". In: *2019 IEEE 10th International Symposium on Sensorless Control for Electrical Drives, SLED 2019*. Turin, 2019-09-09/2019-09-10. Institute of Electrical and Electronics Engineers, Inc., 2019. ISBN 9781728107660. DOI 10.1109/SLED.2019.8896258. (Appendix E)

CONCLUSION AND FURTHER RESEARCH

In this thesis, two main projects the author has been working on since obtaining a Ph.D. degree were presented. The first part of this thesis describes the development of a slip controller for a freight locomotive. This part aims to describe the controller development in a step by step manner. The developed controller is based on adhesion-slip characteristic slope detection. Generally, It is designed to cope with a nonlinearity of the adhesion-slip characteristic and noise that occurs in the system. Moreover, the proposed slip controller does not need to know the train velocity, the wheelset velocity is the only required parameter. The slip controller is designed as modular, and it consists of the adhesion-slip characteristic slope detection part and a controller part with acceleration protection. Moreover, the design and implementation of the controller have to fulfil the maximal timing requirements of 100μs. Another advantage of the controller is a smooth reaction to the appearing slip and thus a smooth limiting of IM's torque. The designed controller has been tested on a real locomotive running on the test track. The test results show that the drive torque utilization was more than 94 % on a dry rail, which is quite a good result.

The second part of the thesis deals with three sources of inaccuracy in FOC IM drive. This part has also originated from the cooperation with the company CRRC. During the development of slip control, the team encountered several problems caused by detuned FOC. To improve FOC's quality and robustness, sources of detuning were more thoroughly analyzed, which led to the development of algorithms for the identification of the magnetizing inductance and rotor time constant. The inverter's nonlinearities and their influence on FOC were analyzed too because their impact on the control quality can be quite significant. Main influences of inaccuracies such as maximal utilizable torque, decreased IM drive dynamics, increased current consumption measured on the testbed in the laboratory were presented in papers [82], [83], [89].

Further Research Orientation

Controlled electric drives will remain an integral part of human life. The increasing deployment of controlled electric drives in everyday life will continue to make demands on their dynamics, effectivity, low cost, and, mainly, efficiency. It will not be possible to meet these requirements and challenges without more precise knowledge of the machine parameters and their implementation into the control structure along with the possibility to account for their change during the drive operation.

Another area that is developing dynamically, mainly due to the financial requirements, is the product testing and development using Hardware-In-the-Loop (HIL) systems. The main goal is to use accurate mathematical models of electrical machines and drives to optimize the development time demands and costs.

Finally, it is expected that a significant subject of interest will be the application of the current methods and approaches to emerging structures of electrical machines supplied by converters based on modern Silicon-Carbide (SiC) and Gallium-Nitride (GaN) semiconductor devices.

LITERATURE

[1] R. Lewis, U. Olofsson, *Wheel-rail interface handbook*. CRC Press, Boca Raton, 2009.

[2] W. Liao, H. Chen, W. Cai and Y. Song, "A novel active adhesion control design for high speed trains without vehicle speed measurement," *Proceedings of the 33rd Chinese Control Conference*, Nanjing, 2014, pp. 221-226.

[3] C. Jenks "Improved Methods for Increasing Wheel/Rail Adhesion in the Presence of Natural Contaminants, " Transit Co-operative Research Program, Research Results Diges, no 17, 1997.

[4] H. Chen, "Factors that infuence the adhesion coefficieent between wheel and rail," *Railway Technology Avalanche*, no. 40, pp. 6, 2012.

[5] Hussain, T. X. Mei, and R. T. Ritchings, "Estimation of wheel–rail contact conditions and adhesion using the multiple model approach", *Vehicle System Dynamics*, vol. 51, no. 1, pp. 32–53, Jan. 2013.

[6] H. Chen, T. Ban, M. Ishida, T. Nakahara, "Experimental instigation of influential factors on adhesion between wheel and rail under wet conditions", Wear, vol. 265, no 9-10, 2008, pp. 1504-1511.

[7] K. Xu, G. Xu, and C. Zheng, 'Novel determination of Wheel-Rail adhesion stability for electric locomotives', *Int. J. Precis. Eng. Manuf.*, vol. 16, no. 4, pp. 653–660, Apr. 2015.

[8] Danzer, J.: *Elektrická trakce 7 - Adheze.* skripta ZČU Plzeň 2013.

[9] D. Kun, L. Kaijun and X. Qunsheng, "Application of Unscented Kalman Filter for the State Estimation of Anti-lock Braking System", *IEEE International Conference on Vehicular Electronics and Safety*, 2006, pp. 130-133.

[10] Rezaeian et al., "Novel Tire Force Estimation Strategy for Real-Time Implementation on Vehicle Applications," in *IEEE Transactions on Vehicular Technology*, vol. 64, no. 6, June 2015, pp. 2231-2241.

[11] Sakai, Y. Tamura and Y. Kuroda, "An efficient solution to 6DOF localization using Unscented Kalman Filter for planetary rovers", IEEE/RSJ *International Conference on Intelligent Robots and Systems*, 2009, pp. 4154-4159.

[12] R. Wang and J. Wang, 'Tire–road friction coefficient and tire cornering stiffness estimation based on longitudinal tire force difference generation', *Control Engineering Practice*, vol. 21, no. 1, pp. 65–75, Jan. 2013.

[13] P. Pichlik and J. Zdenek, "Adhesion Force Detection Method Based on the Kalman Filter for Slip Control Purpose", *Automatika*, vol. 57, no. 2, pp. 405–415, 2016

[14] Sauer, Roger. (2016). A Survey of Computational Models for Adhesion. Journal of Adhesion. 92. 10.1080/00218464.2014.1003210.

[15] Park, D. Y.; Kim, M. S.; Hwang, D. H.: "Hybrid Re-Adhesion Control Method for Traction System of High-speed Railway". *Electrical Machines and Systems (ICEMS)*; 2001. vol. 5, p. 739-742

[16] Huang, J. C.; Xiao, J.; Helmut, W.: "Simulation Study on Adhesion Control of Electric Locomotives Based on Multidisciplinary Virtual Prototyping". *IEEE Industrial Technology*; 2008. p. 1636-1639

[17] J.J. Kalker, "Wheel-rail rolling contact theory", *Wear*, Volume 144, Issues 1–2, 1991, Pages 243-261

[18] L. Wenli, Z. Leiting, and D. Kan, "Performance Analysis of Re-adhesion Optimization Control Based On Full-dimension State Observer", *Procedia Engineering*, vol. 23, pp. 531–536, Jan. 2011.

[19] O. Polach, "Influence of Locomotive Tractive Effort on the Forces Between Wheel and Rail, " *Vehicle System Dynamics*, vol. 35, pp. 7-22, 2001.

[20] J. S. Kim, S. H. Park, J. J. Choi and H. Yamazaki, "Adaptive Sliding Mode Control of Adhesion Force in Railway Rolling Stocks" in *Sliding Mode Control*, InTech, 2011

[21] Adams, G. G.; Nosonovsky, M.: Contact modeling — forces. *Tribology International*; 2000. vol. 33, p. 431-442

[22] Popov, V. L.: *Kontaktmechanik und Reibung*. Springer-Verlag Berlin; 2009.

[23] Čáp, J.: "Početně stanovené adhézní charakteristiky." *Žel. Technika*; 1986. vol. 16, no. 5, p. 229-232

[24] Kraft, K.: "Die Hafttreibung." *Elektrische Bahnen*; 1968. vol. 39, no. 6, p. 142-155

[25] Takaoka, Y.; Kawamura, A.: "Disturbance Observer Based Adhesion Control for Shinkansen." AMC - NAGOYA; 2000. p. 169-174

[26] W. Lang, G. Roth, "Optimale Kraftschlussaustutzung bei Hochleistungs-Schienenfahzeugen" *ETR* vol. 42, no. 1-2 pp. 61-66, 1993

[27] Engel, B.; Beck, H. P.; Alders, J.: "Verschleißreduzierte Radschlupfregelung mit hoher Kraftslußausnutzung". *Elektrische Bahnen*; 1998. vol. 96, no. 6, p. 201-209

[28] Cheok, A. D.; Shiomi, S.: "Combined Heuristic Knowledge and Limited Measurementm Based Fuzzy Logic Antiskid Control for RailwaymApplications." *IEEE Transaction on Systems Man and Cybernetics*; 2000. vol. 30, no

[29] Frylmark, D.; Johnsson, S.: *Automatic Slip Control for Railway Vehicles*. Master's thesis; 2003.

[30] PICHLÍK, Petr. *Strategy of railway traction vehicles wheel slip control*, doctoral thesis. 2018.

[31] Javadi, S.; Nabizadeh, E.: "Fuzzy Logic Slip Control Design for Railway Vehicles". *Recent Researches in System Science*; 2011. p. 202-206

[32] Z. Huang, Z. Xu, B. Chen, R. Zhang, Y. Chen and Q. Peng, "Sliding mode control for urban railway anti-slip system based on optimal slip ratio estimation with forgetting factor recursive least-squares," *2017 36th Chinese Control Conference (CCC)*, Dalian, 2017, pp. 9502-9507.

[33] Asanome, T.; Nonaka, T.; Endo, Y.; Nakazawa, S.; Yoshikawa, H.: "Evaluation of control performance of multi-stage fuzzy reasoning in anti-lock braking system for railways using fuzzy reasoning." *International Conference Modeling Decisions for Artificial Intelligence*; 2005. vol. 2, p. 110-121

[34] Bauer, H.; Pfeiffer, R.; Hahn, K.: "Optimale Kraftschlußausnutzung durch selbstadaptierende Radschlupfregelung am Beispiel eines Drehstrom-Lokomotivantriebes." *Elektrische Bahnen*; 1986. vol. 84, no. 2, p. 43-57

[35] Watanabe, T.; Yamashita, M.: "Basic study of anti-slip control without speed sensor for multiple motor drive of electric railway vehicles." *Power Conversion Conference (PCC)*; 2002. p. 1026-1032

[36] Watanabe, T.: "Application of Anti-Slip Readhesion Control with Adhesion Prediction to Commuter Electric Multiple Units." *Electrical Engineering Research Report*; 2001. no. 12, p. 3-6

[37] P. Pichlík and J. Zděnek, "Train Velocity Estimation Method Based on an Adaptive Filter with Fuzzy Logic", *Journal of Electrical Engineering*. 2017, 2(68), 125-131.

[38] Pichlík, P.; Zoubek, O.; Zděnek, J.; Lettl, J. "Railway Traction Vehicle Longitudinal Velocity Estimation by Kalman Filter", *Proceedings of PIERS 2015 in Prague*. Electromagnetics Academy, 2015, pp. 2518-2521

[39] P. Pichlík and J. Zděnek, "Train velocity estimation by extended Kalman filter," 2016 *8th International Conference on Electronics, Computers and Artificial Intelligence (ECAI)*, Ploiesti, 2016, pp. 1-4.

[40] Buscher, M.; Pfeiffer, R.; Schwartz, H. J.: "Radschlupfregelung für Drehstromlokomotiven". *Elektrische Bahnen*; 1993. vol. 91, no. 5, p. 163-178

[41] Buscher, M.: "*Radschlupfregelung zur maximalen Kraftschlußausnutzung bei elektrischen Traktionsantrieben*." Diss. TH Darmstadt; 1995.

[42] Garcia-Rivera, M.; Sanz, R.; Jose, A.: "An Antislipping Fuzzy Logic Controller for a Railway Traction System." 1997.

[43] Kawamura, A.; Takeuchi, K.; Furuya, T.; Takaoka, Y.; Yoshimoto, K.: "Measurement of the tractive force and the new adhesion control by the newly developed tractive force measurement equipment." *Power Conversion Conference (PCC)*; 2002. p. 879-884

[44] Kawamura, A.; Takeuchi, K.; Furuya, T.; Cao, M.; Takaoka, Y.; Yoshimoto, K.: "Measurement of tractive force and the new maximum tractive force control by the newly developed tractive force measurement equipment." *Electrical Engineering*; 2004. vol. 149, no. 2, p. 49-59

[45] Schreiber, R.; Häse, P.; Gerber, P.: "Innovative Adhäsionsregelung - Versuchsergebnisse mit der BLS Drehstromlokomotive Re 465". *Elektrische Bahnen*; 1996. vol. 94, no. 8,9, p. 230-234

[46] Schreiber, R.; Häse, P.; Ruegg, R.: "Neues Verfahren zur Adhäsionsregelung elektrischer Triebfahrzeuge." *Workshop TU Berlin*; 1996.

[47] Schreiber, R.; Kögel, P.; Häse, P.; Hildenbrand, P.: "Regelung zur optimalen Kraftschlußausnutzung bei Drehstromlokomotiven auf der Basis der Steigung der Kraftschlußkennlinie." *Elektrische Bahnen*; 1995. vol. 93, no. 5, p. 157-173

[48] Schreiber, R.; Kögel, R.: "Identifikationsmethode zur Bestimmung der Adhäsion zwischen Rad und Schiene." *ZEV GA*; 1996. vol. 120, no. 2, p. 48-54

[49] Spiryagin, M.; Lee, K. S.; Yoo, H. H.: "Study on Using Noise for Adhesion Control System of Railway Vehicle." *ICSV14*; 2007.

[50] Spiryagin, M.; Lee, K. S.; Yoo, H. H.: *"Control system for maximum use of adhesive forces of a railway vehicle in a tractive mode." MECHANICAL SYSTEMS AND SIGNAL PROCESSING*; 2008. vol. 22, no. 3, p. 709-720

[51] Huang, J.; Xiao, J.; Zhao, D.; Wang, S.: *"A Wheel Slip Detection Method of Electric Locomotive Based on Time-Frequency Analysis." International Conference on Intelligent Transportation Systems (IEEE ITSC)*; 2014. vol. 17

[52] Huang, J.; Xiao, J.; Helmut, W.: "Simulation Study on Adhesion Control of Electric Locomotives Based on Multidisciplinary Virtual Prototyping." *IEEE Industrial Technology*; 2008. p. 1636-1639

[53] Huang, E. N.; Wu, Z.: "A Review on Hilbert-Huang Transform: Method and its Applications to Geophysical Studies." *Reviews of Geophysics*; 2008. vol. 255, no. 46

[54]] Mei, T. X.; Yu, J. H.; Wilson, D. A.: *"A Mechatronic Approach for Anti-slip Control in Railway Traction." World Congress The International Federation of Automatic Control*; 2007. vol. 17, p. 8275-8280

[55] Mei, T. X.; Hussain, I.: "Detection of wheel-rail conditions for improved traction control." 2010.

[56] Dorf, R. C.; Bishop, R. H.: *Modern Control Systems*. Pearson Prentice Hall; 2005.

[57] PICHLÍK P. and BAUER J., *"Analysis of the Locomotive Wheel Slip Controller Operation During Low Velocity,"* in IEEE Transactions on Intelligent Transportation Systems.doi: 10.1109/TITS.2020.2971832

[58] M. Farasat, A. M. Trzynadlowski and M. S. Fadali, "Efficiency improved sensorless control scheme for electric vehicle induction motors," in *IET Electrical Systems in Transportation*, vol. 4, no. 4, pp. 122-131, Dec. 2014.

[59] P. Vas, *Electrical Machines and Drives: A Space-Vector Theory Approach.* Oxford: Clarendon press, 1992.

[60] M. Sokola, "Vector Control of Induction Machines Using Improved Models," *PhD thesis*, Liverpool John Moores University, Liverpool, U.K., 1998.

[61] F. Giri, *AC Electric Motors Control: Advanced Design Techniques and Applications*. 2. Aufl. ed. New York: Wiley; 2013.

[62] P. Vas, *Sensorless vector and direct torque control*. New York: Oxford University Press; 1998.

[63] M. Popescu, *Induction Motor Modelling for Vector Control Purposes*, Helsinki University of Technology, Laboratory of Electromechanics, Report, Espoo 2000, 144 p.

[64] L. Lupsa-Tataru, "A Flux-Based Expression of Induction Machine Magnetizing Inductance," in IEEE Transactions on Energy Conversion, vol. 25, no. 1, pp. 268-270, March 2010.

[65] D. Chatterjee, "A Simple Leakage Inductance Identification Technique for Three-Phase Induction Machines Under Variable Flux Condition," in IEEE Transactions on Industrial Electronics, vol. 59, no. 11, pp. 4041-4048, Nov. 2012

[66] E. Levi, M. Sokola and S. N. Vukosavic, "A method for magnetizing curve identification in rotor flux oriented induction machines," in IEEE Transactions on Energy Conversion, vol. 15, no. 2, pp. 157-162, June 2000.

[67] R. Kumar, S. Das, P. Syam and A. K. Chattopadhyay, "Review on model reference adaptive system for sensorless vector control of induction motor drives," in IET Electric Power Applications, vol. 9, no. 7, pp. 496-511, 8 2015.

[68] S. Bolognani and M. Zigliotto, "Self-commissioning compensation of inverter non-idealities for sensorless AC drives applications," 2002 International Conference on Power Electronics, Machines and Drives (Conf. Publ. No. 487), Santa Fe, NM, USA, 2002, pp. 30-37.

[69] S. Moulahoum, O. Touhami, R. Ibtiouen and M. Fadel, "Induction Machine Modeling With Saturation and Series Iron Losses Resistance," 2007 IEEE International Electric Machines & Drives Conference, Antalya, 2007, pp. 1067-1072.

[70] O. Kiselychnyk, M. Bodson and J. Wang, "Comparison of Two Magnetic Saturation Models of Induction Machines and Experimental Validation," in IEEE Transactions on Industrial Electronics, vol. 64, no. 1, pp. 81-90, Jan. 2017

[71] T. Tuovinen, M. Hinkkanen and J. Luomi, "Modeling of Saturation Due to Main and Leakage Flux Interaction in Induction Machines," in IEEE Transactions on Industry Applications, vol. 46, no. 3, pp. 937-945, May-june 2010.

[72] T. S. Birch and O. I. Butler, "Permeance of closed-slot bridges and its effect on induction-motor-current computation," in Proceedings of the Institution of Electrical Engineers, vol. 118, no. 1, pp. 169-172, January 1971.

[73] S. Williamson and M. C. Begg, "Calculation of the bar resistance and leakage reactance of cage rotors with closed slots," in IEE Proceedings B - Electric Power Applications, vol. 132, no. 3, pp. 125-132, May 1985.

[74] N. R. Klaes, "Parameters identification of an induction machine with regard to dependencies on saturation," Conference Record of the 1991 IEEE Industry Applications Society Annual Meeting, Dearborn, MI, 1991, pp. 21-27 vol.1.

[75] M. Hinkkanen, A. Repo, J. Luomi, J, "Influence of magnetic saturation on induction motor model selection, "*Proc. ICEM'06,* Chania, Greece, September 2006.

[76] P. Immonen, V. Ruuskanen, J. Nerg, et al, "Inductance saturation of the induction machine as a function of stator voltage and load with steady state AC magnetic finite element solver, "*International Review of Modeling and Simulation (IREMOS),* 2004.

[77] J. Nerg, J. Pyrhonen and J. Partanen, "Finite element modeling of the magnetizing inductance of an induction motor as a function of torque," in IEEE Transactions on Magnetics, vol. 40, no. 4, pp. 2047-2049, July 2004.

[78] M. Hinkkanen, A. Repo, M. Cederholm and J. Luomi, "Small-Signal Modelling of Saturated Induction Machines With Closed or Skewed Rotor Slots," 2007 IEEE Industry Applications Annual Meeting, New Orleans, LA, 2007, pp. 1200-1206.

[79] J. A. A. Melkebeek, "Magnetising-field saturation and dynamic behaviour of induction machines. Part 1: Improved calculation method for induction-machine dynamics," in IEE Proceedings B - Electric Power Applications, vol. 130, no. 1, pp. 1-9, January 1983.

[80] M. Ranta and M. Hinkkanen, "Online identification of parameters defining the saturation characteristics of induction machines," 2012 XXth International Conference on Electrical Machines, Marseille, 2012, pp. 1027-1033.

[81] L. Liu, Y. Guo and J. Wang, "Online Identification of Mutual Inductance of Induction Motor without Magnetizing Curve," 2018 Annual American Control Conference (ACC), Milwaukee, WI, 2018, pp. 3293-3297.

[82] O. Lipcak, J. Bauer and P. Kobrle, "Offline method for determination of nonlinear dependence of machine magnetising inductance utilising parallel operation of current and voltage model," in *IET Power Electronics*, vol. 12, no. 11, pp. 2843-2850, 18 9 2019.

[83] O. Lipcak and J. Bauer, "Offline method for experimental identification of load-dependent saturation of induction motor taking into account variation of inverse rotor time constant," in *IET Power Electronics*, vol. 13, no. 9, pp. 1828-1836, 24 7 2020.

[84] X. Zhang, Y. Zhang, S. Yang, Z. Xie and P. Cao, "An Improved MRAS for Rotor Time Constant Updating in Induction Motor Drives Utilizing Dot Product of Stator Current and Rotor Flux," in *IEEE Transactions on Power Electronics*, vol. 34, no. 9, pp. 8905-8915, Sept. 2019.

[85] G. Shen, W. Yao, B. Chen, K. Wang, K. Lee and Z. Lu, "Automeasurement of the Inverter Output Voltage Delay Curve to Compensate for Inverter Nonlinearity in Sensorless Motor Drives," in IEEE Transactions on Power Electronics, vol. 29, no. 10, pp. 5542-5553, Oct. 2014.

[86] M. Seilmeier, C. Wolz and B. Piepenbreier, "Modelling and model based compensation of non-ideal characteristics of two-level voltage source inverters for drive control application," 2011 1st International Electric Drives Production Conference, Nuremberg, 2011, pp. 17-22.

[87] M. El-daleel and A. Mahgoub, "Accurate and simple improved look-up table compensation for inverter dead time and nonlinearity compensation," 2017 Nineteenth International Middle East Power Systems Conference (MEPCON), Cairo, 2017, pp. 1358-1361.

[88] Mitsubishi Electric. *IGBT Modules Application Note, The 5th Generation [CSTBT™] IGBT Chip Use, 12NF/24NF/24A series.* Mar. 2014. Available at: http://www.mitsubishielectric.com/semiconductors/files/manuals/igbt_note_e.pdf, accessed 16th June 2020.

[89] O. Lipcak and J. Bauer, "Analysis of Voltage Distortion and Comparison of Two Simple Voltage Compensation Methods for Sensorless Control of Induction Motor," *2019 IEEE 10th International Symposium on Sensorless Control for Electrical Drives (SLED)*, Turin, Italy, 2019, pp. 1-6.

[90] P. Cao, X. Zhang and S. Yang, "A Unified-Model-Based Analysis of MRAS for Online Rotor Time Constant Estimation in an Induction Motor Drive," in *IEEE Transactions on Industrial Electronics*, vol. 64, no. 6, pp. 4361-4371, June 2017.

APPENDIX A

PICHLÍK P. and BAUER J., "Analysis of the Locomotive Wheel Slip Controller Operation During Low Velocity," in *IEEE Transactions on Intelligent Transportation Systems*. doi: 10.1109/TITS.2020.2971832 – Early access

Author's contribution: experiment proposal, sensor simulation model development, data analysis and functionality validation, manuscript co-writing.

Analysis of the Locomotive Wheel Slip Controller Operation During Low Velocity

Petr Pichlík and Jan Bauer

***Abstract*— Locomotives are equipped with slip controllers that improve their adhesion utilization and keep wheels slip velocities at appropriate values. The current slip controllers typically correctly work during the regular train run. However, there are some cases when some slip controllers may fail. The correct operation at low velocities is one of the cases in which the slip controller can fail. The long-time response of the velocity measurement that is caused by incremental encoders with a low number of pulses per revolution is causing the problem in this case. The wheel slippage can occur when the adhesion conditions are adverse, and applied forces are high in this case. This paper describes a novel slip controller based on the unscented Kalman filter that correctly works during the train low velocity operation with any adhesion conditions. The slip controller was designed with taking into account all aspects that influence the controller operation. Therefore, the adhesion, electric drive, the slip controller, and problem background are described in the paper. The slip controller functionality is verified on measured data and a mathematical model that was verified on the measured data.**

***Index Terms*— Adhesion, digital control, unscented Kalman filter, rail transportation, velocity control.**

I. Introduction

SLIP controllers that are installed on locomotives enable to limit the slip velocities of the wheelset to the appropriate values and simultaneously transfer the maximum force between wheelsets and rails if the required tractive forces are higher than the maximum transferable forces. The slip controllers also decrease wear of the wheels and rails [1] that are caused by high slip velocity. The maximum transferable force that can be transferred between wheel and rail is limited by the actual adhesion conditions that are unpredictable and unmeasurable during the train operation. The main influences on the adhesion conditions belong to the conditions of rail surfaces that are mainly affected by the weather. Therefore, the adhesion conditions can be considered as random, from the slip controller point of view. An adhesion coefficient describes the adhesion conditions, and the adhesion coefficient is typically depicted as a function of a wheelset slip velocity. The dependence is called an adhesion-slip characteristic. The characteristic is nonlinear and can be divided into a stable area, unstable area, and the maximum point. The adhesion coefficient value increases with the increasing slip velocity in the stable area, and the adhesion coefficient decreases in the unstable area with the increasing velocity. The slip controller has to keep the operating point near the maximum point in the stable area to enable transmission of the maximum possible force with minimum adverse side effects. Moreover, some positive slip velocity for the forces transfer between wheels and rails is needed. Therefore, the entire slip velocity elimination is not possible, and the slip controller has to recognize between the useful slip and unwanted slippage.

Many slip control methods were developed during the last decades. The simplest ones are based on the wheelset velocity control to a constant value. The main disadvantage of those methods is that optimal slip velocity changes with the adhesion conditions change, but the required velocity value is usually constant. The method can be improved by using wheelset acceleration [2], [3]. However, train acceleration changes with train weight. More advanced methods try to determine the maximum point position on the adhesion-slip characteristic, [4]–[6] and [7]. These methods disadvantage is the requirement for permanent work in the unstable area of the adhesion-slip characteristic. The most perspective methods try to determine the slope of the adhesion-slip characteristic. The slope can be detected in two ways. The first principle compares the phase shift between the applied torque and the wheelset angular velocity [8]. The principle requires the addition of a disturbance signal to the required torque, and the method cannot work at the low velocity from its principle. The slope is typically determined by calculating a ratio of the adhesion coefficient derivative according to the slip velocity derivative [9], [10]. The adhesion coefficient cannot be directly measured. Therefore, the coefficient is estimated by observers. Disturbance observers (DO) [11], [12], sliding mode observers [13]–[16] or variants of Kalman filters (KF) [17] are used for the purpose. The main reason for the DO usage is its low computational complexity. However, the main difference between the method based on the DO and the KF or its nonlinear variants is in the approach to noise [18], [19]. The DO does not take noise into account, and the method has to contain a filter for noise elimination. However, the filter increases the estimation time. The nonlinearity of the adhesion-slip characteristic complicates estimation by the linear estimators. Therefore, some variant of the nonlinear estimators like extended Kalman filter (EKF) or unscented Kalman filter (UKF) is more appropriate despite their higher computational requirement. Methods based on the adaptive observer [20] or super-twisting-like algorithm

Manuscript received April 30, 2018; revised July 26, 2019 and December 26, 2019; accepted January 24, 2020. The Associate Editor for this article was R. Goverde. *(Corresponding author: Petr Pichlík.)*

The authors are with the Department of Electric Drives and Traction, Czech Technical University in Prague, Faculty of Electrical Engineering, 16627 Prague, Czech Republic (e-mail: pichlpet@fel.cvut.cz; bauerja2@fel.cvut.cz).

Digital Object Identifier 10.1109/TITS.2020.2971832

was also described [21]. The adhesion has to be taken into account in every case where the force is transferred between wheels and surface, e.g., cars or mobile robots. The cars have to solve a side slip besides. Therefore, the research in automotive is in progress, and the problem with the nonlinearity has to be solved, e.g., by variants of the Kalman filters [22], [23].

Wheelset velocity is used as the input of most of the mentioned methods. Therefore, the velocity measurement is crucial for the proper work of all of them. The wheelset velocity is typically measured by tachometers or odometers [24]. However, primary, the devices are created by incremental encoders that typically have a low number of pulses per revolution [25], and they are disturbed by errors [26]. Therefore, the measurement has a long-time response when the velocity is low. When the response is significantly longer than the calculation period of the slip controller, the slip controller calculation can fail. The train velocity can also be measured by a Global Navigation Satellite System (GNSS) or by Doppler radars. However, the methods have a problem with their reliability or availability. The GNSS cannot be available in all parts of the track [27], and the Doppler radar can be inaccurate when the velocity measurement direction and running direction [28] or the radar can even fail when the surface is smooth [29]. New locomotives use an independent velocity measurement for safety purposes. However, these velocity measurement methods are inappropriate for slip control due to their long-time response.

The problem with low velocity is not typically solved nor mentioned in the literature related to the slip control, and the slip controller can fail. The low velocity is typical for train start or when a heavy train goes uphill just before getting stuck on the track. The proposed slip controller enhancement leans on the wheel velocity estimation when there is no signal from the velocity measurement. The estimation is enabled by estimating the velocity from the applied tractive effort and model of the locomotive. The estimation is accurate in a short period until the first pulses come from the measurement. If the nonlinear adhesion-slip characteristic is taken into account, the appropriate estimators are EKF and UKF because they can cope with the nonlinearity and simultaneously estimate the wheel velocity. The usage of the UKF is more appropriate than the EKF due to the possible divergence of the EKF.

The rest of the paper is organized as follows. The adhesion phenomenon and its influence on the force transfer are described in section II-A. Then, the locomotive electric drive and its model are described in section II-C. The electric drive description contains a description of its mechanical, electrical, and control parts. Based on the mechanical system description, a model that is used by the UKF is presented, which is the fundamental part of the proposed slip controller. Next, the proposed slip controller principle is described in part II-B. The essential part of slip control is the angular velocity measurement that is described in part II-D. Section III describes simulation results. The simulation results are described in part III. The situations are connected with the low velocity for the proposed slip controller based on the UKF, and the proposed slip controller is compared with a classical slip controller method.

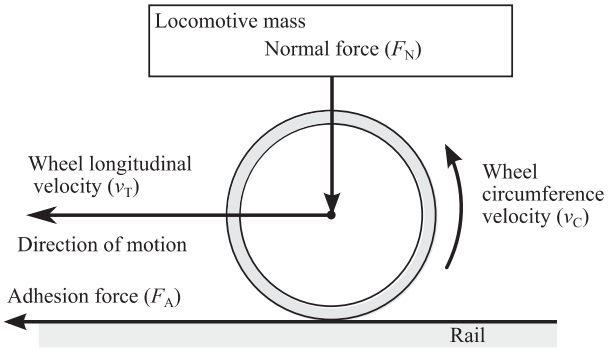

Fig. 1. Wheel with marked velocities and applied forces.

II. Adhesion, Slip Controller and Electric Drive

A. Adhesion Phenomenon

The adhesion phenomenon and related terms are explained at the first because the adhesion strongly influences the locomotive tractive performance, and it is the base of the slip controller design. The wheel that transfers force to a rail has to have a higher circumference velocity than longitudinal velocity [30]. The situation with marked velocities and applied forces are depicted in Fig. 1. The difference between wheel circumference velocity and longitudinal velocity is called a slip velocity (1). Instead of the slip velocity is sometimes used term slip that is a ratio of the slip velocity and the wheel longitudinal velocity. The main applied forces to the wheel are the tractive force and the normal force. The actual value of the tractive force is defined (2). The normal force is not constant, and changes during the train run [31].

$$v_S = v_C - v_T \tag{1}$$

where v_S is the slip velocity, v_C is the wheel circumference velocity, and v_T is the wheel longitudinal velocity that can be considered as a train velocity.

$$F_A = \mu(v_S) \cdot F_N \tag{2}$$

where F_A is the adhesion force, F_N is a normal force, and $\mu(v_S)$ is the adhesion coefficient.

The wheel circumference velocity is typically measured by an incremental encoder that is mounted on the wheelset or motor. The wheel longitudinal velocity is not measured on locomotives, but it is typically estimated because locomotives have all wheels driven. The longitudinal velocity of the train is possible to measure only on electric multiple units that have some non-driven wheels.

The dependence of the adhesion coefficient on slip velocity is depicted in Fig. 2. The shape of the characteristic changes with the rail surface conditions. Therefore, the characteristics of dry rail and wet rail are depicted in the figure. The adhesion-slip characteristics can be divided into a part where the adhesion coefficient increases with slip velocity. This part is from an electrical drive point of view stable because the electric drive can stably operate in part without any slip controller reaction. The adhesion coefficient decreases with increasing slip velocity in the second part of the characteristic.

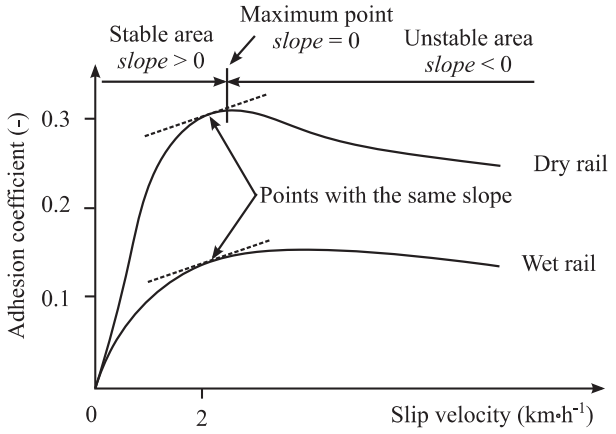

Fig. 2. Example of the adhesion-slip characteristics.

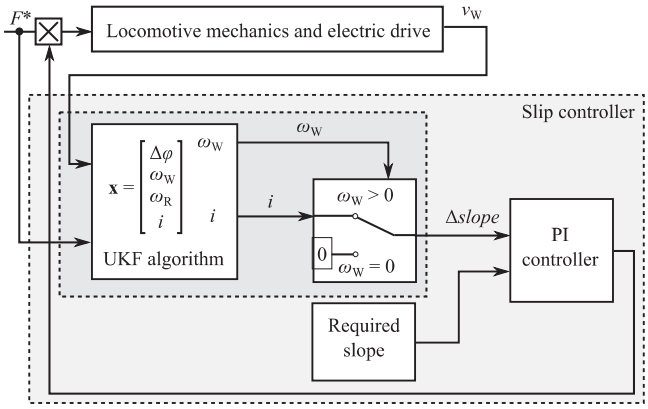

Fig. 3. Proposed slip controller block diagram.

The electric drive cannot permanently work in this part of the characteristic. Between the areas is the maximum point located. The slip controller should keep the operation point in the stable area, or unstable area near the maximum point for the necessary time. This situation can occur by the slip controller operation principle or by the adhesion changes that cause the operating point jumps to the unstable area. The adhesion-slip characteristics also decrease their maximum point value with increasing train velocity. There are also depicted examples of the slope of the curves (dashed line) as tangents in Fig. 2. The slope is the same for both curves, but its position to the maximum point is different, i.e., the method that estimates the adhesion-slip characteristic slope work with variable distance from the maximum point.

B. Proposed Slip Controller

The proposed slip controller is based on the determination of the adhesion-slip characteristic slope (3). The slip controllers widely use this principle. The principles of the slip controllers are based on the assumption that when the slope is positive, the operating point is located in a stable area when the slope is negative, the operating point is located in an unstable area, and when the slope is zero, the operating point is at the maximum point of the adhesion-slip characteristic. The method disadvantage is a requirement of the slip velocity value that is difficult to calculate when all wheelsets are driven.

$$slope = \frac{dF_A}{dv_S} \tag{3}$$

The proposed slip controller consists of an estimation part and controller part, as it is depicted in Fig. 3. The estimation part is based on the UKF and could calculate the slope of the adhesion-slip characteristic. The slip control method based on the UKF was described [36] and [37] in detail. The original method described in [36] is intended for the train velocity estimation and enables to calculate the slope according (3). However, the method requires high additional computational power to calculate the train velocity that is needed for the slip velocity calculation. Therefore, the proposed slip controller is based on the computationally more straightforward principle presented in [37] that enables directly calculate the slope of the adhesion-slip characteristic without slip velocity calculation. The second part of the slip controller is the controller that limits the value of the applied force.

The overall method block diagram is depicted in Fig. 3. The UKF estimates wheelset velocity. The estimated wheelset velocity and the measured wheelset velocity are the values that are used for compensation of a difference between the measurement and estimation. The adhesion-slip characteristic slope is calculated by the UKF directly, and the slope is used as a PI controller input. The calculated slope by the UKF is different from (3) because the UKF does not calculate the actual derivative, but it calculates the change of the adhesion slope. Therefore, the slope calculated by the method is shifted to zero value when the operating point is located in the stable area of the adhesion characteristic. The slope is negative when the operating point is located in the unstable part. The value is marked as $\Delta slope$ in Fig. 3. This behavior is possible due to the neglecting of the tractive force when the measured speed is available. The required $\Delta slope$ that can be zero theoretically is the second input of the PI controller. However, the value should be small negative due to disturbances that cause the calculated $\Delta slope$ oscillations around zero. The PI controller output is limited to values from zero to one, and the output of the PI controller is multiplied by a required motor torque. Thus, the slip controller can only decrease the required motor torque. From the previous description, it is clear that the method cannot work at very low velocity when the measured wheel velocity is zero. In this case, (3) cannot be calculated, and the conventional method output must be zero or positive. On the other hand, the wheel velocity, according to the applied force, can be estimated by the proposed method. Therefore, the proposed method can work from zero value.

The known UKF algorithm is presented, e.g., in [38], and implementation into Matlab software is presented in [39]. However, the UKF algorithm exists in different forms. Therefore, the used algorithm is given next.

$$U^T U = (n + \kappa) \cdot P_k \tag{4}$$

Sigma points and weights calculation:

$$\chi_0 = \hat{x}_k \tag{5}$$

$$\chi_i = \hat{x}_k + U_i\sqrt{n+\lambda}, \quad i = 1, 2, \ldots, n \tag{6}$$

$$\chi_{n+i} = \hat{x}_k - U_i\sqrt{n+\lambda}, \quad i = 1, 2, \ldots, n \tag{7}$$

$$W_0 = \frac{\lambda}{n+\lambda} \tag{8}$$

$$W_i = \frac{1}{2(n+\lambda)}, \quad i = 1, 2, \ldots, 2n \tag{9}$$

State prediction and covariance calculation:

$$\hat{x}_k^- = \sum_{i=0}^{2n} W_i \cdot \eta_i \tag{10}$$

$$P_{xx} = \sum_{i=0}^{2n} W_i \cdot (\eta_i - \hat{x}) \cdot (\eta_i - \hat{x})^T \tag{11}$$

Measurement prediction and covariance calculation:

$$\hat{y}_k = W_0 \cdot \xi_0 + \sum_{i=0}^{2n} W_i \cdot \xi_i \tag{12}$$

$$P_{yy} = W_0^{(P_{zz})} \cdot (\xi_0 - \hat{y}) \cdot (\xi_0 - \hat{y})^T + \sum_{i=0}^{2n} W_i \cdot (\xi_0 - \hat{y}) \cdot (\xi_0 - \hat{y})^T \tag{13}$$

Kalman gain calculation:

$$P_{xy} = \sum_{i=0}^{2n} W_i \cdot (\eta_0 - \hat{x}) \cdot (\xi_0 - \hat{y})^T \tag{14}$$

$$K_k = \frac{P_{xz}}{P_{yy} - R} \tag{15}$$

State estimation calculation:

$$\hat{x}_k = \hat{x}_k^- + K_k \cdot (y_k - \hat{y}_k) \tag{16}$$

Covariance error calculation:

$$P_k^- = P_{xx} + Q \tag{17}$$

$$P_k = P_k^- + K_k \cdot P_{xy}^T \tag{18}$$

where $\hat{x}_k$ is the estimated state vector, $\hat{y}_k$ is an output estimation, y is output vector, χ is a sigma point matrix, λ, α, β and κ are scaling parameters, W_i are weights of χ_i, P_k is an error covariance matrix, P_yy is prediction output error covariance matrix, P_xy is an output error covariance matrix, P_xx is prediction error covariance matrix, K_k is the Kalman gain, ξ is transformed sigma points through nonlinear function g, and η is transformed sigma points through nonlinear function *f*, R is a measurement uncertainty covariance matrix, and Q is a process noise covariance matrix.

The UKF requires correct settings of covariance matrixes for its proper function. The covariance matrixes settings are also mentioned in [39]. The UKF algorithm requires the calculation of the Cholesky factorization. The factorization is calculated from an error covariance matrix P_k. Therefore matrix has to be positive semidefinite. Although the UKF algorithm is well known, the algorithm does not contain the part that ensures the matrix P_k correct value in the basic form. The improvement is suggested in [40].

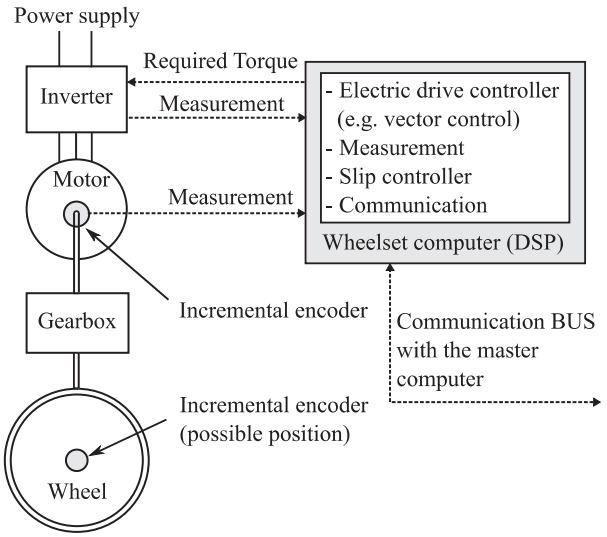

Fig. 4. Block diagram of one locomotive driven axle.

C. Wheelset and Electric Drive Configuration

The typical electric drive configuration of one locomotive driven axle is depicted in Fig. 4. The wheelset is formed by mechanical, electrical, and control components. The wheelset, gearbox, and motor shaft forms mechanical parts. There are connections between the elements and bogie frame like bearings or moving connection of the motor with the bogie frame, but these parts are not crucial for the slip controller description. The electrical part is formed by an inverter, electric motor, and wheelset computer. An induction motor is mainly used with an inverter nowadays, and the electric drive with the induction motor is typically driven by field-oriented control (FOC) or direct torque control (DTC) [32]. The DC motors were used in the locomotives. However, some of the locomotives with the DC motors are still in service. The speed controllers are not a standard part of the control structure of freight locomotives. The wheelset computer is a digital signal processor (DSP). The DPS calculates the FOC or DTC, slip controller, and provides measurement and communication with the master computer.

Most of the slip controllers are typically based on a measurement of the wheelset velocity and applied torque. The motor controller calculates the applied torque, and an incremental encoder measures the wheelset velocity. The incremental encoder can be mounted either on the wheelset or the motor. The position of the incremental encoder on the motor is typical for the electric drive with the induction motor. The motor angular velocity and wheelset angular velocity are different due to the gearbox that decreases the angular velocity to get higher torque on wheelsets. The higher velocity is preferable from the slip controller point of view because the slip controller can work at lower train speeds.

The locomotive computer is designed as a distributed computer that consists of a master computer and slave computers. The slave computers are wheelsets computers that control electric drives, i.e., calculate FOC or DTC and slip controller, and computers for auxiliary devices [33] and [34]. The master

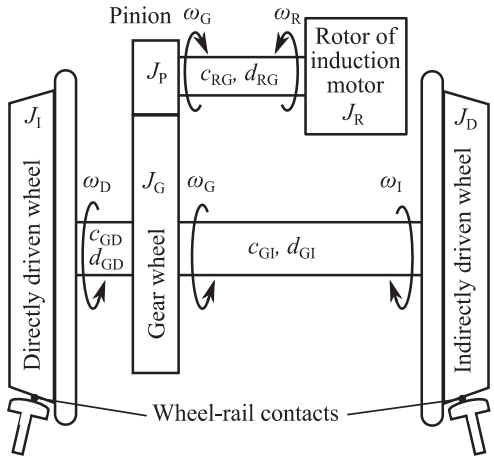

Fig. 5. Five-mass mechanical model.

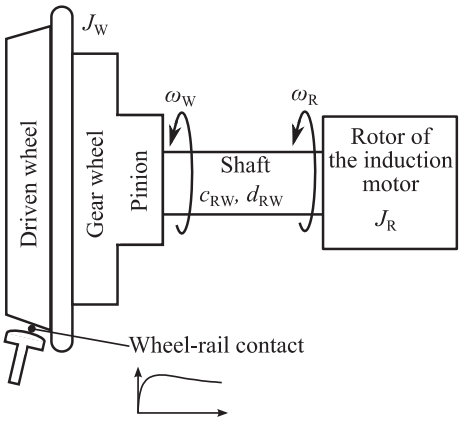

Fig. 6. Two-mass mechanical model.

computer process commands from a driver and communicates with other locomotive computers or other locomotives if they are connected or with wagons. The master computer also commands the slave computers. The wheelset computers control the corresponding electric drives according to commands from the master computer. The wheelset computer measures electrical quantities like currents or voltage and speed that is measured by an incremental encoder. The computer can measure wheel circumference velocity only. The locomotive velocity is determined by locomotive computer from all measured wheelsets velocities as the velocity of the slowest wheelset or by some averaging. However, these methods are not sufficiently effective and can fail when all wheelsets have the same high value of the slip velocity.

For the slip controller based on the UKF mechanical model is required. The whole wheelset mechanics with the electric drive can be modeled as a five-mass model that provides adequate results. However, the five-mass model is complex and contains some unnecessary parts that are not needed for slip controller correct operation [35]. Therefore, a two-mass model is used. The second reason for the usage of the two-mass model is the high complexity of the UKF algorithm, and a more complicated model can cause problems with calculation time. However, the five-mass model is used as a model of the locomotive for simulation purposes. The mechanical system of the five-mass model is depicted in Fig. 5. The five-mass model consists of a rotor element marked by subscript R of the motor, pinion P, gear wheel G that creates a gearbox, and two wheels. The wheel close to the gearbox is called as directly driven wheel D and the second one as indirectly driven wheel I. The masses are represented by their moments of inertia J, and they are connected by the shafts that are represented by their elasticity c and damping d. The rotor and wheel have the different actual values of the angular velocities due to a non-rigid shaft. This non-rigid shaft causes different actual values of the angle of rotation and torsional vibrations between the rotor and wheel that has to be preserved by the model. Therefore, the mechanical system eigenfrequencies were identified on locomotive during measurement, and the five-mass model was tuned to preserve them.

The two-mass model of the mechanical system is depicted in Fig. 6. The two-mass system is created by the rotor of the motor on one side and by the driven wheel, gear wheel and pinion on the second side. The system equations in state-space are defined as follows:

$$\frac{dx}{dt} = f(x(t), u(t)) + w(t) \tag{19}$$

$$y = h(x(t), u(t)) + v(t) \tag{20}$$

where x is a state vector, y is an output vector, u is an input vector, f and h are nonlinear functions, and w and v are noises.

The state vector and the system matrix A of the system are defined as follows:

$$x = \begin{bmatrix} \Delta\varphi \\ \omega_R \\ \omega_W \\ i \end{bmatrix} \tag{21}$$

$$A = \begin{bmatrix} 0 & \frac{1}{J_R} & \frac{1}{J_W} & 0 \\ c_{RW} & -d_{RW} & d_{RW} & 0 \\ c_{RW} & d_{RW} & -d_{RW} & \frac{1}{J_W} \\ 0 & 0 & 0 & -1 \end{bmatrix} \tag{22}$$

where $\Delta\varphi$ is an angle difference between the masses, ω_R is the rotor angular velocity, ω_W is the wheel angular velocity, i is the estimated slope change, J_R is the rotor moment of inertia, J_W is the wheel moment of inertia, c_{RW} is the elasticity of the shaft and d_{RW} is damping of the shaft.

The mechanical system that is described by system matrix A is linear, but the wheel-rail contact causes the nonlinearity due to the adhesion characteristic. Therefore, the system has to consist of the nonlinearity as it is depicted in Fig. 6. The nonlinearity is not included in the system matrix directly, but it is a part of the UKF algorithm.

The parameters for the five-mass model were calculated from the measurement. The moments of inertias were calculated from the dimensions of the parts, the damping depends on the dimensions and materials, and the elasticity can be calculated from eigenvalues. The comparison of the system poles position on the five-mass, two-mass model is depicted

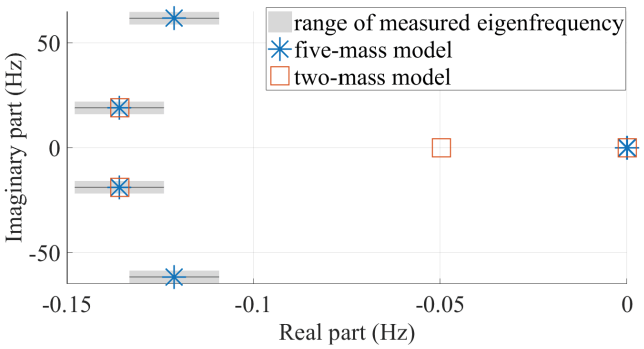

Fig. 7. Comparison of the positions of the poles of the models.

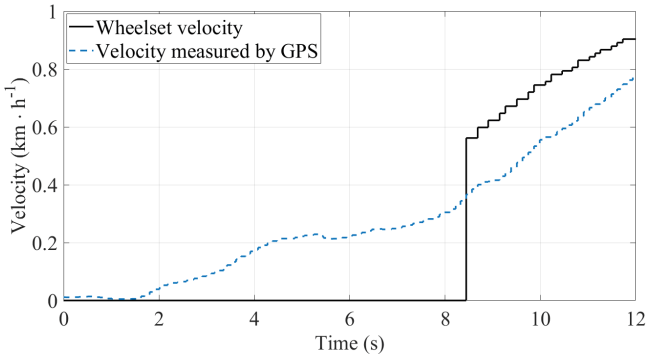

Fig. 8. Velocity measurements during the train start.

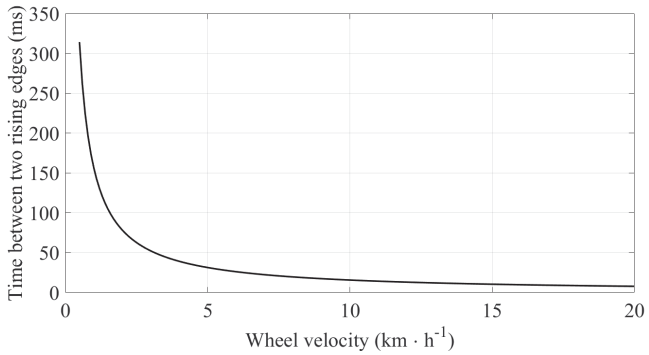

Fig. 9. Dependence of the time between two edges on the velocity.

in Fig. 7. It illustrates the frequencies of the system measured on the locomotive because the exact value of the real part is difficult to determine because not all parameters are precisely known. Therefore, the poles of the models were set in the middle of the interval.

D. Velocity Measurement Principle

The signals from the incremental encoder can be processed according to the period between two edges, or according to the number of edges for a particular time, this method is called as frequency measurement. The period measurement is suitable for low velocities, and frequency measurement is proper for higher velocities [41]. This approach works correctly when the velocity is high enough, but if it is low, the slip controller can have problems, especially during the train starts. Therefore, during the train starts, the applied forces are high, and the measured velocities change slowly due to the measurement principle. Alternatively, the measured velocity can be zero, although the train is moving. This situation is caused by the use of incremental encoders with a low number of pulses per revolution. The number of pulses per one revolution can be in the range from tens to hundreds. The authors made a measurement on a locomotive that has incremental encoders with 90 pulses per revolution, and the incremental encoder was mounted on the wheelset. In this case, the time between two edges is one millisecond when the train velocity is about 157 km $\cdot$ h^{-1}. Moreover, the input signal has to be filtered due to the encoder inaccuracy. The incremental encoders with a low number of pulses per revolution are used because of their robustness because they are mounted on wheelsets or motors that are directly connected with the wheelsets where mechanical shocks and electrical noise is presented. The measured results during the train start are depicted in Fig. 8. The figure depicts wheelset velocity that was measured by an incremental encoder mounted on the motor side and velocity measured by the GPS. The measured wheelset velocity is zero, although the train moves. The GPS velocity is lower due to the slip velocity. The slip velocity is low due to the good adhesion conditions and the low applied force that is approximately 30% of the maximum force. The big first step is caused by the velocity measurement process that incorporates filtration.

The dependence of time between two edges on the velocity is depicted in Fig. 9. The depicted velocity range is from 0.5 km $\cdot$ h^{-1} to 20 km $\cdot$ h^{-1}. The time between two rising edges at velocity 0.5 km $\cdot$ h^{-1}is more than 300 milliseconds. During this time, several hundred of the slip controller calculation occurs with the same velocity information. The time between edges is 7.8 milliseconds at velocity 20 km $\cdot$ h^{-1}. The time is very long if the slip controller calculation period is taken into account. It can be 400 microseconds on newer locomotives and one millisecond on older locomotives.

The situation when the train starts is schematically depicted in Fig. 10. The applied force, wheelset velocity, incremental encoder pulses, calculated velocity, and slip controller timing is depicted in Fig. 10. The applied force is increased in a ramp function to avoid mechanical shock, and the wheelset velocity starts to increase. However, there are low numbers of pulses per revolution of the incremental encoder, and the measured velocity is zero until the second pulse is detected. However, the second pulse can be ignored if the period between the pulses exceeds a pre-set period of measurement between two pulses. Many slip controller calculations were made during the time. Moreover, when the wheelset velocity is measured, it remains for a long time at the constant value. The possible problems that can occur are the stairs with the big step that can cause the failure of methods based on acceleration because the acceleration is high in this case. The result is a decrease of the applied force, and the train can stop. The possible solution is to use a higher filtration that causes a delay of the controller reaction when real slippage occurs. The methods based on state estimators calculate wrong states, and the slip controller also decreases the applied force. Moreover, methods

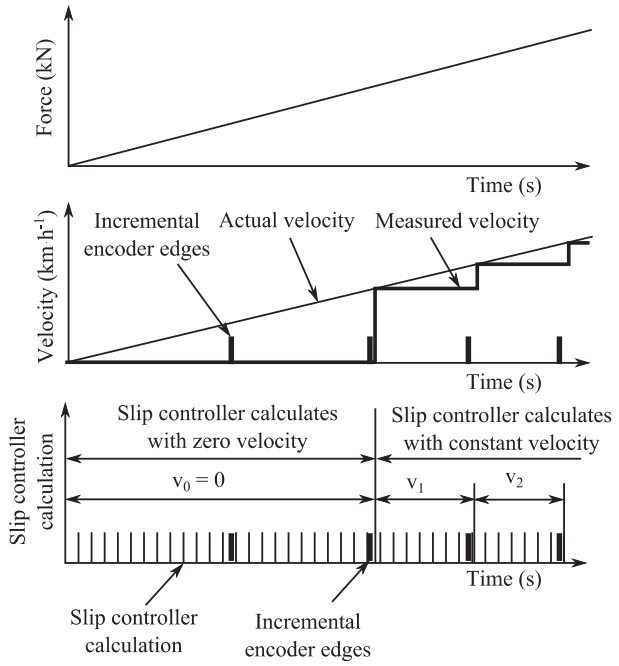

Fig. 10. Wheelset velocity measurements and the slip controller calculation.

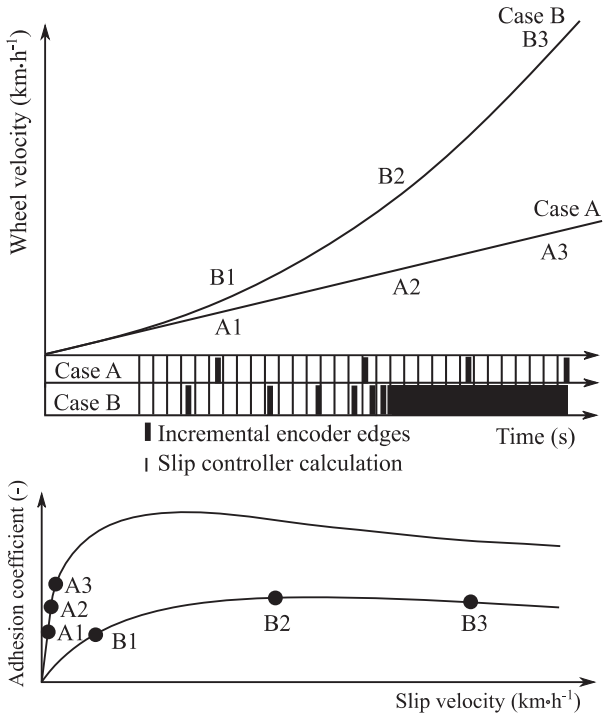

Fig. 11. Wheelset velocity measurements during different adhesion conditions.

that calculate the adhesion-slip characteristic slope as a ratio of the adhesion force F_A derivative according to slip velocity v_S derivative (3) fail from its principle because the slip velocity is zero at the beginning, and next is the slip velocity constant.

The wheelset measurement principle during different adhesion conditions is depicted in Fig. 11. When the adhesion conditions are good, the applied force causes the continuous increase of the wheel velocity, and the operating point continuously goes to the maximum point on the adhesion-slip characteristic. The maximum point is near 2 km · h^{-1}, where the velocity measurement work is acceptable. This situation is marked as a case A in the figure. The different situation occurs when the adhesion conditions are adverse. The applied force simply exceeds the maximum available adhesion force, and the wheelset velocity starts to increase. The high velocity causes an acceptable operation of measurement, and the slip controller can react. However, if the wheelset acceleration is high, the measurement output can be delayed due to the filtration of the measured velocity. Therefore, from the previous description, it is clear that inappropriate velocity measurements cause the problem. The problem can be solved by a method based on a KF because the KF can change a Kalman gain according to the measurement creditability. This feature is not possible in estimators based, e.g., on Luenberger observer or DO. The slippage principle ensures the proposed method functionality at low wheelset velocity. If the slippage is created, the wheel velocity starts to increase because the operating point has to move to the adhesion-slip characteristic maximum value that leads to the higher slip velocity. Therefore, the wheelset velocity has to increase to measurable values at first.

III. Simulation Results

The simulation results of the five-mass model when the locomotive starts during the good adhesions and the model

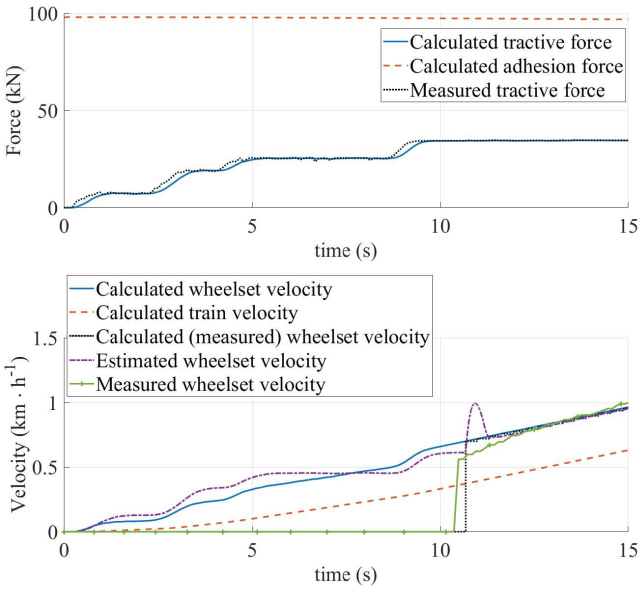

Fig. 12. Simulation result for the train starts with good adhesion conditions.

comparison with measurement on the locomotive are depicted in Fig. 12. The simulated and measured tractive forces applied to the wheelset, and the theoretical maximum value of the adhesion force is depicted in the top of the figure. The calculated wheelset velocity, calculated train velocity, and calculated measured wheelset by the five-mass model, estimated wheelset velocity by the UKF, and measured wheelset velocity on the locomotive are depicted in the bottom of the figure. The measured values and calculated values are very similar. The adhesion force has a very high value because the

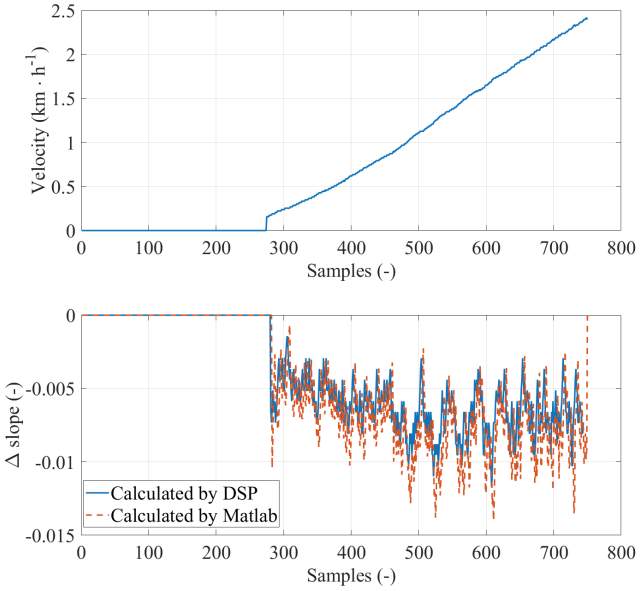

Fig. 13. Comparison of method output calculated by Matlab and DSP.

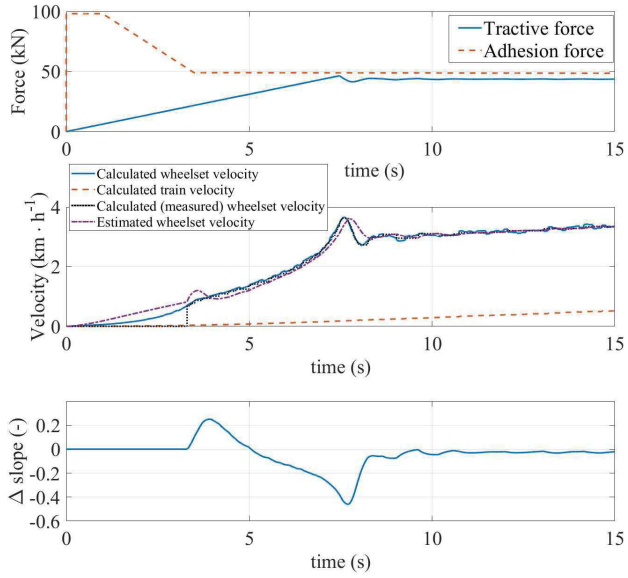

Fig. 14. Simulation result for the case when the adhesion coefficient decrease during the train starts with the proposed slip controller reaction.

train velocity is almost zero. The applied force is gradually increased without any reaction of the slip controller because the applied force is lower than the adhesion force. The adhesions force maximum value depends on normal force and actual adhesion conditions. This maximum gradually decreases with increasing train velocity. This decrease is not obvious too much in this case because the train velocity change is small. The wheelset velocity increases faster than the train velocity due to the applied force increase, and the operating point on the adhesion-slip characteristic moves to the maximum point. Therefore, the slip velocity increases with increasing applied force. The measured velocity has a stair-step course due to the measurement. The estimated velocity follows the actual wheelset velocity when the actual velocity reaches approximately 0.5 km $\cdot$ h^{-1}. The electric drive can work permanently in this mode without the slip controller reaction.

The slip controller was implemented to a digital signal processor (DSP) with 150 MHz frequency to verify that the slip controller can be used for calculation on the locomotive. One cycle of the slip controller calculation takes 95 microseconds. The electric drives of modern locomotives can run with a period of 400 microseconds, and the slip controller run has reserved around 100 microseconds for the calculation. Therefore, the slip controller can be implemented on the locomotive computer. The comparison between the slip controller outputs calculated by Matlab software and DSP on measured data is depicted in Fig. 13. The simulation model in the Matlab was designed to calculate the mechanical part continuously, and the controller runs with 400 microseconds.

The situation with the enabled slip controller and the adhesion decrease is depicted in Fig. 14. The figure contains the estimated wheelset velocity and adhesion characteristic slope change $\Delta slope$ calculated by the slip controller. The slip controller reacts and decreases applied force to avoid the slippage creation. The slip controller reaction is made before the applied force exceeds a maximum adhesion force. Therefore, the operating point is in the stable area of the adhesion-slip characteristic and near the maximum point. When the high slip velocity is suppressed, the slip controller tries to maximize the applied force and get close to the maximum point. The slip velocity is higher than it is depicted in Fig. 12 because the adhesion is lower than in the picture, and a different adhesion-slip characteristic is used. The new characteristic has a maximum point located at the higher slip velocity. The slip controller reacts when the slip velocity is approximately 0.9 km $\cdot$ h^{-1}. The maximum sip velocity is approximately 2.4 km $\cdot$ h^{-1}. The value corresponds to the maximum point on the adhesion-slip characteristic [2]. The oscillations of the UKF output that are transferred to the PI controller output and tractive force are caused by the measurement that is not entirely eliminated by the UKF. The estimated wheelset velocity is delayed about the actual wheelset velocity. UKF settings and measurements cause a delay. The time delay decreases with the increasing wheelset velocity. On the other hand, the estimated velocity does not contain the stairs, and the derivative of the slip velocity is smooth.

The simulation results for the slip controller based on the DO are depicted in Fig. 15. The derivative, according to (3), is depicted in the figure. The DO requires a filter with a high level of filtration. Therefore, the slip controller reaction is delayed, and the slip velocity reaches a high value. Therefore, then the force is significantly decreased to avoid the next increase of the slip velocity. The low filtration causes fail of the method because the output vector starts oscillate due to the stairs on the measured velocity. Moreover, the PI controller that decreases the applied force has to be slow to avoid the DO oscillations. This simulation is made for the comparison of the used slip control method with the proposed slip controller.

There are also different possibilities of the low train velocity, like slowing down to stop, but the traction is not typically

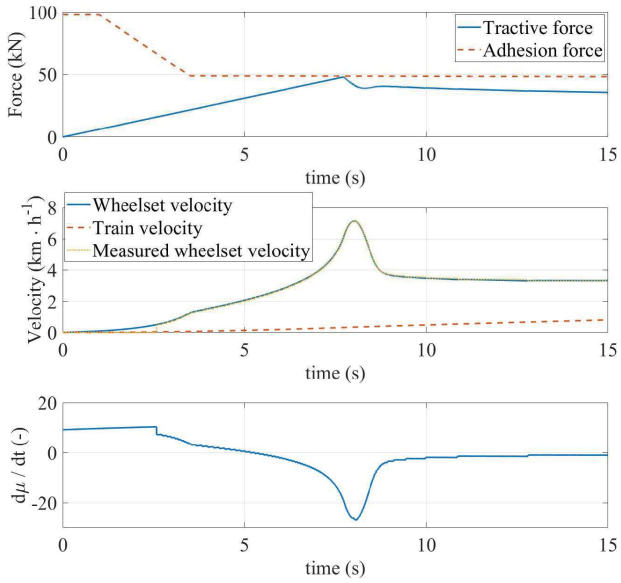

Fig. 15. Simulation result for the case when the adhesion coefficient decrease during the train starts with a slip controller based on the DO reaction.

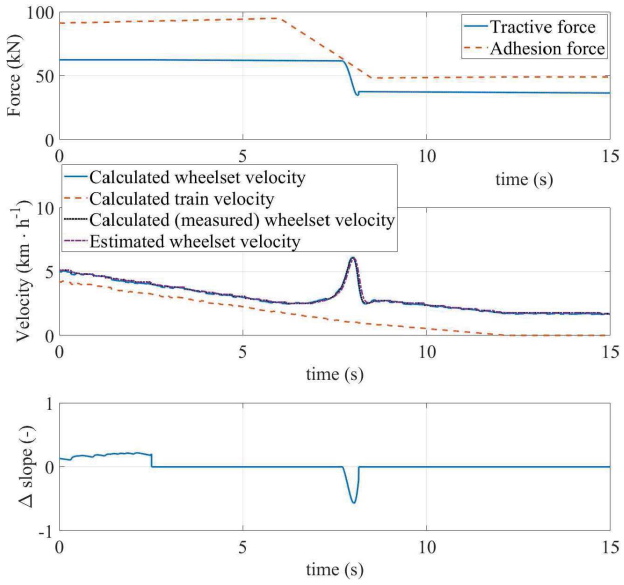

Fig. 16. Simulation results for the case when the train goes to hill climbing.

required in this situation, or the next traction is similar to starting. However, the problem is when the heavy train goes uphill. The low velocity can occur with full tractive effort in the case. The simulation result of hill climbing is depicted in IV. There are adhesion coefficient decrease occurs in the figure. The slip controller can cope with the velocity decrease, but the reaction is worse due to the long-time response of the measurement. However, the slip controller can keep the operating point near the maximum point of the characteristic.

IV. Conclusion

The paper presents the slip controller that correctly works during the low train velocity except for high velocities and can work from zero measured velocity. The low velocity can cause problems for the classical slip controllers. The slip controller performance depends on the electric drive configuration, and its proper work depends on the adhesion conditions. Therefore, the adhesion, proposed slip controller, and the electric drive are described first. The proposed slip controller is based on the UKF that enables the estimation of all required values that are needed for the correct work of the slip controller. The proposed slip controller uses estimated slip velocity instead of measured velocity because the estimated velocity is smoother and closer to the actual wheelset velocity. Therefore, the derivative is also smoother. The proposed slip controller can cope with the high derivative of the slip velocity that occurs due to the stairs on the measured velocity that can cause the failure of the classical methods.

The method functionality is demonstrated in simulation results. The simulation results are made for locomotive starts during good adhesion conditions when train and wheelsets accelerate continuously, and the step time course of the measured wheelset velocity is visible. On the other hand, the estimated wheelset velocity is smoother and closer to the measured velocity when the measurement starts working. The simulations are made for good adhesion conditions and adverse adhesion conditions. When the adhesion conditions became worst, the slip controller reacts and suppresses the slippage at its beginning. The slip velocity increases when the adhesion force decreases. However, the slippage does not occur. The slip controller based on the DO is also used to demonstrate a conventional controller functionally for comparison. The other situation when low velocity can occur is hill climbing when the heavy train can stop in the track. The simulation results are based on the five-mass mathematical model of one wheelset that was set to its eigenfrequencies corresponds with the measured values. The algorithm was implemented to the DSP, and the calculated results are similar to simulation. The next step is software in the loop and hardware in the loop simulations.

References

[1] W.-C. Cai, D.-Y. Li, B. Liu, and Y.-D. Song, "Uniform rolling-wear-based robust adaptive control of high-speed trains in the presence of actuator differences," *IEEE Trans. Intell. Transp. Syst.*, vol. 17, no. 12, pp. 3591–3601, Dec. 2016.

[2] J. Huang, J. Xiao, and H. Weiss, "Simulation study on adhesion control of electric locomotives based on multidisciplinary virtual prototyping," in *Proc. IEEE Int. Conf. Ind. Technol.*, Apr. 2008, pp. 1–4.

[3] M. Yamashita and T. Soeda, "Anti-slip re-adhesion control method for increasing the tractive force of locomotives through the early detection of wheel slip convergence," in *Proc. 17th Eur. Conf. Power Electron. Appl.*, Sep. 2015, pp. 1–10.

[4] T. Ishrat, G. Ledwich, M. Vilathgamuwa, and P. Borghesani, "Identification scheme of maximum traction force using recursive least square for traction control in electric locomotives," in *Proc. IEEE 12th Int. Conf. Power Electron. Drive Syst. (PEDS)*, Dec. 2017, pp. 1120–1125.

[5] S. Sadr, D. A. Khaburi, and J. Rodriguez, "Predictive slip control for electrical trains," *IEEE Trans. Ind. Electron.*, vol. 63, no. 6, pp. 3446–3457, Jun. 2016.

[6] K. Xu, G. Xu, and C. Zheng, "Novel determination of Wheel-Rail adhesion stability for electric locomotives," *Int. J. Precis. Eng. Manuf.*, vol. 16, no. 4, pp. 653–660, Apr. 2015.

[7] K. Lu, Y. Song, and W. Cai, "Robust adaptive re-adhesion control for high speed trains," in *Proc. 17th Int. IEEE Conf. Intell. Transp. Syst. (ITSC)*, Oct. 2014, pp. 1215–1220.

[8] X. Hong, R. Zhang, L. Wu, Y. Li, and K. Wang, "Simulation of adhesion control method based on phase-shift," in *Proc. Int. Conf. Electr. Mach. Syst. (ICEMS)*, Oct. 2013, pp. 2077–2080.

[9] J. He, B. Dou, C. Zhang, L. Liu, and X. Yin, "Anti-slip strategy of locomotives using improved adhesion characteristic curve slope method," in *Proc. Chin. Autom. Congr. (CAC)*, Oct. 2017, pp. 855–860.

[10] L. Wenli, Z. Leiting, and D. Kan, "Performance analysis of re-adhesion optimization control based on full-dimension state observer," *Procedia Eng.*, vol. 23, pp. 531–536, Jan. 2011.

[11] K. Ohishi, "Realization of fine motion control based on disturbance observer," in *Proc. 10th IEEE Int. Workshop Adv. Motion Control*, Mar. 2008, pp. 1–8.

[12] Y. Shimizu, K. Ohishi, T. Sano, S. Yasukawa, and T. Koseki, "Anti-slip re-adhesion control based on disturbance observer considering bogie vibration," in *Proc. Eur. Conf. Power Electron. Appl.*, 2007, pp. 1–10.

[13] Z. Huang, Z. Xu, B. Chen, R. Zhang, Y. Chen, and Q. Peng, "Sliding mode control for urban railway anti-slip system based on optimal slip ratio estimation with forgetting factor recursive least-squares," in *Proc. 36th Chin. Control Conf. (CCC)*, Jul. 2017, pp. 9502–9507.

[14] K. Zhao, P. Li, C. Zhang, J. He, Y. Li, and T. Yin, "Online accurate estimation of the wheel-rail adhesion coefficient and optimal adhesion antiskid control of heavy-haul electric locomotives based on asymmetric barrier Lyapunov function," *J. Sensors*, vol. 2018, Apr. 2018, Art. no. 2740679.

[15] C. Zhang, J. Sun, J. He, and L. Liu, "Online estimation of the adhesion coefficient and its derivative based on the cascading SMC observer," *J. Sensors*, vol. 2017, Jan. 2017, Art. no. 8419295.

[16] Q. Peng, J. Liu, Z. Huang, W. Liu, and H. Li, "Sliding model control based on estimation of optimal slip ratio for railway wheel slide protection using extremum seeking," in *Proc. IEEE Energy Convers. Congr. Exposit. (ECCE)*, Sep. 2016, pp. 1–6.

[17] S. Wang, J. Xiao, J. Huang, and H. Sheng, "Locomotive wheel slip detection based on multi-rate state identification of motor load torque," *J. Franklin Inst.*, vol. 353, no. 2, pp. 521–540, Jan. 2016.

[18] J. Huang, J. Xiao, D. Zhao, and S. Wang, "A wheel slip detection method of electric locomotive based on time-frequency analysis," in *Proc. 17th Int. IEEE Conf. Intell. Transp. Syst. (ITSC)*, Oct. 2014, pp. 1221–1225.

[19] N. H. Jo, C. Jeon, and H. Shim, "Noise reduction disturbance observer for disturbance attenuation and noise suppression," *IEEE Trans. Ind. Electron.*, vol. 64, no. 2, pp. 1381–1391, Feb. 2017.

[20] W.-C. Cai, D.-Y. Li, and Y.-D. Song, "A novel approach for active adhesion control of high-speed trains under antiskid constraints," *IEEE Trans. Intell. Transp. Syst.*, vol. 16, no. 6, pp. 3213–3222, Dec. 2015.

[21] Y. Chen, H. Dong, J. Lu, X. Sun, and L. Guo, "A super-twisting-like algorithm and its application to train operation control with optimal utilization of adhesion force," *IEEE Trans. Intell. Transp. Syst.*, vol. 17, no. 11, pp. 3035–3044, Nov. 2016.

[22] S. Cheng, L. Li, and J. Chen, "Fusion algorithm design based on adaptive SCKF and integral correction for side-slip angle observation," *IEEE Trans. Ind. Electron.*, vol. 65, no. 7, pp. 5754–5763, Jul. 2018.

[23] S. Cheng, L. Li, B. Yan, C. Liu, X. Wang, and J. Fang, "Simultaneous estimation of tire side-slip angle and lateral tire force for vehicle lateral stability control," *Mech. Syst. Signal Process.*, vol. 132, pp. 168–182, Oct. 2019.

[24] J. Otegui, A. Bahillo, I. Lopetegi, and L. E. Diez, "A survey of train positioning solutions," *IEEE Sensors J.*, vol. 17, no. 20, pp. 6788–6797, Oct. 2017.

[25] T. Hata *et al.*, "Anti-slip re-adhesion control based on speed sensor-less vector control and disturbance observer for electric multiple units, series 205-5000 of East Japan Railway Company," in *Proc. IEEE Int. Conf. Ind. Technol.*, Jun. 2004, pp. 772–777.

[26] F. Brugnano, C. Concari, E. Imamovic, F. Savi, A. Toscani, and R. Zanichelli, "A simple and accurate algorithm for speed measurement in electric drives using incremental encoder," in *Proc. 43rd Annu. Conf. IEEE Ind. Electron. Soc. (IECON)*, Oct. 2017, pp. 8551–8556.

[27] K. Kim, S.-H. Kong, and S.-Y. Jeon, "Slip and slide detection and adaptive information sharing algorithms for high-speed train navigation systems," *IEEE Trans. Intell. Transp. Syst.*, vol. 16, no. 6, pp. 3193–3203, Dec. 2015.

[28] L. Yuan, W. Zhao, C. Li, and D. Zhou, "Error correction method for train speed measurement using Doppler radar in train control system," in *Proc. IEEE 11th Int. Symp. Auto. Decentralized Syst. (ISADS)*, Mar. 2013, pp. 1–4.

[29] M. Malvezzi, B. Allotta, M. Rinchi, B. Bruzzo, and P. Bernardi, "OOdometric estimation for automatic train protection and control systems," *Vehicle Syst. Dyn.*, vol. 49, no. 5, pp. 723–739, 2009.

[30] R. Lewis, and U. Olofsson, *Wheel-Rail Interface Handbook*. Boca Raton, FL, USA: CRC Press, 2009, pp. 513–519.

[31] H. Wang, J. Zeng, and R. Luo, "Study on wheel/rail adhesion force and its control of high-speed trains considering aerodynamic loads and track excitations," *Wear*, vol. 314, nos. 1–2, pp. 299–304, Jun. 2014.

[32] S. Sadr, D. A. Khaburi, M. Namazi, A. Shiri, and D. Esmaeil Moghadam, "Modeling of wheel and rail slip and demonstration of the benefit of maximum adhesion control in train propulsion system," in *Proc. IEEE 23rd Int. Symp. Ind. Electron. (ISIE)*, Jun. 2014, pp. 847–852.

[33] J. Zdenek, "Traction vehicle distributed control computer system architecture with auto reconfiguration features and extended DMA support," in *Proc. 13th Int. Power Electron. Motion Control Conf.*, Sep. 2008, pp. 1638–1645.

[34] J. Zdenek, "Distributed control computer backbone communication channel of electric locomotive with effective DMA support," in *Proc. 14th Int. Power Electron. Motion Control Conf. (EPE-PEMC)*, Sep. 2010, pp. T6-27–T6-34.

[35] P. Pichlík and J. Zděnek, "Adhesion force detection method based on the Kalman filter for slip control purpose," *Automatika*, vol. 57, no. 2, pp. 405–415, Jan. 2016.

[36] P. Pichlik and J. Zdenek, "Locomotive velocity estimation for a slip control purpose by an unscented Kalman filter," in *Proc. 18th Int. Sci. Conf. Electr. Power Eng. (EPE)*, May 2017, pp. 1–5.

[37] P. Pichlik and J. Zdenek, "Comparison of locomotive adhesion force estimation methods for a wheel slip control purpose," in *Proc. 9th Int. Conf. Electron., Comput. Artif. Intell.(ECAI)*, Jun. 2017, pp. 1–4.

[38] M. S. Grewal, and A. P. Andrews, *Kalman Filtering Theory and Practice Using MATLAB*, 3rd ed. New York, NY, USA: Wiley, 2008, pp. 330–350.

[39] K. Kyslan, V. Šlapák, V. Fedák, F. Ďurovský, and K. Horváth, "Design of load torque and mechanical speed estimator of PMSM with unscented Kalman filter—An engineering guide," in *Proc. 19th Int. Conf. Elect. Drives Power Electron. (EDPE)*, Oct. 2017, pp. 297–302.

[40] J. Chen, G. Jia, C. Yang, L. Li, X. Ran, and J. Song, "UKF-based adaptive variable structure observer for vehicle sideslip with dynamic correction," *IET Control Theory Appl.*, vol. 10, no. 14, pp. 1641–1652, Sep. 2016.

[41] A. Anuchin, V. Astakhova, D. Shpak, A. Zharkov, and F. Briz, "Optimized method for speed estimation using incremental encoder," in *Proc. Int. Symp. Power Electron. (Ee)*, Oct. 2017, pp. 1–5.

Petr Pichlík received the B.S. and M.S. degrees in electrical engineering from Czech Technical University, Prague, in 2008 and 2011, respectively, and the Ph.D. degree in 2018.

He is currently a Research Worker with the Department of Electric Drives and Traction, Faculty of Electrical Engineering, CTU. His research areas of interest are electric railway traction vehicles, locomotive slip control, and digital control systems.

Jan Bauer received the M.S. and Ph.D. degrees in electrical engineering from Czech Technical University, Prague, in 2007 and 2015, respectively. He is currently an Assistant Professor with the Department of Electric Drives and Traction, Faculty of Electrical Engineering, CTU. His research interests belong to control of electric drives and power converters and digital control of electrical systems.

APPENDIX B

LIPČÁK O. and BAUER J., "Offline method for experimental identification of load-dependent saturation of induction motor taking into account variation of inverse rotor time constant," in *IET Power Electronics*. 2019, ISSN 1755-4543, doi: 10.1049/iet-pel.2019.1361

Author's contribution: method development supervision, experiment proposal, analysis and discussion of measured results, consultation DSP algorithm implementation, analysis of influence to RFOC, paper co-writing

IET Power Electronics

Research Article

IET Journals
The Institution of Engineering and Technology

Offline method for experimental identification of load-dependent saturation of induction motor taking into account variation of inverse rotor time constant

ISSN 1755-4535
Received on 11th November 2019
Revised 24th February 2020
Accepted on 9th March 2020
E-First on 3rd April 2020
doi: 10.1049/iet-pel.2019.1361
www.ietdl.org

Ondrej Lipcak[1] ✉, *Jan Bauer*[1]

[1]*Department of Electric Drives and Traction, Faculty of Electrical Engineering, CTU in Prague, Technicka 2, Prague, Czech Republic*

✉ *E-mail: lipcaond@fel.cvut.cz*

Abstract: Accurate knowledge of induction machine parameters has a direct impact on the overall performance of field-oriented control strategies. In the case of rotor flux oriented control, parameter mismatch causes a discrepancy in the estimated rotor flux position and amplitude. Magnetising inductance is one of the parameters whose detuning has a direct impact on the setpoints of the control loops and estimation of hardly or non-measurable quantities. Conventional iron saturation, which can be obtained by a standard no-load test, is not the only type of saturation occurring in the machine. Depending on the rotor design, the magnetising inductance and the rotor leakage inductance may also strongly saturate as a function of load and, thus, rotor current. Based on the authors' previous work, a new, improved experimental method for identifying the load-dependent saturation of induction motor, which takes into account variation of the inverse rotor time constant, is proposed. Experimental results conducted on 12 kW motor show improved static and dynamic behaviour of the drive compared to the constant parameter model.

1 Introduction

The induction motors (IMs) still belong to the most used electromechanical converters among high-performance electric drives. It is because of their reliability, overloadability, and relatively low-cost production and maintenance. One of the most common control strategies in demanding applications is the rotor flux oriented control (RFOC). To reach high performance and high efficiency of the drive, precise knowledge of the IM equivalent circuit parameters is needed. Those parameters are used within the RFOC to get correct setpoints for the controllers. Inaccurate knowledge of the IM equivalent circuit parameters leads to RFOC detuning, which causes misalignment of the estimated flux position and, thus, inaccuracy of the control [1–3]. Also, today's requirement for reliability and cost reduction lead to the deployment of sensorless control strategies. In the case of a sensorless drive, the negative influence of the incorrect parameters is more pronounced [4–6].

A common cause of the RFOC detuning is the inexact knowledge of the magnetising inductance. Due to the material savings, electrical machines are usually designed so that the rated point lies within the knee of the magnetisation curve. Due to the conventional iron saturation, the magnetising inductance of IM then may vary in a wide range [7, 8]. The saturation characteristics are mostly obtained indirectly out of measured power, voltage, and current during a no-load test [2, 9, 10].

However, as pointed out in [11–16], the IM magnetising inductance may also saturate as a function of torque or rotor current, respectively, especially if the rotor slots are skewed and closed. By the nature of this phenomenon, this dependency is not possible to experimentally determine by the standard no-load test. The majority of papers model the magnetising inductance only as a function of the magnetising current. Only a few works strive to include the influence of the load or torque, respectively [11, 16]. Those papers use mainly finite element methods (FEMs). However, FEM models require knowledge of IM geometry; therefore, they are suitable for prototyping or new machine design.

Some papers try to identify the inductance by observers or model reference adaptive system (MRAS) [17, 18]. However, these methods require precise knowledge of all the other IM parameters. Other authors try to identify the magnetising inductance by signal injection [9, 19–25].

This paper presents a new offline identification method based on a principle presented in [26]. It compares the values of the measured and estimated IM torque and tries to minimise the error between them by adjusting the value of the magnetising inductance. Unlike our previous method, it does not require knowledge of the stator resistance. It does, however, require the knowledge of the rotor resistance, which is naturally not constant and depends on the IM's temperature, but the problem of the rotor resistance temperature dependency is overcome by estimating the value of the rotor inverse time constant. Therefore, intensive cooling is not required as opposed to our previous method.

The paper is organised as follows: in Section 2, basic IM equations that are utilised throughout the paper are presented. A former and improved method of identification of the load-dependent saturation is presented in Section 3. Guidance for implementation of the improved method is outlined in Section 4. Finally, Section 5 is dedicated to the experimental results. These also include a comparison of our method with the previous one, which is focused mainly on showing the robustness of the improved method against changes of the rotor resistance. The experimental part is concluded by an indirect approach of verification of the obtained saturation characteristics in terms of comparison of measured and estimated quantities and dynamic and static behaviour of a 12-kW drive.

2 Field-oriented control and induction motor equations

In this paper, equations describing the so-called T-equivalent circuit depicted in Fig. 1 are utilised for the mathematical description of IM. In the figure, the symbols $\underline{\boldsymbol{\psi}}_1$ and $\underline{\boldsymbol{\psi}}_2$ represent the stator and rotor flux linkage space vectors, respectively, $\underline{\boldsymbol{u}}_1$ represents the stator voltage space vector, $\underline{\boldsymbol{i}}_1$ and $\underline{\boldsymbol{i}}_2$ represent the stator and rotor current space vectors, respectively, R_1 and R_2 denote the stator and rotor resistance, respectively, ω_k is the electrical angular speed of the general reference frame, ω is the rotor electrical angular speed, L_m is the magnetising inductance and

the symbol j represents an imaginary unit ($j^2 = -1$). A squirrel-cage rotor is considered; therefore, the rotor voltage equals zero. The stator inductance L_1 is defined as $L_1 = L_m + L_{1\sigma}$, where $L_{1\sigma}$ is the stator leakage inductance and the rotor inductance L_2 is defined as $L_2 = L_m + L_{2\sigma}$, where $L_{2\sigma}$ is the rotor leakage inductance.

2.1 Rotor flux estimation

In the case of RFOC (Fig. 2), the position of the rotor flux vector and its amplitude are of interest. For a direct RFOC, where the transformation angle between the stationary $\alpha\beta$ and synchronous dq reference frame is calculated from the components of the rotor flux vector, the models are expressed in a stator-fixed coordinate system, therefore $\omega_k = 0$. The commonly used model, called the current model, is given by the following vector equation

$$\frac{d\underline{\boldsymbol{\psi}}_2}{dt} = L_m\tau_r^{-1}\underline{\boldsymbol{i}}_1 - \tau_r^{-1}\underline{\boldsymbol{\psi}}_2 + j\omega\underline{\boldsymbol{\psi}}_2, \tag{1}$$

where

$$\tau_r^{-1} = \frac{R_2}{L_2} \tag{2}$$

is the inverse rotor time constant. The Park transformation angle ϑ is then calculated as $\tan^{-1}(\psi_{2\beta}/\psi_{2\alpha})$.

2.2 Torque estimation

The IM torque can be expressed by many equivalent formulas based on one's choice of state variables. In this paper, a combination of the rotor flux linkage and stator current vector is selected. In the case of Clarke's transformation coefficient equal to 2/3 we get

$$T_{IM} = \frac{3}{2}p_p\frac{L_m}{L_2}(\psi_{2\alpha}i_{1\beta} - \psi_{2\beta}i_{1\alpha}), \tag{3}$$

where p_p is the number of pole-pairs.

3 Load-dependent saturation of induction motor and proposed method for its determination

3.1 Saturation of the magnetising inductance as a function of the rotor current

It is well-known that the magnetising inductance saturates as a function of the magnetising current. This dependency is, for instance, obtainable from the standard no-load test. However, the magnetising inductance may also saturate as a function of the load and, thus, rotor current. Authors in [11, 14] summarise that this phenomenon is caused mainly by skewing of rotor slots. This effect can be further aggravated if the rotor slots are closed.

3.2 Previous method

In [26], a simple and intuitive method for offline identification of the load-dependent saturation of IM was proposed. The method in addition to the IM current model given by (1) also uses the so-called voltage model given by the following set of equations:

$$\begin{aligned}\underline{\boldsymbol{\psi}}_1 &= \int_0^t (\underline{\boldsymbol{u}}_1 - R_1\underline{\boldsymbol{i}}_1)d\tau,\\ \underline{\boldsymbol{\psi}}_2 &= \frac{L_2}{L_m}(\underline{\boldsymbol{\psi}}_1 - \sigma L_1\underline{\boldsymbol{i}}_1),\end{aligned} \tag{4}$$

where $\sigma = 1 - L_m^2/L_1L_2$ is the leakage factor.

Let us suppose that the simplifying assumptions on which the vector equations of IM are derived are valid in practice. Then, in an ideal case, when all the motor parameters are known, there would be no difference between the magnitude of the estimated rotor flux vector from the current (1) and voltage model (4). If the results from the models differ, it means that there has to be some discrepancy in the motor parameters. Assuming that all motor parameters except the magnetising inductance are known, we can adjust the inductance to minimise the following error:

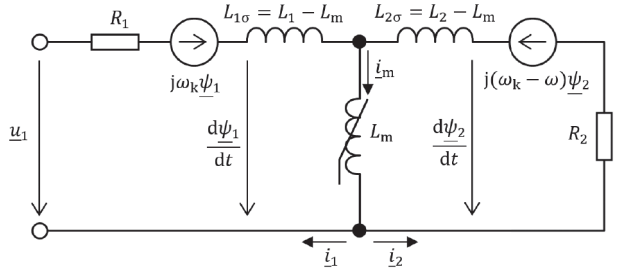

Fig. 1 *T-equivalent circuit of IM*

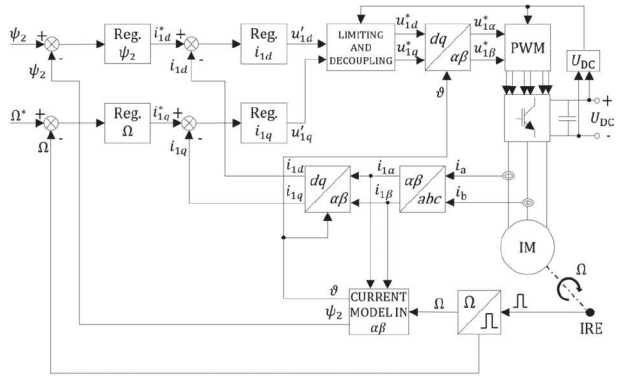

Fig. 2 *Block diagram of direct RFOC*

$$\varepsilon_\psi = \psi_{2VM} - \psi_{2CM}, \tag{5}$$

where ψ_{2VM} and ψ_{2CM} are the amplitudes of the rotor flux vector obtained from (4) and (1), respectively.

To suppress the change of the rotor resistance with temperature, the heavy-load measurements should be made as quickly as possible, and the motor should be cooled by forced convection.

3.3 Improved method

Consider that the IM runs within RFOC and that there is a difference between the measured T and estimated IM torque T_{IM}, i.e.

$$\varepsilon_T = T - T_{IM}. \tag{6}$$

As in the previous section, let us assume the validity of the simplifying assumption for the space-vector theory. Assuming that all parameters except the magnetising inductance are known, this means that the previous error (6) has to depend only on the magnetising inductance, i.e.

$$\varepsilon_T = f(L_m). \tag{7}$$

The following iterative algorithm based on (7) can then be used to obtain the magnetising inductance:

i. Set $k = 0$. Choose an initial value $L_m(k) = L_{m0}$. Choose an incremental inductance ΔL_m; $\Delta L_m \in \mathbb{R}^+$. Specify the minimal tolerance δ; $\delta \in \mathbb{R}^+$.
ii. Calculate $\varepsilon_T(k)$. If $|\varepsilon_T(k)| \le \delta$ then $L_m = L_m(k)$ and the algorithm stops. Otherwise, go to step 3.
iii. If $\varepsilon_T(k) > (\delta/2)$ then calculate $L_m(k+1) = L_m(k) + \Delta L_m$, if $\varepsilon_T(k) < -(\delta/2)$ then calculate $L_m(k+1) = L_m(k) - \Delta L_m$. Increase k by one and go to step 4.

iv. If the convergence is too slow or if the output oscillates, adjust ΔL_{m} by multiplication with relaxation factor $\lambda \in \mathbb{R}^{+}$ and go back to step 2.

It is recommended to average the values of ε_T over multiple sampling periods. After calculating each new inductance, it is also necessary to wait for a few seconds for the drive to reach a new steady-state.

3.4 Reactive-power MRAS for estimation of rotor inverse time constant

To obtain the load-dependent saturation characteristics of IM, it is necessary to carry out measurements in the range of a few per cent of the machine's rated torque to the full machine's rated torque. Measurements at the high load will cause the rotor to heat up, leading to a deterioration in the accuracy of the proposed method.

To overcome the problem of the change of the rotor resistance with the temperature, we propose to implement the estimation of the rotor inverse time constant parallelly to the iteration algorithm. The adopted method is MRAS based on IM reactive power (Q-MRAS) [27–31]. The reference model is given by

$$Q = u_{1\beta} i_{1\alpha} - u_{1\alpha} i_{1\beta}. \tag{8}$$

The adaptive model is given by

$$\hat{Q} = \omega_{\mathrm{s}} L_{\mathrm{l}} \left(i_{1d}^{2} + \sigma i_{1q}^{2} \right). \tag{9}$$

Equation (8) is an expression for instantaneous reactive power, while (9) represents the steady-state reactive power. The synchronous speed can be calculated as

$$\omega_{\mathrm{s}} = \omega + \omega_{\mathrm{slip}}, \tag{10}$$

where ω_{slip} is the electrical slip speed which can be estimated as

$$\omega_{\mathrm{slip}} = \tau_{\mathrm{r0}}^{-1} \frac{i_{1q}}{i_{1d}}. \tag{11}$$

The error for the rotor time constant adaptation mechanism, which is a conventional PI controller, is calculated as

$$\varepsilon_{\tau} = Q - \hat{Q}. \tag{12}$$

The output of the PI controller is the deviation from the initial inverse rotor time constant τ_{r0}^{-1}, i.e.

$$\Delta \tau_{\mathrm{r}}^{-1}(t) = K_{\mathrm{p}} \varepsilon_{\tau}(t) + K_{\mathrm{i}} \int_{0}^{t} \varepsilon_{\tau}(\tau) \mathrm{d}\tau. \tag{13}$$

Finally, the estimated inverse time constant is given by

$$\hat{\tau}_{\mathrm{r}}^{-1} = \tau_{\mathrm{r0}}^{-1} + \Delta \tau_{\mathrm{r}}^{-1}. \tag{14}$$

The block diagram of the Q-MRAS is depicted in Fig. 3.

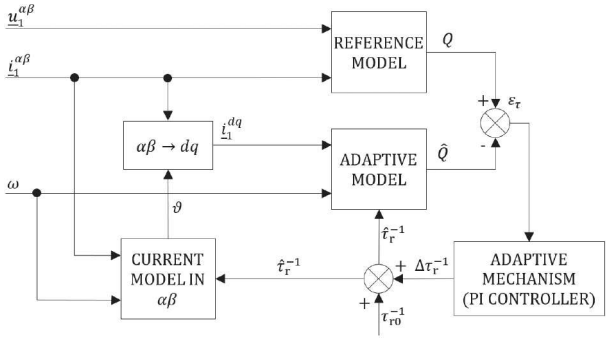

Fig. 3 *Q-MRAS for estimation of inverse rotor time constant*

3.4.1 Practical limitations of Q-MRAS: There are some practical limitations when considering the implementation of the Q-MRAS presented in the previous section. Those were summarised in [30, 31], respectively. The Q-MRAS should be active only if the motor speed and torque are higher than some threshold value. In this paper, the threshold values for the speed and torque were set to 10% of their nominal values.

3.5 Pros and cons of the proposed method

In this section, we shall briefly summarise the advantages and disadvantages of the proposed method. As this paper is intended to improve the method presented in [26] (which will be in the following text addressed as the 'previous method'), differences between those two shall also be emphasised.

3.5.1 Advantages:

i. The method uses the same hardware that is used during the drive regular operation or commissioning.
ii. The method can be automatised if a programmable load is available and if the information about load-torque can be fed into the control algorithm.
iii. The drive runs in the RFOC loop based on the current model (1) in $\alpha\beta$, which is a well-known FOC scheme.
iv. The current model (1) depends only on the magnetising inductance and inverse rotor time constant. Those parameters are calculated or estimated.
v. The current model (1), as opposed to the voltage model (4), is not impaired by the phenomenon of DC offset accumulation during pure integration. Therefore, modified integrators that deteriorate the accuracy of the model are not needed.
vi. The method does not depend on the stator resistance as opposed to the previous method.
vii. It does depend on the rotor resistance; however, the change in the rotor resistance with temperature is considered by estimating the inverse rotor time constant by Q-MRAS. The previous method does not try to compensate for the change of the rotor resistance.

3.5.2 Disadvantages:

i. The method does not work for load torques close to zero because of the Q-MRAS constraints. However, for the light-load measurements, the previous method can be used because the stator and rotor current will be relatively low, which means that the change in the stator and rotor resistance due to the rotor heating will not be significant.
ii. The need for the torque measurement makes the new method more hardware demanding than the previous one. A compromise between the new and previous method would be to implement the rotor time constant estimation into the previous method to eliminate the need for forced cooling. However, there is still the disadvantage of comparing two estimated quantities contrary to the new solution, where an estimated and measurable quantity is compared.
iii. There is still a problem with the uncertainty of the leakage inductances because these are used within the Q-MRAS. The method supposes that the leakage inductances are known accurately or that the effect of their inaccuracy on the output of the method is negligible. Since it is impossible in the case of a T-equivalent circuit to accurately determine the stator and rotor leakage inductance ratio, standardised approaches or rules of thumb have to be used. Also, there is another aspect, and that is the saturation of the rotor leakage inductance for some types of rotor design, as pointed out in [11, 14]. Experimental investigation of this phenomenon seems rather difficult.
iv. The effect of iron losses is neglected. However, it is possible to respect the iron losses in the IM model for the price of more complicated equations.
v. The method assumes that the space-vector theory simplifying assumptions are valid, which, of course, does not apply to a

real machine. It also neglects the effect of higher time and space harmonics. However, in most papers dealing with IM control and parameter estimation, these aspects are usually not taken into account.

vi. Mechanical losses are not taken into account, but in principle, they can be included in the torque equation.

4 Application of the proposed method

4.1 Requirements for initial induction motor parameters

The parameters required for the operation of the iteration algorithm and Q-MRAS are the initial value of the magnetising and leakage inductances and the initial value of the inverse rotor time constant, which is calculated from the initial rotor resistance and rotor inductance.

Any more or less sophisticated method can be used to obtain these parameters. However, since in the case of the current model and the iteration algorithm implementation, these parameters serve only as a starting value, the conventional no-load and locked-rotor test is the obvious choice.

4.2 Q-MRAS parameter update

As for the Q-MRAS, the adaptive model (9) uses the magnetising, stator, and rotor leakage inductances. The problem with the uncertainty of the leakage inductances was briefly acknowledged in Section 3.5.2. The stator inductance is updated using a new value of the magnetising inductance $L_{\mathrm{m}}(k+1)$ as

$$L_{1}(k+1) = L_{\mathrm{m}}(k+1) + L_{1\sigma}, \tag{15}$$

the rotor inductance as

$$L_{2}(k+1) = L_{\mathrm{m}}(k+1) + L_{2\sigma}, \tag{16}$$

and the leakage factor as

$$\sigma(k+1) = 1 - \frac{L_{\mathrm{m}}(k+1)\cdot L_{\mathrm{m}}(k+1)}{L_{1}(k+1)\cdot L_{2}(k+1)}. \tag{17}$$

The estimated inverse rotor time constant includes the rotor inductance, which mostly consists of the magnetising inductance. Therefore, the estimated inverse rotor time constant should vary not only with the rotor temperature but also with the load-independent and load-dependent saturation of IM.

On the one hand, the rotor inductance appears indirectly in the estimated inverse rotor time constant (2), on the other hand, it appears directly in the adaptive model (9) where it is updated according to (16). Strictly speaking, the rotor inductance should appear either as a standalone parameter or as a part of the inverse rotor time constant since the rotor leakage inductance may not be determined accurately, or it may also saturate as the function of the rotor current. In this paper, this discrepancy is neglected since the rotor inductance alone appears only in the leakage factor calculation, and therefore, the effect of the leakage inductance inaccuracy can be neglected [18].

4.3 Compensation of inverter non-linearity

The Q-MRAS reference model (8) uses components of the stator voltage vector in $\alpha\beta$. The inverter output voltage is very hard to measure directly due to its pulsating nature. A common approach to overcome this problem is to use a reference voltage vector within the control algorithm. However, due to the inverter non-linearities, among the most significant ones we can include dead-time and IGBT delayed switching, the fundamental wave of the inverter output voltage does not correspond to the reference voltage.

In this paper, we use a duty-cycle compensation for each leg of the three-phase two-level voltage-source inverter [32]. The relationship between the reference duty-cycle d_x^* and the corrected duty cycle d_x' is given as

$$d_x' = d_x^* + \frac{T_{\mathrm{eff}(x)}}{T_{\mathrm{PWM}}}\mathrm{sgn}(i_x) \quad x = a, b, c, \tag{18}$$

where T_{PWM} is the PWM period, i_x is the respective motor phase current and $T_{\mathrm{eff}(x)}$ is the so-called effective dead-time defined as

$$T_{\mathrm{eff}(x)} = T_{\mathrm{dt}} + T_{\mathrm{on}}(i_x) - T_{\mathrm{off}}(i_x) \quad x = a, b, c, \tag{19}$$

where T_{dt} is the actual dead-time inserted by the microcontroller or driver, $T_{\mathrm{on}}(i_x)$ is the current dependent turn-on time of the IGBT and $T_{\mathrm{off}}(i_x)$ is the current dependent turn-off time of the IGBT. The dependence of the effective dead-time on the collector current (19) was obtained by direct measurement on the inverter.

4.4 Measuring the load-dependent saturation characteristics

Considering the RFOC and steady-state, the d-axis rotor flux can be expressed as

$$\boldsymbol{\psi}_{2d} = \left|\underline{\boldsymbol{\psi}}_{2}\right| = \boldsymbol{\psi}_{2} = L_{\mathrm{m}} i_{1d}. \tag{20}$$

For a given flux, the IM torque can be written as

$$T_{\mathrm{IM}} = \frac{3}{2} p_{\mathrm{p}} \frac{L_{\mathrm{m}}}{L_{2}} \boldsymbol{\psi}_{2d} i_{1q}. \tag{21}$$

Therefore, in this paper, we consider the magnetising inductance as a function of the rotor flux magnitude and torque-producing (q-axis) current component, i.e.

$$L_{\mathrm{m}} = f\left(\left|\underline{\boldsymbol{\psi}}_{2}\right|, i_{1q}\right) = f\left(\boldsymbol{\psi}_{2d}, i_{1q}\right) = f\left(\boldsymbol{\psi}_{2}, i_{1q}\right) \tag{22}$$

The saturation due to the non-linear properties of the magnetic circuit is respected by the dependence $L_{\mathrm{m}} = f(\psi_2)$ and the load-dependent saturation by the dependence $L_{\mathrm{m}} = f(i_{1q})$.

The method can be divided into multiple steps:

i. Initial parameters of the IM are obtained, as discussed in Section 4.1.
ii. RFOC is implemented according to Fig. 2. along with Q-MRAS for the inverse rotor time constant estimation, which was described in Section 3.4.
iii. Inverter non-linearity compensation is implemented, as discussed in Section 4.3.
iv. The motor is running close to the rated speed.
v. The Q-MRAS is started with a set threshold torque.
vi. The dependence (22) should be measured for as many combinations of the rotor flux and torque-producing current as possible. This is done by adjusting the reference flux in the control algorithm along with the torque produced by the variable load.
vii. For the torques lower than the threshold torque set in Q-MRAS, our previous method should be used.

5 Experimental results

5.1 Experimental setup

The RFOC was implemented in C language into TMS320F28335 Delphino DSP. The clock frequency was set to 150 MHz, and the calculation loop of the FOC algorithm was selected to be 200 µs with a 10 kHz PWM. All the experimental data are sampled with 10 ms sampling period. As a drive, a machine set with 12 kW IM coupled with 8.8 kW separately excited DC motor (DCM) was used. The DCM serves as a dynamometer. The nameplate values of the IM and DCM, along with the IM initial model parameters measured by the conventional no-load (for the rated voltage) and locked-rotor test are given in Table 1. A picture of the experimental workplace is shown in Fig. 4.

Table 1 IM and DCM parameters

Induction motor				DC motor	
nominal power	12 kW	R_1	377 mΩ	nominal power	8.8 kW
nominal current	22 A	R_2	225 mΩ	nominal rotor current	38.3 A
nominal voltage	380 V	$L_{1\sigma}$	2.27 mH	nominal rotor voltage	230 V
nominal frequency	50 Hz	$L_{2\sigma}$	2.27 mH	nominal excit. current	2.8 A
nominal PF	0.8	R_{Fe}	202 Ω	nominal excit. voltage	110 V
nominal speed	1460 min^{-1}	L_{m}	82.5 mH	nominal speed	1460 min^{-1}

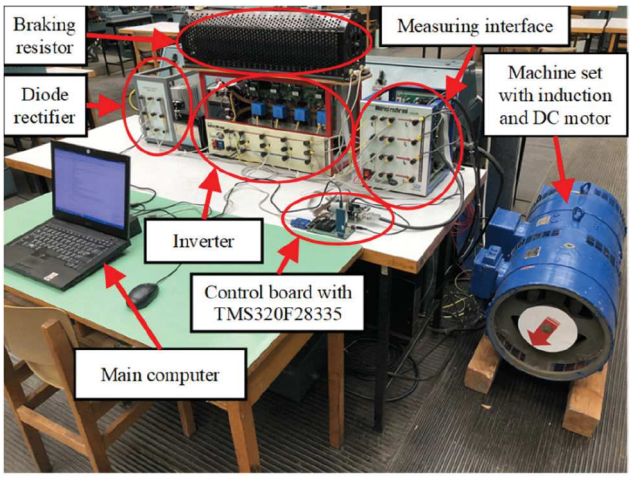

Fig. 4 *Experimental workplace*

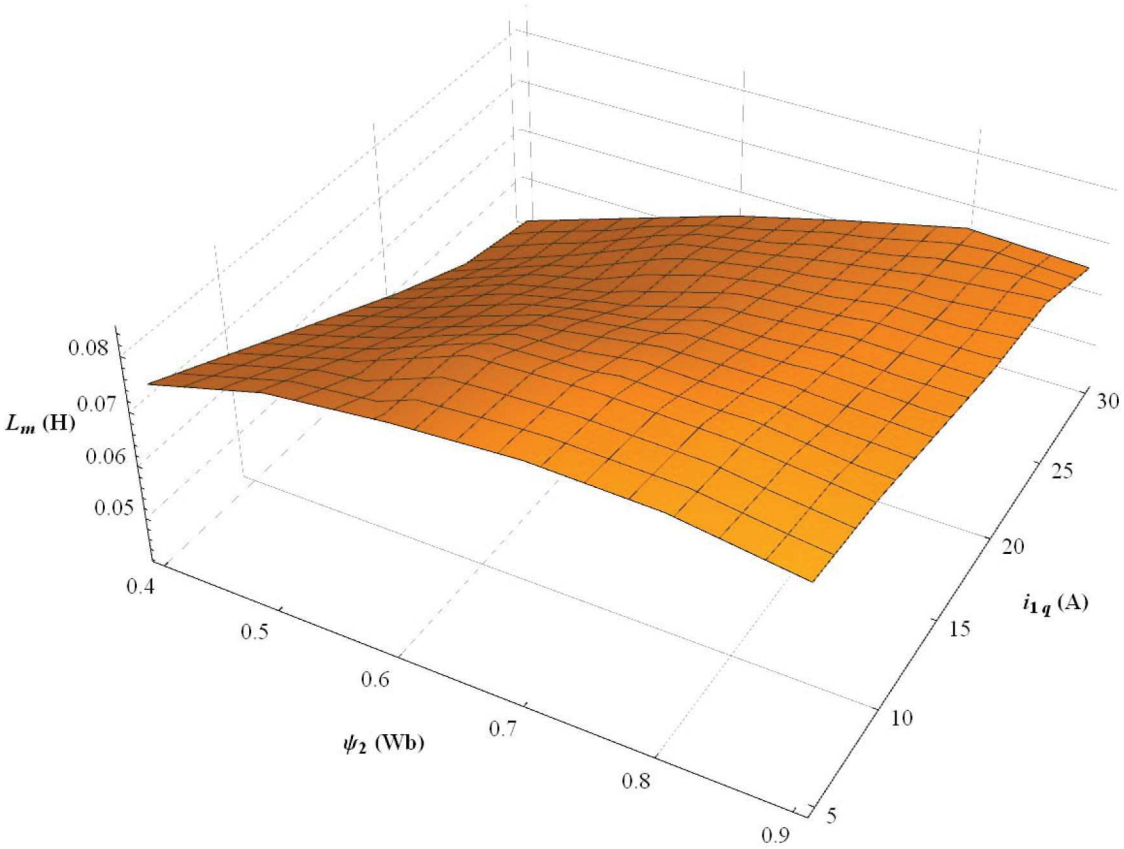

Fig. 5 *Measured dependence* $L_m = f(\psi_2, i_{1q})$

5.2 Measured saturation characteristics

The measured dependence $L_{\mathrm{m}} = f(\psi_2, i_{1q})$ is depicted in the form of a 3D graph in Fig. 5. In the figure, the minimal flux is restricted to 0.4 Wb and the minimal torque-producing current to 5 A. According to the measured characteristics, the magnetising inductance heavily saturates with a load for lower flux levels where the rotor current or slip, respectively, must be high to maintain the torque. The characteristics were implemented as a look-up table.

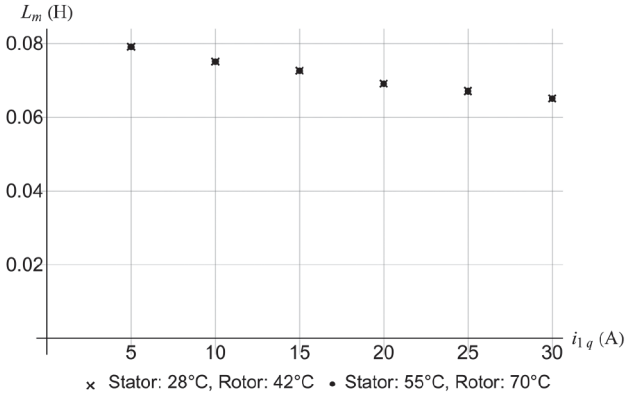

Fig. 6 *Improved method – measured values of $L_m = f(i_{1q})$ for reference rotor flux 0.8 Wb and two different stator and rotor temperatures*

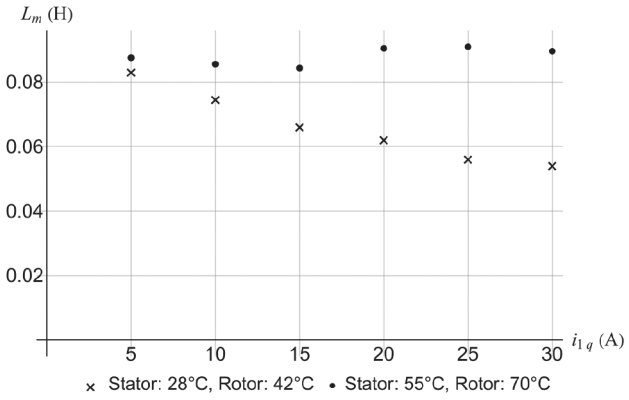

Fig. 7 *Previous method – measured values of $L_m = f(i_{1q})$ for reference rotor flux 0.8 Wb and two different stator and rotor temperatures*

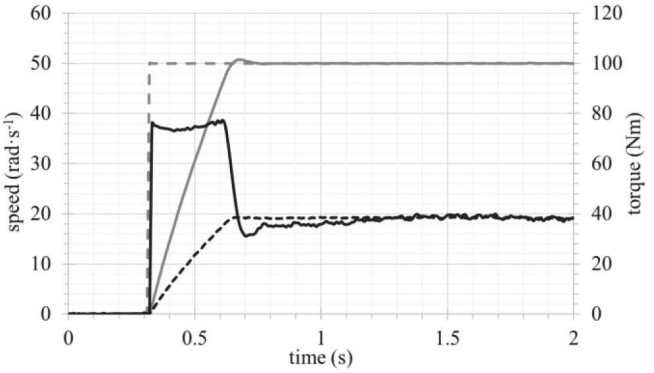

Fig. 8 *Start of the loaded drive from 0 to 50 rad s^{-1} – with L_m and τ_r^{-1} compensation; dashed grey: reference speed, solid grey: measured speed, dashed black: load torque developed by DC dynamometer, solid black: estimated IM torque; reference rotor flux: 0.85 Wb*

5.3 Robustness against thermal changes

To validate the robustness of the improved method against the changes in the rotor resistance, two sets of measurements of the magnetising inductance for two different stator and rotor temperatures were done. In both cases, the reference rotor flux was set to 0.8 Wb.

Fig. 6 shows the measured values for the improved method. The values for both the temperatures are in good accordance, which method robustness against changes in the motor resistance.

Fig. 7 shows the results for the previous method, where, contrary to Fig. 6, change in the stator and rotor winding temperature causes a significant deviation of the measured values.

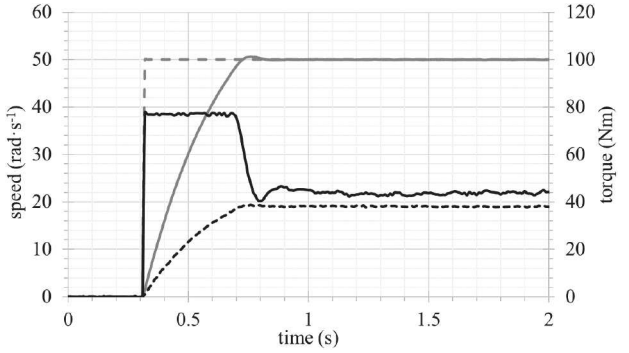

Fig. 9 *Start of the loaded drive from 0 to 50 rad s^{-1} – CPM; dashed grey: reference speed, solid grey: measured speed, dashed black: load torque developed by DC dynamometer, solid black: estimated IM torque; reference rotor flux: 0.85 Wb*

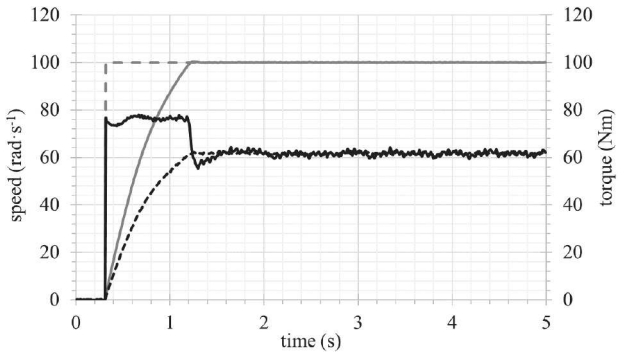

Fig. 10 *Start of the loaded drive from 0 to 100 rad s^{-1} – with L_m and τ_r^{-1} compensation; dashed grey: reference speed, solid grey: measured speed, dashed black: load torque developed by DC dynamometer, solid black: estimated IM torque; reference rotor flux: 0.85 Wb*

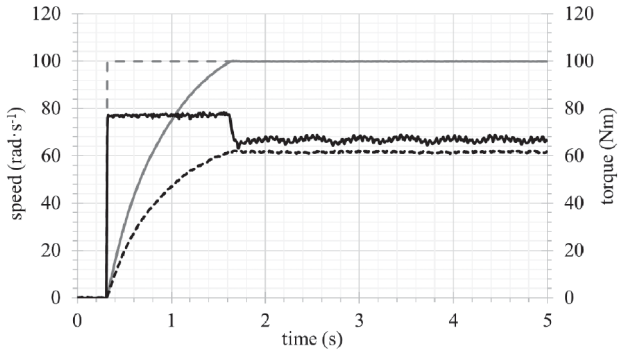

Fig. 11 *Start of the loaded drive from 0 to 100 rad s^{-1} – CPM; dashed grey: reference speed, solid grey: measured speed, dashed black: load torque developed by DC dynamometer, solid black: estimated IM torque; reference rotor flux: 0.85 Wb*

5.4 Comparison against constant parameter model

Figs. 8–13 show the start of the IM drive loaded by DCM for three different reference speed steps: Figs. 8 and 9 – from 0 to 50 rad s^{-1}, Figs. 10 and 11 – from 0 to 100 rad s^{-1} and Figs. 12 and 13 – from 0 to 150 rad s^{-1}. In all the cases, the reference rotor flux is set to 0.85 Wb (corresponding no-load magnetising inductance is 0.0867 H). In Figs. 8, 10, and 12 the magnetising inductance and inverse rotor time constant are compensated. In Figs. 9, 11, and 13, the model uses constant parameters. It can be seen that in the case of the parameter compensation, the start of the drive is always more or less faster. The higher the difference between the initial and final speed, the more significant the difference between the constant parameter model (CPM) and the compensated model. Furthermore, the steady-state measured and estimated torque are in very good accordance in the case of the compensated model as opposed to the

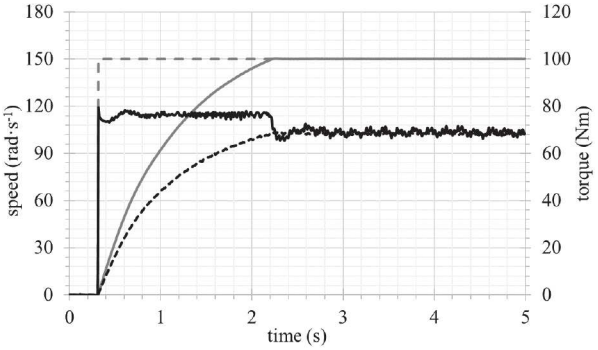

Fig. 12 *Start of the loaded drive from 0 to 150 rad s^{-1} – with L_m and τ_r^{-1} compensation; dashed grey: reference speed, solid grey: measured speed, dashed black: load torque developed by DC dynamometer, solid black: estimated IM torque; reference rotor flux: 0.85 Wb*

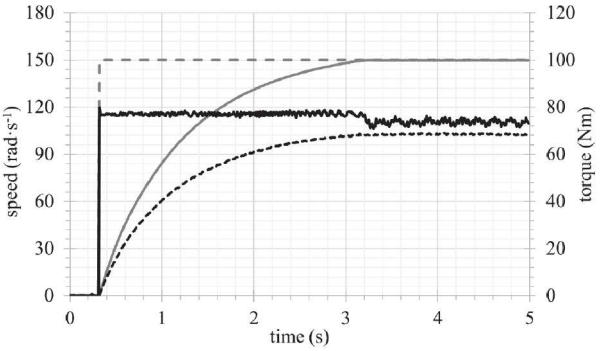

Fig. 13 *Start of the loaded drive from 0 to 150 rad s^{-1} – CPM; dashed grey: reference speed, solid grey: measured speed, dashed black: load torque developed by DC dynamometer, solid black: estimated IM torque; reference rotor flux: 0.85 Wb*

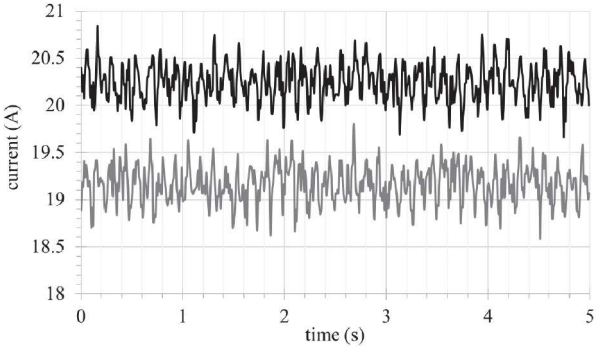

Fig. 14 *Measured current vector amplitude in steady-state – speed: 50 rad s^{-1}, load torque developed by DC dynamometer: 38 Nm; black: CPM, grey: L_m and τ_r^{-1} compensation; reference rotor flux: 0.85 Wb*

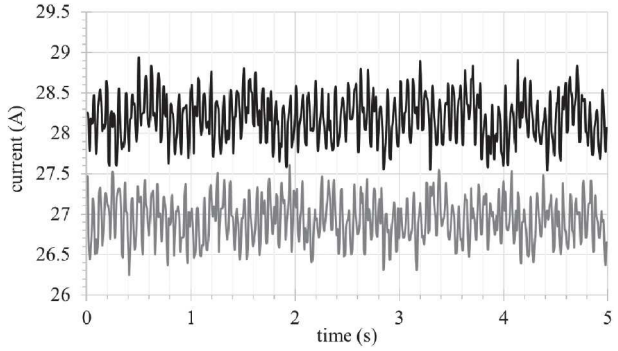

Fig. 15 *Measured current vector amplitude in steady-state – speed: 100 rad s^{-1}, load torque developed by DC dynamometer: 60 Nm; black: CPM, grey: L_m and τ_r^{-1} compensation; reference rotor flux: 0.85 Wb*

CPM, where an error between the estimated and measured torque exists. In the case of the compensated model, a slight ripple in the

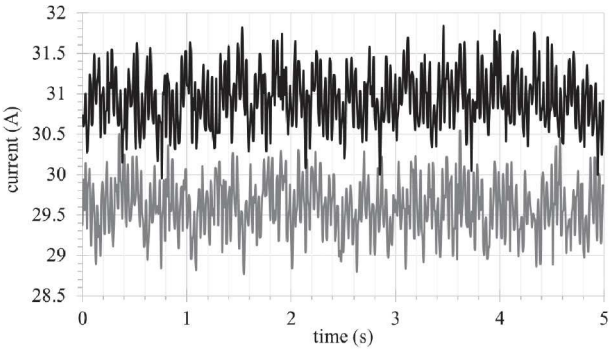

Fig. 16 *Measured current vector amplitude in steady-state – speed: 150 rad s^{-1}, load torque developed by DC dynamometer: 68 Nm; black: CPM, grey: L_m and τ_r^{-1} compensation; reference rotor flux: 0.85 Wb*

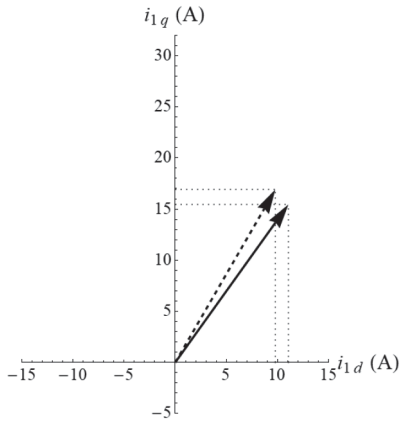

Fig. 17 *Current vector diagram in dq – speed: 50 rad s^{-1}, load torque developed by DC dynamometer: 38 Nm; dashed: CPM, solid: L_m and τ_r^{-1} compensation; reference rotor flux: 0.85 Wb*

calculated torque exists due to the continuous recalculation of the magnetising inductance based on the bilinear interpolation.

Another important consequence of the parameter detuning is shown in Figs. 14–16, where the measured amplitudes of the stator current vector are shown for the corresponding steady-speed cases in Figs. 8–13. In the case of the CPM, the amplitude of the current is higher in all the cases with the average difference around 1 A. Therefore, proper parameter identification and compensation can lead to energy savings because for the same reference flux and speed the drive controlled by the compensated model draws lower current.

Figs. 17–19 shows the current vector diagram for the cases corresponding to Figs. 14–16. The single-value current components are obtained by averaging per 5 s window. In the case of CPM, the flux controller demands lower flux-producing current component which, because of the saturation, produces lower flux than the reference one and, therefore, the speed controller has to demand higher torque-producing current component to maintain the same

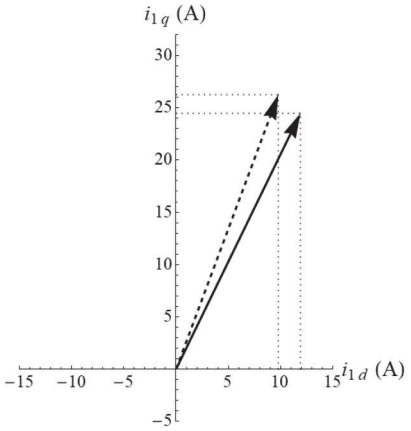

Fig. 18 *Current vector diagram in dq – speed: 100 rad s^{-1}, load torque developed by DC dynamometer: 60 Nm; dashed: CPM, solid: L_m and τ_r^{-1} compensation; reference rotor flux: 0.85 Wb*

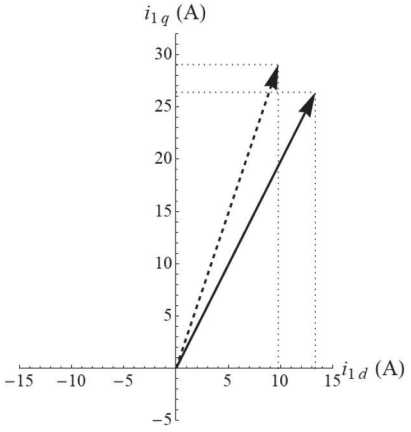

Fig. 19 *Current vector diagram in dq – speed: 150 rad s^{-1}, load torque developed by DC dynamometer: 68 Nm; dashed: CPM, solid: L_m and τ_r^{-1} compensation; reference rotor flux: 0.85 Wb*

torque, which is the cause of the higher current drawn from the source.

6 Conclusion

Load-dependent saturation of an IM is a phenomenon that is often neglected but which, if not considered, can deteriorate the behaviour of the IM drive controlled by the modern control strategies.

In this paper, a novel experimental method for identification of the load-dependent saturation of IM, which respects the variation of the inverse rotor time constant, was presented. The proposed method is intended to be an improved version of our previous method. The main advantages are that the new method does not require knowledge of the stator resistance. Secondly, it respects the variation of the rotor resistance by estimating the inverse rotor time constant and, thirdly, compares the IM estimated quantity (estimated torque) to a measurable quantity (load torque).

According to the experimental results, compared to the constant-parameter model, the compensation of the load-dependent saturation based on the measured values by our proposed method along with the compensation of the inverse rotor time constant by Q-MRAS show improvement of the drive static and dynamic behaviour.

7 Acknowledgments

The research described in this paper was supported by the Student Grant Competition of the Czech Technical University in Prague under grant no. SGS20/062/OHK3/1T/13.

8 References

[1] Levi, E., Lamine, A., Cavagnino, A.: 'Impact of stray load losses on vector control accuracy in current-fed induction motor drives', *IEEE Trans. Energy Convers.*, 2006, **21**, (2), pp. 442–450

[2] Chatterjee, D.: 'A simple leakage inductance identification technique for three-phase induction machines under variable flux condition', *IEEE Trans. Ind. Electron.*, 2012, **59**, (11), pp. 4041–4048

[3] Sokola, M., Levi, E.: 'Combined impact of iron loss and main flux saturation on operation of vector controlled induction machines'. 1996 Sixth Int. Conf. on Power Electronics and Variable Speed Drives, Nottingham, UK, 1996, pp. 36–41

[4] Zaky, M.S., Khater, M.M., Shokralla, S.S., *et al.*: 'Wide speed range estimation with online parameter identification schemes of sensorless induction motor drives', *IEEE Trans. Ind. Electron.*, 2009, **56**, (5), pp. 1699–1707

[5] Levi, E., Wang, M.: 'A speed estimator for high performance sensorless control of induction motors in the field-weakening region', *IEEE Trans. Power Electron.*, 2002, **17**, (3), pp. 365–378

[6] Shen, G., Yao, W., Chen, B., *et al.*: 'Auto measurement of the inverter output voltage delay curve to compensate for inverter nonlinearity in sensorless motor drives', *IEEE Trans. Power Electron.*, 2014, **29**, (10), pp. 5542–5553

[7] Levi, E.: 'Main flux saturation modeling in double-cage and deep-bar induction machines', *IEEE Trans. Energy Convers.*, 1996, **11**, (2), pp. 305–311

[8] Tataru, L.L.: 'A flux-based expression of induction machine magnetizing inductance', *IEEE Trans. Energy Convers.*, 2010, **25**, (1), pp. 268–270

[9] Rasmussen, H., Knudsen, M., Tonnes, M.: 'Parameter estimation of inverter and motor model at standstill using measured currents only'. Proc. IEEE Int. Symp. Ind. Electron., Warsaw, Poland, 1996, pp. 331–336

[10] Levi, E., Kola, M., Vukosavic, S.N.: 'A method for magnetizing curve identification in rotor flux oriented induction machines', *IEEE Trans. Energy Convers.*, 2000, **15**, (2), pp. 157–162

[11] Tuovinen, T., Hinkkanen, M., Luomi, J.: 'Modeling of saturation due to main and leakage flux interaction in induction machines', *IEEE Trans. Ind. Appl.*, 2010, **46**, (3), pp. 937–945

[12] Gerada, C., Bradley, K., Sumner, M., *et al.*: 'Evaluation and modelling of cross saturation due to leakage flux in vector controlled induction machines'. IEEE Int. Electric Machines and Drives Conf., Madison, WI, USA, 2003, pp. 1983–1989

[13] Klaes, N.R.: 'Parameter identification of an induction machine with regard to dependencies on saturation', *IEEE Trans. Ind. Appl.*, 2003, **29**, (6), pp. 1135–1140

[14] Hinkkanen, M., Repo, A., Luomi, J.: 'Influence of magnetic saturation on induction motor model selection'. Proc. ICEM'06, Chania, Greece, September 2006

[15] Immonen, P., Ruuskanen, V., Nerg, J., *et al.*: 'Inductance saturation of the induction machine as a function of stator voltage and load with steady state AC magnetic finite element solver'. Int. Review of Modeling and Simulation (IREMOS), 2004, 7, (3)

[16] Nerg, J., Pyrhonen, J., Partanen, J.: 'Finite element modeling of the magnetizing inductance of an induction motor as a function of torque', *IEEE Trans. Magn.*, 2004, **40**, (4), pp. 2047–2049

[17] Ranta, M., Hinkkanen, M.: 'Online identification of parameters defining the saturation characteristics of induction machines', *IEEE Trans. Ind. Appl.*, 2013, **49**, (5), pp. 2136–2145

[18] Liu, L., Guo, Y., Wang, J.: 'Online identification of mutual inductance of induction motor without magnetizing curve'. 2018 Annual American Control Conf. (ACC), Milwaukee, WI, USA, 2018, pp. 3293–3297

[19] Bertoluzzo, M., Buja, G.S., Menis, R.: 'Self-commissioning of RFO IM drives: one-test identification of the magnetization characteristic of the motor', *IEEE Trans. Ind. Appl.*, 2001, **37**, (6), pp. 1801–1806

[20] Zigliotto, M., Carraro, M.: 'Automatic parameter identification of inverter-fed induction motors at standstill', *IEEE Trans. Ind. Electron.*, 2014, **61**, (9), pp. 4605–4613

[21] Bellini, A., Bifaretti, S.: 'A method for magnetizing curve identification in vector controlled induction motor drives'. Proc. Int. SPEEDAM, Taormina, Italy, May 2006, pp. 955–959

[22] He, Y., Wang, Y., Feng, Y., *et al.*: 'Parameter identification of an induction machine at standstill using the vector constructing method', *IEEE Trans. Power Electron.*, 2012, **27**, (2), pp. 905–915

[23] Wang, K., Yao, W., Chen, B., *et al.*: 'Magnetizing curve identification for induction motors at standstill without assumption of analytical curve functions', *IEEE Trans. Ind. Electron.*, 2015, **62**, (4), pp. 2144–2155

[24] Jiayang, R., Shanming, W.: 'Estimation of saturation characteristic of induction motors by injecting sinusoidal currents with customized low frequency'. 17th Int. Conf. on Electrical Machines and Systems (ICEMS), Hangzhou, China, 2014, pp. 3166–3174

[25] Kalamen, L., Rafajdus, P., Sekerak, P., *et al.*: 'A novel method of magnetizing inductance investigation of self-excited induction generators', *IEEE Trans. Magn.*, 2012, **48**, (4), pp. 1657–1660

[26] Lipcak, O., Bauer, J., Kobrle, P.: 'Offline method for determination of non-linear dependence of machine magnetising inductance utilising parallel operation of current and voltage model', *IET Power Electron.*, 2019, **12**, (11), pp. 2843–2850

[27] Maiti, S., Chakraborty, C., Hori, Y., *et al.*: 'Model reference adaptive controller-based rotor resistance and speed estimation techniques for vector controlled induction motor drive utilizing reactive power', *IEEE Trans. Ind. Electron.*, 2008, **55**, (2), pp. 594–601

[28] Cao, P., Zhang, X., Yang, S.: 'A unified-model-based analysis of MRAS for online rotor time constant estimation in an induction motor drive', *IEEE Trans. Ind. Electron.*, 2017, **64**, (6), pp. 4361–4371
[29] Cao, P., Zhang, X, Yang, S., *et al.*: 'Reactive-power-based MRAS for online rotor time constant estimation in induction motor drives', *IEEE Trans. Power Electron.*, 2017, **33**, (12), pp. 10835–10845
[30] Mapelli, F.L., Bezzolato, A., Tarsitano, D.: 'A rotor resistance MRAS estimator for induction motor traction drive for electrical vehicles'. XXth Int. Conf. on Electrical Machines, Marseille, France, 2012, pp. 823–829
[31] Mapelli, F.L., Tarsitano, D., Cheli, F.: 'A rotor resistance MRAS estimator for EV induction motor traction drive based on torque and reactive stator power: simulation and experimental results'. Int. Conf. on Electrical Machines (ICEM), Berlin, Germany, 2014, pp. 31–37
[32] Lipcak, O., Bauer, J.: 'Analysis of voltage distortion and comparison of two simple voltage compensation methods for sensorless control of induction motor'. IEEE Int. Symp. on Sensorless Control for Electrical Drives, Torino, Italy, September 2019

APPENDIX C

LIPČÁK, O.; BAUER, J.; KOBRLE, P. “Offline Method for Determination of Nonlinear Dependence of Induction Machine Magnetising Inductance Utilising Parallel Operation of Current and Voltage Model“, *IET Power Electronics*. 2019, ISSN 1755-4543. doi: 10.1049/iet-pel.2018.6321

Author’s contribution: method implementation supervision, analysis of measured results, experiment proposal, paper co-writing

IET Power Electronics

Research Article

IET Journals
The Institution of Engineering and Technology

Offline method for determination of non-linear dependence of machine magnetising inductance utilising parallel operation of current and voltage model

ISSN 1755-4535
Received on 6th December 2018
Revised 13th June 2019
Accepted on 17th June 2019
doi: 10.1049/iet-pel.2018.6321
www.ietdl.org

Ondrej Lipcak[1] ✉, *Jan Bauer*[1], *Pavel Kobrle*[1]

[1]*Department of Electric Drives and Traction, Czech Technical University in Prague, Prague, Czech Republic*

✉ *E-mail: lipcaond@fel.cvut.cz*

Abstract: The simplest mathematical models of the induction motor (IM) use the presumption of the machine's linear magnetising characteristics. However, this may hold only in a limited operating range of the electric drive. It is well known that the magnetising inductance saturates as a function of the magnetising current due to the non-linear properties of the magnetic circuit. However, this is not the only type of saturation. Depending on the design of the rotor, the machine's magnetising and leakage inductances may also saturate as a function of the rotor current. A new experimental method is proposed here. It identifies the dependence of the *T* equivalent circuit magnetising inductance on the rotor flux and torque producing current component using parallel operation of the so-called current and voltage model of the IM.

1 Introduction

The advancement of the induction motor (IM) control strategies goes hand in hand with the progress in the area of IM mathematical modelling and with the development of the digital signal processors (DSP), where, based on the mathematical model of the IM, inner variables of the IM such as flux, torque, or speed are calculated. The simplest models of IM are based on its equivalent circuits, where the machine parameters such as inductances and resistances are often considered to be constant [1–4]. Although this simplification may be sufficient for open-loop applications, in the case of high dynamics field-oriented control (FOC) or sensorless schemes, this presumption may lead to the reduced accuracy and stability of the control [4, 5]. The mismatch between the actual parameters of the machine and its mathematical model leads to an incorrect estimation of the controlled machine quantities. The magnetising inductance has a significant influence on the accuracy of the rotor flux estimation and in connection with the unknown and temperature-dependent rotor and stator resistance causes misalignment of the flux vector position and amplitude [4]. As a result, it degrades the estimation of torque and thus destabilises the control.

The easiest method of obtaining parameters for the IM model is the indirect calculation from the measured voltages and currents during a no-load and locked-rotor test [6]. The only parameter of the squirrel cage IM equivalent circuit that can be measured directly is the stator resistance. Moreover, the magnetising inductance that is usually calculated indirectly varies with respect to the magnetising current. The dependence of the magnetising inductance on the magnetising current can be easily explained by the non-linear behaviour of the ferromagnetic circuit and can be obtained using the conventional no-load test of IM. There are mathematical models considering this type of saturation of the machine in the literature [1, 4, 7–10]. However, it has been noted that the magnetising inductance may also significantly depend on the rotor current, especially when the rotor bars are skewed and the rotor slots are closed [11–15]. Furthermore, such a rotor arrangement can also lead to an intense saturation of the rotor leakage inductance with respect to the rotor current. If the geometry and the material specification of the machine are known, finite element analysis (FEA) can be used to model all the presented types of the magnetising inductance saturation [11, 15–17]. However, sometimes the geometry and the precise material specification of the machine are unknown, and, therefore, an experimental identification is needed.

In [18], small signal model of IM considering the saturation of the magnetising and rotor leakage inductance was used for estimation of IM parameters based on the time–stepping FEA. It has been shown that if the magnetising inductance is considered to saturate only as the function of the magnetising current as in [19], then the model only fits well at the lowest frequencies.

This paper aims to present an experimental offline method of identifying the dependence of the *T* equivalent circuit magnetising inductance on the reference value of the rotor flux linkage vector and torque producing current component. It belongs to a group of methods using a frequency converter such as those presented in [20, 21]. It is based on the parallel operation of the so-called current and voltage model of IM. The proposed strategy utilises information from the two independent IM models and adjusts the inductance value until the results of both models are comparable. The method is relatively simple to implement because it is based on the two well-known IM models for the rotor flux estimation, and it also utilises the same hardware that is used during the normal drive operation. Another advantage is that it can be automatised if a programmable load is available.

Magnetising inductance variation and its influence on the IM drive behaviour presented in this paper was experimentally verified by means of the stability and accuracy of the rotor flux model reference adaptive system (RFMRAS) sensorless control of 12 kW IM drive. The experimental results show that the proposed identification of the magnetising inductance, among others, significantly improves the estimation of the currents, which can be important, e.g. for predictive control strategies [22, 23].

2 Field-oriented control

The key idea of the FOC of the IM is to convert the three-phase machine into a control structure that is formally identical to the one of separately excited DC machine. Fig. 1 shows the basic FOC block diagram. The IM control is performed in a coordinate system rotating synchronously. The real axis *d* is chosen to coincide with the rotor flux vector. The imaginary axis *q* is then perpendicular to the flux vector. The stator current vector $\underline{i}_1$ is decomposed into a so-called flux producing component i_{1d} and torque producing component i_{1q} that, in this reference frame, are DC values. This is carried out mathematically as a multi-step process. First,

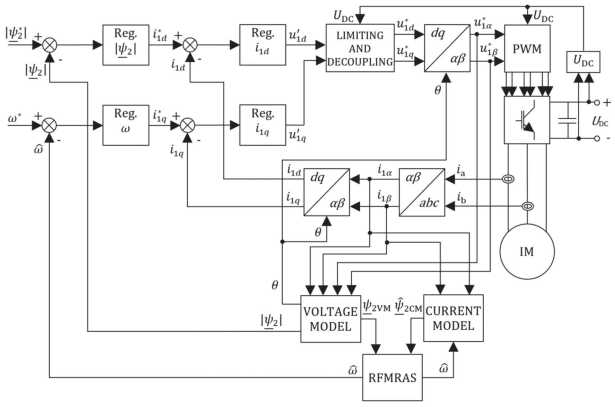

Fig. 1 *Block diagram of rotor flux MRAS sensorless FOC*

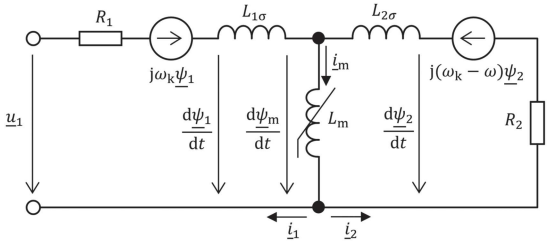

Fig. 2 *T equivalent circuit of an induction motor*

prerequisites that ensure acceptable mathematical complexity of the problem are formed. These usually include the presumption of non-variant machine parameters such as constant resistances and self- and mutual inductances. Also, the magnetic circuit is considered to be lossless, and the machine is considered to be geometrically symmetrical with sinusoidal windings evenly spread around the uniform smooth air gap. Also, the rotor quantities are recalculated onto the stator side. The three-phase quantities are transformed by Clarke and Park transform into a reference frame rotating with an arbitrary angular velocity ω_k with respect to the stator. The transforms reduce the number of equations and remove the periodic dependence of the stator and rotor mutual inductances. After that, the basic IM equations in the arbitrary reference frame are obtained

$$\begin{aligned}
\underline{u}_1 &= R_1\underline{i}_1 + \frac{\mathrm{d}\underline{\psi}_1}{\mathrm{d}t} + \mathrm{j}\omega_k\underline{\psi}_1 \\
\underline{u}_2 &= 0 = R_2\underline{i}_2 + \frac{\mathrm{d}\underline{\psi}_2}{\mathrm{d}t} + \mathrm{j}(\omega_k - \omega)\underline{\psi}_2 \\
\underline{\psi}_1 &= L_1\underline{i}_1 + L_m\underline{i}_2 \\
\underline{\psi}_2 &= L_2\underline{i}_2 + L_m\underline{i}_1,
\end{aligned} \tag{1}$$

where $\underline{\psi}_1$ and $\underline{\psi}_2$ are the stator and rotor magnetic flux space vectors, respectively, $\underline{u}_1$ and $\underline{u}_2$ are the stator and rotor voltage space vectors, respectively, $\underline{i}_1$ and $\underline{i}_2$ are the stator and rotor current space vectors, respectively, R_1 and R_2 are the stator and rotor resistances, respectively, ω_k is the electrical angular speed of the reference frame, ω is the rotor electrical angular speed, L_m is the magnetising inductance and the symbol j marks imaginary unit. A squirrel cage rotor is considered, therefore, $\underline{u}_2 = 0$. The stator inductance L_1 is defined as $L_1 = L_m + L_{1\sigma}$, where $L_{1\sigma}$ is the stator leakage inductance and the rotor inductance L_2 as $L_2 = L_m + L_{2\sigma}$, where $L_{2\sigma}$ is the rotor leakage inductance. The magnetising current vector is defined according to the scheme in Fig. 2 as $\underline{i}_m = \underline{i}_1 + \underline{i}_2$ and the magnetising flux space vector as $\underline{\psi}_m = L_m\underline{i}_m$. Equations (1) describe the so-called *T* equivalent circuit depicted in Fig. 2. If the saturation of the magnetising inductance is considered, then it is necessary to complete (1) with an equation respecting this dependence. In this paper, it is assumed that the magnetising inductance can be expressed as a function of the rotor flux magnitude and torque producing current component, i.e.

$$L_m = f\left(\left|\underline{\psi}_2\right|, i_{1q}\right). \tag{2}$$

2.1 Models of induction motor

There are many possible orientations of FOC strategies. The one most commonly used that is also considered throughout this paper is the rotor flux linkage vector orientation (RFOC). Therefore, the modelling aims to form a set of differential equations with the rotor flux space vector as the unknown variable and measurable quantities such as currents, voltages, or speed as the independent input variables. Two important mathematical models used within the control structure can be derived out of the basic IM (1). The models are expressed in the stator reference frame ($\omega_k = 0$). The real and imaginary axis of this frame is denoted as α and β, respectively.

The first model, known as the current model (subscript CM), is represented by the following vector equation:

$$\frac{\mathrm{d}\underline{\psi}_{2\mathrm{CM}}}{\mathrm{d}t} = \frac{L_m R_2}{L_2}\underline{i}_1 - \frac{R_2}{L_2}\underline{\psi}_{2\mathrm{CM}} + \mathrm{j}\omega\underline{\psi}_{2\mathrm{CM}}. \tag{3}$$

In this case, the input variables are the stator current vector and the electrical angular speed of the rotor.

The second model, known as the voltage model (subscript VM), is represented by the following vector equation:

$$\frac{\mathrm{d}\underline{\psi}_{2\mathrm{VM}}}{\mathrm{d}t} = \frac{L_2}{L_m}\left(\underline{u}_1 - R_1\underline{i}_1 - \sigma L_1\frac{\mathrm{d}\underline{i}_1}{\mathrm{d}t}\right), \tag{4}$$

where σ is the leakage factor defined as $\sigma = 1 - L_m^2/L_1L_2$. Here, the input variables are stator the current and voltage vectors.

For an inner motor torque, the following equation can be derived

$$T_i = \frac{3}{2}p_p\frac{L_m}{L_2}\left|\underline{\psi}_2\right|i_{1q}, \tag{5}$$

where p_p denotes pole-pairs of the machine. For the magnitude of the rotor magnetic flux space vector, the following equation is valid in a steady state

$$\left|\underline{\psi}_2\right| = L_{\mathrm{m}} i_{1d}\,. \tag{6}$$

The torque and flux producing current components are separately regulated, decoupled and afterwards, the reference stator voltage vector $\underline{u}_1^*$ that is an output from the current controllers is fed to the modulator. In this case, the direct FOC has been used.

2.2 Estimation of speed utilising rotor flux model reference adaptive system

There are multiple MRAS schemes based on different motor quantities [24], although the principle is the same—one model serves as a reference model that does not require the estimated quantity as an input (the rotor speed in our case) and the other model serves as an adaptive model that uses the estimated quantity as feedback [25]. The models are evaluated parallelly. Then, Popov's criterion of hyperstability is applied to the MRAS system. In this way, we obtain an expression for an error variable that is fed into an adaptive mechanism, which is a conventional PI controller whose output is the desired estimated quantity [26].

In this paper, the rotor flux linkage MRAS depicted in Fig. 3 is used. The voltage model (4) is used as the reference model and the CM (3) as the adaptive one. It can be derived that the error to be minimised by the PI controller is as follows

$$\varepsilon = \hat{\psi}_{2\alpha\mathrm{CM}}\psi_{2\beta\mathrm{VM}} - \hat{\psi}_{2\beta\mathrm{CM}}\,\psi_{2\alpha\mathrm{VM}}, \tag{7}$$

where the symbols with circumflex denote the output values of the adaptive model.

The output of the PI controller, i.e. the estimated speed, is calculated as

$$\hat{\omega}(t) = K_p\varepsilon(t) + K_i\int_0^t \varepsilon(\tau)\mathrm{d}\tau\,. \tag{8}$$

3 Induction machine saturation

Conventionally, the magnetising inductance is considered to saturate only as a function of the magnetising current. However, the main and the rotor leakage flux may also saturate as a function of the rotor current. References [11, 14] summarise that this dependency is caused mainly by skewing of rotor slots that produces an interaction between the main flux and the rotor leakage flux. This effect can be further aggravated if the rotor slots are closed.

3.1 Flux linkage models

The disadvantage of the *T* model is that it is over parameterised [14]. Furthermore, the method of distributing the measured leakage inductance between the stator and the rotor side is unclear. These problems can be surmounted by other flux linkage models such as Γ or inverse-Γ model. The inverse-Γ model (Fig. 4) places the total leakage inductance onto the stator side and the Γ (Fig. 5) onto the rotor side. Table 1 presents the scaling coefficients for both models.

3.2 Selection of equivalent circuit

It is clear that the parameters of the Γ and the inverse-Γ model depend on the respective coupling factors [14, 27]. Reference [14] suggests that the parameter variations of the Γ model or the T model are generally easier to model due to the strong and complicated dependence of the inverse-Γ circuit coupling factor k_{r} on the rotor current that also causes the dependence of the rotor resistance R_{r} on the operating point. Γ model is particularly suitable for stator flux oriented FOC [2] and its use would introduce a computational burden during the scaling calculations, therefore, despite its disadvantages, T equivalent circuit has been selected for the FOC implementation.

3.3 Proposed method

As mentioned in the introduction, it is impossible to measure the inductances directly. The inductances are usually calculated from the measured currents and voltages obtained during different operating points of the machine. If the geometry of the machine is known, it is possible to analyse the saturation of the magnetising inductance either with respect to the magnetising or rotor current with FEA.

3.4 Requirement for initial induction motor parameters

Initial measurements must be carried out to enable the operation of the proposed scheme. It is necessary to obtain all the T equivalent model parameters including stator and rotor resistances. The resistances should be measured as accurately as possible while keeping the winding temperature at an ambient level. The accuracy of the acquisition of the magnetising inductance is not crucial because in the context of the proposed method it serves only as a starting point. The magnitude of leakage inductance is usually only a few percent of the magnetising inductance, so it can be expected that some small relative errors will not significantly influence results.

As for the preliminary measurements, conventional no-load and locked-rotor tests have been performed. The stator resistance has

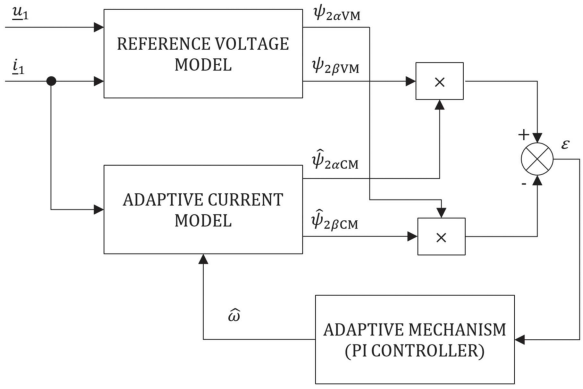

Fig. 3 *Rotor flux MRAS*

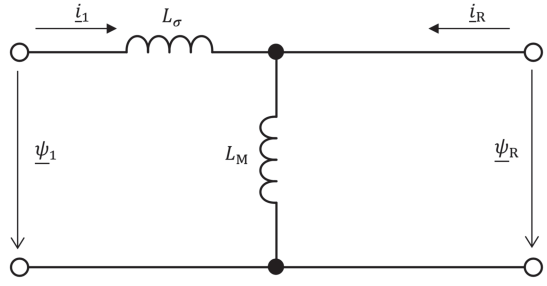

Fig. 4 *Flux linkage inverse-Γ equivalent circuit of an induction motor*

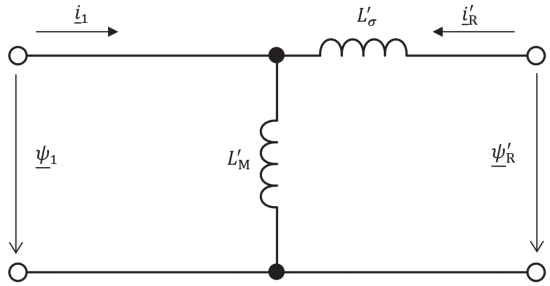

Fig. 5 *Flux linkage Γ equivalent circuit of an induction motor*

Table 1 Scaling coefficient and scaled parameters for Γ and inverse-Γ equivalent circuits

	Coupling factor	Scaled rotor flux linkage	Scaled rotor current	Scaled magnetising inductance	Scaled rotor resistance	Total leakage inductance
inverse-Γ model	$k_r = L_m/L_2$	$\underline{\psi}_r = k_r\underline{\psi}_2$	$\underline{i}_r = \underline{i}_2/k_r$	$L_m = k_r L_m$	$R_r = k_r^2 R_2$	$L_\sigma = L_{1\sigma} + k_r L_{2\sigma}$
Γ model	$k_s = L_m/L_1$	$\underline{\psi}'_r = \underline{\psi}_2/k_s$	$\underline{i}'_r = k_s\underline{i}_2$	$L'_m = L_m/k_s$	$R'_r = R_2/k_s^2$	$L'_\sigma = L_{1\sigma}/k_s + L_{2\sigma}/k_s^2$

Table 2 Induction motor and DC motor parameters

Induction motor				DC motor	
nominal power	12 kW	R_1	377 mΩ	nominal power	8.8 kW
nominal current	22 A	R_2	225 mΩ	nominal rotor current	38.3 A
nominal voltage	380 V	$L_{1\sigma}$	2.27 mH	nominal rotor voltage	230 V
nominal frequency	50 Hz	$L_{2\sigma}$	2.27 mH	nominal field current	2.8 A
nominal PF	0.8	R_{Fe}	202.1 Ω	nominal field voltage	110 V
nominal speed	1400 min^{-1}	L_m	82.5 mH	nominal speed	1400 min^{-1}

been measured by Ohm's method. The obtained results are given in Table 2.

3.5 Method explanation

The proposed method utilises the RFMRAS sensorless direct FOC scheme. The philosophy behind the method is that, physically, there must exist one value of the magnitude of the rotor magnetic flux space vector in the system. Therefore, if the outputs from the current and voltage model are different, it has to mean that there is a mismatch in some of the motor parameters. So, under the presumption that the stator and rotor resistances and the leakage inductances are known with sufficient accuracy then the dissimilar approximation of the estimated quantity from both of the models must be caused by an incorrect value of the magnetising inductance in the specific operating point.

The main objective is to find such value of the magnetising inductance at which both voltage and CM will yield the same approximation of the rotor flux. This has to be carried out for multiple references of the rotor flux and at the same time for multiple loading torques of the motor from zero to (ideally) rated one because the magnetising inductance also depends on the non-measurable rotor current or load torque, respectively. The magnetising inductance is, therefore, corrected with respect to the reference value of the torque producing current component because it is impossible to measure the rotor current of the squirrel cage motor directly. This selection can be justified by the results from [15, 16] and also by (5) and (6) because, for a given set point of the rotor flux, the torque is proportional to the torque producing current component.

During the measurement, the influence of change or uncertainty of the other machine parameters must be suppressed as much as possible. The stator and rotor resistances were kept during the measurement close to the measured values by a forced air convection. The measured leakage inductances and their stator to rotor ratio, which was chosen to be 1:1, are treated as constant. This is due to the fact that the stator leakage inductance is not expected to change much [11, 14] and the value of the leakage inductance is typically only a few percent of the magnetising one.

4 Acquisition of stator voltage

Accurate information about the actual stator voltage vector is essential for the voltage model. Basically, the stator voltage cannot be measured directly because it is formed by the space vector modulation (SVM) of two-level voltage-source inverter (VSI) (Fig. 6) [28]. One possible technique is to reconstruct the stator voltage vector from the measured DC-link voltage and microcontroller's output logical signals for VSI drivers [1]. Another method is to use a reference value of the stator vector, i.e. the input to the modulator as an input to the voltage model [28]. This technique, although simple, requires proper compensation of the VSI most significant non-idealities such as dead-time, finite switching characteristics of the IGBTs and their voltage drop. The mean value of the distorted inverter line-to-neutral voltage (u_{x0} in Fig. 6) considering dead-time and finite IGBT switching can be expressed as

$$U_{AV(x)} = U_{AV0(x)} - \frac{1}{T_{PWM}} U_{DC} T_{eff} \mathrm{sgn}(i_x) \quad x = a, b, c, \tag{9}$$

where U_{AV} is the actual mean value of the inverter line-to-neutral voltage, U_{AV0} is the ideal inverter line-to-neutral voltage without the distortion, T_{PWM} is the period of the PWM, U_{DC} is the DC-link voltage, i_x denotes the respective phase currents and T_{eff} is so-called effective dead-time calculated as

$$T_{eff} = T_{dt} + T_{on} - T_{off}, \tag{10}$$

where T_{dt} is the dead-time inserted in order to prevent shoot-through of the DC link and T_{on} and T_{off} represent the turn-on and the turn-off time of the semiconductor switches, respectively, whose magnitudes generally depend strongly on the collector current [29].

To compensate the inverter non-idealities, a simple compensation based on the correction of the output duty cycle for each leg of the voltage source inverter has been implemented

$$s_{cor(x)} = s_{mod(x)} + \frac{T_{eff}}{T_{PWM}} \mathrm{sgn}(i_x) \quad x = a, b, c, \tag{11}$$

where $s_{mod(x)}$ is the output duty cycle from the modulator and $s_{cor(x)}$ is the corrected duty cycle. Furthermore, if the respective phase currents are lower than certain threshold current I_{th}, the corrected duty cycle is calculated as [30]

$$s_{cor(x)} = s_{mod(x)} + \frac{T_{eff}}{T_{PWM}} \frac{i_x}{I_{th}} \quad x = a, b, c\,. \tag{12}$$

The effective dead-time is chosen to be constant until the threshold current when the dependence begins to decrease linearly to zero. Both the effective dead-time and the threshold current have been determined experimentally. The voltage drop on the diodes and transistors has been neglected.

5 Implementation of voltage model

For the implementation of the voltage model, it is better to rearrange (4) into a different form, when the stator magnetic flux vector is calculated first, and then it is substituted into an algebraic equation in order to obtain the rotor magnetic flux vector [30]

$$\underline{\psi}_{1VM} = \int_0^t (\underline{u}_1 - R_1 \underline{i}_1)\, \mathrm{d}\tau, \tag{13}$$

$$\underline{\psi}_{2\mathrm{VM}} = \frac{L_2}{L_\mathrm{m}}\left(\underline{\psi}_{1\mathrm{VM}} - \sigma L_1 \underline{i}_1\right). \tag{14}$$

Unfortunately, it is not possible to implement (13) with a pure integrator because this equation is, contrary to (3), prone to the accumulation of the DC offset error (infinite gain of the pure integrator for zero frequency signals). Therefore, a modified integrator with DC offset elimination proposed in [30] has been used during the implementation of (13) and (14). Block scheme of the integrator is depicted in Fig. 7.

The scheme forces the endpoint of the stator magnetic flux vector onto a circular trajectory around the origin of coordinates (arising DC component causes the circle to drift away from the origin) by minimising the following error using a PI controller

$$\hat{\underline{\psi}}_{\mathrm{off}} = \hat{\underline{\psi}}_{1\mathrm{VM}}\left(1 - \frac{\left|\hat{\underline{\psi}}_{1\mathrm{CM}}\right|}{\left|\hat{\underline{\psi}}_{1\mathrm{VM}}\right|}\right). \tag{15}$$

6 Experimental setup

The FOC was implemented in the C language into TMS320F28335 Delphino DSP. The clock frequency was set to 150 MHz, and the calculation loop of the FOC algorithm was selected to be 100 µs which corresponds to 10 kHz PWM. As the drive, machine set with 12 kW IM coupled with 8.8 kW separately excited DC motor was used. The nominal values of the set along with IM parameters measured by the conventional no-load and locked-rotor tests are given in Table 2.

6.1 Data measurement

The motor should be brought near to the rated speed to minimise the negative effect of the inaccurate evaluation of the stator voltage and to minimise the relative influence of the voltage drop across the stator resistance.

For multiple combinations of the reference magnitude of the rotor magnetic flux and the reference torque producing component, the magnetising inductance has been adjusted in such way, that both the current and the voltage model yield approximately the same results. These operating points have been selected to cover as many combinations of the rotor flux and torque producing current set points as possible. The heavy-load measurements were made as short as possible, and the motor has been intensively cooled by forced air convection to minimise the change of the stator and rotor resistances with the temperature during the loading process. Fig. 8 shows the 3D graph of the obtained experimental data.

6.2 Verification of the obtained results

The proposed method for estimation of the magnetising inductance L_m for multiple motor operating points has been verified using the

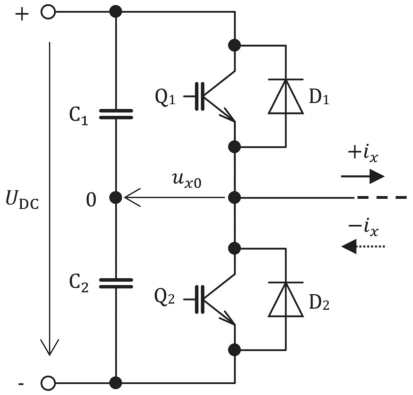

Fig. 6 *One leg of two-level VSI*

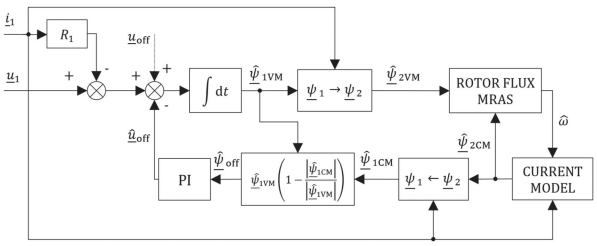

Fig. 7 *Modified integrator with DC offset elimination based on the current model*

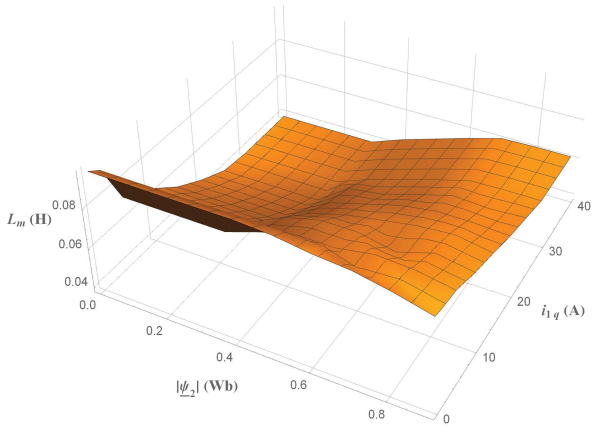

Fig. 8 *Measured dependence of the magnetising inductance on the magnitude of the rotor magnetic flux vector and torque producing current component*

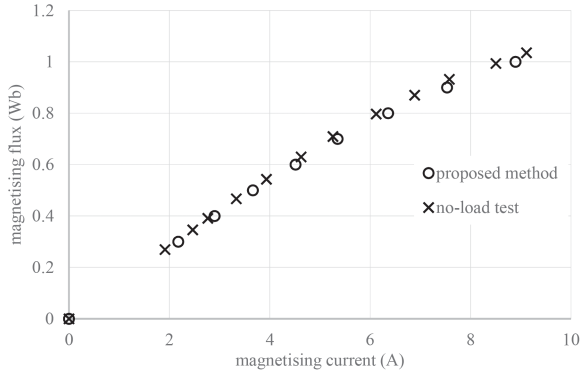

Fig. 9 *Comparison of the magnetising curve reconstructed from the proposed method and the standard no-load test*

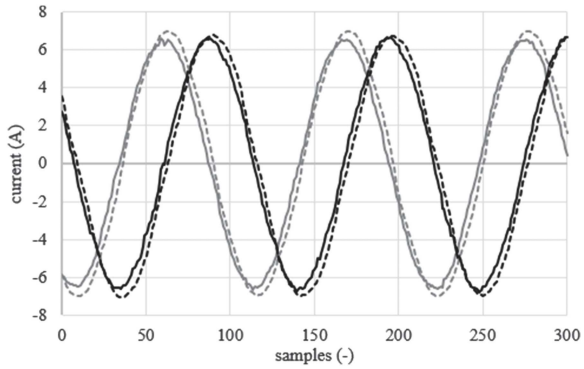

Fig. 10 *Measured (solid) and estimated (dashed) α (red) and β (blue) components of stator current vector with inductance correction; load torque: 0 Nm, reference flux: 0.6 Wb, reference speed: 100 rad·s^{-1}*

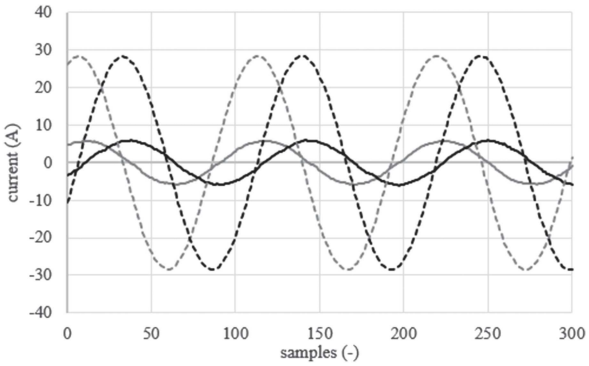

Fig. 11 *Measured (solid) and estimated (dashed) α (red) and β (blue) components of stator current vector without inductance correction; load torque: 0 Nm, reference flux: 0.6 Wb, reference speed: 100 rad·s^{-1}*

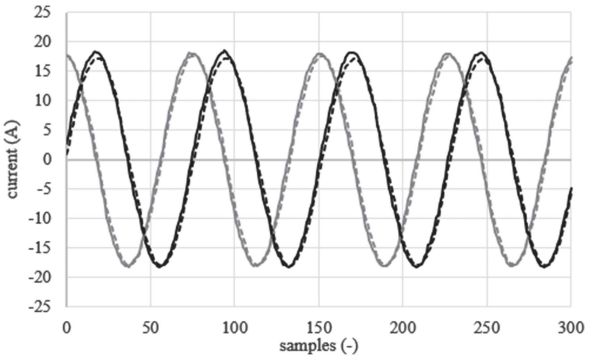

Fig. 12 *Measured (solid) and estimated (dashed) α (red) and β (blue) components of stator current vector with inductance correction; load torque: 25 Nm, reference flux: 0.6 Wb, reference speed: 100 rad·s^{-1}*

estimated and measured torque and the estimated and measured stator current vector of IM drive. By combining (3) and (4), we obtain an expression for the stator current estimator

$$\frac{\mathrm{d}\hat{\underline{i}}_1}{\mathrm{d}t} = -\frac{R_2L_\mathrm{m}^2 + L_2^2R_1}{\sigma L_1L_2^2}\hat{\underline{i}}_1 + \frac{1}{\sigma L_1}\underline{u}_1 + \frac{L_\mathrm{m}R_2}{\sigma L_1L_2^2}\underline{\psi}_{2\mathrm{CM}} - \mathrm{j}\omega\frac{L_\mathrm{m}}{\sigma L_1L_2}\underline{\psi}_{2\mathrm{CM}}. \tag{16}$$

If the measured and observed current vectors are identical in multiple drive operating points, it can be assumed that the values of the magnetising inductance measured by the proposed method are correct.

The torque has been measured using a separately excited DC machine. The following well-known torque equation gives the relationship among the DC machine torque, magnetic flux, and armature current

$$T_\mathrm{m} = C\Phi i_\mathrm{DC} = C_\Phi i_\mathrm{DC}, \tag{17}$$

where C is the construction constant of the machine, Φ is the total magnetic flux created by the excitation winding, i_DC is the armature current and C_Φ is the constant when considering fixed excitation.

6.3 Experimental verification

The measured data was implemented into the DSP in the form of a 3D array. Bilinear interpolation is used to calculate the corrected value of the magnetising inductance. The drive has been tested in terms of the accuracy of the estimated quantities. Also, the influence on the stability of the sensorless RFMRAS FOC has been investigated, too. Furthermore, a comparison of the proposed method with the standard no-load test is also presented for no-load operation.

Fig. 9 shows a comparison of the magnetising curve identified by the described method and by the standard no-load test. It can be seen that the agreement between the two data is very good. For the no-load operation $\underline{\psi}_2 \simeq \underline{\psi}_\mathrm{m}$. The magnetising curve can then be easily reconstructed using the measured data from the proposed method.

Figs. 10–15 present the comparison of estimated and measured components of the stator current space vector for different references of the rotor angular speed and different load conditions. The reference magnitude of the rotor magnetic flux is in all cases set to 0.6 Wb (the rated value 0.875 Wb). The figures are presented in three pairs. The first graph shows the results with the implemented inductance correction and the second shows a comparison of the results when considering the single value of the magnetising inductance measured by the no-load test during the nominal voltage (0.0825 H). The implemented correction of the magnetising inductance significantly improves the performance of the current estimator during the different conditions and ensures a good match of the observed and measured quantities.

Fig. 16 shows the estimated and measured current components with the inductance correction for the reference speed 2 rad·s^{-1} which is the stability threshold that is not possible to reach without the voltage and inductance compensation. The reference value of the rotor flux is set to 0.8 Wb.

Figs. 17 and 18 present the torque response of the drive after applying step load torque to the shaft during reference speed 100 rad·s^{-1} and reference flux 0.7 Wb for both the constant and variable inductance. In the case of the corrected inductances, the torque values calculated based on the results from the current and voltage model differ from each other and from the measured torque by several Nm. However, in the case of the constant inductance, the difference is about five times greater. In this case, the response of the drive would be dependent on which model is used within the control loop.

Figs. 19 and 20 show the reference, measured and estimated rotor speed during drive reversal from 50 to −50 rad·s^{-1} with and without the inductance compensation. The reference value of the

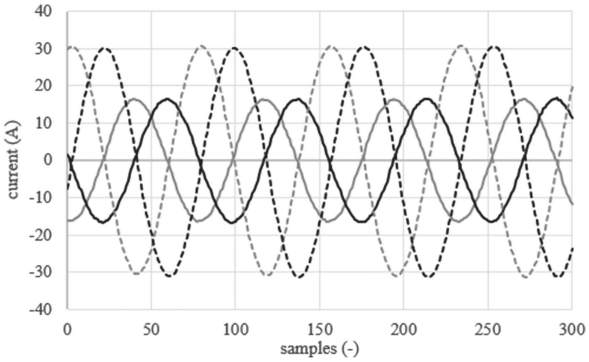

Fig. 13 *Measured (solid) and estimated (dashed) α (red) and β (blue) components of stator current vector without inductance correction; load torque: 25 Nm, reference flux: 0.6 Wb, reference speed: 100 rad·s^{-1}*

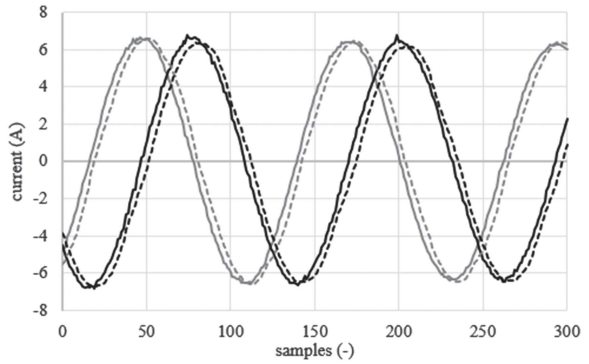

Fig. 14 *Measured (solid) and estimated (dashed) components of stator current space vector with inductance correction; load torque: 0 Nm, reference flux: 0.6 Wb, reference speed: 50 rad·s^{-1}*

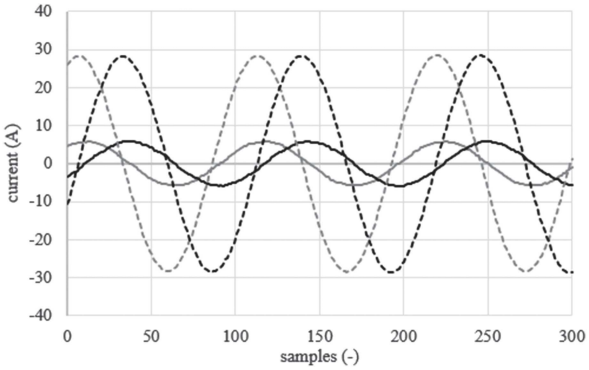

Fig. 15 *Measured (solid) and estimated (dashed) components of stator current space vector without inductance correction; load torque: 0 Nm, reference flux: 0.6 Wb, reference speed: 50 rad·s^{-1}*

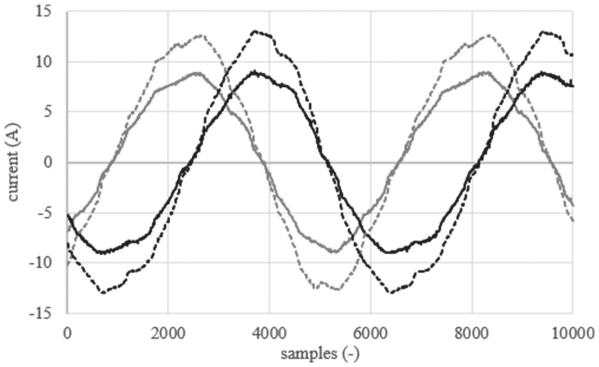

Fig. 16 *Measured (solid) and estimated (dashed) components of stator current space vector with inductance correction, load torque: 0 Nm, reference flux: 0.9 Wb, reference speed: 2 rad·s^{-1}*

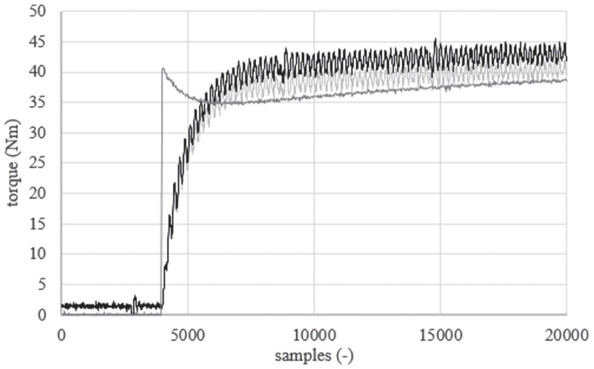

Fig. 17 *Step load – measured (black) and calculated (blue – voltage model, red – current model) torque with inductance correction; reference flux: 0.7 Wb, reference speed: 100 rad·s^{-1}*

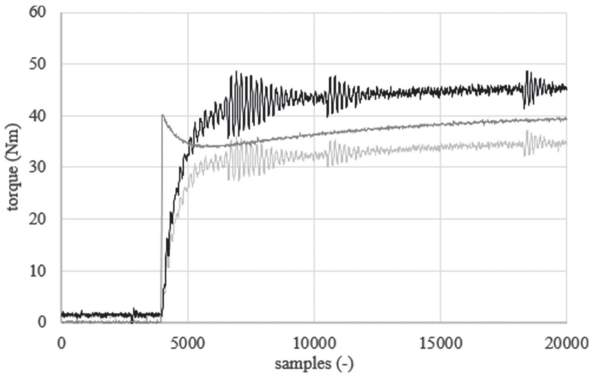

Fig. 18 *Step load – measured (black) and calculated (blue – voltage model, red – current model) torque without inductance correction; reference flux: 0.7 Wb, reference speed: 100 rad·s^{-1}*

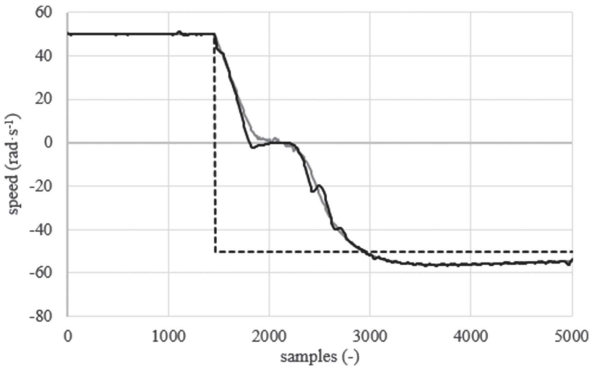

Fig. 19 *Drive reversal from 50 to −50 rad·s^{-1}; reference (black), measured (red) and estimated (blue) rotor speed with inductance correction; reference flux: 0.8 Wb*

rotor flux was set to 0.8 Wb. In the case of the inductance compensation, the reversal is much smoother, faster and with greater stability of the estimated speed, too. It can be seen that the implemented inductance compensation improves the sensorless control in terms of the drive response.

7 Conclusion

Accurate knowledge of the magnetising inductance is essential if the drive operates in the field-weakening region or if it is controlled in an energy optimisation mode. Also, proper knowledge of the magnetising inductance, which can vary with magnetising and rotor current, is important for modern predictive control strategies.

In this paper, an offline experimental method of identifying the non-linear dependence of IM magnetising inductance on the setpoint of the rotor flux and stator torque producing current component has been presented. The method utilises the parallel

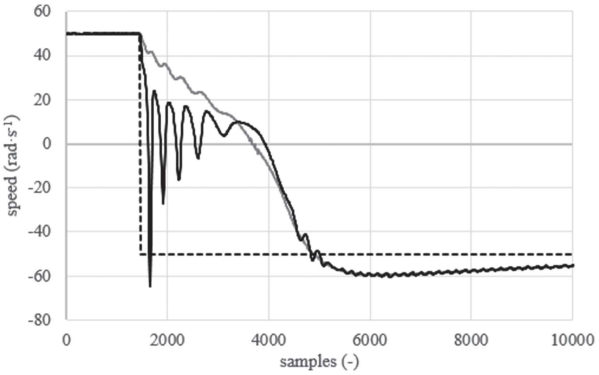

Fig. 20 *Drive reversal from 50 to −50 rad·s^{-1}; reference (black), measured (red) and estimated (blue) rotor speed without inductance correction; reference flux: 0.8 Wb*

operation of two rotor flux observers that are commonly used in conjunction with RFMRAS. Experimental verification of the obtained results performed on a 12 kW induction drive without speed sensor indicates substantial consistency between observed and measured motor quantities compared to the single value inductance model. In addition, the overall performance and stability of the RFMRAS sensorless FOC have been significantly improved.

8 Acknowledgment

The research described in this paper was supported by the Student Grant Competition of the Czech Technical University in Prague under grant no. SGS19/065/OHK3/1T/13.

9 References

[1] Vas, P.: '*Sensorless vector and direct torque control*' (Oxford University Press, UK, 1998)

[2] Quang, N.P., Dittrich, J.: '*Vector control of three-phase AC machines: system development in the practice*' (Springer-Verlag, Germany, 2008, 1. Aufl. ed.)

[3] Popescu, M.: 'Induction motor modelling for vector control purposes'. Report, Helsinki University of Technology, Laboratory of Electromechanics, Espoo, Finland, 2000, 144p

[4] Sokola, M.: 'Vector control of induction machines using improved models'. PhD thesis, Liverpool John Moores University, Liverpool, UK, 1998

[5] Wang, M.: 'Parameter variation effects in sensorless vector controlled induction machines'. PhD thesis, Liverpool John Moores University, Liverpool, UK, 1999

[6] Vas, P.: '*Parameter estimation, condition monitoring, and diagnosis of electrical machines*' (Clarendon, UK, 1993)

[7] Sullivan, C.R., Sanders, S.R.: 'Models for induction machines with magnetic saturation of the main flux path', *IEEE Trans. Ind. Appl.*, 1995, **31**, (4), pp. 907–917

[8] Slemon, G. R.: 'Modelling of induction machines for electric drives', *IEEE Trans. Ind. Appl.*, 1989, **25**, (6), pp. 1126–1131

[9] Moulahoum, S., Touhami, O., Ibtiouen, R., *et al.*: 'Induction machine modeling with saturation and series iron losses resistance'. IEEE Int. Electric Machines & Drives Conf., Antalya, Turkey, 2007, pp. 1067–1072

[10] Kiselychnyk, O., Marc, B., Jihong, W.: 'Comparison of two magnetic saturation models of induction machines and experimental validation', *IEEE Trans. Ind. Electron.*, 2017, **64**, (1), pp. 81–90

[11] Tuovinen, T., Hinkkanen, M., Luomi, J.: 'Modeling of saturation due to main and leakage flux interaction in induction machines', *IEEE Trans. Ind. Appl.*, 2010, **46**, (3), pp. 937–945

[12] Gerada, C., Bradley, K., Sumner, M., *et al.*: 'Evaluation and modelling of cross saturation due to leakage flux in vector controlled induction machines'. IEEE Int. Electric Machines and Drives Conf., 2003. IEMDC'03, Madison, WI, USA, 2003, 3, pp. 1983–1989

[13] Klaes, N.R.: 'Parameter identification of an induction machine with regard to dependencies on saturation', *IEEE Trans. Ind. Appl.*, 1993, **29**, (6), pp. 1135–1140

[14] Hinkkanen, M., Repo, A., Luomi, J.: 'Influence of magnetic saturation on induction motor model selection'. Proc. ICEM'06, Chania, Greece, September 2006

[15] Immonen, P., Ruuskanen, V., Nerg, J., *et al.*: 'Inductance saturation of the induction machine as a function of stator voltage and load with steady state AC magnetic finite element solver', *Int. Rev. Model. Simul.*, 2004, **7**, pp. 450–456

[16] Dannerer, G., Seebacher, R.R., Krischan, K., *et al.*: 'Modeling the induction machine's main inductance as a function of the magnetizing and the torque building component of the stator current'. 2008 18th Int. Conf. on Electrical Machines, Vilamoura, Portugal, 2008, pp. 1–6

[17] Ling, Z., Libing, Z., Siyuan, G., *et al.*: 'Equivalent circuit parameters calculation of induction motor by finite element analysis', *IEEE Trans. Magn.*, 2014, **50**, (2), pp. 833–836

[18] Hinkkanen, M., Repo, A., Cederholm, M., *et al.*: 'Small-signal modelling of saturated induction machines with closed or skewed rotor slots'. 2007 IEEE Industry Applications Annual Meeting, New Orleans, LA, USA, 2007, pp. 1200–1206

[19] Melkebeek, J.A.A.: 'Magnetising-field saturation and dynamic behaviour of induction machines. Part 1: improved calculation method for induction-machine dynamics', *IEE Proc. B, Electr. Power Appl.*, 1983, **130**, (1), pp. 1–9

[20] Levi, E., Sokola, M., Vukosavic, S.N.: 'A method for magnetizing curve identification in rotor flux oriented induction machines', *IEEE Trans. Energy Convers.*, 2000, **15**, (2), pp. 157–162

[21] Chatterjee, D.: 'A novel magnetizing-curve identification and computer storage technique for induction machines suitable for online application', *IEEE Trans. Ind. Electron.*, 2011, **58**, (12), pp. 5336–5343

[22] Karlovsky, P., Lettl, J.: 'Induction motor drive direct torque control and predictive torque control comparison based on switching pattern analysis', *Energies*, 2018, **11**, (7), p. 1793

[23] Rodriguez, J., Cortes, P.: '*Predictive control of power converters and electrical drives*' (Wiley-IEEE Press, USA, 2012)

[24] Kumar, R., Das, S., Syam, P., *et al.*: 'Review on model reference adaptive system for sensorless vector control of induction motor drives', *IET Electr. Power Appl.*, 2015, **9**, (7), pp. 496–511

[25] Rao, P., Nakka, J., Shekar, R.: 'Sensorless vector control of induction machine using MRAS techniques'. 2013 Int. Conf. on Circuits, Power and Computing Technologies (ICCPCT), Nagercoil, India, 2013, pp. 167–175

[26] Schauder, C.: 'Adaptive speed identification for vector control of induction motors without rotational transducers', *IEEE Trans. Ind. Appl.*, 1992, **28**, (5), pp. 1054–1061

[27] Fligl, S., Bauer, J., Vlcek, M., *et al.*: 'Analysis of induction machine T and Γ circuit coequality for use in electric drive controllers'. 2012 13th Int. Conf. on Optimization of Electrical and Electronic Equipment (OPTIM), Brasov, Romania, 2012, pp. 659–664

[28] Bolognani, S., Zigliotto, M.: 'Self-commissioning compensation of inverter non-idealities for sensorless AC drives applications'. 2002 Int. Conf. on Power Electronics, Machines and Drives (Conf. Publ. No. 487), Sante Fe, NM, USA, 2002, pp. 30–33

[29] Salt, D.E., Drury, D., Holliday, D., *et al.*: 'Compensation of inverter nonlinear distortion effects for signal-injection-based sensorless control', *IEEE Trans. Ind. Appl.*, 2011, **47**, (5), pp. 2084–2092

[30] Lipcak, O., Bauer, J.: 'Optimization of voltage model for MRAS based sensorless control of induction motor'. AETA 2018 - Recent Advances in Electrical Engineering and Related Sciences: Theory and Application, Ostrava, Czech Republic, 2019 (LNEE, **554**)

APPENDIX D

LIPČÁK, O., J. BAUER a M. CHOMÁT. „Reactive Power MRAS for Rotor Resistance Estimation Taking Into Account Load-Dependent Saturation of Induction Motor“. In: *2019 International Conference on Electrical Drives & Power Electronics (EDPE)*. Nový Smokovec, The High Tatras, 2019-09-24/2019-09-26. Košice: Technical University of Košice, 2019. s. 255-260. ISSN 1339-3944. ISBN 978-1-7281-0389-1. DOI 10.1109/EDPE.2019.8883887.

Author's contribution: Method conceptualization, consultation of DSP algorithm implementation and functionality validation, validity of result confrontation, paper co-writing

Reactive Power MRAS for Rotor Resistance Estimation Taking Into Account Load-Dependent Saturation of Induction Motor

Ondrej Lipcak
Department of Electric Drives and Traction
Czech Technical University in Prague
Prague, Czech Republic
lipcaond@fel.cvut.cz

Jan Bauer
Department of Electric Drives and Traction
Czech Technical University in Prague
Prague, Czech Republic
bauerja2@fel.cvut.cz

Miroslav Chomat
Department of Electric Drives and Traction
Czech Technical University in Prague
Prague, Czech Republic
chomat@fel.cvut.cz

***Abstract*—The accuracy of induction motor (IM) drive with employed field-oriented control depends on precise identification of the IM equivalent circuit parameters. Those parameters can change significantly during the drive operation. Therefore, an adaptation of the IM model parameters is needed for a high-performance drive. Estimators based on model reference adaptive system (MRAS) are not computationally demanding, but they a priori exhibit sensitivity to the other, non-estimated parameters. This paper analyses the influence of the proper knowledge of the magnetizing inductance on the accuracy of the rotor resistance estimator based on the traditional reactive power MRAS. The paper also takes into account the load-dependent saturation of the IM, which is often omitted during the analysis and shows that the implemented load-dependent magnetization characteristic improves the MRAS and drive performance. Simulation and experimental results conducted on 12 kW IM are presented.**

Keywords—Induction motor modeling, MRAS, induction motor saturation, parameter estimation, parameter sensitivity

I. INTRODUCTION

The field-oriented control (FOC) belongs to the most employed control strategies for variable speed drives with a requirement for high dynamics [1]-[2]. Usually, induction motors (IM) are used as the prime electromechanical converter. That is because of their robustness, easy maintenance, and low cost. Contrary to the permanent magnet synchronous machines or separately excited DC machines, the direct excitation of the EMF is missing in the case of IM. Therefore, the EMF is produced in IM by FOC algorithm.

In the case of rotor flux oriented FOC, the flux position and amplitude cannot be measured directly. Therefore, an equivalent model of the IM that estimates the magnitude and position of the flux space vector is needed. The accuracy of the model is dependent on the employed set of equations and knowledge of the IM equivalent circuit parameters [1]-[3]. Those parameters such as stator and rotor resistance, leakage inductances, and magnetizing inductance are usually obtained from the conventional no-load and locked rotor tests. However, for a high-performance drive, the constant parameter models are not suitable, because the change of the stator and rotor resistance with temperature and magnetizing inductance with the saturation will cause an error in the amplitude and position of the estimated rotor flux which will lead to miscalculations of other quantities such as torque [3]. Moreover, the control strategies with a reduced number of sensors (e.g., for speed and current) become popular recently [5]-[8], which leads to increased requirements on the IM model accuracy. Thus compensation of the parameters with temperature and the current level is needed.

Several methods can compensate for the parameter variation with the temperature. The first set of methods uses a thermal model of the machine, but for this, the temperature sensor, that is not always included is needed. The second set of methods tries to estimate the resistance variation utilizing signal injection and estimation of the rotor time constant. The main drawback of these methods is that the injected signal can influence the behavior and performance of the drive [3]. The third group of methods is based on the estimation through observers. There are many known algorithms for estimation of the speed and other motor parameters such as Kalman filters (KF), various types of observers (Luenberger Observer, Gopinath Observer), model reference adaptive systems (MRAS), fuzzy controllers and artificial neural networks (ANN) [1]-[13]. All of them have different requirements for the computational burden and required input quantities. Kalman filters give good accuracy of the estimate but are computationally very demanding [2], [5]-[6]. ANN requires a vast amount of memory space, and it also needs to learn first [7].

MRAS estimators can be simple and computationally not demanding, but their main drawback is, that they suppose that every parameter but the estimated one is accurately known [2]-[3], [9]-[13]. That is also the case of the traditional reactive power based MRAS that is, on the one hand, insensitive to the variation of the rotor resistance but on the other hand sensitive to the variation of the magnetizing inductance [9]-[13]. The magnetization characteristic of the unloaded machine can be measured offline and stored as a look-up table (LUT). However, it has also been shown that the magnetizing inductance may strongly saturate as a function of the rotor current or load, respectively [14]-[15]. This type of saturation is usually not taken into account.

978-1-7281-0389-1/19/$31.00 ©2019 IEEE

This paper analyses the sensitivity of the traditional reactive power MRAS to the inaccuracy of the magnetizing inductance for a steady-state and transient IM operation using mathematical analysis and simulations. It also experimentally shows the importance of taking into account the load-dependent saturation of the magnetizing inductance. The load and flux-dependent magnetization characteristics were measured offline by the method proposed in one of our previous papers [16]. Simulations and experiments are conducted on 12 kW IM.

II. Induction Motor Models and Estimators

In this paper, equations describing the so-called T-equivalent IM circuit depicted in Fig. 1 are utilized for the mathematical description of the IM. In the figure, the symbols $\underline{\psi}_1$ and $\underline{\psi}_2$ represent the stator and rotor flux linkage space vectors, respectively, $\underline{u}_1$ represents the stator voltage space vector, $\underline{i}_1$ and $\underline{i}_2$ represent the stator and rotor current space vectors, respectively, R_1 and R_2 denote the stator and rotor resistances, respectively, ω_k is the electrical angular speed of the general reference frame, ω is the rotor electrical angular speed, L_m is the magnetizing inductance and the symbol j marks imaginary unit ($\mathrm{j}^2 = -1$). A squirrel-cage rotor is considered; therefore, the rotor voltage is equal to zero. The stator inductance L_1 is defined as $L_1 = L_\mathrm{m} + L_{1\sigma}$, where $L_{1\sigma}$ is the stator leakage inductance and the rotor inductance L_2 is defined as $L_2 = L_\mathrm{m} + L_{2\sigma}$, where $L_{2\sigma}$ is the rotor leakage inductance. The torque equation is given by (p_p is the number of motor pole-pairs and $\alpha\beta$ is the stator fixed-coordinate system)

$$T_\mathrm{e} = 1.5 p_\mathrm{p} \frac{L_\mathrm{m}}{L_2}\left(\psi_{2\alpha} i_{1\beta} - \psi_{2\beta} i_{1\alpha}\right). \tag{1}$$

A. Rotor Flux Estimator

In the case of rotor flux oriented FOC, it is necessary to obtain the magnitude and position of the rotor flux linkage vector. For this purpose, mathematical models of the IM are used. For the direct vector FOC, where the transformation angle between the stationary and synchronous coordinate system is calculated from the components of the rotor flux vector, it is convenient to express the models in the stator-fixed coordinate system, therefore $\omega_\mathrm{k} = 0$. The commonly used model, called the current model, is given by the following vector equation

$$\frac{\mathrm{d}\underline{\psi}_2}{\mathrm{d}t} = \frac{L_\mathrm{m} R_2}{L_2}\underline{i}_1 - \frac{R_2}{L_2}\underline{\psi}_2 + \mathrm{j}\omega\underline{\psi}_2. \tag{2}$$

The transformation angle for Park transformation is in case of the direct FOC calculated as $\vartheta = \tan^{-1}(\psi_{2\beta}/\psi_{2\alpha})$.

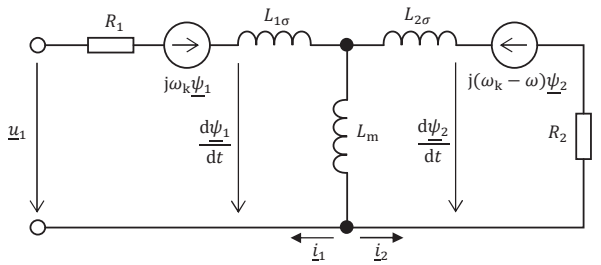

Fig. 1 T-equivalent circuit of IM

B. Current Estimator

Unfortunately, the rotor resistance of a squirrel-cage rotor IM cannot be measured directly. Therefore, in the part of this paper dedicated to the experimental verification, an indirect approach has been selected. The approach lies within the comparison of the measurable currents and the estimated currents given by

$$\frac{\mathrm{d}\underline{i}_1}{\mathrm{d}t} = C_1\underline{i}_1 + C_2\underline{u}_1 + C_3\underline{\psi}_2 - \mathrm{j}\omega C_4\underline{\psi}_2, \tag{3}$$

where

$$C_1 = -\frac{R_2 L_\mathrm{m}^2 + L_2^2 R_1}{\sigma L_1 L_2^2}, \quad C_2 = \frac{1}{\sigma L_1}, \quad C_3 = \frac{L_\mathrm{m} R_2}{\sigma L_1 L_2^2}, \quad C_4 = \frac{L_\mathrm{m}}{\sigma L_1 L_2}. \tag{4}$$

III. Reactive Power MRAS for Rotor Resistance Estimation

One of the possible techniques of the rotor resistance estimation is the Model Reference Adaptive System (MRAS) approach [3], [9]-[13]. The advantage of MRAS is that contrary to Kalman filter or artificial neural network, it leads to much simpler equations [3]. Its disadvantage is that it supposes that the error is caused by the estimated value only [3]. Therefore, in principle, it does not consider the other factors that may influence the estimation.

In this paper, MRAS based on reactive power for resistance estimation proposed in is used. The reference model is given by

$$Q = u_{1q} i_{1d} - u_{1d} i_{1q}, \tag{5}$$

where d and q denote real and imaginary axis, respectively of the synchronous reference frame.

The adaptive model is given by

$$\hat{Q} = \omega_\mathrm{s} L_1\left(i_{1d}^2 + \sigma i_{1q}^2\right), \tag{6}$$

where $\sigma = 1 - L_\mathrm{m}^2/L_1 L_2$ is the leakage factor. Equation (5) is an expression for instantaneous reactive power, while (6) represents steady-state reactive power.

The synchronous speed can be calculated as

$$\omega_\mathrm{s} = \omega + \omega_\mathrm{slip}, \tag{7}$$

where ω_slip is the electrical slip speed which can be estimated as

$$\omega_\mathrm{slip} = \frac{L_\mathrm{m} R_2 i_{1q}}{L_2 \psi_2}, \tag{8}$$

alternatively, for a constant flux as

$$\omega_\mathrm{slip} = \frac{R_2 i_{1q}}{L_2 i_{1d}}. \tag{9}$$

Due to the noise rejection, reference values i_{1d}^*, i_{1q}^* and ψ_{2d}^* are commonly used instead of the actual ones in practice [10]-[11]. It can be seen that (6) is dependent on the rotor resistance, directly and indirectly. The direct dependence is caused by the appearance of the rotor resistance in (8) and (9), respectively, which are used for the slip speed estimation. The indirect dependence lies within the current model equation (2) because the wrong value of the rotor resistance influences the calculation of the transformation angle that is used for the $\alpha\beta \rightarrow dq$ transformation.

The error for the rotor resistance adaptation mechanism, which is a conventional PI controller, is calculated as

$$\varepsilon_{\mathrm{R}} = Q - \hat{Q}. \tag{10}$$

The output of the PI controller is the deviation from the initial rotor resistance $R_{2\mathrm{init}}$

$$\Delta R_2(t) = K_{\mathrm{p}}\varepsilon_{\mathrm{R}}(t) + K_{\mathrm{i}}\int_0^t \varepsilon_{\mathrm{R}}(\tau)\mathrm{d}\tau. \tag{11}$$

Finally, the estimated resistance is given by

$$\hat{R}_2 = R_{2\mathrm{init}} + \Delta R_2. \tag{12}$$

The block diagram of the rotor resistance MRAS is depicted in Fig. 2.

IV. Sensitivity to Changes in Magnetizing Inductance

It is clear from (2) and (6)-(9) that the estimated value of the reactive power depends on the accurate knowledge of the magnetizing inductance. The influence of the leakage inductances is expected to be much less significant since the value of the leakage inductances in case of higher power IMs represent only a few percent of the magnetizing one.

A. Steady-State Analysis

In [12] and [13], the sensitivity of the estimated reactive power to changes in the rotor resistance has been studied using an error indicator calculated as

$$\varepsilon_{\mathrm{Q}} = \frac{Q - \hat{Q}}{|\underline{i}_1|^2} = \frac{\Im[Z\underline{i}_1\bar{i}_1] - \Im[\hat{Z}\underline{i}_1\bar{i}_1]}{|\underline{i}_1|^2} = \Im[Z] - \Im[\hat{Z}], \tag{13}$$

where $\bar{i}_1$ denotes conjugated current space vector. The impedances Z fulfills the following relation

$$\underline{u}_1 = Z\underline{i}_1. \tag{14}$$

In the papers mentioned above, the impedances Z and $\hat{Z}$ were derived from a steady-state inverse-Γ equivalent circuit. For T-equivalent circuit (Fig. 3), the impedance Z can be calculated as

$$Z = R_1 + \mathrm{j}L_{1\sigma}\omega_{\mathrm{s}} + \frac{\mathrm{j}L_{\mathrm{m}}\omega_{\mathrm{s}}\left(R_2\frac{\omega_{\mathrm{s}}}{\omega_{\mathrm{slip}}} + \mathrm{j}L_{2\sigma}\omega_{\mathrm{s}}\right)}{R_2\frac{\omega_{\mathrm{s}}}{\omega_{\mathrm{slip}}} + \mathrm{j}(L_{2\sigma}\omega_{\mathrm{s}} + L_{\mathrm{m}}\omega_{\mathrm{s}})}. \tag{15}$$

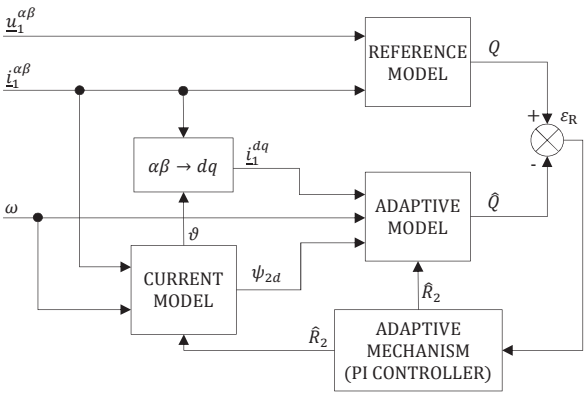

Fig. 2 Reactive power MRAS for rotor resistance estimation

In this paper, the change of the estimated reactive power with the change of the magnetizing inductance is of interest. Therefore, the impedance $\hat{Z}$ is calculated by replacing L_{m} in (15) with $L_{\mathrm{m}} + \Delta L_{\mathrm{m}}$, where ΔL_{m} is the inductance error. Taking an imaginary part of (15) yields

$$\Im[Z] = \omega_{\mathrm{s}}\left(L_2 - \frac{L_1 L_{\mathrm{m}}^2\omega_{\mathrm{slip}}^2}{R_2^2 + L_1\omega_{\mathrm{slip}}^2}\right). \tag{16}$$

Out of (16), it is evident that this approach is advantageous from the point of view that it uses only the IM parameters along with the synchronous and slip speed and not IM state and input variables such as currents or voltages.

In order to obtain graphical visualization of the error indicator ε_{Q}, numerical values of IM parameters of rated power 12 kW obtained from the conventional no-load and locked-rotor tests given in TABLE I were used. The value of the magnetizing inductance corresponds to the no-load test at the rated voltage.

Fig. 4 depicts the dependence of $\varepsilon_{\mathrm{Q}}/\Im[Z]$ on ΔL_{m} expressed in the percentual error of the nominal magnetizing inductance for different slip speeds and the synchronous speed equal to the nominal value. The slip speeds are expressed in terms of the percentage of the nominal one. It can be seen, that for the slip speeds greater than 50 % of the nominal value, the curves appear to be approximately linear in this scale and relatively close to each other. Also, the sign of the inductance error corresponds to the sign of the error indicator. In the case of slip speeds below the 25 % of the nominal value, the error indicator significantly rises, and the sign of the error indicator now does not correspond to the sign of the magnetizing inductance percentage error.

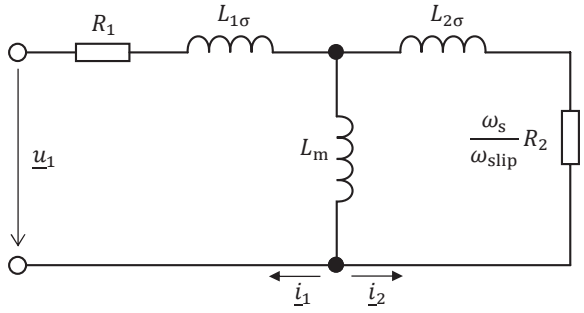

Fig. 3 Steady-state IM T-equivalent circuit

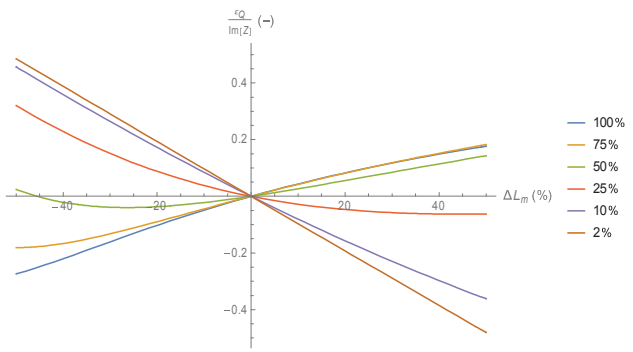

Fig. 4 Dependence of $\varepsilon_{\mathrm{Q}}/\Im[Z]$ on the percentual change of the magnetizing inductance for different slip speeds

TABLE I. INDUCTION MOTOR NAMEPLATE PARAMETERS AND MEASURED VALUES BY NO-LOAD AND LOCKED-ROTOR TESTS

Nominal power	12 kW	R_1	377 mΩ
Nominal current	22 A	R_2	355 mΩ
Nominal voltage	380 V	$L_{1\sigma}$	2.27 mH
Nominal frequency	50 Hz	$L_{2\sigma}$	2.27 mH
Nominal power factor	0.8	R_{Fe}	202 Ω
Nominal speed	1460 min^{-1}	L_{m}	82 mH

B. *The Response of Reactive Power MRAS to Step Changes in Magnetizing Inductance*

The direct FOC based on the current model (2) along with the reactive power MRAS for the rotor resistance estimation, was implemented into Matlab/SIMULINK. The default parameters for the IM model are the ones given in TABLE I. In the simulations, the influence of the step change of the magnetizing inductance on the behavior of the MRAS was observed.

Fig. 5 shows the situation where the drive was brought to the speed of 150 rad·s^{-1} with load torque 70 Nm. The reference flux was set to 0.8 Wb. After reaching the steady-state, the MRAS was turned on, and multiple-step changes of the magnetizing inductance in the IM model were applied. The rotor resistance in the IM model was kept at the actual value. The solid line represents the ratio between the estimated and actual resistance and the dashed line then the ratio between the changed inductance value and the default value that was used in the control model.

It can be seen that the estimator converges to the actual resistance value if the magnetizing inductance in the IM model is equal to the value in the control model and that every change in the magnetizing inductance triggers a transient during which the estimated resistance converges to value different from the actual one. The lower the magnetizing inductance, the higher the estimated resistance which is an expected result because for a given flux level the IM torque is proportional to the slip speed which contains the product of the rotor resistance and magnetizing inductance in the numerator.

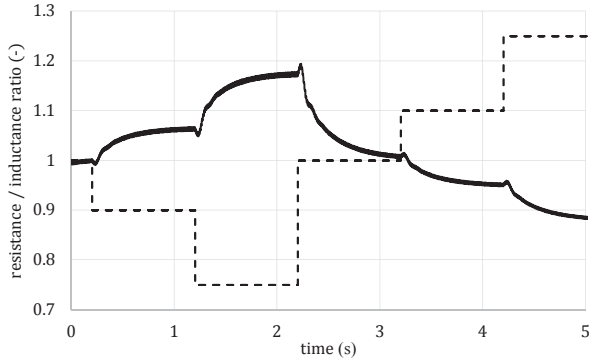

Fig. 5 Reaction of the reactive power MRAS to the step change of the magnetizing inductance; reference rotor flux: 0.8 Wb, reference rotor speed: 150 rad·s^{-1}, load torque: 70 Nm; solid – ratio of estimated resistance to actual resistance, dashed – ratio of changed inductance value to the default value

V. IMPROVING THE ACCURACY OF THE ROTOR RESISTANCE ESTIMATION

According to the previous chapters of this paper, it is clear that the main drawback of the MRAS estimation scheme for the rotor resistance lies within the fact that it relies on the accurate identification of the magnetizing inductance as also pointed out in [12]-[13]. It is a well-known phenomenon that the magnetizing inductance saturates with the magnetizing current [2]-[3]. This dependence can be quite easily determined, for example, by the standard no-load test. However, the magnetizing inductance may also saturate with the rotor current or load, respectively, [14]-[15]. References [12]-[13] suggest that the compensation algorithm should be active only if the rotor speed and load torque are higher than some threshold value. However, the magnetizing inductance identified during the no-load conditions may significantly vary from the actual inductance during the load conditions [14]-[15].

In [16] we proposed a simple and intuitive method for offline identification of the load-dependent saturation of IM which besides the IM current model given by (2) also utilizes the so-called voltage model given by the following set of equations

$$\begin{aligned} \underline{\psi}_1 &= \int_0^t \left(\underline{u}_1 - R_1 \underline{i}_1\right) \mathrm{d}\tau \\ \underline{\psi}_2 &= \frac{L_2}{L_{\mathrm{m}}} \left(\underline{\psi}_1 - \sigma L_1 \underline{i}_1\right). \end{aligned} \tag{17}$$

The outline of the method will be given in the next chapter.

A. *Identification of Load-Dependent Induction Motor Saturation*

In an ideal case, when all the motor variables are known, there would be no difference between the estimated rotor flux vector from the current (2) and voltage model (17). If the results from the models differ, it means there has to be some mismatch in the motor parameters. The only parameter that can be measured directly is the stator resistance, which can be then corrected according to the winding temperature. In the case of the leakage inductances, it is unclear how to distribute the measured value between the stator and rotor winding. However, the leakage inductance usually presents only a few percent of the magnetizing one. Therefore, it is supposed that a standard distribution 1:1 will not significantly affect the operation of both models. As for the rotor resistance, it is supposed that its initial value is identified by sufficient accuracy by an appropriate offline method.

The method lies within numerical minimalization of the following error by adjusting the value of the magnetizing inductance L_{m}

$$\varepsilon_\psi = \psi_{2\mathrm{VM}} - \psi_{2\mathrm{CM}}, \tag{18}$$

where $\psi_{2\mathrm{VM}}$ and $\psi_{2\mathrm{CM}}$ are the amplitudes of the rotor flux vector obtained from (17) and (2), respectively. The minimalization has to be performed for multiple combinations of the reference flux and torque. In order to suppress the change of the rotor resistance with temperature, the heavy-load measurements should be made as quick as possible, and the rotor should be cooled by forced convection.

VI. Experimental Results

The FOC was implemented in the C language into TMS320F28335 Delphino DSP. The clock frequency was set to 150 MHz, and the calculation loop of the FOC algorithm was selected to be 200 µs with 10 kHz PWM. As for the drive, machine set with 12 kW IM coupled with 8.8 kW separately excited DC motor has been used. The nominal values of the IM along with the IM parameters measured by the conventional no-load and locked-rotor tests are the ones given in TABLE I. The speed is measured by an incremental encoder.

A. Measured Data

To assess the validity of the experimental rotor resistance estimation, the ability of the MRAS to follow the change of the temperature of the rotor winding was tested. The motor was brought to speed 130 rad·s^{-1}. Then, load torque equaled to 40 Nm was applied. Next, the MRAS and the inductance correction were activated. Then the change of the estimated resistance with the rotor temperature was observed. Fig. 6 shows the measured dependence of the relative change of the rotor resistance with respect to the change of the rotor temperature. The measured values follow an approximately linear trend, which is an expected result for a metal conductor. The dashed line represents a linear regression of the measured data.

Fig. 7 and Fig. 8 represent measured and estimated components of the stator current vector in $\alpha\beta$ for two different situations. The reference speed was set to 130 rad·s^{-1}, the reference flux to 0.8 Wb and the load torque to 40 Nm. In Fig. 7, the magnetizing inductance was equal to the single value obtained from the no-load test, and the MRAS was active. The estimated current components are then shifted in phase and exhibit a difference in amplitude of approx. 2 A. In Fig. 8, the magnetizing inductance correction and the MRAS were active. The estimated and measured current components exhibit a small difference (approx. 1 A) in amplitude but compared to the case without the inductance compensation it can be seen that there is nearly zero phase shift

Fig. 9 and Fig. 10 show the drive response on step input of reference speed. According to recommendations in [12] and [13], respectively, the MRAS was active only if torque and speed were higher than a threshold value. The threshold speed was set to 0.1 p.u. and the threshold torque to 0.25 p.u.

In both cases, the rotor resistance estimator converges to steady-state value but in the case of Fig. 10, where the magnetizing inductance was constant and equal to the value obtained from the no-load test, the drive behavior is deteriorated. Based on the observation of the measured and calculated torque after the mechanical transient, it can be concluded that the value of the estimated resistance does not correspond to the real one because there is a difference of approx. 10 Nm between the measured and calculated torque. On the contrary, it can be stated that the estimated steady-state resistance value in Fig. 9 is close to the real one because the measured and calculated torque after the mechanical transient are almost identical. Also, the drive reaches the reference speed faster.

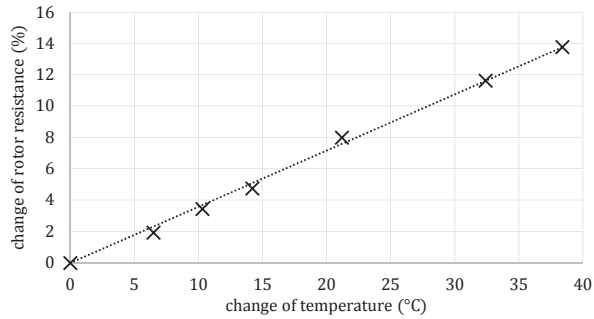

Fig. 6. Relative change of the estimated rotor resistance with the temperature

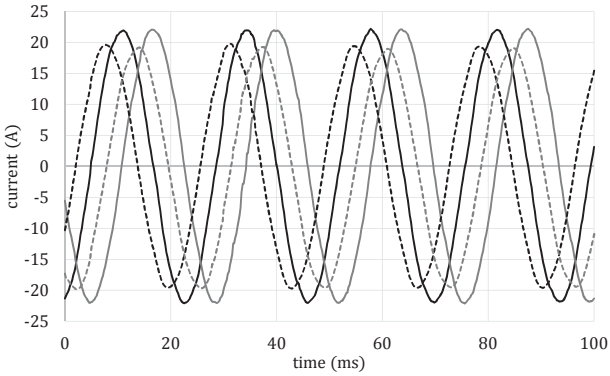

Fig. 7. Measured (solid) and estimated (dashed) α (black) and β (grey) components of the stator current vector; MRAS – active, inductance correction – inactive; reference speed: 130 rad·s^{-1}, reference flux: 0.8 Wb, load torque: 40 Nm

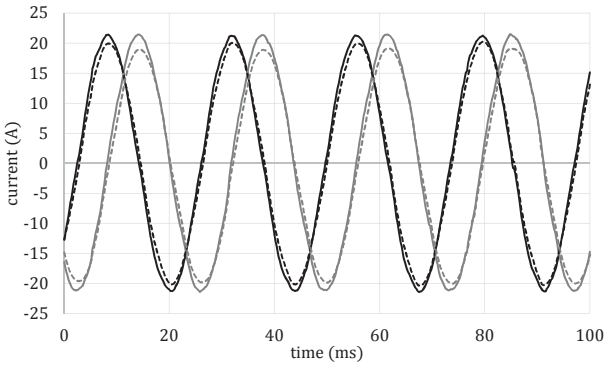

Fig. 8. Measured (solid) and estimated (dashed) α (black) and β (grey) components of the stator current vector; MRAS – active, inductance correction – active; reference speed: 130 rad·s^{-1}, reference flux: 0.8 Wb, load torque: 40 Nm

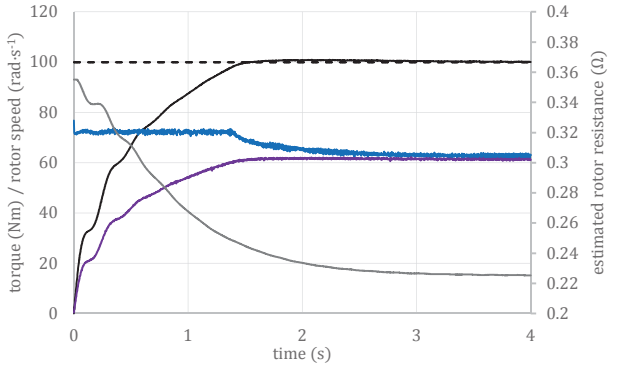

Fig. 9. The response of the drive on step reference speed – reference speed (black dashed), measured speed (black solid), calculated IM torque (blue), measured torque (purple), estimated rotor resistance (grey); MRAS – active, inductance correction – active; reference flux: 0.8 Wb

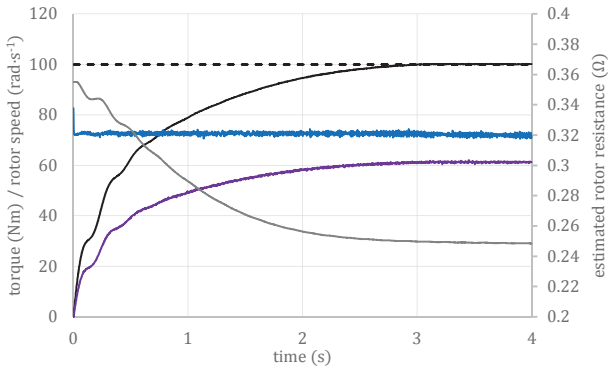

Fig. 10. The response of the drive on step reference speed – reference speed (black dashed), measured speed (black solid), calculated IM torque (blue), measured torque (purple), estimated rotor resistance (grey); MRAS – active, inductance correction – inactive; reference flux: 0.8 Wb

VII. Conclusion

In this paper, analysis of the sensitivity of reactive power MRAS for rotor resistance estimation to the changes in the magnetizing inductance has been studied. By mathematical analysis based on the impedance of the T-equivalent induction motor circuit, it was shown that the uncertainty in the magnetizing inductance is more significant at lower slip speeds. In simulations, it was shown that the adequately tuned MRAS estimator, on the one hand, converges to steady-state value under inaccurate inductance conditions and is also able to follow the step changes in the magnetizing inductance, but on the other hand, the steady-state resistance value does not correspond to the actual one. Finally, it was experimentally shown that neglecting the load-dependent saturation of the induction motor causes the wrong estimation of the resistance and other quantities such as currents or torque and also generally worsens the drive dynamics.

Acknowledgment

The research described in this paper was supported by the Student Grant Competition of the Czech Technical University in Prague under grant No. SGS19/065/OHK3/1T/13.

References

[1] N.P. Quang and J. Dittrich, *Vector Control of Three-Phase AC Machines: System Development in the Practice*. 1. Aufl. ed. Berlin, Heidelberg: Springer-Verlag; 2008.

[2] P. Vas, *Sensorless Vector and Direct Torque Control*. Oxford, Oxford University Press, 1998.

[3] M. Sokola, "Vector Control of Induction Machines Using Improved Models," *Ph.D. dissertation*, Liverpool John Moores University, Liverpool, 1998.

[4] G. Jo and J. Choi, "Gopinath Model-Based Voltage Model Flux Observer Design for Field-Oriented Control of Induction Motor," in *IEEE Transactions on Power Electronics*, vol. 34, no. 5, pp. 4581-4592, May 2019.

[5] P. Brandstetter, M. Dobrovsky, M. Kuchar, CST. Dong and HH. Vo, "Application of BEMF-MRAS with Kalman filter in sensorless control of induction motor drive," *Electrical Engineering*, vol. 99, no. 4, pp. 1151-1160.

[6] J. Talla, Z. Peroutka, V. Blahnik and L. Streit, "Rotor and stator resistance estimation of induction motor based on augmented EKF," *2015 International Conference on Applied Electronics (AE)*, Pilsen, 2015, pp. 253-258.

[7] P. Brandstetter and M. Kuchar, "Sensorless control of variable speed induction motor drive using RBF neural network," *Journal of Applied Logic*, 24, pp. 97-1a08, 2017

[8] K. Zeb, W. Uddin, A. Haider, S. Belal, C.A. Mehmood, M.A. Khan and H.J. Kim 2018, "Robust speed regulation of indirect vector control induction motor using fuzzy logic controllers based on optimization algorithms," *Electrical Engineering*, vol. 100, no. 2, pp. 787-802.

[9] S. Maiti, C. Chakraborty, Y. Hori and M. C. Ta, "Model Reference Adaptive Controller-Based Rotor Resistance and Speed Estimation Techniques for Vector Controlled Induction Motor Drive Utilizing Reactive Power," in *IEEE Transactions on Industrial Electronics*, vol. 55, no. 2, pp. 594-601, Feb. 2008.

[10] P. Cao, X. Zhang and S. Yang, "A Unified-Model-Based Analysis of MRAS for Online Rotor Time Constant Estimation in an Induction Motor Drive," in *IEEE Transactions on Industrial Electronics*, vol. 64, no. 6, pp. 4361-4371, June 2017.

[11] P. Cao, X. Zhang, S. Yang, Z. Xie and Y. Zhang, "Reactive-Power-Based MRAS for Online Rotor Time Constant Estimation in Induction Motor Drives," in *IEEE Transactions on Power Electronics*, vol. 33, no. 12, pp. 10835-10845, Dec. 2018.

[12] F. L. Mapelli, A. Bezzolato and D. Tarsitano, "A rotor resistance MRAS estimator for induction motor traction drive for electrical vehicles," *2012 XXth International Conference on Electrical Machines*, Marseille, 2012, pp. 823-829.

[13] F. L. Mapelli, D. Tarsitano and F. Cheli, "A rotor resistance MRAS estimator for EV induction motor traction drive based on torque and reactive stator power: Simulation and experimental results," *2014 International Conference on Electrical Machines (ICEM)*, Berlin, 2014, pp. 31-37.

[14] M. Hinkkanen, A.-K. Repo and J. Luomi, "Influence of magnetic saturation on induction motor model selection," *in Proc. ICEM'06*, Chania, Greece, Sept. 2006.

[15] T. Tuovinen, M. Hinkkanen and J. Luomi, "Modeling of Saturation Due to Main and Leakage Flux Interaction in Induction Machines," in *IEEE Transactions on Industry Applications*, vol. 46, no. 3, pp. 937-945, May-June, 2010.

[16] O. Lipcak, J. Bauer and P. Kobrle, "Offline Method for Determination of Nonlinear Dependence of Induction Machine Magnetising Inductance Utilising Parallel Operation of Current and Voltage Model" *accepted manuscript in IET Power Electronics*. 2019.

APPENDIX E

LIPČÁK, O. a J. BAUER. :Analysis of Voltage Distortion and Comparison of Two Simple Voltage Compensation Methods for Sensorless Control of Induction Motor:. In: *2019 IEEE 10th International Symposium on Sensorless Control for Electrical Drives*, SLED 2019. 2019 IEEE 10th International Symposium on Sensorless Control for Electrical Drives, Turin, 2019-09-09/2019-09-10. Institute of Electrical and Electronics Engineers, Inc., 2019. ISBN 9781728107660. DOI 10.1109/SLED.2019.8896258.

Author's contribution: Analysis of transistor non-linearities, measurement method proposal, analysis and interpretation of measured results, final DSP compensation algorithm validation, paper co-writing

Analysis of Voltage Distortion and Comparison of Two Simple Voltage Compensation Methods for Sensorless Control of Induction Motor

Ondrej Lipcak
Department of Electric Drives and Traction
Czech Technical University in Prague
Prague, Czech Republic
lipcaond@fel.cvut.cz

Jan Bauer
Department of Electric Drives and Traction
Czech Technical University in Prague
Prague, Czech Republic
bauerja2@fel.cvut.cz

***Abstract*—Many algorithms of induction motor sensorless control need accurate knowledge of the stator voltage vector. However, the machine is in most cases supplied by a two-level voltage-source inverter; therefore, the voltage is distorted by the inserted dead-time and also by nonlinearities of the semiconductor switches. This paper analyzes a distortion caused by the dead-time and delayed IGBT switching in terms of distorting voltage vector. An offline measurement is performed to obtain the inverter model. Then, an analysis of two simple volt-seconds-based compensation methods (compensation of the reference voltage vector and duty cycle, respectively) on the accuracy of the speed estimation of a sensorless field-oriented control based on the rotor flux model reference adaptive system is performed. The analyzed methods use either the full inverter model implemented as a look-up table or its trapezoidal approximation. Outline on computational complexity and discussion on finding optimal coefficients for the trapezoidal model are given, too.**

Keywords—induction motor, field-oriented sensorless control, model reference adaptive system, voltage-source inverter nonlinearities identification, IGBT

I. INTRODUCTION

Induction motors (IM) belong to the most popular electromechanical converters [1]. Their domination in the industrial sphere is caused mainly due to their distinct advantages such as simple construction, robustness, low maintenance, low cost, and high reliability [1]. Their disadvantage, i.e., the dependence of the rotor speed on the supply frequency that had restricted their use in variable speed drives in the past has been successfully surpassed by the development of control strategies such as field-oriented control (FOC) [1]-[4]. High computation power of today's digital signal processors (DSP) permits practical implementation of even complicated control algorithms such as speed sensorless control that becomes more and more popular [3]-[5]. In some algorithms of the sensored and many algorithms of the sensorless FOC, it is necessary to know the actual stator voltage vector applied to the motor terminals [1]-[5]. However, if a PWM controlled voltage-source inverter (VSI) is used to supply the machine, it becomes complicated and hardware demanding to measure the stator voltage directly. Because of that, the voltage is mostly determined indirectly [6].

The commonly used approach is based on using the reference voltage vector (i.e., input to the modulator) as the input to the control model [6]-[11]. This method is simple and can be quite efficient, but one must deal with a key problem, and that is a nonlinear behavior of the VSI caused by the semiconductor switches, i.e., the finite turn-on and turn-off times and the voltage drop. The voltage is further distorted by the necessary protective time, i.e., dead-time [7]-[11]. Proper compensation of the inverter most significant nonlinearities is essential in order to achieve good accuracy of the IM models and thus sensorless motor control [9]-[10],[12].

The compensation techniques can be either hardware or software-based [7]-[8]. The more preferred software compensation strategies can be generally divided into three categories [7]: current analysis-based method, estimator-based methods, and instantaneous average voltage methods (also called volt-seconds compensation methods). The average voltage methods require information about the motor currents [7]-[12] and can be further divided into square-wave models, trapezoidal models and more precise models based on a look-up table (LUT) or analytical functions that try to model the zero current clamping effect accurately [10]. The parameters for the more sophisticated models are usually obtained by the DC test or direct VSI measurement [9]-[12].

This paper analyses the influence of two simple volt-seconds based methods on the accuracy of speed estimation using sensorless FOC based on the rotor flux model reference adaptive system (RFMRAS). These methods include compensation of the reference voltage entering modulator and compensation of the duty cycle for the VSI. The compensation characteristic is evaluated using either the measured inverter model implemented as a LUT or its trapezoidal approximation. Comparison of the computational burden of the individual cases is presented, too.

This paper is organized as follows: after a brief overview of the used IM mathematical models and structure of the RFMRAS, an expression for the distorting voltage space vector taking into account current dependent distortion in each VSI leg caused by the dead-time and IGBT switching is derived. Then, the model of laboratory inverter obtained by direct measurement of the switching times for different values of the collector current is presented. After that, mathematical expressions for the two different compensation methods are presented. The paper is concluded by experimental results measured for 12 kW IM controlled by TMS320F28335. The experimental results include a comparison of the computational burden of the two different compensation methods and two different VSI models and also their influence on the accuracy of the speed estimation of the RFMRAS-based sensorless FOC. Also, the process of finding optimal coefficients for the trapezoidal model is discussed, too.

978-1-7281-0766-0/19/$31.00 ©2019 IEEE

II. Induction Motor Models

The IM models for the rotor flux oriented FOC are deducible from the IM basic equations and in this paper are expressed in the stationary ($\alpha\beta$) reference frame. The first possible model that uses the measured values of the stator currents and rotor angular speed is called the current model (subscript CM) [2]

$$\frac{\mathrm{d}\underline{\psi}_{2\mathrm{CM}}}{\mathrm{d}t} = \frac{L_\mathrm{m}R_2}{L_2}\underline{i}_1 - \frac{R_2}{L_2}\underline{\psi}_{2\mathrm{CM}} + \mathrm{j}\omega\underline{\psi}_{2\mathrm{CM}}, \tag{1}$$

where $\underline{\psi}_2$ is the rotor flux linkage space vector, $\underline{i}_1$ is the stator current space vector, R_2 is the rotor resistance, ω is the electrical angular speed of the rotor, L_m is the magnetizing inductance, L_2 is the rotor inductance and symbol j marks imaginary unit ($\mathrm{j}^2 = -1$).

The second, voltage model (subscript VM), is based on the knowledge of the current and voltage vector applied to the IM terminals [2]

$$\frac{\mathrm{d}\underline{\psi}_{2\mathrm{VM}}}{\mathrm{d}t} = \frac{L_2}{L_\mathrm{m}}\left(\underline{u}_1 - R_1\underline{i}_1 - \sigma L_1\frac{\mathrm{d}\underline{i}_1}{\mathrm{d}t}\right), \tag{2}$$

where $\underline{u}_1$ is the stator voltage space vector, R_1 is the stator resistance, L_1 is the stator inductance and σ is the leakage factor defined as $\sigma = 1 - L_\mathrm{m}^2/L_1L_2$. This model is, apart from the fact that it requires the proper knowledge of the stator voltage as input, also prone to accumulation of DC offset error. A possible solution to this negative phenomenon can be found, for example, in [13].

For the inner motor torque T_i, the following equation expressed in the stator-fixed coordinate system can be derived (p_p denotes the number of motor pole-pairs)

$$T_\mathrm{i} = \frac{3}{2}p_\mathrm{p}\frac{L_m}{L_2}\left(\psi_{2\alpha}i_{1\beta} - \psi_{2\beta}i_{1\alpha}\right). \tag{3}$$

III. Rotor Flux Model Reference Adaptive System

For sensorless control of IM, there are numerous MRAS schemes based on different motor quantities [5]. In the case of RFMRAS that is used within this paper, the following error to be minimized can be derived [14]

$$\varepsilon = \hat{\psi}_{2\alpha\mathrm{CM}}\psi_{2\beta\mathrm{VM}} - \hat{\psi}_{2\beta\mathrm{CM}}\,\psi_{2\alpha\mathrm{VM}}, \tag{4}$$

where the circumflex denotes the output values of the adaptive current model. The estimated speed is the output of the adaptation mechanism, which is a conventional PI controller. The block diagram of the RFMRAS is depicted in Fig. 1.

IV. Analysis of the Selected Inverter Nonlinearities

In the case of FOC of IM, the stator voltage vector applied to the motor terminals is mostly formed by space vector modulation (SVM) calculated by the microcontroller [2]. The microcontroller generates switching signals for the VSI drivers in such manner that the dead-time T_dt delays the control signal for switching on the respective IGBT; the control signal for turning off is sent without delay [2].

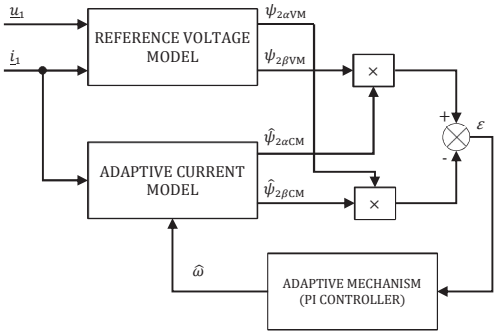

Fig. 1. Block diagram of RFMRAS

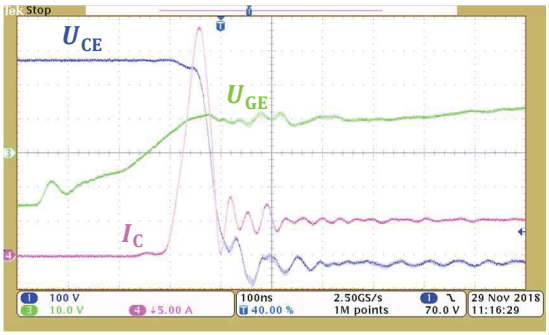

Fig. 2. Switching on IGBT module CM100DY-24NF

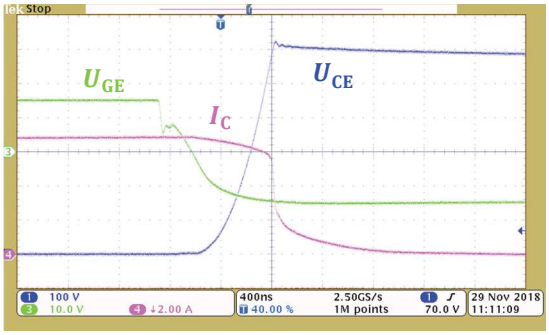

Fig. 3. Switching off IGBT module CM100DY-24NF

Fig. 2 shows the process of switching on IGBT and Fig. 3 then the process of switching off. The IGBT switching characteristics are generally dependent on the collector current I_C, junction temperature T_j, collector-emitter voltage U_CE, gate-emitter voltage U_GE, the value of the used gate resistor R_G and the load type [15]. The impact of the magnitude of the collector current on the turn-off times is usually much more significant than in the case of the turn-on times [15].

A. Distortion of the VSI Output Voltage

By a simple graphical analysis [6], it can be concluded that T_on increases and T_off decreases the resulting distortion caused by the dead-time T_dt. Therefore, we can define the so-called effective dead-time for each VSI leg as [9]

$$T_{\mathrm{eff}(x)} = T_\mathrm{dt} + T_\mathrm{on}(i_x) - T_\mathrm{off}(i_x) \quad x = \mathrm{a,b,c}. \tag{5}$$

The average distortion of the inverter line-to-neutral voltage (defined according to Fig. 4) per modulation period T_PWM can then be expressed as [9]

$$\Delta u_{x0} = \frac{T_{\mathrm{eff}(x)}}{T_\mathrm{PWM}}U_\mathrm{DC}\mathrm{sgn}(i_x) \quad x = \mathrm{a,b,c}. \tag{6}$$

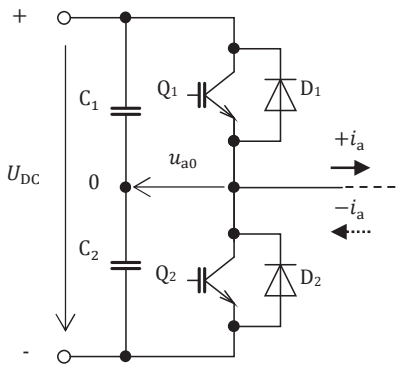

Fig. 4. One leg of two-level VSI

The switching characteristics of the IGBTs are, among others, strongly dependent on the collector current [9]. The effective dead-time for each VSI leg is, therefore, a function of the respective phase current

$$T_{\mathrm{eff}(x)} = f(i_x) \quad x = \mathrm{a,b,c}. \tag{7}$$

The distortion of the motor line-to-neutral voltages per modulation period can be expressed as a function of the distorting inverter line-to-neutral voltages as

$$\begin{bmatrix}\Delta u_\mathrm{a}\\ \Delta u_\mathrm{b}\\ \Delta u_\mathrm{c}\end{bmatrix} = \frac{1}{3}\begin{bmatrix}2\,\mathrm{sgn}\,i_\mathrm{a} & -\mathrm{sgn}\,i_\mathrm{b} & -\mathrm{sgn}\,i_\mathrm{c}\\ -\mathrm{sgn}\,i_\mathrm{a} & 2\,\mathrm{sgn}\,i_\mathrm{b} & -\mathrm{sgn}\,i_\mathrm{c}\\ -\mathrm{sgn}\,i_\mathrm{a} & -\mathrm{sgn}\,i_\mathrm{b} & 2\,\mathrm{sgn}\,i_\mathrm{c}\end{bmatrix}\cdot\begin{bmatrix}\Delta u_{\mathrm{a0}}\\ \Delta u_{\mathrm{b0}}\\ \Delta u_{\mathrm{c0}}\end{bmatrix}. \tag{8}$$

Using the definition of space vector, we can define a distorting voltage space vector as

$$\Delta\underline{u}_1 = K[1 \quad \mathbf{a} \quad \mathbf{a}^2]\cdot\begin{bmatrix}\Delta u_\mathrm{a}\\ \Delta u_\mathrm{b}\\ \Delta u_\mathrm{c}\end{bmatrix}, \tag{9}$$

where K is the transformation coefficient, and $\mathbf{a}$ is the rotational unity operator defined as $\mathbf{a} = \exp(\mathrm{j}2/3\pi)$.

Substitution of (8) to (9) yields after a few mathematical arrangements

$$\Delta\underline{u}_1 = K\begin{bmatrix}\mathrm{sgn}\,i_\mathrm{a}\\ \mathrm{sgn}\,i_\mathrm{b}\\ \mathrm{sgn}\,i_\mathrm{c}\end{bmatrix}^\mathrm{T}\cdot\begin{bmatrix}a_1 & 0 & 0\\ 0 & a_2 & 0\\ 0 & 0 & a_3\end{bmatrix}\cdot\begin{bmatrix}\Delta u_{\mathrm{a0}}\\ \Delta u_{\mathrm{b0}}\\ \Delta u_{\mathrm{c0}}\end{bmatrix}, \tag{10}$$

where

$$\begin{aligned} a_1 &= \left(\frac{2}{3} - \frac{1}{3}\mathbf{a} - \frac{1}{3}\mathbf{a}^2\right) = 1\\ a_2 &= \left(-\frac{1}{3} + \frac{2}{3}\mathbf{a} - \frac{1}{3}\mathbf{a}^2\right) = \mathbf{a}\\ a_3 &= \left(-\frac{1}{3} - \frac{1}{3}\mathbf{a} + \frac{2}{3}\mathbf{a}^2\right) = \mathbf{a}^2. \end{aligned} \tag{11}$$

Therefore, (10) can be rewritten as

$$\Delta\underline{u}_1 = K\begin{bmatrix}\mathrm{sgn}\,i_\mathrm{a}\\ \mathrm{sgn}\,i_\mathrm{b}\\ \mathrm{sgn}\,i_\mathrm{c}\end{bmatrix}^\mathrm{T}\cdot\begin{bmatrix}1 & 0 & 0\\ 0 & \mathbf{a} & 0\\ 0 & 0 & \mathbf{a}^2\end{bmatrix}\cdot\begin{bmatrix}\Delta u_{\mathrm{a0}}\\ \Delta u_{\mathrm{b0}}\\ \Delta u_{\mathrm{c0}}\end{bmatrix}, \tag{12}$$

which after separation to real and imaginary part gives

$$\begin{aligned} \Delta u_\alpha &= K\left[\mathrm{sgn}\,i_\mathrm{a}\,\Delta u_{\mathrm{a0}} - \frac{1}{2}\mathrm{sgn}\,i_\mathrm{b}\,\Delta u_{\mathrm{b0}} - \frac{1}{2}\mathrm{sgn}\,i_\mathrm{c}\,\Delta u_{\mathrm{c0}}\right]\\ \Delta u_\beta &= K\frac{\sqrt{3}}{2}[\mathrm{sgn}\,i_\mathrm{b}\,\Delta u_{\mathrm{b0}} - \mathrm{sgn}\,i_\mathrm{c}\,\Delta u_{\mathrm{c0}}]. \end{aligned} \tag{13}$$

V. Determination of the Compensation Characteristics

A practical approach is used to determine the dependence of the T_{on} and T_{off} times on the collector current I_C. The testing conditions are $U_{\mathrm{CE}} = 560$ V, $U_{\mathrm{GE}} = \pm 15$ V, $R_\mathrm{G} = 6.8\,\Omega$, $T_\mathrm{j} = 25$ °C and an inductive load. The laboratory VSI contains IGBT modules CM100DY-24NF from Mitsubishi Electric. Concept 2SD106AI-17 circuits are used as gate drivers. The maximum continuous collector current of the IGBT modules is $I_\mathrm{C} = 100$ A and the maximum collector-emitter voltage is $U_{\mathrm{CE}} = 1{,}2$ kV. A snubber capacitor 1000 V; 1.5 μF is connected to each of the modules. The T_{on} time is measured as the delay between the rising edge of the microcontroller's output control signal and the actual transition of the collector-emitter voltage U_{CE}. The transition of the U_{CE} is measured in the instant when $U_{\mathrm{CE}} = 0.5U_{\mathrm{DC}}$, which in the case of a linear transition approximates the average voltage value per modulation period [9]. The T_{off} time is measured as the interval between the falling edge of the microcontroller's output control signal and the actual transition of the collector-emitter voltage U_{CE}. The transition of the U_{CE} is also measured in the instant when $U_{\mathrm{CE}} = 0.5U_{\mathrm{DC}}$.

Fig. 5 shows the measured dependence of the effective dead-time T_{eff} calculated according to (5) on the collector current I_C. In accordance with [10], the point (0,0) is added to the measured values. The actual dead-time inserted by the microcontroller was chosen to be $T_{\mathrm{dt}} = 2$ μs. For the purpose of simplification, the measured characteristic is sometimes approximated by a trapezoidal model given by a following piecewise function

$$T_{\mathrm{eff}}(I_\mathrm{C}) = \begin{cases} kI_\mathrm{C} & \text{for } I_\mathrm{C} \le I_{\mathrm{th}}\\ kI_{\mathrm{th}} & \text{for } I_\mathrm{C} > I_{\mathrm{th}}. \end{cases} \tag{14}$$

For the collector current smaller than some threshold value I_{th}, the compensation characteristic is linear with tangent k, and for a higher value than the threshold current, the compensation characteristic is constant.

Fig. 6 shows the visualization of the voltage distortion caused by the dead-time and switching delay of the IGBTs for $T_{\mathrm{PWM}} = 100$ μs, $U_{\mathrm{DC}} = 540$ V and $\cos\varphi = 0.7$. The current vector amplitude is equal to 0.3 p.u., the voltage vector amplitude is equal to 0.1 p.u. and the synchronous frequency is equal to 0.1 p.u. which corresponds to the low-speed operation of IM. The distorting voltage vector is calculated using (13) based on the measured data in Fig. 5.

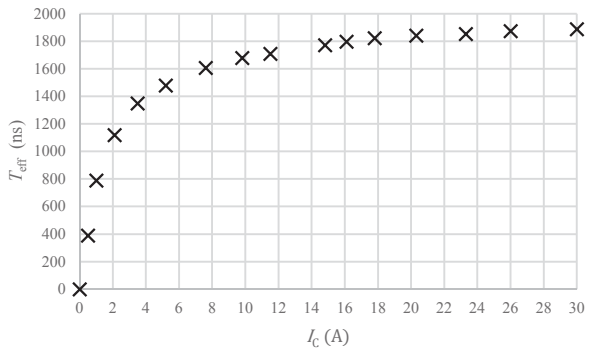

Fig. 5. Measured dependence of the effective dead-time on the collector current

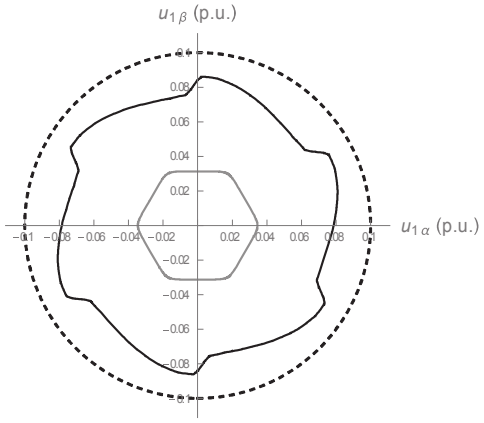

Fig. 6. Reference voltage (dashed black), distorting voltage (grey) and the resulting voltage (black solid); $U_{\mathrm{DC}} = 540$ V, $T_{\mathrm{PWM}} = 100$ µs, $\cos\varphi = 0.7$, current amplitude 0.3 p.u., voltage amplitude 0.1 p.u. and synchronous frequency 0.1 p.u.

Fig. 7 shows the phase error between the distorted and the reference voltage vector for the same operating conditions as in the case of Fig. 6. The solid line represents the instantaneous phase error and the dashed line the average phase error per one electrical revolution.

VI. Basic Voltage Compensation Methods

Among the simplest algorithms for the voltage compensation, we can include methods that either adjust the reference voltage vector entering the modulator or that adjust the duty cycle for the respective VSI leg. In the first case, the distorting voltage components (13) are added to the components of the reference voltage vector

$$\begin{aligned} u'_{1\alpha} &= u^*_{1\alpha} + \Delta u_{1\alpha} \\ u'_{1\beta} &= u^*_{1\beta} + \Delta u_{1\beta}. \end{aligned} \tag{15}$$

For SVM, it is convenient to define the duty-cycle d_x for each VSI leg such that the average value of the corresponding inverter line-to-neutral voltage u_{x0} per modulation period equals to $-U_{\mathrm{DC}}/2$ if $d_x = 0$ and $+U_{\mathrm{DC}}/2$ if $d_x = 1$. This can be mathematically expressed as

$$u_{x0} = (2d_x - 1)\frac{U_{\mathrm{DC}}}{2} \quad x = \mathrm{a, b, c.} \tag{16}$$

Using (6), the relationship between the reference u^*_{x0} and the compensated inverter line-to-neutral voltage u'_{x0} can be written as

$$u'_{x0} = u^*_{x0} + \frac{T_{\mathrm{eff}(x)}}{T_{\mathrm{PWM}}} U_{\mathrm{DC}} \mathrm{sgn}(i_x) \quad x = \mathrm{a, b, c.} \tag{17}$$

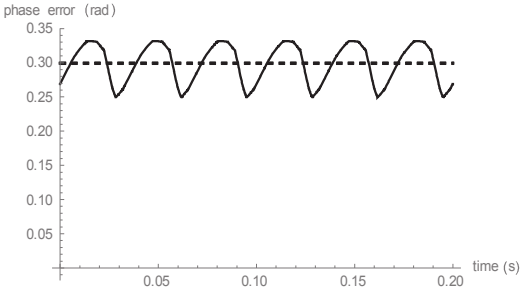

Fig. 7. Phase error between the distorted and reference voltage vector per one electrical revolution – instantaneous error (solid), average error (dashed); $U_{\mathrm{DC}} = 540$ V, $T_{\mathrm{PWM}} = 100$ µs, $\cos\varphi = 0.7$, current amplitude 0.3 p.u., voltage amplitude 0.1 p.u. and synchronous frequency 0.1 p.u.

Dividing (17) by $U_{\mathrm{DC}}/2$ and substituting for u'_{x0} and u^*_{x0} from (16) yields the following relation between the reference d^*_x and the compensated duty cycle d'_x

$$d'_x = d^*_x + \frac{T_{\mathrm{eff}(x)}}{T_{\mathrm{PWM}}} \mathrm{sgn}(i_x) \quad x = \mathrm{a, b, c.} \tag{18}$$

The compensation characteristic $T_{\mathrm{eff}(x)}$ can then be either based on the measured values of the effective dead-time (Fig. 5) or the equation (14) of the simplified trapezoidal model.

VII. Experimental Results

The different compensation techniques presented in Chap. VI are tested in terms of accuracy of the sensorless FOC based on the RFMRAS. The voltage model makes the sensorless RFMRAS FOC vulnerable to low-speed, low-torque operation when the reference stator voltage becomes low, and, therefore, the distortion of the reference voltage by the VSI nonlinearities becomes significant.

A. Experimental Setup

The sensorless RFMRAS FOC was implemented in the C language into TMS320F28335 Delphino DSP. The clock frequency was set to 150 MHz, and the calculation loop of the FOC algorithm was selected to be 100 µs, which corresponds to 10 kHz PWM. As a drive, machine set with 12 kW IM coupled with 8.8 kW separately excited DC motor has been used. The nameplate values of the IM along with the IM parameters measured by the conventional no-load and locked-rotor tests are given in Tab. 1.

B. Determination of the Optimal Parameters for the Trapezoidal Model

The parameters for the piecewise function (14) were obtained by minimization of the following error by the simulated annealing algorithm

$$e(k, I_{\mathrm{th}}) = \left| \left|\Delta\underline{\tilde{u}}_1\right| - \left|\Delta\underline{\hat{u}}_1(k, I_{\mathrm{th}})\right| \right|, \tag{19}$$

where $\left|\Delta\underline{\tilde{u}}_1\right|$ is the amplitude of the distorting voltage vector calculated using the measured compensation characteristic in Fig. 5 and $\left|\Delta\underline{\hat{u}}_1\right|$ is the amplitude of the distorting voltage vector calculated using the approximation of the measured characteristic by (14). The conditions were the same as in the case of Fig. 6. The resulting values are $I_{\mathrm{th}} = 2.35$ A and $k \cdot I_{\mathrm{th}} = 1.710$ µs. Fig. 8 shows the difference between the reference and actual voltage when the compensation characteristic is approximated by the piecewise function, and the parameters are obtained by minimization of (19). The price paid for the simplification is that the resulting voltage (solid line) contains higher harmonics that, in principle, cannot be eliminated by the trapezoidal model.

Nominal power	12 kW	R_1	0.377 Ω
Nominal current	22 A	R_2	0.25 Ω
Nominal voltage	380 V	$L_{1\sigma}$	0.00227 H
Nominal frequency	50 Hz	$L_{2\sigma}$	0.00227 H
Nominal power factor	0.8	R_{Fe}	202.1 Ω
Nominal speed	1460 min^{-1}	L_{m}	0.078 H

Tab. 1. IM nameplate parameters and measured values used by the mathematical models

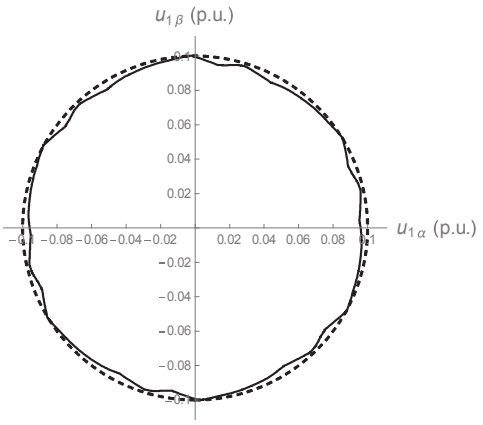

Fig. 8. Reference voltage (dashed) and compensated voltage (solid) with piecewise function; $I_{\mathrm{th}} = 2.35\ \mathrm{A}$, $k \cdot I_{\mathrm{th}} = 1.709\ \mu\mathrm{s}$, $U_{\mathrm{DC}} = 540\ \mathrm{V}$, $T_{\mathrm{PWM}} = 100\ \mu\mathrm{s}$, $\cos\varphi = 0.7$; current amplitude 0.3 p.u., voltage amplitude 0.1 p.u. and synchronous frequency 0.1 p.u.

C. *Comparison of the Computational Burden of the Different Compensation Methods*

For the implementation of algorithms for real-time control, it is also necessary to take into account the computational burden imposed on the DSP. For this reason, a comparison has been made for the two different compensation techniques based on (15) and (18), respectively, that were either based on the linear interpolation between the measured data $T_{\mathrm{eff}} = f(I_{\mathrm{C}})$ or the simplified approximation by the piecewise function (14).

Tab. 2 shows the measured computational times for the individual cases. It can be seen that adjusting the duty-cycle is about 1 µs less computationally demanding for both the interpolation and the piecewise function. The interpolation is then approximately 2.5 more time demanding than the evaluation of the piecewise function. It is worth noticing that in order to save the computational time in the case of the interpolation, the array was not always being searched from the beginning but because the current in IM is a continuous quantity, the searching started from the array index remembered in the previous step.

D. *Accuracy of the RFMRAS-Based Speed Estimation*

The individual compensation methods and compensation characteristics were tested in terms of accuracy of the estimated speed by RFMRAS during the drive reversal from $50\ \mathrm{rad}\cdot\mathrm{s}^{-1}$ to $-50\ \mathrm{rad}\cdot\mathrm{s}^{-1}$. The reference rotor flux was set to 0.8 Wb. The results are shown in Fig. 9. to Fig. 13. In the figures, the dashed line corresponds to the reference speed, the grey line then denotes measured, and the black line estimated rotor speed.

First of all, it can be seen that the voltage compensation (Fig. 9 to Fig. 12) in all the cases significantly improves the drive behavior compared to the case without compensation (Fig. 13) where the estimated speed exhibits quite heavy oscillations. Otherwise, based on the observations of Fig. 9 to Fig. 12 it can be concluded that both the compensation of the reference voltage vector and the duty cycle seem equivalent, which is an expected result. Concerning the difference between the compensation characteristics based on LUT (Fig. 9 and Fig. 11) and trapezoidal model (Fig. 10 and Fig. 12), it can be stated, that in both cases the estimated speed exhibits a drop when approaching the value $10\ \mathrm{rad}\cdot\mathrm{s}^{-1}$ that is more significant for the trapezoidal model. The absolute value of the maximum difference between the measured and estimated speed for Fig. 9 to Fig. 13 is captured in Tab. 3.

Interpolation using (15)	9.9 µs
Piecewise function using (15)	4.5 µs
Interpolation using (18)	8.8 µs
Piecewise function using (18)	3.4 µs

Tab. 2. The average computational time of the voltage compensation methods

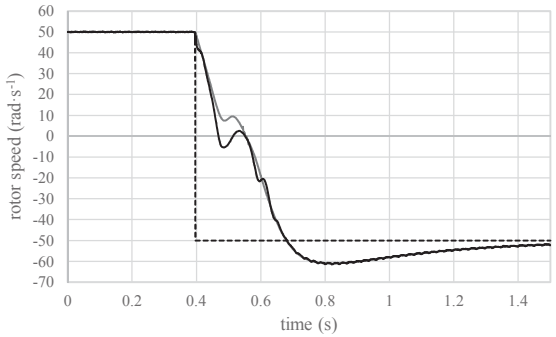

Fig. 9. Drive reversal from $50\ \mathrm{rad}\cdot\mathrm{s}^{-1}$ to $-50\ \mathrm{rad}\cdot\mathrm{s}^{-1}$; compensation of the reference voltage vector based on LUT; black dashed – reference speed, grey – measured speed, black – estimated speed; reference rotor flux 0.8 Wb

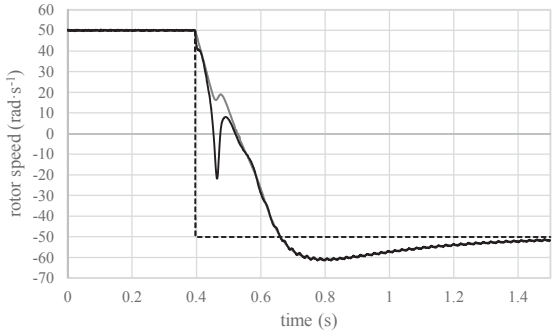

Fig. 10. Drive reversal from $50\ \mathrm{rad}\cdot\mathrm{s}^{-1}$ to $-50\ \mathrm{rad}\cdot\mathrm{s}^{-1}$; compensation of the reference voltage vector based on the trapezoidal model; black dashed – reference speed, grey – measured speed, black – estimated speed; reference rotor flux 0.8 Wb

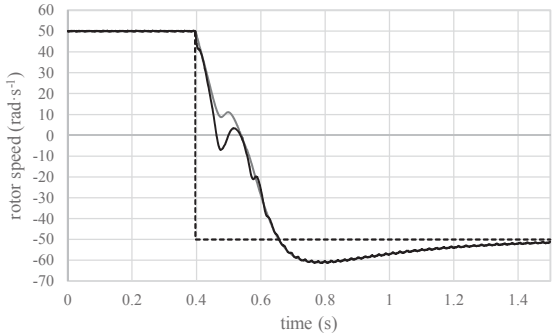

Fig. 11. Drive reversal from $50\ \mathrm{rad}\cdot\mathrm{s}^{-1}$ to $-50\ \mathrm{rad}\cdot\mathrm{s}^{-1}$; compensation of the duty-cycle based on LUT; black dashed – reference speed, grey – measured speed, black – estimated speed; reference rotor flux 0.8 Wb

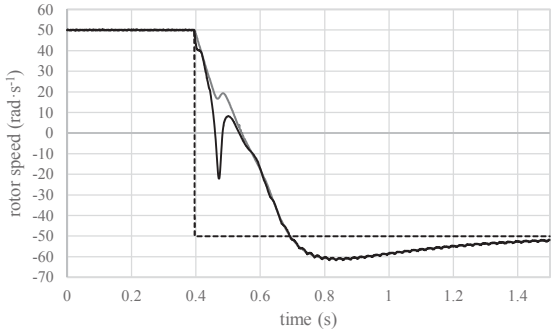

Fig. 12. Drive reversal from $50\ \mathrm{rad}\cdot\mathrm{s}^{-1}$ to $-50\ \mathrm{rad}\cdot\mathrm{s}^{-1}$; compensation of the duty-cycle based on the trapezoidal model; black dashed – reference speed, grey – measured speed, black – estimated speed; reference rotor flux 0.8 Wb

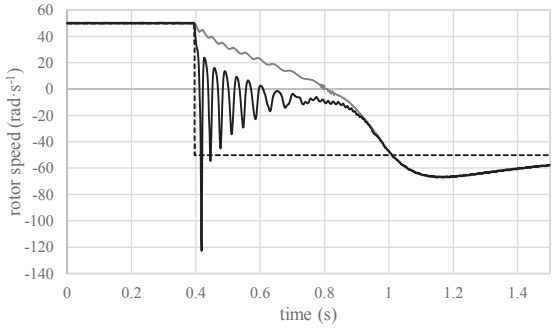

Fig. 13. Drive reversal from $50\ \mathrm{rad}\cdot\mathrm{s}^{-1}$ to $-50\ \mathrm{rad}\cdot\mathrm{s}^{-1}$; without compensation; black dashed – reference speed, grey – measured speed, black – estimated speed; reference rotor flux 0.8 Wb

Interpolation using (15)	13.6 rad ·s^{-1}
Piecewise function using (15)	38.5 rad ·s^{-1}
Interpolation using (18)	15.9 rad ·s^{-1}
Piecewise function using (18)	40 rad ·s^{-1}
Without compensation	167 rad ·s^{-1}

Tab. 3. The absolute value of the difference between the estimated and measured speed for Fig. 9. to Fig. 13.

VIII. Conclusion

In this paper, two simple compensation techniques of the voltage distortion caused by the dead-time and delayed IGBT switching (compensation of the reference voltage vector and duty-cycle, respectively) were tested in terms of the accuracy of the estimated IM speed by RFMRAS and computational complexity. As for the compensation characteristics, full inverter model measured by the direct measurement on the laboratory VSI implemented as LUT and its trapezoidal approximation implemented as piecewise function were considered. It has been shown that the compensation of the duty-cycle gives the same results as the compensation of the reference voltage but is, at the same time, less computationally demanding. By mathematical analysis of the distorting voltage vector, it was also shown that the trapezoidal model could not eliminate the higher harmonics even if its parameters were determined by mathematical optimization method. The trapezoidal model exhibits slightly worse performance compared to the LUT but its implementation can be considered if it is desirable to further reduce the necessary computational time. The speed estimation and the overall drive performance was significantly deteriorated when the voltage distortion was not compensated, which shows the significance of proper voltage compensation for sensorless control.

Acknowledgment

Research presented in this paper was supported by the Technology Agency of the Czech Republic under project No. TE02000103 and by the Student Grant Competition of the Czech Technical University in Prague under grant No. SGS19/065/OHK3/1T/13.

References

[1] F. Giri, *AC Electric Motors Control: Advanced Design Techniques and Applications*. 2. Aufl. ed. New York: Wiley; 2013.

[2] N.P. Quang and J. Dittrich, *Vector Control of Three-Phase AC Machines: System Development in the Practice*. 1. Aufl. ed. Berlin, Heidelberg: Springer-Verlag; 2008.

[3] P. Vas, *Sensorless vector and direct torque control*. New York: Oxford University Press; 1998.

[4] M. Popescu, *Induction Motor Modelling for Vector Control Purposes*, Helsinki University of Technology, Laboratory of Electromechanics, Report, Espoo 2000, 144 p.

[5] R. Kumar, S. Das, P. Syam and A. K. Chattopadhyay, "Review on model reference adaptive system for sensorless vector control of induction motor drives," in *IET Electric Power Applications*, vol. 9, no. 7, pp. 496-511, 8 2015.

[6] S. Bolognani and M. Zigliotto, "Self-commissioning compensation of inverter non-idealities for sensorless AC drives applications," *2002 International Conference on Power Electronics, Machines and Drives (Conf. Publ. No. 487)*, Sante Fe, NM, USA, 2002, pp. 30-37.

[7] Y. Wang, W. Xie, X. Wang and D. Gerling, "A Precise Voltage Distortion Compensation Strategy for Voltage Source Inverters," in *IEEE Transactions on Industrial Electronics*, vol. 65, no. 1, pp. 59-66, Jan. 2018.

[8] Z. Shen and D. Jiang, "Dead-Time Effect Compensation Method Based on Current Ripple Prediction for Voltage-Source Inverters," in *IEEE Transactions on Power Electronics*, vol. 34, no. 1, pp. 971-983, Jan. 2019.

[9] D. E. Salt, D. Drury, D. Holliday, A. Griffo, P. Sangha and A. Dinu, "Compensation of Inverter Nonlinear Distortion Effects for Signal-Injection-Based Sensorless Control," in *IEEE Transactions on Industry Applications*, vol. 47, no. 5, pp. 2084-2092, Sept.-Oct. 2011.

[10] G. Shen, W. Yao, B. Chen, K. Wang, K. Lee and Z. Lu, "Automeasurement of the Inverter Output Voltage Delay Curve to Compensate for Inverter Nonlinearity in Sensorless Motor Drives," in *IEEE Transactions on Power Electronics*, vol. 29, no. 10, pp. 5542-5553, Oct. 2014.

[11] M. Seilmeier, C. Wolz and B. Piepenbreier, "Modelling and model based compensation of non-ideal characteristics of two-level voltage source inverters for drive control application," *2011 1st International Electric Drives Production Conference*, Nuremberg, 2011, pp. 17-22.

[12] M. El-daleel and A. Mahgoub, "Accurate and simple improved lookup table compensation for inverter dead time and nonlinearity compensation," *2017 Nineteenth International Middle East Power Systems Conference (MEPCON)*, Cairo, 2017, pp. 1358-1361.

[13] O. Lipcak and J. Bauer, "Optimization of Voltage Model for MRAS Based Sensorless Control of Induction Motor," presented at the 5th International Conference on Advance Engineering – Theory and Applications, Ostrava, Czech Republic, 2018.

[14] C. Schauder, "Adaptive speed identification for vector control of induction motors without rotational transducers," in *IEEE Transactions on Industry Applications*, vol. 28, no. 5, pp. 1054-1061, Sept.-Oct. 1992.

[15] Mitsubishi Electric. *IGBT Modules Application Note, The 5th Generation [CSTBT™] IGBT Chip Use, 12NF/24NF/24A series*. Mar. 2014. Available at: http://www.mitsubishielectric.com/semiconductors/files/manuals/igbt_note_e.pdf, accessed 10th December 2018.